The University of Nottingham

Mitigating the Scintillation Effect on GPS Signals Based on Parameters from Standard Geodetic Receivers

Chendong Li

BEng (Hons)

Thesis submitted to the University of Nottingham for the degree of Doctor of Philosophy

December 2021

Doctoral research is also a journey for mentality cultivation.

Abstract

With the increase of human demands the development of science and technology, the Global Navigation Satellite System (GNSS) has become an increasingly vital technology. Signals broadcast by GNSS are affected by various errors during propagation, where the ionosphere is one of the largest error sources. Though the first order ionospheric error can be mitigated through the method of ionosphere-free combination, it is still hard to globally predict and mitigate the effect of ionospheric scintillation, a phenomenon caused by the irregularities in the ionosphere. Scintillation can lead to fluctuations in signal phase and strength, thus resulting in measurement errors, unreliable signal tracking performance, cycle slips, and even losses of lock. These effects are particularly significant in applying Precise Point Positioning (PPP), a positioning technique where the reference station is not required. The scintillation effect has been significantly mitigated based on scintillation parameters S4 and σ_ϕ in past methods, generated with high-rate GNSS data (typically at 50 Hz). However, the availability of high-rate data is less, thus limiting the global scintillation research. This leads to the purpose of this thesis, using parameters obtained with the low-rate data to mitigate the scintillation effect. The parameters are Multipath Parameter (MP) and rate of change of Total Electron Content Index (ROTI) in this thesis, which can be computed from 1/30 Hz data.

First, the research investigated the relationship between the parameters obtained from low-rate data (i.e., MP and ROTI), and scintillation parameters S4, σ_ϕ. Both temporal and spatial relationships were evaluated based on the statistical tools Structural Similarity (SSIM), Pearson Correlation Coefficient (CC), and variograms. Based on the results, it was suggested that MP and ROTI are spatiotemporally correlated with S4 and σ_ϕ during scintillation events. However, it was uncertain whether the observed scintillation events were caused by the real scintillation or false alarms due to the multipath effect. Thus, an integrated methodology to distinguish the scintillation event from multipath was developed in the second research part of this thesis. According to the results, all the detected scintillation events are real, and the methodology has more functionality than past methods, where the hybrid event can be identified for the first time and scintillation parameters are not necessary. Finally, a method to mitigate the effects of

scintillation on PPP is developed based on MP, ROTI, S4 and σ_ϕ, where the scintillation parameters are optional. Three strategies are proposed: satellite removal, observation removal, and weighting. The results show that the performances of observation removal and weighting strategies are comparable to or even better than those of past methods. The highest improvements obtained using the two strategies are 91.7% and 93.1%, respectively. Furthermore, MP and ROTI can mitigate scintillation more substantially than S4 and σ_ϕ sometimes, and vice versa.

Acknowledgments

First, I would like to express my thanks to my supervisors, Dr. Nicholas Hamm, Dr. Craig Hancock, Dr. Sreeja Veettil and Dr. Chong You for their help, guidance and advice during my doctoral research period. Especially Nick and Craig, I can receive suggestions from them whenever I get into trouble. Though I went through the supervisor change due to Craig's leave, I did not experience anything bad, which is not a typical situation according to what I heard from others. On the contrary, I felt like that I had two first supervisors that was a wonderful experience. I would like to express my most profound appreciation to Sreeja for commenting on the details of my writing every time I finished the paperwork.

CIGALA/CALIBRA project funded by the European Commission (EC) and International GNSS Service are gratefully acknowledged for providing scintillation data and GPS products, respectively.

I wish also to express my gratitude to my internal examiners Prof. Terry Moore and Dr. Panagiotis Psimoulis for their comments and feedback on my work during annual reviews from a different perspective so that I can further improve my work.

Also, I am grateful for the sincere cooperation of Dr. Dongsheng Zhao, Prof. Galera Monico, Dr. Tu Tang, Dr. Francis Ochieng, Prof. Gethin Roberts, Yuchen Yang and Caleb Kelly for papers and patents and I am honored to spend the time during my doctoral period with them. Mr. Huib de Ligt was acknowledged for his help with programming when I began with my Ph.D. Additionally, I want to thank all friends I met at UNNC for their moral supports that made my doctoral life more interesting.

I also acknowledge UNNC for providing financial support and research space during the first three years of my doctoral period.

Last but not least, I would always thank my parents for their mental and material support

throughout my whole Ph.D. They are the most extensive support for me to complete my Ph.D. A particular thank goes to my girlfriend Ella Liu who helped me get through the sad moments.

Contents

List of Figures

List of Tables

Abbreviations

BDS	BeiDou Navigation Satellite System
BLIMF	Band-Limited IMFs
C/N_0	Carrier to Noise Ratio
CC	Correlation Coefficient
CCSTDDEV	Standard Deviation Code/Carrier Divergence
CEEMD	Complementary Ensemble Empirical Mode Decomposition
CEIS	Convective Equatorial Ionospheric Storm
CM	Covariance Matrices
CMC	Iono-Corrected Code Minus Carrier
CME	Coronal Mass Ejection
CNAV	Civil Navigation
COSPAR	Committee of Space Research
CoV	Coefficient of Variation
CSRS	Canadian Spatial Reference System
CTIM	Coupled Thermosphere-Ionosphere Model
DCBs	Differential Code Biases
DLL	Delay Lock Loop
DOP	Dilution of Precision
EC	European Commission
ECEF	Earth-Centered Earth-Fixed
EEMD	Ensemble Empirical Mode Decomposition
EKF	Extended Kalman Filter
EMD	Empirical Mode Decomposition
ESF	Equatorial Spread F
ET	Extreme Threshold
FAIM	Fully Analytic Low- and Mid-Latitude Ionospheric Model
FLIP	Field Line Interhemispheric Plasma Model
FT	First Threshold

GAPS	Global Positioning System Analysis and Positioning Software
GDI	Gradient Drift Instability
GDOP	Geomertic Dilution of Precision
GLONASS	Global Orbiting Navigation Satellite System
GNSS	Global Navigation Satellite System
GPS	Global Positioning System
GTIM	Global Theoretical Ionospheric Model
HF	High Frequency
I	In-phase
ICED	Ionospheric Conductivity and Electron Content
ICEEMDAN	Improved Complementary Ensemble Empirical Mode Decomposition
IERS	International Earth Rotation and Reference System Services
IF	Ionosphere-Free
IGS	International GNSS Service
IMF	Intrinsic Mode Functions
IMUs	Inertial Measurement Unites
IPP	Ionospheric Piece Point
IQR	Interquartile Range
IRI	International Reference Ionosphere
ISMR	Ionospheric Scintillation Monitoring Receiver
KF	Kalman Filter
LF	Low Frequency
LNAV	Legacy Navigation
LOS	Light of Sight
LS	Least Square
LSQ	Least Square Stochastic
MBOC	Multiplexed Binary Offset Carrier
MCS	Multicomponent Signal
MEOs	Medium Earth Orbits
MF-DFA	Multifractal-Detrended Fluctuation Analysis

MP	Multipath Parameter
MPF	Ionosphere-Free Combination of Multipath Parameter 1 and Multipath Parameter 2
MT	Mild Threshold
NBP	Narrow Band Power
NWRA	NorthWest Research Associates
PCV	Phase Center Variations
PEA	Parameter Value against Elevation and Azimuth
PIM	Parameterized Real Time Ionospheric Specification Model
PLL	Phase Lock Loop
PPP	Precise Point Positioning
PRN	Pseudo Random Noise
Q	Quadra-phase
QC	Quality Control
RAIM	Receiver Autonomous Integrity Monitoring
RHCP	Right-Hand Circularly Polarized
RINEX	Receiver Independent Exchange Format
RMSE	Root Mean Square Error
ROT	Rate of Total Electron Content
ROTI	Rate of Change of Total Electron Content Index
RT	Rayleigh-Taylor
RTK	Real-Time Kinematic
SA	Selective Availability
SAPS	Subauroral Polarization Streams
STD	Standard Deviation
SEDs	Storm-Enhanced Densities
SI	Signal Intensity
SLIM	Semi-empirical Low-Latitude Ionospheric Model
SNR	Signal-to-Noise Ratio
SSIM	Structural Similarity

ST	Second Threshold
TDIM	Time Dependent Ionospheric Model
TEC	Total Electron Content
TEQC	Translation, Editing, and Quality Checking
TGI	Temperature Gradient Instability
TIGCM	Thermosphere-Ionosphere Global Circulation Model
UHF	Ultra High Frequency
URSI	International Radio Science Union
UV	Ultra Violet
VHF	Very High Frequency
VMD	Variational Mode Decomposition
WBMOD	Wide Band Model
WBP	Wide Band Power

1. Introduction

Global Navigation Satellite System (GNSS) is a general term for navigation systems that offer global or regional positioning services, which includes four prominent constellations, United States of America's Global Positioning System (GPS), Russian Federation's Global Orbiting Navigation Satellite System (GLONASS), Europe's Galileo and China's BeiDou Navigation Satellite System (BDS) (Hofmann-Wellenhof et al. 2008). Any geographical location on Earth can be accurately mapped using a GNSS receiver recording these satellite signals. GNSS has become vital for various commercial, civil and military applications worldwide, including, for instance, in structural health monitoring, navigation services for vehicles, civil aviation, and precision agriculture. A series of these applications can make a considerable impact on the continuous development of the world economy.

With the growth of human demands, increasingly higher accuracy and availability of GNSS are required for some advanced applications such as deformation monitoring, precision agriculture and autonomous driving. However, a number of errors still exist that affect the operation of GNSS. As the GNSS signals propagate from satellites to receivers, they pass through the Earth's atmosphere, encompassing the troposphere and ionosphere (Karaim et al. 2018). The neutral gas molecules in this layer can cause refraction and reflection effects on temperature, pressure, and moisture signals for the troposphere. As neutral molecules in the outer atmosphere are ionized by solar ultraviolet rays, an ionized layer called the ionosphere is formed. When signals pass through the ionosphere, they are delayed by dense free electrons and ions. Both the tropospheric and first-order ionospheric delays can be modeled to mitigate the resulting errors to a certain extent. However, a number of irregularities caused by the interaction of the solar wind and the Earth's geomagnetic field also exist in the ionosphere, which leads to detrimental effects on GNSS operation.

Ionospheric scintillation is one of the most common effect on GNSS signals caused by the ionosphere, which mainly occurs in the auroral to polar regions and equatorial to low latitude

areas. The Kwajalein Island in the Pacific region and the Ascension Island in the South Atlantic Ocean have the most substantial scintillation impacts (Klobuchar 1996). Scintillation appears more often during the local post-sunset period than other periods. Moreover, during equinoxes there is a frequent occurrence of scintillation. Solar and geomagnetic activities vitally affect the occurrence of scintillation. Thus, scintillation occurs considerably more frequently during the peak of the solar cycle. In addition, scintillation primarily occurs at low and high latitude areas and is rarely observed at mid-latitude regions. According to de Oliveira Nascimento Brassarote et al. (2017), scintillation is most active between September and March over Brazilian longitudes that are the equatorial to low latitude regions and weakest in the other months. However, the situation is reversed in the equatorial regions of the Northern Hemisphere due to the opposite seasons. The influence of season is slight in high latitude regions. According to Jiao et al. (2013), scintillation events are typically more potent and longer-lasting in the spring and the autumn. According to Van Dierendonck et al. (1993), two parameters, S4 and σ_ϕ can be used to describe ionospheric scintillation. S4 and σ_ϕ respectively represent the measure of scintillation on amplitude and phase of the GNSS signals, which are calculated through the standard deviation of signal power normalized by the mean value and standard deviation of the carrier phase, respectively. Pi et al. (2017) showed that the signal intensity fluctuates more significantly than phase during scintillation. Thus, S4 values are usually larger than σ_ϕ values at low latitude regions. The two parameters can only be obtained from high-rate data with a typical frequency of 50 Hz, where it is relatively hard to acquire high-rate data compared to low-rate data. It was proposed that the S4 index can be obtained from 10 Hz data(Rodrigues and Moraes 2019). Then, an alternative amplitude scintillation index namely S4c that is highly correlated with S4 can be obtained from 1 Hz data (Luo et al. 2020). Then, an alternative phase scintillation index namely $\sigma_\emptyset$ that is highly correlated with σ_ϕ can also be computed from the 1 Hz data proposed by Nguyen et al. (2019). Hence, it is possible to research scintillation using conventional GNSS receivers already. However, using data with lower frequency can further popularize the scintillation research. According to IGS (2021), on average, about 500 stations provide 1/30 Hz data, while fewer than 170 stations provide 1 Hz data per day. In addition, 30s data has been available since 1991, while 1 Hz data became available in 2001. Moreover, the volume of one-day 1/30 Hz data is about 2.5 Mbytes, while that of one-day 1 Hz data is around

20 Mbytes. Thus, it is significantly more convenient to use 1/30 Hz data than 1 Hz data to research scintillation in terms of spatial coverage, temporal coverage and data volume. Scintillation can result in GNSS signal degradation or even failure to lock the receiver to the satellite signals. The corresponding satellites cannot be used in position estimation under this condition (Sreeja et al. 2011a). The positioning may completely fail when the number of tracked satellites is less than four, the minimum number required in the positioning algorithm. In southern China, many cities, like Sanya and Hong Kong, are located in the low latitude area, where scintillation occurs actively and frequently. What is more, scintillation is even detected in the mid-latitude area in China (Fang et al. 2012). According to He et al. (2016), signal acquisition and tracking could be degraded by more than 13% under strong scintillation, which leads to positioning errors of centimeters or even meters. This may have destructive effects on accurate positioning applications. Based on the current situation, it is necessary to develop an effective method to reduce the effects of scintillation.

Though a series of methods based on scintillation indices S4 and σ_ϕ have been proposed to mitigate the scintillation effects on positioning (Aquino et al. 2007; Aquino et al. 2009; Park et al. 2017; Sreeja et al. 2020), high-rate data that can derive S4 and σ_ϕ are less available than low-rate data, which limits the application of the above-mentioned approaches. Thus, to research the scintillation mitigation on a global scale, parameters that can be generated from low-rate data and characterize scintillation are needed to mitigate scintillation effects. In previous research, it was found that the rate of change of Total Electron Content Index (ROTI) can be a proxy to S4 and σ_ϕ to a certain degree, where the relationship between ROTI and scintillation is not present sometimes, however (Basu et al. 1999; Yang and Liu 2016; Carrano et al. 2019; Olwendo et al. 2018; Acharya and Majumdar 2019). Thus, another parameter should be proposed to better characterize scintillation together with ROTI in this thesis. The research on the relationship between multipath and scintillation was initiated by Van Dierendonck et al. (1993), where the multipath effect caused the inflation of scintillation parameters. This conclusion was supported by Romano et al. (2013), where S4 was contaminated by multipath, especially at an elevation lower than 30°. Then, the relationship between a parameter, namely Multipath Parameter (MP) from Translation, Editing, and Quality Checking (TEQC) software and σ_ϕ was found by

Hancock et al. (2017), where it was the first time that the parameter of multipath was shown to be contaminated by scintillation. Furthermore, both MP and ROTI (standard parameters) can be extracted from the data with 1/30 or 1/60 Hz frequency. Thus, MP and ROTI satisfy the basic requirements to replace S4 and σ_ϕ for the global characterization and mitigation of scintillation. However, the relationship between standard parameters, especially MP, and scintillation parameters should be further investigated to lay the theoretical empirical foundation for scintillation mitigation on the basis of the former. Thus, the spatiotemporal relationship between the S4 and σ_ϕ, MP and ROTI should be investigated when a high variability of scintillation parameters was observed.

Precise Point Positioning (PPP) is one of the techniques applied for GNSS data processing, where the reference station is unnecessary compared with conventional techniques. PPP is sensitive to loss of lock as it needs to converge for the first 20-60 minutes (Xiang et al. 2020). Thus, PPP is vulnerable to scintillation that typically causes loss of lock. Therefore, the PPP output is suitable to show the effect of scintillation and corresponding scintillation mitigation results. In PPP, the Kalman filter (KF), similar to Least Square (LS), is a typical algorithm for converging the original observations to a stable and accurate position during the GNSS positioning process. According to Tanir Kayikçi and Karaaslan (2017), the calculations using the KF are relatively faster than LS, and KF is more sensible to evaluate the short-term variation of parameters, where parameters of ionosphere typically change instantaneously. Thus, KF is more suitable for further algorithms development in this thesis.

1.1. Aim

For current GNSS applications, especially those requiring high accuracy, scintillation is one of the urgent problems to be solved. In addition, scintillation parameters are computed from high-rate data that is less available than low-rate. Hence, the ultimate goal of this Ph.D. thesis is to use MP and ROTI to develop novel mitigation strategies against scintillations for the PPP technique. Based on this, the research objectives of this Ph.D. thesis are stated below.

1.2. Objectives

Then, the critical objectives addressed in this thesis are listed as follow:

1) To investigate the visual and quantitative spatiotemporal relationship between MP, ROTI and S4, σ_ϕ.
2) To propose a novel methodology to distinguish scintillation from multipath in GNSS signals based on MP and ROTI, where S4 and σ_ϕ are unnecessary.
3) To develop new strategies in positioning algorithms to mitigate the scintillation effect on PPP and improve the accuracy based on MP and ROTI.

Before the research on the development of algorithms, it is necessary to understand the features and influences of the error source, i.e., the ionosphere and ionospheric scintillation in this thesis. Furthermore, to develop mitigation methods based on past practices and the positioning technique PPP as well as the algorithms KF, several key points were successively investigated in Chapter 2 and 3 following the introduction chapter: 1) the nature of the ionosphere and ionospheric scintillation; 2) the characteristics of the ionosphere and ionospheric scintillation; 3) the effect of ionospheric irregularities on GNSS signals and the positioning results; 4) the modeling and existing methods for mitigating the effect of scintillation; 5) the characteristics of PPP and the Kalman filter (KF) stochastics model.

1.3. Overview

This Ph.D. thesis includes seven chapters as shown in Table 1.1, where Chapters 4-6 are the core chapters containing the whole idea of algorithm development.

Table 1.1 Schematic for the thesis outline.

Chapter 1	Introduction, aim and objectives
Chapter 2	GPS Principles
Chapter 3	Background
Chapter 4	Relationship analysis between parameters
Chapter 5	Methodology to distinguish between scintillation and multipath
Chapter 6	PPP improvement
Chapter 7	Synthesis

Chapter 1 presents a brief introduction of GNSS and ionospheric scintillation, the aim and objectives of this thesis.

Chapter 2 describes GPS principles that provide knowledge on how the positioning is achieved through basic observations. To begin with, the history and three types of observables are briefly introduced. Then, it provides an introduction to the data processing method PPP and its key components. The core principle of PPP is the integration of error correction models, the functional model and the KF stochastics model. Thus, all types of error models are presented, where the ionospheric error model is emphatically described. Finally, it establishes the Un-differenced PPP functional and the KF stochastics model, where the KF can be absorbed into the functional model to accomplish the positioning function in PPP.

Chapter 3 consists of two parts, the parameters applied in this thesis and the background knowledge of the ionosphere. The introduction to the ionosphere provides comprehensive knowledge on the characteristics of the ionosphere and scintillation, which is the theoretical basis of the algorithm development. The existing methods that effectively mitigate scintillation effects on GNSS provide the empirical basis. Then, four parameters S4, σ_ϕ, MP and ROTI are introduced according to their formulae, and their relationships are analyzed and discussed on this basis. Based on both theoretical and practical bases, the novel algorithm is proposed and introduced in Chapter 6.

Chapter 4 is the first research chapter. This chapter investigates the temporal and spatial relationships between S4, σ_ϕ and MP, ROTI, respectively, using time series plots and 2D maps. It starts with the investigation of the relationship among the four parameters analyzed in past research. Then, the data and equipment employed in this research chapter are described, including data selection in both equatorial and polar regions due to significantly different scintillation characteristics in the two regions. In the methodology, the detailed steps for data processing and generating the plots and maps are introduced. In addition to graphs, three statistical tools were used to quantify the results, in this chapter, structural similarity index

(SSIM), Pearson correlation coefficient (CC), variograms and variograms.

Chapter 5 is the second research chapter. It is indeterminate that the scintillation effect or multipath effect causes the scintillation-like event that occurred in the data of this thesis. Thus, this chapter proposes a novel and systematic methodology to distinguish ionospheric scintillation from the multipath event. This chapter evaluated the shortcomings of past methods in distinguishing scintillation events from false alarms.

Chapter 6 is the algorithm chapter that describes the effectiveness of the proposed algorithm. Based on the relationship between scintillation and standard parameters suggested in Chapter 4 and the event type identification methodology in Chapter 5, three strategies in mitigating scintillation effects are proposed. This chapter successively introduces the necessity of the novel algorithm, the strategies, data, instrumentation and applied software in introductive sections. The methodology section describes the establishment of three strategies based on both scintillation and standard parameters. Then, results including a visualization example on one day and statistical outcomes on 14 scintillation days are presented, analyzed and discussed. This chapter concludes with the novelty and effectiveness of the proposed strategies in scintillation mitigation.

Chapter 7 is the synthesis chapter that comprehensively analyzes, discusses and concludes the research methods and results in this thesis. Based on Chapters 4-6, the contributions of the methods and results to the professional field and their inter-relationships are discussed first. It is followed by a summary of the results and conclusions, presented based on the three objectives proposed in this thesis. Finally, recommendations for possible future work are given.

1.4. List of publications

Chapter 4:

- HANCOCK, C. M., **LI, C.**, ZHAO, D., SREEJA, V. V. & CHONG, Y. Respective Statistical Analysis of the Correlation between Scintillation Parameters and MP&ROTI. Proceedings of International Symposiumon GNSS 2018, 21-23, November

2018 Bali, Indonesia.

- **LI, C.**, HANCOCK, C. M., SREEJA, V. V. & YOU, C. Spatial Analysis of the Correlation between Scintillation Parameters and MP&ROTI. 2020 European Navigation Conference (ENC), 23-24 Nov. 2020 Dresden, Germany. IEEE, 1-9. https://doi.org/10.23919/ENC48637.2020.9317345
- **LI, C.**, HANCOCK, C. M., HAMM, N. A. S., SREEJA, V. & YOU, C. 2020. Analysis of the Relationship between Scintillation Parameters, Multipath and ROTI. Sensors, 20. https://doi.org/10.3390/s20102877.

Chapter 5 (accepted):

- **LI, C.**, HANCOCK, C. M., SREEJA, V. V., ZHAO, D., MONICO, J. F. G. & HAMM, N. A. S. 2022. A Novel Methodology to Distinguish Ionospheric Scintillation from Multipath in GNSS Signals. GPS Solutions.

2. Positioning principles

This chapter introduces the GPS and how to obtain the receiver's position from basic observations. To begin with, the GPS and its three types of observations are presented. It is followed by introducing the Precise Point Positioning (PPP), one of the most common techniques for GNSS data processing. Specifically, four critical components of PPP are presented, including the error modeling, the functional model, Kalman filter and the stochastic model. Based on observations of GPS and principles of PPP, the positioning function can be achieved, which lays a practical foundation for the algorithm development in Chapter 6.

2.1. GPS system

GPS is a satellite-based navigation system that is owned and developed by United States government. It is one of four GNSS that is capable of providing global positioning and timing service, where the other three are GLONASS from Russia, Galileo from European Union and BeiDou from China. The GPS satellites are distributed into 6 medium Earth orbits (MEOs) at an altitude of 20,180 km and an inclination angle of about 55° relative to the Earth’s equator. The period of orbit is one-half a sidereal day, which is about 11 hours and 58 minutes, which leads to around four minutes ahead when a satellite passes over the same location every day.

All GPS satellites transmit L-band signals at two frequencies, 1575.42 MHz (L1) and 1227.60 MHz (L2). The first Block IIF satellite was launched in May 2010, which can transmit signals at a third frequency, 1176.45 MHz (L5) (Ng 2010). All three frequencies are derived from a fundamental GPS frequency (10.23 MHz). In order to distinguish the information from different satellites, pseudo random noise (PRN) sequences are assigned to satellites, which range from 1 to 32. The Coarse/Acquisition (C/A) code is modulated onto L1 carrier for civilian applications and Precision code (P code) is modulated onto both L1 and L2 carrier which can be encoded as P(Y) code with anti-spoofing techniques and are available for military applications only.

2.1.1. Modernization

The modernization of GPS consists of five aspects, including space segment, control segment,

new civil signals, modernized civil navigation (CNAV) message and termination of selective availability (National Oceanic and Atmospheric Administration 2021). As of 2011-06-15, the expansion plan on GPS constellation namely Expandable 24 has been completed by the 50th Space Wing Public Affairs (2011). With this expansion plan, the coverage of GPS satellites has increased and the signal has become more robust to be acquired. In addition, a series of modernized satellites have been launched or are planned, including GPS Block IIR-M, GPS Block IIF, GPS III and GPS Follow-On (National Oceanic and Atmospheric Administration 2021). Block IIR-M satellites are upgraded versions of IIR satellites launched between 2005 and 2009, which provides L2C signal and novel military M code signals. Block IIF satellites provides the third civil signal on L5 frequency (L5) with more advanced atomic clocks, higher accuracy, signal strength and quality can be acquired, which have been launched between 2010 and 2016. As for the up-to-date block, GPS III is able to supply the fourth civil signal L1C with improved signal reliability, accuracy and integrity, which starts to be launched in 2018. So far, the fifth GPS III satellite has been successfully launched into orbit by the Space Force (Space and Missile Systems Center Public Affairs 2021).

For the GPS control segment, a variety of ground equipment is used to track and transmit information to the GPS satellites, which includes a master control station, an alternate master control station, 11 ground and remote tracking antennas, and 16 monitor stations (National Oceanic and Atmospheric Administration 2021). Herein, the ground and remote tracking stations cover all continents. The master control station is in charge of the whole GPS constellation, which utilizes the data from monitor stations to generate satellite locations and then navigation message. The master station is also capable of monitoring the behavior of the constellation to guarantee that the system operates under the optimal status. In case the master station fails, an optional master station can be used as a backup.

In terms of signals, three new civil signals have been designed for civilian use, L2C, L5 and L1C. In addition to the legacy civil signal L1 C/A, there are four signals that can be used by civilians. L2C was proposed for commercial use as the first new civil signal, which can be combined with L1 C/A signal to eliminate the majority of the ionospheric error. Additionally,

L2C has a stronger effective power and is less affected by surrounding obstacles than L1 C/A so that it is faster to acquire more reliable signal using L2C (National Oceanic and Atmospheric Administration 2021). Furthermore, L5 was proposed primarily for meeting the needs of safe transportation. With stronger power and wider bandwidth, L5 is planned to be applied for improving fuel efficiency and it can also be used for ionospheric error elimination when used in combination with L1 C/A, even more robust than L2C. Moreover, L1C is the latest signal proposed to provide interoperability between GPS and other satellite systems through a modulation scheme namely Multiplexed Binary Offset Carrier (MBOC) that further improves the operation range and reliability of GPS (National Oceanic and Atmospheric Administration 2021). As of 2021-06-15, there are 23, 16 and 4 GPS satellites able to broadcast L2C, L5 and L1C signals, respectively. Thus, L5 and L1C are still of limited use when L2C signal has been extensively researched and applied though L2C is still pre-operational as L5 and L1C. In addition, a modern CNAV message format is applied to the new signals, which is more flexible and accurate in contrast to the legacy navigation (LNAV) message of L1 C/A. Though the CNAV message is still pre-operational due to incompletely deployed new civil signals, CNAV messages are available for familiarizing users and device development.

The GPS selective Availability (SA) was adopted by the DoD to degrade the positioning accuracy by imposing interference signal on the radio wave signal so that only licensed users could conduct high-accuracy positioning. Then, SA was disabled by President Bill Clinton in May 2000 for more accurate application by civilians. The termination of SA considerably improved the civil positioning accuracy from hundreds of meters to tens of meters.

2.1.2. Observables

Three types of observables are provided by GNSS namely pesudorange (code), carrier phase and Doppler observations, respectively, where different techniques are used to yield distances between satellites and receivers. With at least four distance measurements, the receiver position can be computed using the distance intersection method.

2.1.2.1. Pesudorange observations

The pesudorange measures the distance through the transmitting time of the signal from the phase centre of the satellite antenna to that of the receiver antenna. The travel time is the difference between the reception time of the receiver and the transmission time of the satellite. Then, the distance is equal to the product of the speed of light and the travel time. The travel time is derived through the ranging codes that are contained in GNSS signals. Through maximum correlation analysis performed by the Delay Lock Loop (DLL) between the received code from the satellite and the code replica generated in the receiver, the movement of the code replica in time can be obtained, which is the transmitting time (Xu 2007):

$$\Delta t_r^s = \widetilde{t_r} - \widetilde{t^s} = (t_r + \delta t_r) - (t^s + \delta t^s) \quad 2.1$$

$$P = c_l \cdot \Delta t_r^s \quad 2.2$$

where Δt_r^s is the transmission time; $\widetilde{t_r}$ is the raw reception time; $\widetilde{t^s}$ is the raw emission time; t_r is the reception time without clock error; t^s is the emission time without clock error; δt_r is the receiver clock offset; δt^s is the satellite clock offset; P is the pesudorange measurement; c_l is the speed of light in vacuum. The code replica is generated from the clock used in the receiver while the emitted signal is derived from the clock used in the satellite. Thus, synchronization errors are present in the obtained distance as it can be seen from equation 2.1 and 2.2. Furthermore, a variety of errors are generated on the way that signals pass through. All these errors lead to the difference between the measured pesudorange and the geometric distance, thus the inaccurate positioning results. Moreover, the signal path is slightly different from the true path as the signal can be refracted/bended by the transmitting medium (Xu 2007). The relation between pesudorange measurement and true range can be represented with equation 2.3:

$$P_i = \rho + c_l(\delta_r - \delta^s) + c_l(B_r - b^s) + I_i + Tr + Ti + Re + M_i + \epsilon \quad 2.3$$

where i is 1 or 2, representing two frequencies; ρ is the true geometric distance between the

satellite and receiver; δ_r is the receiver clock error; δ^s is the satellite clock error; B_r is code bias caused by receiver hardware delay; b^s is code biases caused by satellite hardware delay; I is the ionospheric delay; Tr is the tropospheric delay; Ti is the Earth tide and ocean loading tide effects; Re is the relativistic effects; M is the multipath error (i.e., multipath pseudo range error); and ϵ represents other unconsidered errors. The clock errors can be obtained through the orbit information of satellites which is transmitted together with the navigation message (Xu 2007). Moreover, clock error corrections with higher precision and frequency are provided by the International GNSS Service (IGS) data centres. With modelled corrections of other errors, the modelled true range can be calculated with equation 2.3. Furthermore, the geometric range can also be written as:

$$\rho = \sqrt{(x_s - x^r)^2 + (y_s - y^r)^2 + (z_s - z^r)^2} \qquad 2.4$$

where (x_s, y_s, z_s) and (x^r, y^r, z^r) respectively denote the Cartesian coordinates of satellites and receivers. The coordinate of satellites can also be obtained from the navigation message. Thus, with modelled true range and the position of satellites, the position of receivers can be computed using simultaneous equations.

2.1.2.2. Carrier phase observation

Similar to pesudorange, the carrier phase observation is acquired through maximum cross-correlation analysis performed by Phase Lock Loop (PLL) between the carrier phase signal received from satellites and that generated by receiver. However, only the fractional phase can be measured, which leaves the unknown integer ambiguity to be fixed during the positioning algorithm (Xu 2007):

$$\Phi_r^s = (\Phi_r + f\delta t_r) - (\Phi^s + f\delta t^s) + N_r^s \qquad 2.5$$

where Φ_r^s is the measured phase; Φ_r is the phase generated by receivers; Φ^s is the phase received from satellites; N_r^s is the integer ambiguity; f is the frequency of signals. The ambiguity remains constant unless caused by environmental effects such as ionospheric

scintillation, multipath and tropospheric effects. According to Xu (2007), the accuracy of carrier phase observation is better than 1% of the wavelength with modern GNSS receivers, which is about 0.19 and 0.24 centimeters respectively for L1 and L2 signals. Thus, the carrier phase observation is hundreds times more accurate than the pesudorange observation. Moreover, synchronism and other errors are also present in the carrier phase measurement. Therefore, the carrier phase observation can also be represented as:

$$\Phi_r^s = \frac{\rho}{\lambda} + \frac{c_l}{\lambda}(\delta_r - \delta^s) + \frac{c_l}{\lambda}(B_r - b^s) + N_r^s - \frac{I_i}{\lambda} + \frac{Tr}{\lambda} + \frac{Ti}{\lambda} + \frac{Re}{\lambda} + \frac{M_{PR_i}}{\lambda} + \frac{\epsilon}{\lambda} \quad 2.6$$

$$L_r^s = \rho + c_l(\delta_r - \delta^s) + c_l(B_r - b^s) + \lambda N_r^s - I_i + Tr + Ti + Re + m_i + \epsilon \quad 2.7$$

$$\phi_r^s = \lambda L_r^s \quad 2.8$$

where λ is the wavelength of signals; ϕ_r^s is the carrier phase measurement in meters; m is the multipath carrier phase error. It is notable here that the carrier phase measurement contains the integer ambiguity and negative sign of ionospheric delay as compared with pesudorange.

2.1.2.3. Doppler observation

The Doppler effect is defined by Xu (2007) as frequency change of the electromagnetic signal caused by the relative movement of the satellite and receiver, which increases when the satellite gets close to the receiver and decreases otherwise. The Doppler frequency shift should be predicted to obtain the satellite signal, which is a procedure during GNSS signal tracking (Xu 2007). Then, the phase change is predicted with predicted Doppler frequency shift. After that, the Doppler frequency shift is updated by comparing the measured and predicted phase change, which is a co-product from the carrier phase measurement. Moreover, it is also defined that the Doppler observation is the instantaneous rate of change of carrier phase (Xu 2007). Thus, the equation of Doppler observation can be obtained with the derivation of equation 2.7 with respect to the time:

$$D = \dot{\rho} + c_l(\dot{\delta_r} - \dot{\delta^s}) + c_l(\dot{B_r} - \dot{b^s}) - \dot{I_l} + \dot{Tr} + \dot{Re} + \dot{m_l} + \dot{\epsilon} \quad 2.9$$

where the integer ambiguity term is eliminated and the other terms are differentiated.

2.2. PPP

Since PPP was introduced by Zumberge et al. (1997) in 1997, it became an alternative to conventional techniques for GNSS data processing, such as real-time kinematic (RTK). As compared with RTK, the most significant advantage is that no reference station is necessary for PPP that uses undifferenced carrier phase and pesudorange observations. Thus, PPP applications are not spatially restricted by vicinal reference stations as RTK is. With precise satellite orbit and clock products as well as the development of error modellings, positioning results can be achieved with centimeter or even millimeter accuracy. However, an additional process namely initial convergence becomes necessary so as to fix the original integer ambiguity, which lasts 15 to 30 minutes for GPS, for instance. It also results in PPP being sensitive to cycle slips. The PPP technique presumes the satellite orbits and clocks are consistent and error models as well as the orbit/clock products are consistent with those used in the global organizations such as IGS (Kouba et al. 2017). This can be achieved by applying of the same international standards including, but not limited to, International Earth Rotation and Reference System Services (IERS) conventions.

2.2.1. Errors and corrections

There are a variety of errors need to be modelled and corrected in PPP algorithm, including tropospheric errors, phase center variations (PCV), phase wind-up effect, the solid Earth tide, the polar tide, the ocean tide loading, orbit and clock errors, Differential Code Biases (DCBs), the relativistic effect, the Sagnac effect, ionospheric errors and multipath. The ionospheric error is the primary error to be mitigated in this thesis, which is detailed in section 2.2.1.1. In addition, the multipath also involves in the algorithm development, which is introduced in section 2.2.1.2. The other errors are briefly presented in the following paragraph.

The tropospheric delay is divided into two components, hydrostatic (dry) and wet delay, where the former is dependent on the pressure and temperature while the latter is dependent on the water vapor in the air. According to Kouba et al. (2017), around 90% of the tropospheric error is

attributed to the hydrostatic delay. For more accurate positioning outputs, the effect of PCV should be considered. The antenna reference point is the center point of the antenna base. The mechanical antenna phase center is the physical center point of the device component that is above the antenna reference point. However, the actual phase center is typically above the mechanical antenna phase center. Moreover, the positions of electrical antenna phase center are different for signals with different frequencies. Thus, an offset between the electrical and mechanical antenna phase center should be accounted for if an accurate absolute position is required. According to Kouba et al. (2017), GNSS signals are right-hand circularly polarized (RHCP) electromagnetic waves. However, RHCP signals results that carrier phase measurements varies with the changing orientation of antennas. This is called phase wind-up effect. Furthermore, the solid Earth tide, the polar tide and the ocean tide loading are respectively caused by gravitational attraction forces of the Sun and Moon (Abdel-salam 2005), variation of the Earth's skewing axis and gravitational force induced by periodic ocean tide (Melachroinos et al. 2008; Abdel-salam 2005). In addition, the orbit and clock information should be obtained when using PPP. The satellite clock error can be modeled, while the receiver clock error cannot. Typically, the receiver clock bias is set as the unknown aside from the three location parameters so that it can be solved with four equations, thus setting the minimum number of visible satellites as four (Karaim et al. 2018). For orbit errors, though satellite positions are provided in broadcast navigation message, the error still remains at around 1.1 m (Warren and Raquet 2003) as the satellite orbit is predicted using a curve fit that differs from the real orbit (Noureldin et al. 2013). Moreover, as introduced in section 2.1, there are different PRN codes for the signal with certain frequency, such as P and C/A codes. As hardware delays vary for different codes, a systematic error namely Differential Code Biases (DCBs) appears when using different types of signals for positioning. As satellites are tens of thousands of kilometers above the Earth surface, the Earth gravitational potential on satellites are less than that compared to receivers on ground. Moreover, satellites move significantly faster than receivers. These two factors lead to the difference between the satellite and receiver clock (Abdel-salam 2005) that is known as the relativistic effect. According to Ashby and Spilker (1996), the Sagnac effect is caused by the rotation of the Earth during signal transmitting between the satellite and the receiver that results in the error up to hundreds of nanoseconds.

2.2.1.1. Ionospheric errors

As aforementioned, significant errors are encountered when radio signals propagate through the ionosphere. Due to the ionization of molecules caused by solar radiation, free electrons and ions are generated that delay the pesudorange measurements and advance carrier phase measurements. The delay in code measurements and the advance in phase measurements are separately represented by equation 2.10 and 2.11 (Yuan 2000):

$$I_g = \int_r^s (n_g - 1) dl \tag{2.10}$$

$$I_p = \int_r^s (n_p - 1) dl \tag{2.11}$$

where n_g is the group refractive index; n_p is the phase refractive index; l represents the propagation path; s and r respectively represent satellite and receiver. Based on the equation of refractive index (equation 3.2-3.7), n_p can be simplified and rewritten with following expression (Bassiri and Hajj 1993; Datta-Barua et al. 2008):

$$n_p = 1 - \frac{1}{2}X - \frac{1}{2}XY|cos\,\theta| - \frac{1}{8}X^2 - \frac{1}{4}XY^2\,cos^2\,\theta$$
$$-\frac{1}{4}XY^2(cos^2\,\theta + sin^2\,\theta), |cos\,\theta| \gg \frac{Y\,sin^2\,\theta}{2(1-X)} \tag{2.12}$$

where X and Y are respectively given by equation 3.3 and 2.13:

$$Y = \frac{Y_T}{sin\theta} \tag{2.13}$$

where Y_T is given by equation 3.5. Then, n_g can be calculated according to n_p:

$$n_g = n_p + f\frac{dn_p}{df} = 1 + \frac{1}{2}X + XY\,cos\,\theta + \frac{3}{8}X^2 + \frac{3}{4}XY^2\,cos^2\,\theta + \frac{3}{4}XY^2 \tag{2.14}$$

The first order ionospheric error is related to the first two terms of equation 2.12 and 2.14, which accounts for the majority of the delay and can be mitigated using the ionosphere-free (IF) combination. By substituting equation 2.12 into 2.11, the ionospheric error can be obtained:

$$I_p = -\int_r^s \frac{1}{2} X\, dl - \int_r^s \frac{1}{2} X\, Y\, cos\,\theta\ dl - \int_r^s \frac{1}{8} X^2\, dl - \int_r^s \frac{1}{4} XY^2\, cos^2\,\theta\ dl - \int_r^s \frac{1}{4} XY^2 \quad 2.15$$

Substituting Y and X (equation 2.13 and 3.3) into 2.15 (Bassiri and Hajj 1993; Datta-Barua et al. 2008):

$$I_p = -\frac{q_i}{f^2} - \frac{s_i}{2f^3} - \frac{r_i}{3f^4} \quad 2.16$$

$$q_i = 40.3 \int_r^s N_e\, dl \quad 2.17$$

$$s_i = 2.2567 \cdot 10^{12} \int_r^s N_e B\, cos\,\theta\, dl \quad 2.18$$

$$r_i = r_1 + r_2 + r_3 \quad 2.19$$

$$r_1 = 2437.1 \int_r^s {N_e}^2\, dl \quad 2.20$$

$$r_2 = 4.7377 \cdot 10^{22} \int_r^s N_e B^2\, cos^2\,\theta\ dl \quad 2.21$$

$$r_3 = 4.7377 \cdot 10^{22} \int_r^s N_e B^2\, dl \quad 2.22$$

where $-\frac{q_i}{f^2}$, $-\frac{s_i}{2f^3}$ and $-\frac{r_i}{3f^4}$ are first, second and third order ionospheric delay in phase measurements, respectively. Similarly, substituting equations 2.13 and 3.3 into equations 2.14 and 2.10 gives the ionospheric delay of code measurements:

$$I_g = \frac{q_i}{f^2} + \frac{s_i}{f^3} + \frac{r_i}{f^4} \quad 2.23$$

where $\frac{q_i}{f^2}$, $\frac{s_i}{f^3}$ and $\frac{r_i}{f^4}$ are first, second and third order ionospheric delay in code measurements, respectively. In order to simplify the calculation, the first order delay is usually assumed to be the only term that causes error. Thus, the ionosphere-free combination is derived to eliminate the first order error:

$$L_{IF} = \frac{f_1^2 L_1 - f_2^2 L_2}{f_1^2 - f_2^2} \quad 2.24$$

$$P_{IF} = \frac{f_1^2 P_1 - f_2^2 P_2}{f_1^2 - f_2^2} \quad 2.25$$

where L_{IF} and P_{IF} are the ionosphere-free phase and code combination respectively; f_1 and f_2 are the signal frequency; P_1 and P_2 are the pseudorange observable for two frequencies; L_1 and L_2 are the phase observable for two frequencies. However, this assumption neglects the influence of higher-order delays that remain in the IF combination. In order to look into the detail of higher-order errors, substitute equation 2.7 and 2.16 into 2.24:

$$L_{IF} = \frac{f_1^2\left(\rho - \frac{q}{f_1^2} - \frac{s}{2f_1^3} - \frac{r}{3f_1^4} + \epsilon_o\right) - f_2^2\left(\rho - \frac{q}{f_2^2} - \frac{s}{2f_2^3} - \frac{r}{3f_2^4} + \epsilon_o\right)}{f_1^2 - f_2^2} = \rho + \frac{s}{2f_1 f_2 (f_1 + f_2)} + \frac{r}{3f_1^2 f_2^2} + \epsilon_o \quad 2.26$$

where all other errors including the integer ambiguities are absorbed into the term ϵ_o. In the same way, the corresponding formula for code observable can be obtained by substituting equation 2.3 and 2.23 into 2.25:

$$P_{IF} = \rho - \frac{s}{f_1 f_2 (f_1 + f_2)} - \frac{r}{f_1^2 f_2^2} + \epsilon_o. \quad 2.27$$

According to Axelrad and Brown (1996) and Klobuchar (1996), the ionospheric errors in three orders respectively reach 2×10^{-4}, 2×10^{-7} and 2×10^{-8} under the worst case ionospheric condition. Based on these values, higher-order errors contribute much less than 1% to the total ionospheric error. At other times, the proportion of higher-order errors are even within 0.1%. As the first-order ionospheric delay is about tens of meters, the magnitude of higher-order errors is in centimeter or even millimeter. However, when intense ionospheric activities occur caused by strong solar activity, the size of the total ionospheric error can reach hundreds of meters that also leads to a significant increase of several tens of centimeters in higher-order delay. Therefore, higher-order errors should also be taken into account when strong ionospheric activities occur, such as scintillation.

2.2.1.2. Multipath

Multipath is a common interference in GNSS that is fundamentally generated when multiple signal paths reach the receiver as illustrated in Figure 2.1. This can be caused by signal reflections due to nearby obstacles, such us buildings, trees, mountains, etc. Thus, multipath is usually more severe in urban and valley areas. However, the path geometry, signal characteristics of multipath and how it changes with the environment are still not entirely understood. Thus, it is difficult to effectively mitigate the multipath effect though the research on the multipath has lasted for four decades. What is more, as signals transmitting at low altitude are more likely to encounter obstacles, multipath is typically more significant at low elevation. Thus, elevation cut-off is one of the most commonly-used ways for mitigating multipath though a part of data is simultaneously removed. Furthermore, the diffraction and refraction of the signal caused by the atmosphere are also the reasons of multipath. Multipath can lead to the signal degradation and phase shift and ultimately to positioning errors, which typically accounts for the major error budget in accurate applications (Smyrnaios et al. 2013). Thus, the selection of the receiver position is vital as multipath is not deterministic and cannot be eliminated (Karaim et al. 2018). Furthermore, the effect of multipath on code measurements is significantly more severe than that on carrier phase measurements. In addition, multipath error is supposed to be periodic if the receiver position remains unchanged. For GPS, the error repeats every sidereal day i.e. 23 hours, 56 mins and 4 seconds. Therefore, with long-time analysis, the repeatable error can be evaluated. Moreover, there are several types of parameters that can be used as the indicator of multipath, such as Signal-to-Noise Ratio (SNR) (Bilich and Larson 2007; Špánik and Hefty 2017), iono-corrected code minus carrier (CMC) (Khanafseh et al. 2018), Standard Deviation Code/Carrier divergence (CCSTDDEV) (Van Dierendonck et al. 1993; Romano et al. 2013; D'Angelo et al. 2015), multipath parameter (MP) (Estey and Meertens 1999; Li et al. 2020; Hancock et al. 2017), etc. In this thesis, MP is used to evaluate the multipath intensity and the equation of MP is introduced in section 3.3.3.

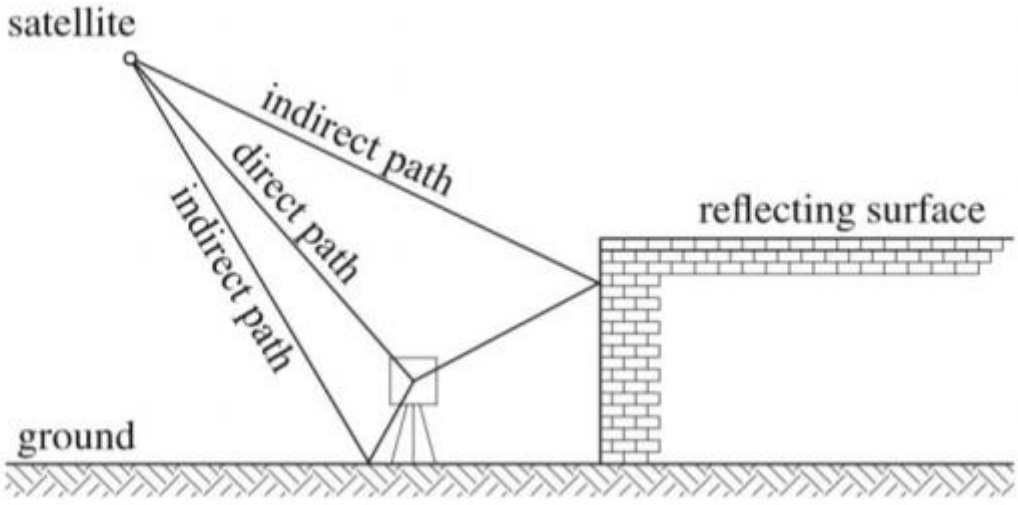

Figure 2.1 Multipath effect (Figure 5.8 of Hofmann-Wellenhof et al. (2008)).

2.2.2. Un-differenced PPP functional model

The observation and IF equations have been introduced above. The PPP employs the un-differenced IF combinations in positioning process, where the first order ionospheric error has been eliminated. Without considering the higher order ionospheric error, the IF combinations can be expressed in detail:

$$P_{IF} = \rho + c_l(\delta_r - \delta^s) + c_l\left(B_{IF,r} - {b_{IF}}^s\right) + Tr + M_{IF,i} + \epsilon_{IF} \quad 2.28$$

$$L_{IF} = \rho + c_l(\delta_r - \delta^s) + c_l\left(B_{IF,r} - {b_{IF}}^s\right) + Tr + \frac{f_1^2\lambda_1 N_1 - f_2^2\lambda_2 N_2}{f_1^2 - f_2^2} + m_{IF,i} + \epsilon_{IF} \quad 2.29$$

where IF represents IF combinations. With the precise products of clock and orbit, the term δ^s can be obtained. The tropospheric delay term Tr consists of a modelled component and a correction component:

$$Tr = Tr_0 + MF \cdot dTr \quad 2.30$$

where Tr_0 is the modelled component; dTr is the correction component that is an additional parameter to be estimated in the state vector and MF indicates mapping function. As the

lumped ambiguity $\frac{f_1^2\lambda_1 N_1 - f_2^2\lambda_2 N_2}{f_1^2 - f_2^2}$ is estimated as a float parameter in PPP, the hardware delay $c_l\left(B_{IF,r} - {b_{IF}}^s\right)$ and the lumped ambiguity is combined into one single parameter (Lonchay 2019):

$$HA = c_l\left(B_{IF,r} - {b_{IF}}^s\right) + \frac{f_1^2\lambda_1 N_1 - f_2^2\lambda_2 N_2}{f_1^2 - f_2^2} \quad 2.31$$

where HA indicates hardware and ambiguity. In addition, the multipath term is typically neglected for both static and kinematic applications, the former due to the selection of appropriate station with less multipath and the latter due to fast variation of the receiver geometry. Thus, IF equations become:

$$P_{IF} = \rho + c_l(\delta_r - \delta^s) + Tr_0 + MF \cdot dTr + \epsilon_{IF} \quad 2.32$$

$$L_{IF} = \rho + c_l(\delta_r - \delta^s) + Tr_0 + MF \cdot dTr + HA + \epsilon_{IF}. \quad 2.33$$

It is assumed that the observed number of satellites is g. Thus, numbers of equations and unknowns are $2g$ and g+5, respectively. The unknown variables include three location parameters Δx, Δy and Δz, the receiver clock error δ_r, the tropospheric error dTr and g combined parameter HA (Afifi and El-Rabbany 2016):

$$x = \begin{bmatrix} \Delta x \\ \Delta y \\ \Delta z \\ \delta_r \\ dTr \\ HA^1 \\ \vdots \\ HA^g \end{bmatrix} \quad 2.34$$

where x is the state vector that contains the unknown parameters. The PPP model is formed also based on a matrix that contains the state coefficients namely design matrix (Afifi and El-Rabbany 2016):

$$H = \begin{bmatrix} (x_0 - x^1)/\rho_0^1 & (y_0 - y^1/\rho_0^1) & (z_0 - z^1)/\rho_0^1 & c & MF^1 & 0 & \cdots & 0 \\ \vdots & \vdots & \vdots & \vdots & \vdots & \vdots & \vdots & \vdots \\ (x_0 - x^g)/\rho_0^g & (y_0 - y^g)/\rho_0^g & (z_0 - z^g)/\rho_0^g & c & MF^g & 0 & \cdots & 0 \\ (x_0 - x^1)/\rho_0^1 & (y_0 - y^1/\rho_0^1) & (z_0 - z^1)/\rho_0^1 & c & MF^1 & 1 & \cdots & 0 \\ \vdots & \vdots & \vdots & \vdots & \vdots & \vdots & \vdots & \vdots \\ (x_0 - x^g)/\rho_0^g & (y_0 - y^g)/\rho_0^g & (z_0 - z^g)/\rho_0^g & c & MF^g & 0 & \cdots & 1 \end{bmatrix} \quad 2.35$$

$$\rho_0 = \sqrt{(x^s - x_0)^2 + (y^s - y_0)^2 + (y^s - y_0)^2} \quad 2.36$$

where H indicates design matrix; x_0, y_0 and z_0 are *a priori* values for the receiver coordinate and ρ_0 is the *a priori* distance between the satellite and the receiver. In addition, the prefit and postfit residual vectors are used for estimating the state vector (Lonchay 2019):

$$Pre = \begin{bmatrix} P_{IF}^1 - P_{0,IF}^1 \\ \vdots \\ P_{IF}^g - P_{0,IF}^g \\ L_{IF}^1 - L_{0,IF}^1 \\ \vdots \\ L_{IF}^g - L_{0,IF}^g \end{bmatrix} \quad 2.37$$

$$Post = \begin{bmatrix} Post_1 \\ \vdots \\ Post_m \\ Post_{m+1} \\ \vdots \\ Post_{2m} \end{bmatrix} \quad 2.38$$

where Pre and $Post$ represent prefit and postfit residual vectors respectively; $P_{0,IF}$ and $L_{0,IF}$ are *a priori* values of the IF code and phase measurements. Finally, the matrix equation representing the relation between vectors and the matrix is:

$$Pre = Hx + Post. \quad 2.39$$

Then, the Kalman filter is introduced as the critical tool in GNSS for data processing to obtain the positioning output.

2.2.3. Kalman filter

Kalman filter (KF) as the core algorithm during the GNSS positioning process is used to converge the original measurements containing errors to a more accurate result. There are two

major procedures in KF, prediction and update which iterate for all the measurements (Axelrad and Brown 1996). Figure 2.2 shows the flowchart on how to apply Kalman filter step by step.

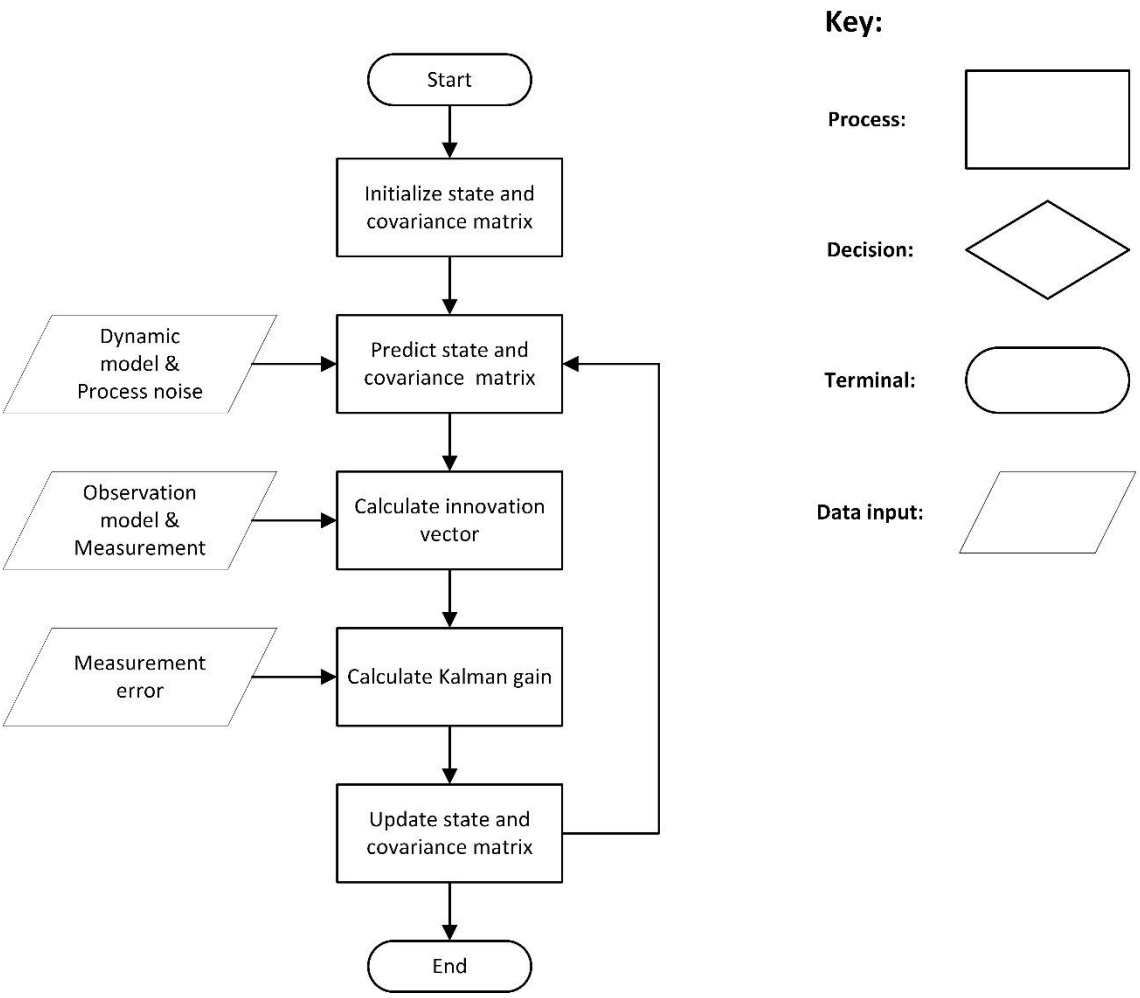

Figure 2.2 Flowchart of Kalman filter

As shown in Figure 2.2, the state and covariance matrix are initialized first, where the covariance matrix is the estimation of state error. Then, with inputting a dynamic model and process noise, the state and the covariance matrix are predicted based on the initialized or the updated at previous epoch. A constant velocity model is a typical dynamic model in GNSS. After that, innovation vector is calculated as the difference between the input and predicted measurement. Next, Kalman gain can be obtained by inputting the measurement error. Afterwards, the state and the covariance matrix can be updated using Kalman gain as the weight of the innovation vector. The output is used in the next iteration until all the measurements are processed.

2.2.3.1. Formulae

The state at is predicted using the dynamic model and the state at the previous epoch:

$$x_{k/k-1} = \Phi x_{k-1/k-1} \quad 2.40$$

where x is the state; $k/k-1$ represents the prediction at the epoch k from the epoch $k-1$; and $k-1/k-1$ represents the updated at epoch $k-1$; Φ is the dynamic model, also known as the transition matrix. The corresponding covariance matrix is also predicted as:

$$P_{k/k-1} = \Phi P_{k-1/k-1}\Phi^T + Q_{k-1} \quad 2.41$$

where P is the covariance matrix of the state; Φ^T is the transpose of the dynamic model; Q is the process noise covariance. The innovation vector is formed as:

$$y_k = z_k - H_k x_{k/k-1} \quad 2.42$$

where y is the innovation vector; z is the measurement; H is the observation model. Afterwards, Kalman gain is calculated as follow:

$$K_k = P_{k/k-1}H_k^T(H_k P_{k/k-1}H_k^T + R_k)^{-1} \quad 2.43$$

where K is Kalman gain; R is the measurement error covariance. Next, updating is applied to the state and corresponding covariance matrix in formulae 2.44 and 2.45 respectively:

$$x_{k/k} = x_{k/k-1} - K_k y_k \quad 2.44$$

$$P_{k/k} = (I - K_k H_k)P_{k/k-1} \quad 2.45$$

where I is the identity matrix. After that, the iteration is implemented for all the observations. However, KF can only be applied for linear estimation, which is not suitable for GNSS

application. Thus, Extended KF (EKF) is applied instead where the dynamic and observation models are replaced by nonlinear ones (Axelrad and Brown 1996). Therefore, formulae 2.40 and 2.42 are separately replaced with formulae 2.46 and 2.47:

$$x_{k/k-1} = \phi(x_{k-1/k-1}) \quad 2.46$$

$$y_k = z_k - h(x_{k/k-1}) \quad 2.47$$

where ϕ and h are nonlinear dynamic and observation models respectively. Moreover, Φ and H_k for covariance matrix computation are defined with Jacobians instead:

$$\Phi = \frac{\partial \phi}{\partial x}\bigg|_{x_{k-1/k-1}} \quad 2.48$$

$$H_k = \frac{\partial h}{\partial x}\bigg|_{x_{k/k-1}} \quad 2.49$$

It is enough to perform positioning by applying EKF with the priori information of process and measurement noise, which may not be available (Guo and Zhang 2014). Adaptive robust KF (ARKF) can be used to overcome this problem. The only difference between ARKF and EKF is that an adaptive factor is applied to the Kalman gain and measurement noise covariance. Thus, the equation 2.43 is replaced with equations 2.50-2.54:

$$K_k{}' = \frac{1}{\alpha_k} P_{k/k-1} H_k^T \left(\frac{1}{\alpha_k} H_k P_{k/k-1} H_k^T + R_k{}'\right)^{-1} \quad 2.50$$

$$\alpha_k = \begin{cases} 1, & |\bar{Y}_k| \le c_0 \\ \frac{c_0}{|\bar{Y}_k|}\left(\frac{c_1 - |\bar{Y}_k|}{c_1 - c_0}\right)^2, & c_0 < |\bar{Y}_k| \le c_1 \\ 0, & |\bar{Y}_k| > c_1 \end{cases} \quad 2.51$$

$$\bar{Y}_k = \frac{\sum_{i=1}^{n_k} y_k{}^2}{\sum_{i=1}^{n_k} \sigma_{y_k}^2} \quad 2.52$$

$$R_k{}' = R_k / \gamma_k \quad 2.53$$

$$\gamma_k = \begin{cases} 1, & |v_k| \le k_0 \\ \frac{k_0}{|v_k|}\left(\frac{k_1 - |v_k|}{k_1 - k_0}\right)^2, & c_0 < |v_k| \le k_1 \\ 0, & |v_k| > k_1 \end{cases} \quad 2.54$$

where α_k and γ_k are inflation factors; c_0, c_1, k_0 and k_1 are constants with empirical values: $1.5<c_0<3.0$, $3.0<c_1<8.0$, $1.5<k_0<3.0$ and $3.0<k_1<8.0$; σ_{y_k} is the standard deviation of y_k; n_k is the innovation numbers; v_k is the standardized residual. With the inflation factors varying from 0 to 1, the influence of outliers in measurements can be compensated.

2.2.4. Stochastic model

The stochastic model is applied when the system is nondeterministic and the model is established based on random variables with statistical properties. In stochastic models, variables include parameters, the condition of the system and the state characteristics, where the correlation between variables is also random. In GNSS, the accuracy of observations, the correlation between observations, the system dynamics and the variation of unknown parameters accords with the characteristics of the stochastic model.

As aforementioned, there are three types of observations: pseudorange, carrier phase and Doppler, which have different accuracies. Additionally, the accuracy for the measurement at each epoch also varies. Thus, two types of stochastic models should be applied here for modelling the interval correlation for serial measurements of a certain type of observation and relative correlation between different types of observations, respectively (Abdel-salam 2005).

As codeless receivers are typically applied in modern GNSS application, it is assumed that there is no correlation between observations on L1 and L2. Thus, the modelling for correlation between observations on different frequencies are not considered. The basic stochastic model can be expressed as (Lonchay 2019):

$$P = \sigma^2 I_g = \begin{bmatrix} \sigma^2 & & \\ & \ddots & \\ & & \sigma^2 \end{bmatrix} \quad 2.55$$

where P is the covariance matrix of measurements; I_g is the identity matrix with size of observed satellite number and σ^2 is the variance of observations which can be acquired with an alignment of the receiver (de Bakker et al. 2009) . Thus, the same variance is assigned to all observations, which is assumed based on the theoretical situation. However, the stochastic behavior for the interval correlation is fundamentally caused by the diverse environment of each signal path with different factors such as observation type, elevation angle, receiver type, etc. Thus, the accuracy of each measurement varies with the signal path environment. The effect degree of the factors can be quantified by the weight equations summarized by Mohammed (2017) that includes multipath effects, SNR, residuals, etc. Herein, the elevation weighting equation is one of the most typically used one expressed by Black and Eisner (1984) as:

$$wt = \delta_m \cdot \frac{1.001}{\sqrt{0.002001 + sin^2(ele)}} \quad 2.56$$

where wt represents weight; δ_m is the selected measurement noise or the standard deviation (STD) of the noise that is typically 3 m for the code and 0.03 m for the carrier phase and ele is the satellite elevation. By inputting the weight into the stochastic model, the variance matrix becomes:

$$P = \begin{bmatrix} wt_1^2 & & \\ & \ddots & \\ & & wt_g^2 \end{bmatrix} \quad 2.57$$

Furthermore, the relative correlation between different types of observations only exists when code measurements are smoothed by carrier phase measurements, where the correlation is established and the covariance matrix is non-diagonal. Aside from observations, the system dynamics and parameters are also stochastic as illustrated in the Kalman filter section (2.2.3.1), where the model is established for the unknown process and measurement noise covariance matrices (CMs). The optimization of the design is dependent on the estimation quality of the CMs, which shows the importance of the modelling for them. As introduced by Duník et al. (2017), there are two types of methods that can be applied for CMs estimation: feedback and feedback-free, where the unknown parameters of the CMs are updated synchronously with the unknown state in the former method and an estimator is applied to predict the measurement error for all epochs and the measurement error is used to estimate CMs in the latter method. Furthermore, with the process and measurement noise CMs, the unknown parameters in the state vector that contains positional parameters, receiver clock, tropospheric error and integer ambiguities are modelled where the theory of Random Walk or first order Gauss Markov are applied (Brown and Hwang 1997).

2.3. Conclusions

This chapter has reviewed how positioning is realized through observations and the functional model, KF stochastic model in PPP. Starting from introducing GPS and its observation equations, this chapter introduced PPP that is the data processing technique applied in this thesis. The error correction is a crucial step in PPP. Thus, all types of errors were discussed, especially the ionospheric error that is the primary error source to be addressed in this thesis. Then, the functional model in PPP was presented, which could help initiate the state and the observation model in KF based on observation equations. Using KF, the original observations could be converged to a constant and accurate result, i.e. positioning. Furthermore, the introduction of these concepts, especially KF, provided ideas for scintillation mitigation. The measurement error covariance matrix in KF is used to weight observations from different satellites. Thus, it is possible to use this matrix to down-weighting and reduce the scintillation effect.

3. Key concepts

After the review of the GNSS positioning theory, this chapter provides a detailed introduction to the ionosphere, scintillation and scintillation parameters. The chapter begins with an introduction on the characteristics of the ionosphere and scintillation, their effects on GNSS, scintillation modelling and mitigation methods that provide ideas for the development of scintillation mitigation algorithm presented in this PhD thesis. Then, different parameters are introduced and the theoretical relationship between scintillation parameters, multipath parameter (MP) and rate of change of Total Electron Content Index (ROTI) are analyzed in order to lay a foundation for the analysis of spatiotemporal relationship in the Chapter 4.

3.1. The ionosphere

There is an atmospheric layer that lies above the Earth with an altitude from around 50 km to 1000 km, activated by high energy radiations from the Sun, which causes the neutral atoms and molecules in this layer to be ionized (Kelley 1989a). This layer is known as the ionosphere. In the presence of the ionosphere, radio waves may encounter delay or advance in propagation speed, reflection, refraction and diffraction.

The ionization process produces free electrons and ions. A free electron can be captured by a positive ion, which is known as the reverse process to ionization namely recombination. Ionization dominates at higher altitudes, where the gas density is low. When the gas becomes dense at lower altitudes, the recombination prevails. This leads to different ionic compositions at different altitudes in the ionosphere and separates the ionosphere into several layers. As shown in Figure 3.1, ionosphere is composed of three parts respectively namely D, E and F layers, where the F layer is the outermost and the D layer is the innermost. The altitude ranges of the D, E and F layers are around 48-90 km, 90-150 km and 150-500 km respectively. Due to exposure to ultra violet (UV) and X-rays from the Sun most, F layer has the highest plasma density, which is divided into F1 and F2 layers at daytime because of different functions of molecular ions (Kelley 1989a). The atmosphere can also be divided into several layers according to the temperature, where the primary layer is the thermosphere with altitude from about 100 to 500

km. The temperature in the thermosphere rises with altitude. It is because that ionization intensity increases at higher altitude caused by solar radiation. Though the neutral air is denser at lower altitude and the recombination dominates instead of ionization, which produces energy, recombination also leads to the emission of a photon that carries away the generated energy.

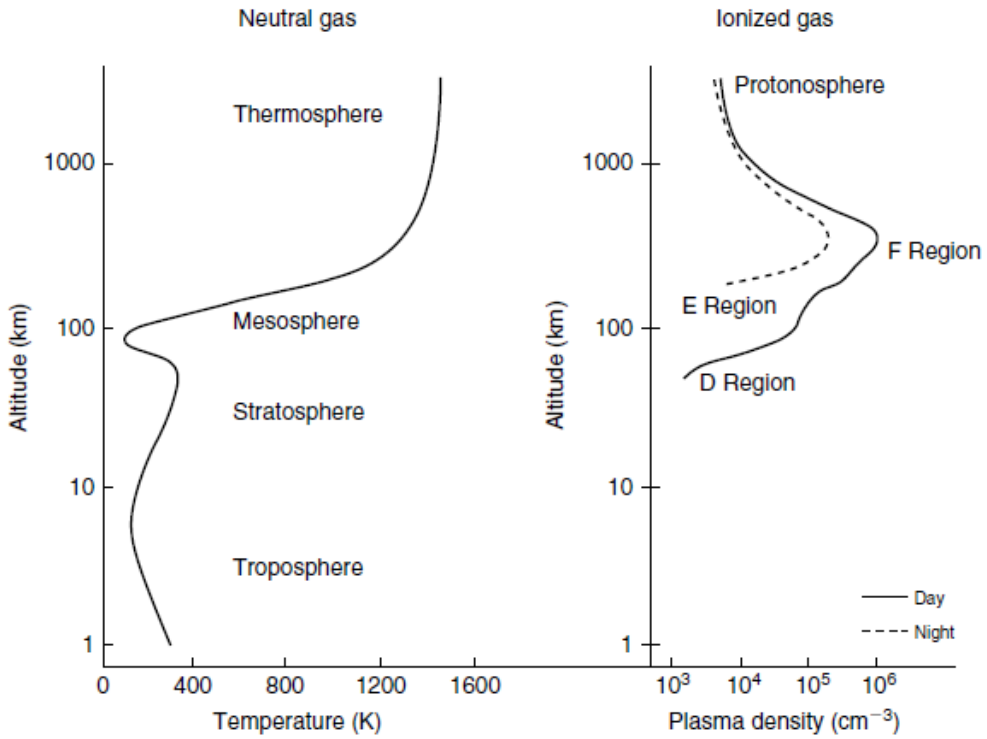

Figure 3.1 Different layers of atmosphere (left) and ionosphere (right) (Figure 1.1 of Kelley (1989a))

The Sun is the major component of the Solar System that accounts for the majority of the mass of the system. Hydrogen and helium are the main constituents of the Sun, which respectively accounts for about 70% and 28% of its mass (Lonchay 2019). In the centre of the Sun, tons of hydrogen are fused into helium each second, generating tons of energy (Stix 2002). The intensity of ionization is dependent on the activity of the Sun. The solar activity is periodic and can be determined by the number of the sunspots. The peak repeats every 11 year, which is called solar cycle and identified with the equation (Davies 1990):

$$R = k(10g + s) \quad 3.1$$

where R is Wolf number; k is the observatory coefficient; g is the sunspot groups number; s is the individual sunspots number. As the solar cycle approaches to its peak, the sunspots increase in number and size. Meanwhile, another phenomenon on the Sun namely solar flare may also occur close to sunspot groups. A solar flare suddenly brightens the surface of the Sun and release energy from the Sun's corona. Furthermore, a coronal mass ejection (CME) often follows a solar flare that erupts plasmas. In addition, both phenomenon are closely related to magnetic reconnection of the Sun that is defined as the realignment of the magnetic lines of magnetic fields in two opposite directions. Energy is also released during this process. Therefore, the ejected plasmas and energy that reaches the Earth leads to the aforementioned ionization process of the Earth's ionosphere, and thus the positioning errors in GNSS applications.

According to frequency, the signal can be divided into multiple sections, such as Low Frequency (LF), High Frequency (HF), Very High Frequency (VHF), Ultra High Frequency (UHF), etc. The influence of the ionosphere on radio signals varies with signal frequency. When a signal with a frequency lower than 5MHz hits the ionosphere, the signal is bounced back by the ionosphere, which supports remote radio signal transmissions (NASA 2021). However, the ionosphere can also influence the radio signal that is transmitted to the Earth from space, such as the signal from satellites to receivers in GNSS applications, where the UHF signals of GNSS allows them to pass through the ionosphere. The GNSS signal may be deflected or diffracted when it travels through the high density plasma in the ionosphere. Thus, ionospheric error is one of the most important error sources in GNSS positioning. Though the majority of the ionospheric effect can be mitigated by ionosphere-free (IF) combination with dual frequency signals, the influence of ionospheric irregularities still exists and leads to severe positioning errors.

The ionospheric irregularities phenomena occurring in the F layer of equatorial region is usually named as equatorial spread F (ESF) or convective equatorial ionospheric storm (CEIS) (Kelley

1989a). This originates from the observation by Berkner and Wells (1934) using ionosondes that the range or frequency of the deflected echo was spread. It has been shown that the radar signal was Doppler-shifted because of the irregularities motion in the line-of-sight propagation (Kelley 1989a). It was proposed by Dungey (1956) that the formation of CEIS is driven by the Rayleigh-Taylor (RT) instability. First, perturbation electric fields are built up due to accumulation of charge and divergence on weak original perturbations. Then, the fields caused a drift of the plasma from high to low density. Thus, a more intense perturbation is created due to the plasma drift as shown in Figure 3.2. Therefore, the ionospheric irregularities can result in several phenomena, where the ionospheric scintillation is one of the most severe error sources of GNSS.

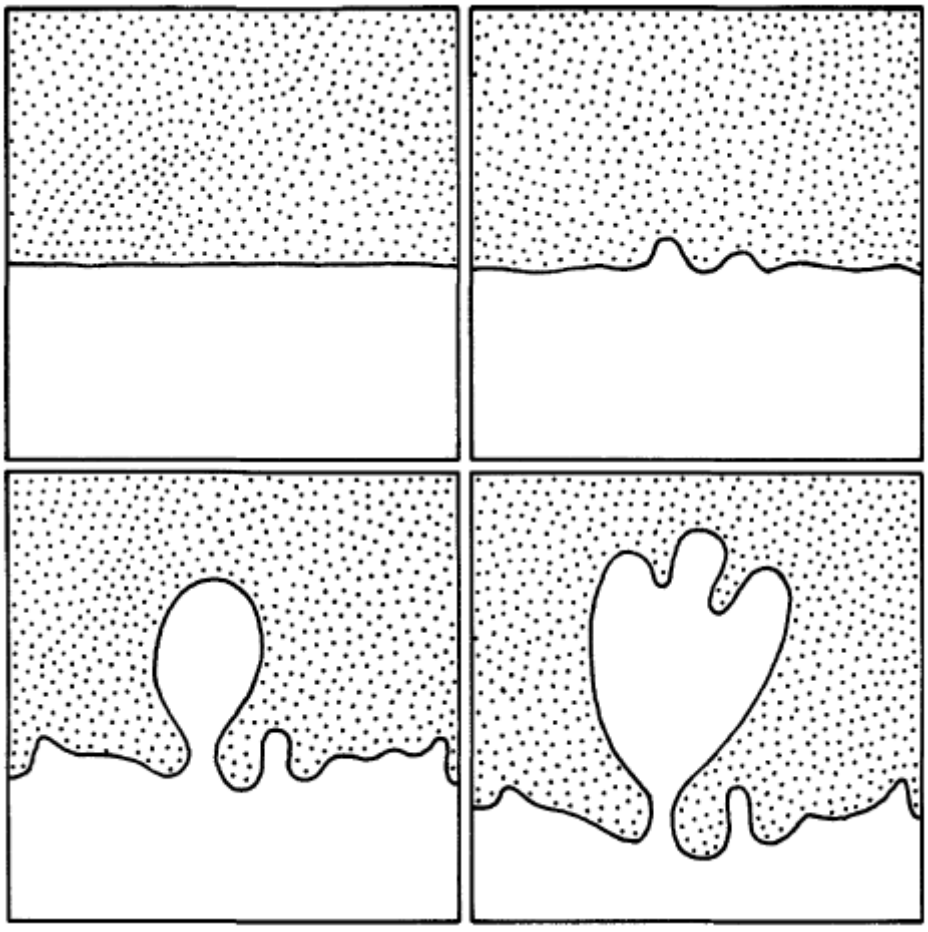

Figure 3.2 The variation of the perturbation with photos of the hydrodynamic RT instability (Figure 4.8 in Kelley (1989b)).

3.1.1. Ionospheric models

In consideration of the effect of ionosphere on GNSS applications, a variety of ionospheric models have been developed in past five decades. Ionospheric models can be mainly classified into three types: theoretical, parametric and statistical empirical models according to Cander et al. (1998). Theoretical models are created on the basis of the fundamental physical and chemical theories or first principles. Parametric models are derived by simplifying theoretical models in accordance with several parameters. Thus, parametric models can be more easily to be used in practical applications than theoretical models. Moreover, empirical models are generated based on processed data and observations. Therefore, empirical models are even more compatible with practical operations than the others. Different models have different characteristics, such as precision, resolution, complexity, real-time capabilities, input data type, etc. However, it should be noted that no single model can have all the characteristics (Cander et al. 1998). Thus, the selection of suitable model becomes significant. Several typical ionospheric models are introduced as follows in more detail.

As initiated by Anderson (1973) and further developed by Decker et al. (1994), Global Theoretical Ionospheric Model (GTIM) is one of the earliest theoretical ionospheric models. Originally, GTIM was proposed only for modelling low-latitude F region (Anderson 1973), which was generalized to mid- and high-latitudes during following years (Decker et al. 1994). According to Decker et al. (1994), GTIM is similar to the Time Dependent Ionospheric Model (TDIM) developed by (Schunk 1988) with the same method for modelling the F region ionosphere. However, GTIM solved the continuity and momentum equations for a single species while TDIM solved those for numerous species. Thus, it is more suitable to apply GTIM under the situation with limited computer resources and TDIM for more comprehensive output. There are more theoretical models available, such as Coupled Thermosphere-Ionosphere Model (CTIM), Thermosphere-Ionosphere Global Circulation Model (TIGCM), Field Line Interhemispheric Plasma Model (FLIP), etc. *(Cander et al. 1998)*. Generally, theoretical models are more complicated than the other two types, in not only the processing phase but also the inputting phase, which limits the application of theoretical models.

For simpler and faster computation, Semi-empirical Low-latitude Ionospheric Model (SLIM) as a parametric model was developed by Anderson et al. (1987) which employs exponential functions for profile reproductions with several coefficients generated from other theoretical models. SLIM covers 24 hours from 24° N to 24° S with the spatial and temporal resolution of 2° and 30 minutes respectively. As compared with Chui and Bent models, the result obtained with SLIM rationally accords with the observations (Anderson et al. 1987). However, SLIM cannot provide electron densities at regions other than F layer at low latitude. Therefore, by using the form of the Chiu model and fitting coefficients into the SLIM profile, a Fully Analytic low- and mid-latitude Ionospheric Model (FAIM) was developed by Anderson et al. (1989) that also covers mid-latitude areas. It was shown that the behavior of FAIM and SLIM was improved at low latitude regions as compared with Chiu model and FAIM agreed with SLIM more at topside than bottomside portion at equatorial regions (Anderson et al. 1989). Moreover, there are more parametric models that works globally, such as Ionospheric Conductivity and Electron Content (ICED) based on sunspot number, Parameterized real time Ionospheric specification Model (PIM), etc (Cander et al. 1998). It is easy to use parametric models in real-time.

International Reference Ionosphere (IRI) is an empirical model that was developed and upgraded by the IRI Working Group, a joint enterprise of the Committee of Space Research (COSPAR) and the International Radio Science Union (URSI) (Cander et al. 1998). IRI-90 is introduced in this research (Bilitza et al. 1990). As empirical models are established based on past data records, eight data sources are designed for IRI-90 (Bilitza et al. 1990). For the electron density profile, it is separated into six layers in the IRI: the topside, the F2 layer, the F1 layer, the intermediate layer, the E-valley and the E-bottomside and D layer. In general, the IRI is evaluated by Cander et al. (1998) that the plasma density profile is modelled with high quality in IRI from the ground to the F layer peak though the topside should be improved and continuous electron density can be acquired with IRI while the continuity in first derivatives of space needs further research.

3.1.2. Ionospheric effects on GNSS

As summarized by Klobuchar (1996), the ionosphere mainly has eight types of impacts on GNSS: 1) group delay; 2) phase advance; 3) Doppler shift; 4) Faraday rotation of linearly polarized signals; 5) bending of the signal path; 6) pulse distortion 7) amplitude scintillation 8) phase scintillation. The refraction effect on signals is one of the most significant cause of ionospheric errors. When radio waves propagate from the space through the ionosphere, radio waves may refract due to variable refractive index in the ionosphere, which leads to delay or advance of signal propagation speed or even change of the signal path. Thus, information gap arises due to the difference between the actual and planned state of signals that is the origin of the measurement error in GNSS. To quantify the refraction effect on GNSS signals, the function refractive index n has been derived by Appleton and Hartree (Klobuchar 1996):

$$n^2 = 1 - \frac{X}{1-iZ-\frac{Y_T^2}{2(1-X-iZ)} \pm [\frac{Y_T^4}{4(1-X-iZ)^2}+Y_L^2]^{0.5}} \quad 3.2$$

$$X = \frac{N_e e^2}{\epsilon_0 m\omega^2} = \frac{f_n^2}{f^2} \quad 3.3$$

$$Y_L = \frac{eB_L}{m\omega} = \frac{f_H cos\theta}{f} \quad 3.4$$

$$Y_T = \frac{eB_T}{m\omega} = \frac{f_H sin\theta}{f} \quad 3.5$$

$$Z = \frac{v}{\omega} \quad 3.6$$

$$\omega = 2\pi f \quad 3.7$$

where f_p is the plasma frequency, typically less than 20 MHz; f is the system operating frequency; N_e is the plasma density; e is the electron charge, equal to -1.602×10^{-19} coulomb; B is the magnitude of the magnetic field; ϵ_0 is the free space permittivity, equal to 8.854×10^{-12} farad/m; m is the rest mass of an electron, equal to 9.107×10^{-31} kg; θ is the angle between the signals and the magnetic field of the Earth; v is the frequency of the electroneutral collision, approximately 10^4; f_H is the frequency of the electron gyro, typically equal to 1.5 MHz.

3.1.2.1. Group delay and phase advance

Based on the refractive index, the group delay and phase advance respectively for pesudorange

and carrier phase measurements can be derived, which is introduced in section 2.2.1.1.

3.1.2.2. Doppler shift

Due to variable electron density and refractive index, extra Doppler shift occurs to signals when they pass through the ionosphere. According to Klobuchar (1996), the Doppler shift caused by the Total Electron Content (TEC) variation can exceed the geometric component for satellites in high-altitude orbits. The maximum rate of change of TEC (ROT) is about 0.1×10^{16} el/(m^2·s), This can generate the frequency shift of 0.085 Hz and 0.109 Hz at GPS L1 and L2, respectively, which are significantly lower than the bandwidth of the carrier tracking loop and can be corrected with dual-frequency observations like the first-order ionospheric error.

3.1.2.3. Faraday rotation

When a linearly polarized wave propagates in magnetized plasma along the direction of the magnetic field, the polarization plane rotates in the forward direction of magnetized plasma, which is known as the Faraday rotation effect (Klobuchar 1996; Michael et al. 2005). GNSS signals propagate with right-hand circular polarization, which is not influenced by Faraday rotation. However, a part of mobile rovers are still applied with the linear polarization, which are subject to a signal intensity loss of approximately 3dB. In extreme cases, the rotation reaches 90° when satellites are viewed in different directions which results in the signal strength loss increase to more than 30 dB. This loss of signal strength is destructive to the positioning behavior of GNSS and may lead to a complete loss of lock. However, if an advanced receiving antenna is used, which also transmits the signal with right-hand circular polarization, Faraday rotation is no longer an issue.

3.1.2.4. Signal path bending

When the radio wave is slanted from one transparent medium into another with a different refractive index, the propagation direction of the wave changes, which is known as the refraction effect. Thus, the signal path is altered when the signal transmits in the ionosphere due to its variable refractive index. According to Millman and Reinsmith (1974), the refraction error decreases as the elevation increases. Thus, with an appropriate elevation cutoff, the refraction

effect can be mitigated to a level that will not cause a problem, which is typically selected as 10 degree. The application of the elevation cutoff can also mitigate the majority of the multipath and tropospheric effects at low elevation.

3.1.2.5. Pulse distortion

The pulse distortion occurs when the input signal bandwidth exceeds the capacity of the system bandwidth. As aforementioned, spread spectrum pseudo random noise (PRN) is applied to GNSS signals, which may be dispersed by the ionosphere. Thus, the arrival time of the pulse waveform delays due to dispersion effect. According to Millman (1965), the delay is more critical when magnitudes of the system and signal bandwidths are comparable. In other words, higher signal bandwidth can reduce the effect of pulse distortion. The C/A and P codes respectively employ PRN noise with bandwidth of 2 MHz and 20 MHz, where the P code observation is barely influenced by the dispersion effect due to its high bandwidth (Klobuchar 1996).

Aside from these effects, the ionosphere can also lead to a more severe effect, rapid fluctuations in both amplitude and phase of GNSS signals. The phenomenon that causes this effect is called ionospheric scintillation, which can cause range errors, cycle slips and even losses of lock. Thus, scintillation is one of the most important issues to be addressed in GNSS applications and detailed introduction of scintillation is covered in the next section.

3.2. Ionospheric scintillation

When signals enters an irregular medium in the ionosphere, the amplitude and phase of signals may also become irregular that leads to a drop of signal amplitude and the shift of signal phase, known as ionospheric scintillation (Kintner et al. 2007). Ionospheric scintillation is one of the most severe error sources that can degrade the quality of satellite signal tracking or even lead to loss of lock on satellites, thus causing significant errors in GNSS receiver operation and positioning (Sreeja et al. 2011b). Under amplitude scintillation, the signal intensity can not only be destructively decreased but also be constructively enhanced. The temporary enhancement on signal intensity is barely useful to GNSS users but the decrease in signal intensity can degrade

GNSS applications, especially when the signal amplitude drops below the tracking loop threshold and the signal should be re-acquired. (Klobuchar 1996). Under phase scintillation, the signal phase inconsistently fluctuates in addition to regular variation due to rate of TEC, which may cause the signal spectrum to spread out resulting in loss of phase lock for receivers with a narrow bandwidth (e.g., 1 Hz). Usually, problems in receiver loop lock occur when the change in phase only exceeds 1 radian at L1 (Klobuchar 1996). Hence, scintillation is one of the most critical problems that should be solved for GNSS applications. Research on the characteristics of scintillation can provide ideas for solving this problem. The occurrence of scintillation is affected by several factors, such as time period, season, solar activity, latitude etc. According to Klobuchar (1996), scintillation is not strong between April and August in the American, African and Indian regions and the reverse is true in the other months. In addition, scintillation usually occurs after local sunset. Furthermore, the intensification of solar activity can directly lead to the occurrence of amplitude scintillation, and thus signal intensity fades as shown in Figure 3.3. Finally, the latitudinal variation of scintillation is one of the most typical characteristics, introduced in detail as follow.

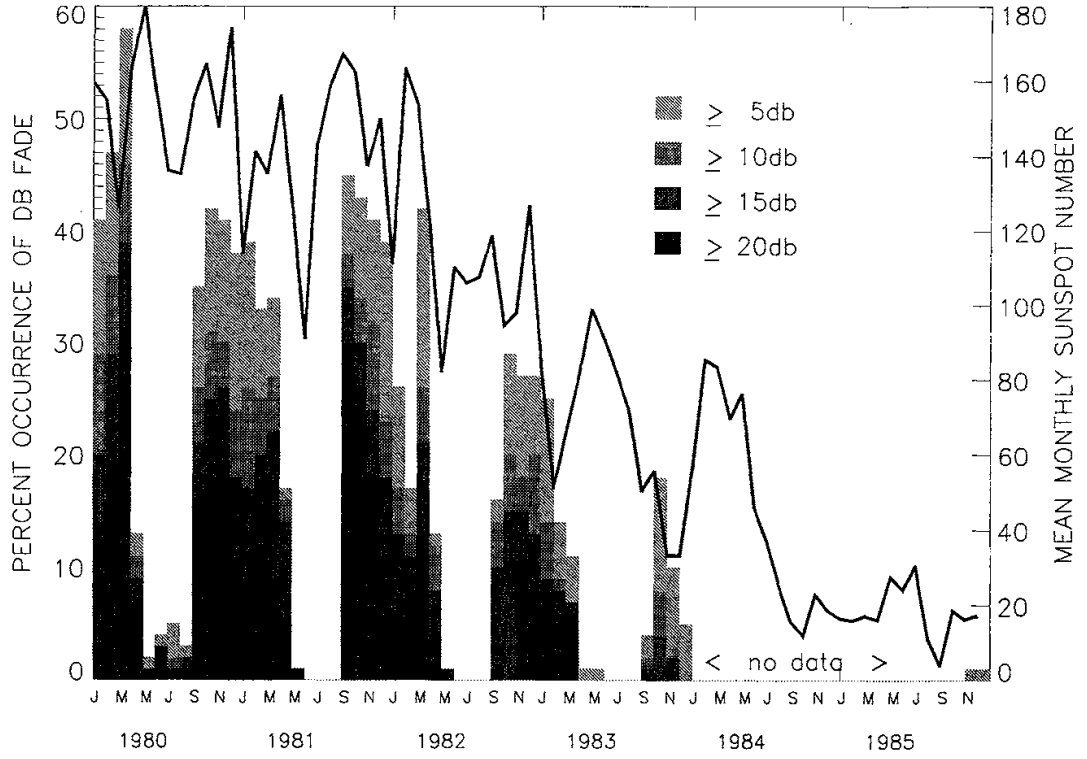

Figure 3.3 The relationship between the signal intensity fade and mean monthly sunspot number at Ascension Island during 1980-1985 (Figure 7 in (Basu et al. 1988)).

3.2.1. Scintillation at different latitudes

Ionospheric scintillations mainly occurs in the equatorial and auroral regions which respectively may extend up to ±20° geomagnetic latitudes from the equator and ±65° geomagnetic latitudes from the polar regions, and occasionally in the mid-latitude regions. Moreover, scintillation that happens in different latitude regions can be attributed to different causes and therefore have different characteristics.

3.2.1.1. Scintillation at low latitudes

Scintillation is more severe with broader coverage at low latitude than the other regions, which almost covers half of the Earth (Klobuchar 1996). The major cause of scintillation at equatorial and low latitude regions is ESF as mentioned in section 3.1. According to Calvert (1962), ESF is a type of ionospheric phenomenon recorded in the ionograms as a spread in frequency that occurs in the ionospheric F region between 15º and -15º in latitude. This is caused by scattering of plasma density ionospheric irregularities, which is also explained in Figure 3.4, Ionosphere rapidly reshapes and ESF moves poleward and upward, which produces an ionospheric hole (bubble), which has been proved to be related with scintillation (Kintner et al. 2007). Moreover,

at equatorial regions, irregularities are usually shaped as rod-like structures expanding along the geomagnetic field lines, which can even reach 1000 km in altitude under extreme conditions (Béniguel et al. 2009).

Equatorial and low latitude scintillation mainly occurs during the local sunset period (Basu et al. 1988; Béniguel et al. 2009) which may reach the peak at around 9pm local time (Skone et al. 2001). For the low latitude regions, intense scintillations principally occur between 1 hour after local sunset and the midnight (Klobuchar 1996). It has been analyzed by Jiao and Morton (2015) that equatorial and low latitude scintillation has more disastrous effects and have longer durations and is primarily independent of geomagnetic activity as compared with scintillation occurring in other geographic locations. Furthermore, according to the case study by Doherty et al. (2003), amplitude scintillation arises more frequently than phase scintillation at low latitudes. Thus, scintillation at low latitudes leads to more power fading than phase shift, therefore, losses of lock (Humphreys et al. 2010).

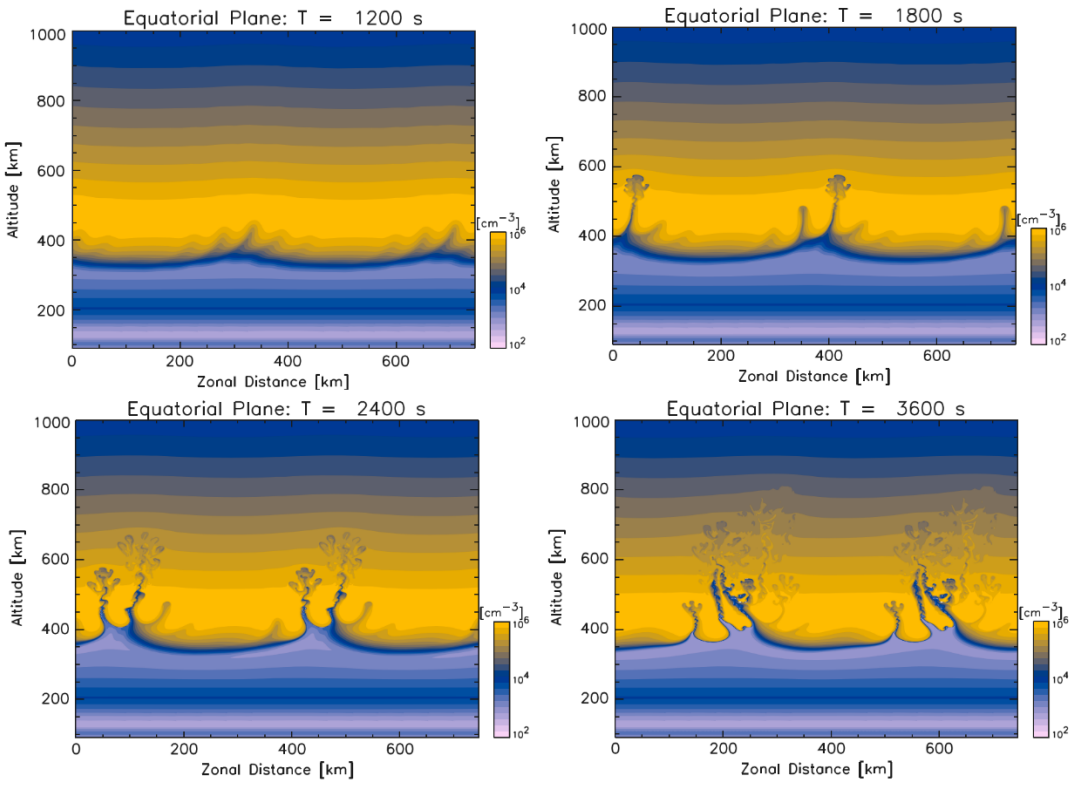

Figure 3.4 ESF event simulation at numerical times. At equatorial areas, the time after sunset is characterized by F-region instabilities. Due to the interruption occurs to the ionization caused by solar radiation, reorganization procedures result in the formation of low-density layers under the ionized layers. Because of the appearance of RT instabilities, bubbles or plumes in the free-electron density, appear at

bottom of the F-region and upward propagate through the F-region. The characteristic size and duration of plasma bubbles are respectively around 100 km and 2-3 hours, which, however, range from centimeters to tens of kilometers and seconds to hours, separately. In the free-electron density, the intense and frequent scintillation is attributed to the anisotropy (Figure 4 of Yokoyama et al. (2015)).

3.2.1.2. Scintillation at midlatitudes

Scintillation is relatively inactive at midlatitudes leading to negligible consideration of midlatitude scintillation in research. However, moderate or even strong scintillation are observed through receivers located in Blacksburg (37.205°N, 80.417°W) (Jean et al. 2017), Nicosia (35.18°N, 33.38°E) (Sreeja et al. 2017), Nanjing (31.97°N, 118.81°E) (Fang et al. 2012), respectively. In addition, (Eltrass et al. 2016) also suggests that scintillation with severe impact could occur at midlatitudes, which may be induced by the cascading procedures of the temperature gradient instability (TGI) and the gradient drift instability (GDI) under strong geomagnetic storms. Furthermore, Basu et al. (2002) explained that the type of irregularities is caused by southward propagation of northern lights at midlatitudes. Another explanation indicating short-time inner-magnetospheric electric field and ionospheric density gradients caused by the phenomenon named subauroral polarization streams (SAPS) or storm-enhanced densities (SEDs) leads to scintillation (Kintner et al. 2007). In addition, the occurrence of midlatitude scintillation is relatively dependent on the solar activity and geomagnetic conditions (Romano et al. 2008), where the former follows the 11-year pattern. Therefore, though scintillation is comparatively rare in midlatitudes, it is still worth to research on this region, especially with the next peak approaching and the solar activity becoming increasingly active.

3.2.1.3. Scintillation at high latitudes

For high-latitude, it is explained that polar cap patches create the ionospheric irregularities in the F region, therefore, resulting in scintillation (Béniguel et al. 2009; Coker et al. 2004). Polar cap patches are defined as regions of dense plasma propagating away from the sun through polar cap, which is presumed to be associated with GDI (Coker et al. 2004). Moreover, E region ionization relevant to auroral electron precipitation causing the TEC fluctuations can be another reason of high-latitude scintillation (Coker et al. 1995). Though scintillation could be caused by different reasons, scintillation at high latitudes are predominately detected under intense geomagnetic conditions (Basu et al. 2002; Li et al. 2010; Keskinen and Ossakow 1983; Doherty et al. 2003). It is also suggested by Jiao and Morton (2015) that high latitude scintillation is significantly dependent on the occurrence of geomagnetic field activity. According to Klobuchar (1996), though the scintillation effect is not as critical at high latitudes as it is at

equatorial areas, it can last up to several days without being restricted by the sunset. Another distinct characteristic of high-latitude scintillation is that phase fluctuations are more frequent and severe than amplitude fluctuations in contrast to low-latitude scintillations, which could occur at all local times (Jiao and Morton 2015).

3.2.2. Ionospheric scintillation modelling

Essentially, the ionospheric scintillation is the phenomenon of signal fluctuations caused by reflection, refraction and diffraction when transmitting through electron density irregularities that alters the original intensity, path and phase of signals. Based on the fundamental definition, several theories have been developed to research on scintillation data, which includes Weak-scatter theory, the Rytov approximation, single, thin or multipath phase screen and multiple-scatter theory (Priyadarshi 2015). Scintillation is regarded as a stochastic event. Thus, the theoretical statistics of scintillation should accords with the Gaussian distribution with zero mean. There are three major types of scintillation models: theoretical, global climatological and empirical models (Priyadarshi 2015).

The first theoretical model namely F-layer scintillation model was proposed by Fremouw and Rino (1973) dedicated to estimating theoretical values of scintillation indices for trans-ionospheric VHF/UHF signal propagation with the input of geomagnetic latitude, time of the day, day of the year and sunspot number. However, only mean scintillation conditions instead of specific fluctuant results of scintillation parameter could be obtained in this model. Thus, this model could not be applied to evaluate the details of scintillation events compared with other models, such as Wide Band Model (WBMOD). The effectiveness of the F-layer scintillation model for displaying the scintillation has been shown by Fremouw and Rino (1973) through comparison between the result obtained with the model and the observations from the geostationary satellites in Ghana. Additionally, the proposal of the F-layer scintillation model led to the establishment of another further developed model namely WBMOD.

The WBMOD ionospheric scintillation model is a global climatological model developed by NorthWest Research Associates (NWRA) (Fremouw and Secan 1984). WBMOD consists of

two parts, an ionosphere model and a propagation model, which are applied for deriving the distribution and basic characterization of the plasma density irregularities, and the impacts of these irregularities on the signal, respectively. Herein, the ionosphere model is established based on a significant amount of scintillation data from the several experiments and the propagation model is created based on the phase screen model (Priyadarshi 2015). WBMOD was improved by Secan et al. (1995) at equatorial regions by using a more extensive database. Thus, the percentage of time that the scintillation intensity exceeds a certain threshold instead of the mean intensity could be obtained and the prediction of scintillation activity was satisfactory up to 2 hours earlier than the observation in the anomaly region.

Atmospheric Explorer D data was applied by Basu et al. (1981) for modelling high-latitude scintillations. Similar to WBMOD, Basu's model was also established based on the phase screen model of weak scintillation (Rino 1979a). The establishment of this empirical model is primarily divided into two steps, determination of RMS plasma irregularity amplitude and conversion of the plasma density morphology into the scintillation model. However, the application of this model was limited to the period of northern winter with sunspot minimum due to lack of data.

According to Priyadarshi (2015), these 3 models are capable of characterizing ionospheric scintillation though the precision is not always satisfactory for a short period of time, summarized in Table 3.1. There are numerous other models in each category, such as the Aarons Model (Aarons 1985), the Franke and Liu Model (Franke and Liu 1985) in the theoretical type, the Global Ionospheric Scintillation Model (GISM) (Béniguel 2002) in the climatological type, and Wernik, Alfonsi, and Materassi Model (Wernik et al. 2007) in the empirical type. All types of models have their limitations and scope of application. Based on the same fundamental theory of radio wave transmission in disordered media, each model was developed according to a variety of factors such as region, weather, sensitivity to solar event conditions, etc. The theoretical model typically unsuccessfully generates the global morphology under intense solar activities while the empirical model is more robust in scintillation prediction with higher accuracy under intense solar activities (Priyadarshi 2020). The scintillation model cannot be

corrected after its algorithm is derived. This limits the application of the model, which means the model should be reestablished if it needs to be modified. When the empirical model is applied, the latest data should be used for establishing the model. However, recent data might not be available. Thus, the data collected during last solar cycle is used under this condition, which may lead to bias.

Table 3.1 Summary of ionospheric scintillation modelling

Model name	F-layer scintillation model	WBMOD	Basu's model
Model type	Theoretical	Global climatological	Empirical
Advantage	Foundation to the WBMOD	The operating scenario can be specified by users	More robust in scintillation prediction
Disadvantage	Only average scintillation conditions can be obtained	Cannot reflect patchy character of the equatorial scintillation	Limited to the northern winter under sunspot minimum conditions

3.2.3. Effects on GNSS

As mentioned above, the operation of GNSS can be affected by a series of factors, in which the ionosphere is the most dominant source. Ionospheric scintillation is one of most active phenomenon present in the ionosphere, which can lead to rapid fluctuations in the amplitude and phase of GNSS signals. Furthermore, a significant characteristic of scintillation is that signals with lower frequencies are more susceptive to scintillation than those with higher frequencies (Delay et al. 2015; Jiao and Morton 2015). Thus, the L2 signal is usually affected more than the L1 signal. In addition, the ionospheric irregularities that cause scintillation are small in size (usually hundreds of meters), suggesting that the influence of the same scintillation event on two receivers several kilometers apart can be completely different. Therefore, the error correction extracted from the reference station may not be accurate for the rover and it may even fail to apply the Differential-GNSS or real-time kinematic (RTK) technique under scintillation events (Elmas 2013). Though Precise Point Positioning (PPP) applications do not need

reference stations, it is also sensitive to scintillations as the PPP algorithm is heavily dependent on carrier phase measurements that are ambiguous (Lonchay 2019). Scintillation can be generally categorized into three levels: weak, moderate and strong. However, there is no uniform standard for defining the boundary between levels. Moreover, as the magnitude of signal power usually fluctuates more dramatically than phase, the threshold for classifying levels for S4 differs from that for σ_ϕ. For instance, it is defined by Marques et al. (2018) that the value of S4(σ_ϕ) lower than 0.5(0.4) is regarded as weak and that higher than 1(0.8) is regarded as strong. However, according to Vilà-Valls et al. (2020), the value of S4(σ_ϕ) lower than 0.4(0.25) is regarded as weak and that higher than 0.6(0.5) is regarded as strong. Therefore, different criteria are selected for different results, which is relatively subjective. It has been observed by Sreeja et al. (2011b) that the tracking loops were more significantly affected under a higher scintillation level. Thus, under varying intensity of scintillation and difference between the signal and plasma frequency, the positioning reliability of GNSS can be influenced to different degrees: range measurement errors, cycle slips or even complete loss of lock.

3.2.3.1. Cycle slips

The presence of phase scintillation could lead to an increase in the Doppler shift of GNSS signals so that cycle slips may occur (Susi et al. 2014). Luo et al. (2017) have characterized that more than 70% of cycle slips occur under intense scintillation. A variety of methods have been developed to detect and repair cycle slips (Cai et al. 2013; Luo et al. 2017) even under scintillation conditions (Ji et al. 2013). However, strong scintillation is capable of causing continuous cycle slips during a short time period that may lead to failure in repairing cycle slips (Banville et al. 2010). Cycle slip is the discontinuity of carrier phase measurements during a certain time period when the satellite is supposed to be visible. That means one or several parts of data utilized for position estimation are lost, which certainly reduces the positioning quality. Furthermore, the presence of cycle clips could increase the complexity of ambiguity resolution process for carrier phase measurements and result in errors or even re-convergence. Thus, cycle slips can severely affect both RTK (Farooq et al. 2020) and PPP (Lonchay 2019) applications, which are strongly dependent on carrier phase measurements.

3.2.3.2. Receiver signal tracking performance

The delay lock loop (DLL) and the phase lock loop (PLL) are two tracking loops respectively for the pseudorange and carrier phase measurement, where the PLL maintains the minimum phase difference between received and local signals, and the DLL keeps maximum correlation between the received and local signals. The effect of scintillation on PLL is larger than on DLL

(Hegarty et al. 2001). Thus, the carrier phase measurement is more susceptible to scintillation than the code measurement. Therefore, both RTK and PPP are sensitive to scintillation in terms of receiver signal tracking performance. The frequency pull-in range of PLL is the maximum tolerable mismatch between the received and the internally estimated signals, which is also known as the maximum frequency step (Humphreys et al. 2010). However, when scintillation leads to phase shift in the signal, the error variance of PLL increases so that the frequency step imported to the PLL may exceed the maximum value, and thus, fail in phase lock. Under extreme scintillation conditions, the PLL cannot recover from a loss of lock for a long time. According to (Elmas et al. 2011), the occurrence of scintillation leads to intense fluctuations of carrier phase tracking error which exceeds 0.26-0.3 radians. Under this condition, the PLL cannot work properly. In addition, Aquino et al. (2007) and Aquino et al. (2009) proposed to use the variance of the output error of the receiver DLL and PLL to assess the tracking performance. Then, the PLL tracking jitter variance map was proposed by Sreeja et al. (2011a) to visually evaluate the tracking performance, where the jitter variances calculated from the data intensely fluctuates in the presence of scintillation.

3.2.3.3. Losses of lock

According to Humphreys et al. (2010), a PLL may not recover after a long time period of cycle slips under strong amplitude scintillation, which leads the baseband signal power to decrease by higher than 13 dB or even 20 dB in L2C signals (Pi et al. 2017). When the signal intensity drops below the threshold of the DLL or PLL, the DLL/PLL frequency is further detuned and the signal is completely lost as a consequence (Lonchay 2019). Even worse, such condition cannot be avoided even with high-quality GNSS receivers under strong scintillation. In this case, data gaps are observed in observation files.

In the case of loss of lock, the signals need to be reinitialized. Especially for PPP applications, it typically takes 20-60 minutes for convergence (Xiang et al. 2020). By comparison, the convergence time of RTK is substantially shorter, which is typically less than 10 minutes (Siejka 2018). Thus, PPP is more susceptible to losses of lock than RTK. Thus, the dual frequency observations may decline to the single frequency observation that leads to the failure in the IF combination and thus the first-order ionospheric delay correction. In addition, losses of lock may directly result in the reduction of number of available satellites tracked by GNSS receivers that leads to the degradation of satellite geometry and consequently the dilution of

precision (DOP). As a consequence, the quality of data that can be applied for positioning decreases, which degrades the positioning quality. Under some extreme circumstances when several satellites cannot be locked due to scintillation and the other satellites are severely affected by multipath, the number of satellites with high quality are even insufficient for operating positioning algorithms that leads to complete failure of obtaining receiver location.

3.2.3.4. Measurement errors

When scintillation is not so intense that cycle slips and losses of lock are not caused, the tracking performance are degraded instead. Then, the degraded pseudorange and carrier phase measurements are input into the positioning algorithms, which produces position outputs with higher ranging errors. The positioning error doubled (Linty et al. 2018) or even increased by two orders of magnitude during a short period (Pi et al. 2017) when encountering scintillation events. According to He et al. (2016), errors caused by scintillation on carrier phase and pseudorange methods can respectively reach 3 cm and 10 m, which can be seen as destructive impact on GNSS applications, especially those requiring high accuracy.

3.2.4. Existing mitigation methods

As ionospheric scintillation leads to disastrous impacts on GNSS applications, a variety of research has been carried out for mitigating the scintillation effect, which includes ionospheric modelling, satellite evaluation, constellation combination, etc. The scintillation models have been introduced in section 3.2.2.

In addition to modelling, numerous techniques have been developed to improve the positioning algorithm. According to Aquino et al. (2007), the tracking error variances of GNSS receiver DLL modelled according to the model of Conker et al. (2003) were used to weight the least square stochastic (LSQ) model. The application of the Conker model was based on three assumptions (Conker et al. 2003): 1) the amplitude scintillation was not correlated with the phase scintillation while modelling; 2) DLL error variance was estimated independent of phase scintillation; 3) the DLL/PLL SNRs were regarded to be constant. Note here that Conker model is valid only when S4 of L1 signal does not exceed 0.707, otherwise the condition of loss of lock is assumed. By weighting the LSQ model with tracking jitter variance for code measurements, the height positioning RMS was shown to be improved by 17–21% (Aquino et

al. 2007). Furthermore, the tracking error variance of PLL was also used to evaluate the degradation degree of the carrier phase measurements and applied as the weight of the LSQ model (Aquino et al. 2009). As compared with the tracking error variance of DLL, that of PLL contained phase scintillation and oscillator noise components in addition to amplitude scintillation components (Conker et al. 2003). By applying tracking error variance of both DLL and PLL to weight LSQ model, the improvement of height RMS increased up to 38% (Aquino et al. 2009). Two limitations were proposed by Elmas (2013) for this method. First, the Conker model was invalid when S4(L1) exceeds 0.707, where it was assumed that losses of lock were encountered. However, it has been detected by Elmas (2013) that the lock is still maintained even if S4(L1)>0.707 sometimes. Additionally, it is not easy to retrieve the spectral strength and slope required for computing the error variance component relevant to the phase scintillation, especially for the high frequency signal. For solving the first limitation, a modified version of Conker model, named Conker′ model was proposed, where S4′ was derived instead of S4 (Park et al. 2017). In the Conker′ model, the normalization of signal-to-noise ratio (SNR) was implemented at each second in S4′ instead of each minute in S4 that is the only difference as compared with original Conker model (Park et al. 2017). Furthermore, another strategy namely IQ approach based on the signal post-correlation in-phase (I) and quadra-phase (Q) samples was developed by Elmas (2013) that was able to overcome both limitations. It has been shown by Park et al. (2017) that the 3D positioning RMS was improved up to 77.3% and 58.3% respectively using Conker′ models and IQ approach under strong scintillation. In addition, Sreeja et al. (2020) applied α-μ model (de Oliveira Moraes et al. 2014) instead of Conker model to calculate the tracking error variances of DLL and PLL as the weight of the LSQ model. The α-μ model was developed based on the α-μ distribution of Yacoub (2007), which was an extended model of the Conker model. In other words, the Conker model was a specific case of α-μ model. Thus, α-μ model was able to analyze a wider range of situations. By applying the α-μ model to weight LSQ model, the 3D positioning RMS was improved by about 62-75% (Sreeja et al. 2020).

Vani et al. (2019) proposed an integrated methodology for mitigation of scintillation effects using the weighting strategy. First, a novel functional model was used to correct the

measurement errors of carrier phase observables. Compared with the conventional functional model, new terms related to scintillation are added: $dScint_{PR_i}(t)$ and $\lambda \cdot dScint_{\phi_i}(t)$, time-varying range errors in code and phase measurements caused by scintillation. However, there was a problem left in the first process, which was the scintillation error term related to the integer ambiguity. Therefore, the LSQ stochastic model was weighted based on the scintillation error term in the second process. However, as $dScint_{PR_i}$ was not available, no extra weight was applied to the code measurements, which meant the weight of code measurements was assigned with the constant empirical value. As for carrier phase measurements, an empirical function was applied as the weight by Vani et al. (2019). Under strong scintillation, losses of lock occur which may lead to fails in obtaining $\lambda \cdot dScint_{\phi_i}$. In this case (third process), Vani et al. (2019) suggested that an upper bound value of $\lambda \cdot dScint_{\phi_i}$ was used. Meanwhile, a time window was used to detect losses of lock close to the current epoch. All the values were empirically estimated and tested (Vani et al. 2019). By applying the whole methodology, the 3D positioning root mean square error (RMSE) was improved by up to 80% in PPP and the scintillation effect was completely eliminated in the optimal case.

In addition to weighting LSQ models, there was a more easy-to-use method to mitigate the scintillation impact, i.e., removing the satellites affected by the scintillation. Bougard et al. (2013) attempted to detect and exclude scintillation affected satellites from the positioning calculation using the technique namely receiver autonomous integrity monitoring (RAIM). Furthermore, an analysis called w-test values was conducted to confirm the satellites to exclude. By removing satellites influenced by the scintillation, the PPP resilience to the scintillation was considerably improved.

Additionally, wavelet filtering is another alternative way to mitigate the scintillation effect. The empirical mode decomposition (EMD) is an adaptive and efficient data analysis method to decompose signals into a finite number of intrinsic mode functions (IMF) through a sifting process along with mode mixing (Huang et al. 1998). However, the sifting process and mode mixing as well as lacking of mathematical theory restrict EMD in turn (Wu and Huang 2009), where the mode mixing typically causes signal intermittency. The intermittence could result in

mistakes in signal distribution identification and indistinctness of physical significance of IMFs. Thus, a new method namely Ensemble EMD (EEMD) was developed to overcome these problems, where the true IMF components were defined as the mean of the trails ensemble and a Gaussian white noise was added to each signal before decomposition (Wu and Huang 2009). Therefore, the addition of white noise was able to cancel out the noise in trials and the ensemble mean remained as the persistent part. However, the white noise may also lead to the generation of irrelevant components of modes that caused the residual of noise if its amplitudes were inappropriate. Hence, Yeh et al. (2010) proposed a further novel method called Complementary EEMD (CEEMD), where both positive and negative white noises were added so that the residual of the white noise was completely removed. CEEMD effectively reduced the time consumption in computation and the noise of the final residue. However, even CEEMD was confined by a multicomponent signal (MCS). By combining with multifractal-detrended fluctuation analysis (MF-DFA), Miriyala et al. (2015) managed to mitigate the scintillation effect on the carrier to noise ratio (C/N_0) data through CEEMD. In the experiment conducted by Miriyala et al. (2015), the C/N_0 value dropped to 31 dB-Hz due to scintillation and methods EMD-MF-DFA, EEMD-MF-DFA and CEEMD-MF-DFA respectively improved the C/N_0 value to 38.64, 38.03 and 39.2 dB-Hz, at least 6 dB-Hz more than the conventional technique.

Another signal decomposition technique, namely variational mode decomposition (VMD) was developed by Dragomiretskiy and Zosso (2014), which could decompose nonstationary MCS into a number of sparse band-limited IMFs (BLIMF) by searching the optimal solution of the constrained variational model. The VMD algorithm primarily contained two updating loops for the set of all modes and corresponding center frequencies, which were achieved with the Wiener filter. Thus, VMD modes were close to the center frequencies that led to high robustness in sampling and noise detection. By applying VMD-DFA algorithm, the signal noise of 13 to 14 dB was mitigated that was 3 to 4 dB more than the CEEMD-DFA. In addition, another advantage of VMD-DFA was its feasibility in precisely separating the frequency components that were close together as compared with conventional techniques. It has also been shown by Ahmed et al. (2019) that VMD-MF-DFA has effectively denoised over half both synthetic and real amplitude scintillation at most according the standard deviation (STD) and RMSE

performance of positioning results, which was more superior than CEEMD-MF-DFA and VMD-DFA.

To further optimize the effectiveness of signal decomposition, an improved CEEMD with adaptive noise (iCEEMDAN) has been proposed by Colominas et al. (2014) and developed by Honório et al. (2017), which addressed the drawbacks of CEEMD. The iCEEMDAN separated the first and the following decompositions as the first residue and mode contained the original signal and the following decompositions were iterative based on previous residue. By integrating iCEEMDAN, VDM and DFA, the iCEEMDAN–VDM-DFA algorithm was proposed by Dey et al. (2021). As stated by Dey et al. (2021), the proposed method further improved the intensity of synthetic signal by 2.29 dB and decreased the real S4 values by 0.17 at most as compared with VMD-DFA algorithm. Furthermore, the proposed method effectively improved the STD of signal around 30% and 10% in average respectively for simulated and real signals, where the best improvement for RMSE of signals even reached 69.7% and 85.9%, respectively.

Even with the above methods, losses of signal lock and cycle slips are still the primary problems under strong scintillation conditions, which are relatively severe when using a single satellite constellation. Therefore, it was proposed that the data of GPS and GLONASS could be integrated to obtain more reliable positioning solutions under moderate to strong scintillation (Marques et al. 2018), which improved the positioning RMS by 63% in height and 57% in 3D compared to using GPS alone. Dabove et al. (2020) also integrated data from GPS, GLONASS and Galileo to mitigate scintillation effects on PPP, with a 46% shorter convergence period and a 51% lower RMS in height under intense scintillation compared to using GPS alone. By applying an integrated novel adaptive architecture named MF-On-ARKF, RMSE of light of sight (LOS) phase considerably decreased under both single- and multi-frequency condition, which improved the synchronization performance (Vilà-Valls et al. 2020).

3.3. Parameters

The research in this thesis on the algorithm development to mitigate scintillation effects is based on a variety of parameters. The four primary parameters used in this thesis are introduced: S4,

σ_ϕ, MP and ROTI. Then, the relationship between these parameters is investigated based on past research. In addition, the theoretical relationship is also researched on the basis of the formulae, which lays the foundation for the analysis in Chapter 4.

3.3.1. S4

The index S4 is traditionally applied to monitor the amplitude scintillation. According to Van Dierendonck et al. (1993), the raw value of S4 is computed from raw signal intensity (SI) of signals which is the difference between Narrow Band Power (NBP) and Wide Band Power (WBP), calculated as below:

$$WBP = \sum_{i=1}^{20}\left(I_i^2 + Q_i^2\right) \tag{3.8}$$

$$NBP = \left(\sum_{i=1}^{20} I_i\right)^2 + \left(\sum_{i=1}^{20} Q_i\right)^2 \tag{3.9}$$

where I_i and Q_i are the 1000 Hz in-phase and quadraphase samples. Then total S4 (raw S4), which includes errors caused by environment, is defined as follows:

$$S4_T = \sqrt{\frac{\langle SI^2\rangle - \langle SI\rangle^2}{\langle SI\rangle^2}} \tag{3.10}$$

where $\langle * \rangle$ represents the expected value over a certain time period, which is 60 seconds here. As the raw intensity measurement contains a series of ambient noises, which needs to be removed, SI is detrended. Herein, SI is filtered by a sixth-order low-pass digital Butterworth filter (Dierendonck and Arbesser-Rastburg 2004). Specifically, each detrended SI is obtained by dividing raw SI by the corresponding low-pass filter:

$$SI_k = \frac{(NBP - WBP)_k}{(NBP - WBP)_{lpf,k}} \tag{3.11}$$

where k represents the serial number. After detrending SI, the ambient noise of S4 is also supposed to be removed. This can be achieved by applying the mean signal-to-noise density over the interval of interest (60 seconds). Thus, the part of S4 induced by ambient noise is (Van

Dierendonck et al. 1993):

$$S4_{N_0} = \sqrt{\frac{100}{S/N_0}\left[1 + \frac{500}{19\,S/N_0}\right]} \tag{3.12}$$

where S/N_0 represents the signal-to-noise density. Finally, the modified S4 can be calculated by subtracting the ambient noise part from the total S4

$$S4 = \sqrt{\frac{\langle SI_k{}^2\rangle - \langle SI_k\rangle^2}{\langle SI_k\rangle^2} - \frac{100}{\overline{S/N_0}}\left[1 + \frac{500}{19\,\overline{S/N_0}}\right]} \tag{3.13}$$

where $\overline{S/N_0}$ is the average value of S/N_0 over 60 seconds.

3.3.2. σ_ϕ

The other index, σ_ϕ is traditionally used to monitor phase scintillation, which is derived from the standard deviation of the carrier phase measurements from satellite signals (Dierendonck and Arbesser-Rastburg 2004). Similar to amplitude scintillation, the carrier phase measurements also need to be detrended. According to Van Dierendonck et al. (1993), 50 Hz raw carrier phase measurements are filtered by a sixth-order high-pass Butterworth filter with a 0.1 Hz cutoff frequency that is similar to the low-pass filter applied to SI. However, it was found by Mushini et al. (2012), McCaffrey and Jayachandran (2019) and Ghobadi et al. (2020) that the choice of fixed 0.1 Hz for the cutoff frequency is not reasonable. Instead, the ideal value of cutoff frequency should vary with the Fresnel frequency in the presence of irregularities. In the case of Ghobadi et al. (2020), the cutoff frequency ranges from 0.73 to 0.83 Hz, substantially larger than 0.1 Hz. Thus, an adaptive cutoff frequency should be used. However, in this thesis, the raw data to calculate σ_ϕ is not available. Therefore, the default 0.1 Hz cutoff frequency is still applied in this thesis. After detrending, the standard deviation of filtered phase measurements are calculated over five different time intervals of 1, 3, 10, 30 and 60 seconds for every 60 seconds, where the result with 60 seconds interval is used in this thesis.

3.3.3. MP

Multipath is a type of interference to GNSS receivers which is caused by reflected signals. In this thesis, a 30° satellite elevation mask is applied to all the parameters, which removes most of the multipath effects. An assumption is then made that in general, MP values that are higher than average for signals above 30° during scintillation events are likely to be affected by scintillation and not multipath, which depends on antenna type, environment, etc. MP1 and MP2 can be calculated using equations 3.14 and 3.15 defined in (Estey and Meertens 1999):

$$MP1 \equiv P_1 - \left(1 + \frac{2}{a-1}\right) L_1 + \left(\frac{2}{a-1}\right) L_2 = M_1 + B_1 - \left(1 + \frac{2}{a-1}\right) m_1 + \left(\frac{2}{a-1}\right) m_2 \quad 3.14$$

$$MP2 \equiv P_2 - \left(\frac{2a}{a-1}\right) L_1 + \left(\frac{2a}{a-1} - 1\right) L_2 = M_2 + B_2 - \left(\frac{2a}{a-1}\right) m_1 + \left(\frac{2a}{a-1} - 1\right) m_2 \quad 3.15$$

where M_i is the pseudorange multipath for frequency i; $a \equiv \frac{f_1^2}{f_2^2}$, where f_i is the frequency of signal; B_i is the bias terms, which is defined as

$$B_1 \equiv -\left(1 + \frac{2}{a-1}\right) n_1\lambda_1 + \left(\frac{2}{a-1}\right) n_2\lambda_2 \quad 3.16$$

$$B_2 \equiv -\left(\frac{2a}{a-1}\right) n_1\lambda_1 + \left(\frac{2a}{a-1} - 1\right) n_2\lambda_2 \quad 3.17$$

where $n_i\lambda_i$ is the integer wavelength phase ambiguity for frequency i. MP1 and MP2 are generated using the quality control (QC) command of the Translation, Editing, and Quality Checking (TEQC) software on the receiver independent exchange format (RINEX) version 3.11 files obtained from the three stations, which include both observation and navigation files (Estey and Meertens 2014).

3.3.4. ROTI

ROTI was first defined by Pi et al. (1997) to detect the presence of scintillation in the ionosphere. TEC (total electron content), defined as the total number of electrons integrated along the path between a receiver and satellite, is obtained first. Raw TEC values can be calculated with equations 3.18-3.20 (Ciraolo et al. 2007; Mendillo and Klobuchar 2006):

$$\frac{I_1}{I_2} = \frac{f_2^2}{f_1^2} \quad 3.18$$

$$P_1 - P_2 = I_1 - \frac{f_1^2}{f_2^2} I_1 \quad 3.19$$

$$STEC = \frac{1}{40.3}\left(\frac{f_1^2 f_2^2}{f_1^2 - f_2^2}\right)(P_2 - P_1) \quad 3.20$$

where $STEC$ is the slant TEC representing the TEC along the satellite-receiver link; I, P and f were respectively defined in equations 2.3 and 2.5. Then, $ROTI$ is defined as the standard deviation of the rate of $STEC$ (ROT) as (Pi et al. 1997):

$$ROT_{t_n} = \frac{VTEC_{t_n} - VTEC_{t_{n-1}}}{t_n - t_{n-1}} \quad 3.21$$

$$ROTI = \sqrt{\langle ROT^2 \rangle - \langle ROT \rangle^2} \quad 3.22$$

In this thesis, the ROTI estimated over a 5-min interval is used, which was originally defined by Pi et al. (1997). Additionally, a moving average is applied in ROTI calculation so that the time interval is the same as other parameters.

3.3.5. Relationship between parameters

The research on ionospheric scintillation has lasted for decades. S4 and σ_ϕ are the two parameters that respectively characterize amplitude and phase scintillation. These were defined in more detail in section 3.3.1 and 3.3.2 separately. As S4c and $\sigma_{Ø}$ explained in Chapter 1 can be generated from data with a frequency of at least 1 Hz, the relationship between these scintillation parameters and others from low-rate data was investigated so that the effect of scintillation can be assessed with low-rate data, which are more densely distributed. Therefore, with the global network like International GNSS Service (IGS), it is possible to realize the global coverage of scintillation monitoring. In this thesis, MP and ROTI are the two parameters that are used to study the relationship with scintillation. The past research on MP and ROTI with scintillation are reviewed in the following sub-sections.

3.3.5.1. Scintillation and MP

According to Van Dierendonck et al. (1993), the fast varying multipath still remains in scintillation parameters after detrending though the long-term multipath had been removed, which can lead to false observations of scintillation events. Compared with the long-term multipath, the rapidly varying multipath is caused by fast-moving objects such as trucks, trains, planes, etc. Thus, it is more difficult to separate and remove the fast varying multipath. In addition, Romano et al. (2013) have also shown that, the measurement of S4 and σ_ϕ could be negatively influenced by the multipath effects. They showed that the presence of obstacles in the vicinity of receivers could lead to the increase of S4 that showed some agreement with areas of MP measured using Standard Deviation Code/Carrier divergence (CCSTDDEV). Romano et al. (2013) also showed that a high percentage of the higher S4 values and CCSTDDEV were below 30°. Therefore, scintillation observations could be contaminated by multipath effects. However, the majority of this influence can be mitigated by applying a satellite elevation angle cutoff. The relationship between MP values from the TEQC software and σ_ϕ was observed by Hancock et al. (2017) through occurrence number plots and time series plots from data collected in Hong Kong, which provided initial evidence that the study of the relationship between MP and scintillation parameters might be interesting.

Based on equations 3.16 and 3.17, the calculation of MP contains the integer ambiguity that needs to be resolved during GNSS positioning. According to a number of past studies (Marques et al. 2016; Sreeja et al. 2020; Nguyen et al. 2019), ionospheric scintillation may lead to unsuccessful ambiguity resolution. From this perspective, abnormal MP values can be obtained due to scintillation that fails ambiguity resolution. In addition, it is true that the first order ionospheric delay has been mitigated in equations 3.16 and 3.17, which accounts for more than 99% of the total ionospheric delay as introduced in section 2.2.1.1. Higher-order errors are at the centimeter or even millimeter level while the first order error can reach tens of meters. Thus, higher-order errors can be usually neglected. However, the magnitude of higher-order errors can increase up to tens of centimeters when extreme solar activities occur. Under this condition, higher-order errors should be considered in MP calculations. Equation 3.14 and 3.15 can be

rearranged as:

$$MP1 \equiv\ P_1 - L_1 - \frac{2}{\alpha-1}(L_1 - L_2) \quad 3.23$$

$$MP2 \equiv\ P_2 - L_2 - \frac{2\alpha}{\alpha-1}(L_1 - L_2) \quad 3.24$$

Then, substitute equation 2.3 and 2.7 into equation 3.23 and 3.24:

$$MP1 = M_1 - \left(1 + \frac{2}{\alpha-1}\right)m_1 + \left(\frac{2}{\alpha-1}\right)m_2 - \left(1 + \frac{2}{\alpha-1}\right)n_1\lambda_1 + \left(\frac{2}{\alpha-1}\right)n_2\lambda_2 + I_{g,1} - I_{p,1} - \frac{2}{\alpha-1}(I_{p,1} - I_{p,2}) \quad 3.25$$

$$MP2 = M_2 - \left(\frac{2\alpha}{\alpha-1}\right)m_1 + \left(\frac{2\alpha}{\alpha-1} - 1\right)m_2 - \left(\frac{2\alpha}{\alpha-1}\right)n_1\lambda_1 + \left(\frac{2\alpha}{\alpha-1} - 1\right)n_2\lambda_2 + I_{g,2} - I_{p,2} - \frac{2\alpha}{\alpha-1}(I_{p,1} - I_{p,2}) \quad 3.26$$

where $I_{g,1}$ and $I_{g,2}$ are ionospheric delays of L1 and L2 code measurements, respectively and $I_{p,1}$ and $I_{p,2}$ are ionospheric advance of L1 and L2 phase measurements, respectively. As higher-order errors are counted in, 2.16 and 2.23 are substituted into equation 3.25 and 3.26 and the ionospheric delay part (the second line of equation 3.25 and 3.26) can be expressed as:

$$\begin{aligned} MP1_I &= \frac{q_i}{f_1^2} + \frac{s_i}{f_1^3} + \frac{r_i}{f_1^4} - \left(-\frac{q_i}{f_1^2} - \frac{s_i}{2f_1^3} - \frac{r_i}{3f_1^4}\right) - \frac{2}{\alpha-1}\left[-\frac{q_i}{f_1^2} - \frac{s_i}{2f_1^3} - \frac{r_i}{3f_1^4} - \left(-\frac{q_i}{f_2^2} - \frac{s_i}{2f_2^3} - \frac{r_i}{3f_2^4}\right)\right] \\ &= \frac{3f_1^2f_2 - 2f_1^3 - f_2^3}{2f_1^3f_2(f_1^2 - f_2^2)}s_i + \frac{4f_1^2f_2^2 - 2f_1^4 - 2f_2^4}{3f_1^4f_2^2(f_1^2 - f_2^2)}r_i \quad 3.27 \\ MP2_I &= \frac{q_i}{f_2^2} + \frac{s_i}{f_2^3} + \frac{r_i}{f_2^4} - \left(-\frac{q_i}{f_2^2} - \frac{s_i}{2f_2^3} - \frac{r_i}{3f_2^4}\right) - \frac{2\alpha}{\alpha-1}\left[-\frac{q_i}{f_1^2} - \frac{s_i}{2f_1^3} - \frac{r_i}{3f_1^4} - \left(-\frac{q_i}{f_2^2} - \frac{s_i}{2f_2^3} - \frac{r_i}{3f_2^4}\right)\right] \\ &= \frac{-3f_1f_2^2 + f_1^3 + 2f_2^3}{2f_1f_2^3(f_1^2 - f_2^2)}s_i + \frac{-4f_1^2f_2^2 + 2f_1^4 + 2f_2^4}{3f_1^2f_2^4(f_1^2 - f_2^2)}r_i \end{aligned} \quad 3.28$$

where $MP1_I$ and $MP2_I$ are the ionospheric error part of MP1 and MP2 respectively. As shown in equation 3.27 and 3.28, MP1 and MP2 increases as the ionospheric activity becomes intense which indicates the relationship between MP and scintillation. Thus, only the scintillation events that produce extreme disturbances on signals or even lead to cycle slip can

result in the dramatic fluctuation of MP, which means that not all scintillation events lead to high MP values. Therefore, the relationship between scintillation and MP cannot always be found during scintillation periods.

3.3.5.2. Scintillation and ROTI

The relationship between ROTI and scintillation has been investigated previously (Basu et al. 1999; Yang and Liu 2016; Carrano et al. 2019; Olwendo et al. 2018; Acharya and Majumdar 2019). The scatter plot and the time series plot were common methods used in recent studies to demonstrate the relationship between ROTI, S4 and σ_ϕ (Basu et al. 1999; Yang and Liu 2016; Carrano et al. 2019; Olwendo et al. 2018). Additionally, the relationship between ROTI and scintillation has been shown to be affected by changes in satellite elevation angle (Yang and Liu 2016). Correlation coefficients have shown distinctly higher values when the satellite elevation angle exceeded 60° when compared to satellites with elevation angles lower than 60°. However, this investigation focused on elevations higher than 30°, focusing on satellites with higher elevation angles thus taking advantage of the stronger relationship between scintillation and ROTI shown by Yang and Liu (2016).

Acharya and Majumdar (2019), used statistical analysis to conclude that the probability density distribution of S4 can be obtained using ROTI, thereafter, the occurrence probability of scintillation could be estimated. Therefore, Acharya and Majumdar (2019) gave the conclusion about strong evidence of a relationship between ROTI and S4. In addition, Carrano et al. (2019) also demonstrated the theoretical relationship between ROTI and S4 and has demonstrated that this relationship was highly dependent on the sampling rate. They also provided reasons why this relationship varied between different dates and in different regions.

Investigations (Basu et al. 1999; Carrano et al. 2019; Olwendo et al. 2018; Acharya and Majumdar 2019) focused on S4, where σ_ϕ was not investigated. Therefore, the investigation on σ_ϕ was less thorough than that on S4 based on the past research (Basu et al. 1999; Carrano et al. 2019; Olwendo et al. 2018; Acharya and Majumdar 2019). Though σ_ϕ was investigated by Yang and Liu (2016), a comparison of how both scintillation indices were related to ROTI was not

undertaken. According to Yang and Liu (2016), S4 was more correlated with ROTI than σ_ϕ, which might be caused by the relative inactivity of σ_ϕ (σ_ϕ and S4 respectively showed a maximum value less than 0.4 and higher than 0.9).

Carrano et al. (2019) used Rino's power law scintillation model (Rino 1979a; Rino 1979b) to rewrite the formula of ROTI to search for the relationship between S4 and ROTI:

$$ROTI^2(\delta t) = \frac{\langle |TEC(t+\delta t) - TEC(\delta t)|^2 \rangle}{\delta t^2} = \frac{\langle \left|TEC(r) - TEC(r + V_{eff}\delta t)\right|^2 \rangle}{\delta t^2} = \frac{c^2}{\delta t^2} D_{\delta\varphi}(V_{eff}\delta t) \quad 3.29$$

where δt is the sampling interval; r is the satellite position; V_{eff} is the effective scan velocity; c = -0.186523 TEC/rad transforms phase measurements in radians at GPS L1 frequency to TEC units (1 TECU = 10^{16} electron/m^2); $D_{\delta\varphi}(y) = \langle |\varphi(r) - \varphi(r + V_{eff}\delta t)|^2 \rangle$ is the phase structure function. Carrano et al. (2019) noted here that formula 3.29 neglects the diffraction effect on the phase which means that the phase perturbation is assumed to be caused by irregularities with a scale size of the signal wavelength. In addition, statistical homogeneity is also assumed because $D_{\delta\varphi}$ is supposed to be independent of r (Rino 1979b). With the formula 14 in (Rino 1979b), equation 3.29 can be converted into a theoretical model (Carrano et al. 2019):

$$ROTI^2(\delta t) = \frac{c^2}{\delta t^2}\left\{r_e^2 \lambda^2 \sec\theta \left(\frac{2\pi}{1000}\right)^{2v+1} C_k L\right\} G \cdot \frac{\Gamma(v-1/2)}{2\pi\Gamma(v+1/2)}\left[\frac{1 - 2\left|q_0 V_{eff}\delta t/2\right|^{v-1/2} K_{v-1/2}(q_0 V_{eff}\delta t)/\Gamma(v-1/2)}{q_0^{2v-1}}\right] \quad 3.30$$

where r_e is the classical electron radius; λ is the free-space wavelength; θ is the propagation nadir angle at the IPP; $C_k L$ is the irregularity strength; v has relation to the irregularity spectral index as $p^{(3)} = 2v + 1$ and the phase spectral index as $p = 2v$; G is the phase enhancement factor, which represents the impact of irregularity anisotropy on the phase fluctuation statistics (Rino 1979a); q_0 is the outer scale wavelength; Γ is the gamma function; K is the 2nd kind Bessel function; The difference between the quantities on the first and second line of equation 3.30 is that they are dependent on the irregularity strength $C_k L$ and temporal

separation δt, respectively, where $C_k L$ is independent of the signal frequency and propagation geometry (Carrano et al. 2019).

With the same model, the amplitude scintillation index can be indicated as equation 31 in (Rino 1979a):

$$S_{4w}^2 = \left\{ r_e^2 \lambda^2 \, sec\, \theta \left(\frac{2\pi}{1000}\right)^{2v+1} C_k L \right\} \rho_F^{2v-1} F_s(v) \wp(v) \tag{3.31}$$

where the subscript w indicates weak scatter measure, compared with strong scatter measure; $\wp$(v) is a combined geometry and propagation factor, equation 34 in (Rino 1979a); ρ_F^2 is the Fresnel scale.

$$F_s(v) = \frac{\Gamma[(5/2-v)/2\,]}{2^{v+1/2}\sqrt{\pi}\Gamma[v/2+1/4](v-1/2)} \tag{3.32}$$

And

$$\rho_F^2 = \frac{\lambda Z_R \, sec\, \theta}{2\pi} \tag{3.33}$$

where Z_R is the reduced vertical propagation distance past the phase screen (Rino 1979a), which indicates the curvature of the propagating phase fronts. By dividing ROTI with S4:

$$\frac{ROTI^2(\delta t)}{S_{4w}^2} = \frac{c^2}{\delta t^2} \frac{1}{\rho_F^{2v-1} F_s(v)} \frac{G}{\wp(v)} \cdot \frac{\Gamma(v-1/2)}{2\pi\Gamma(v+1/2)} \left[\frac{1-2\left|q_0 V_{eff} \delta t/2\right|^{v-1/2} K_{v-1/2}(q_0 V_{eff} \delta t)/\Gamma(v-1/2)}{q_0^{2v-1}} \right]. \tag{3.34}$$

In order to further simplify the equation, the scale-free approximation is applied to the phase structure function (Rino 1979b). When the spatial separation is sufficiently small, the limit $q_0 \to 0$ is valid with the range, $0.5 < v < 1.5$ (Rino 1979b). Thus, equation 3.30 is simplified as (Carrano et al. 2019):

$$ROTI^2(\delta t) \sim \frac{c^2}{\delta t^2}\left\{r_e^2\lambda^2\, sec\,\theta\left(\frac{2\pi}{1000}\right)^{2v+1} C_k L\right\} G \cdot \left[\frac{2\Gamma\left(\frac{3}{2}-v\right)}{2\pi\Gamma\left(v+\frac{1}{2}\right)(2v-1)2^{2v-1}}\right] \cdot \left|V_{eff}\delta t\right|^{2v-1},$$

$$0.5 < v < 1.5. \qquad 3.35$$

In a similar way, the equation 3.34 becomes:

$$\frac{ROTI^2(\delta t)}{S_{4w}^2} \sim \frac{c^2}{\delta t^2}\frac{G}{\wp(v)} \cdot \left\{\frac{1}{F_s(v)}\frac{2\Gamma(3/2-v)}{2\pi\Gamma(v+1/2)(2v-1)2^{2v-1}}\right\}\left|\frac{V_{eff}\delta t}{\rho_F}\right|^{2v-1}, 0.5 < v < 1.5. \qquad 3.36$$

The result can be simplified. According to Carrano et al. (2016), the infinite axial ratio limit can be applied to ionospheric irregularities like scintillation in the equator, where there is a relationship between the geometrical factors $\wp$ and G:

$$\frac{\wp}{G} \sim \frac{\Gamma(v)}{\sqrt{\pi}\Gamma\left(v+\frac{1}{2}\right)} \qquad 3.37$$

Substituting equation 3.37 into 3.36 and simplifying it:

$$\frac{ROTI^2(\delta t)}{S_{4w}^2} \sim \frac{c^2}{\delta t^2}\left\{\frac{2^{1-2v}\sqrt{\pi}}{\Gamma(v)} csc\left[\frac{\pi}{4}(1+2v)\right]\right\}\left|\frac{V_{eff}\delta t}{\rho_F}\right|^{2v-1}, 0.5 < v < 1.5. \qquad 3.38$$

Based on past research on the spectral index, v is chosen to be 1.25 (Carrano et al. 2019) in order to simplify equation 3.38:

$$\frac{ROTI(\delta t)}{S_{4w}} \sim \frac{0.25}{\delta t}\left|\frac{V_{eff}\delta t}{\rho_F}\right|^{0.75}. \qquad 3.39$$

3.4. Conclusions

This chapter presented several key concepts, including the ionosphere, its scintillation and parameters used in this thesis. First, the characteristics of the ionosphere were described. It was followed by introducing ionospheric effects on GNSS, where the ionospheric scintillation was elaborated, demonstrating the necessity to mitigate scintillation effects. Further, the past methods to mitigate scintillation effects were discussed. To the best of the author's knowledge,

no method has so far been proposed using parameters from data with frequency less than 1 Hz to mitigate scintillation effects. In addition, these past methods provided the initial ideas for scintillation mitigation, including satellite evaluation, observation weighting, constellation combination, etc. Moreover, four parameters throughout this thesis were used, S4, σ_ϕ, MP and ROTI. MP and ROTI (standard parameters) can be obtained from data with frequency less than 1 Hz. S4 and σ_ϕ (scintillation parameters) were used as conventional parameters to represent scintillation. Thus, the relationship between S4, σ_ϕ and MP, ROTI was discussed based on past research. Especially, the relationship was evaluated based on parameter equations, providing the theoretical possibility to use standard parameters to detect and mitigate scintillation effects. Actually, in addition to MP and ROTI, SNR was also found to be related to S4 in past research. Bong et al. (2015) showed that SNR is inversely proportional to S4, where the regressions of SNR as a function of S4 are respectively estimated under weak, moderate and strong scintillation. Furthermore, the tracking error variance affected by scintillation has been modelled by Conker et al. (2003) based on SNR. Then, the tracking variance error was used to mitigate scintillation effects on GNSS signals as discussed in section 3.2.4. In addition, SNR was also used to model multipath effects (Bilich and Larson 2007; Špánik and Hefty 2017). Thus, SNR has been thoroughly researched for error modelling or mitigation, so SNR is not used in this thesis.

4. Analysis of the relationship between scintillation parameters, multipath and ROTI

Scintillation is characterized by S4 and σ_ϕ that can be generated from 50Hz data. Then, the alternative scintillation indices S4c and $\sigma_\emptyset$ explained in Chapter 1 can be obtained from 1Hz data, which is still less available than the low-rate data (at 1/30 Hz) all around the world. To popularize the study of scintillation, this chapter proposed to use multipath parameter (MP) and rate of change of Total Electron Content Index (ROTI) that could be acquired from standard geodetic receivers to characterize scintillation. Using GPS data obtained on six days in total from three stations, namely PRU2 and SAO0P located in Sao Paulo, Brazil and SNA0P located in Antarctica, respectively, both the time series plots and 2D maps were generated to investigate the relationship of scintillation indices with MP and ROTI. To prevent most of the effect of the multipath effect and the unstable environment at low elevation, a 30-degree satellite elevation mask was applied to all the data. As not all the multipath effect can be eliminated with the elevation mask, the environment of SAO0P and SJCU station was characterized at chapter 5 to support that fluctuations of all parameters at high elevation were more likely to be caused by scintillation instead of multipath, where the latter station was also located in Sao Paulo, Brazil with an ionospheric scintillation monitoring receiver (ISMR).

The purpose of this chapter is to investigate the relationship of S4 and σ_ϕ with MP and ROTI. Several objectives are set as follows:

(1) Compared the time series plots of the four parameters to observe the temporal relationship to confirm if during periods of scintillation all parameters were similarly affected.
(2) Thereafter, two types of 2D maps were constructed, mean value maps and occurrence percentage maps, where the former was to evaluate whether abnormally high value areas were in similar spatial regions and the latter was to investigate the referred areas with clearer outputs. As equatorial and low latitude scintillation mainly occurs at night and in the early morning local time, the maps were first generated with a period of 6 h.
(3) Furthermore, maps with 5 min intervals were generated to observe the relationship during times when the largest variation of the parameters were observed.
(4) Finally, the structural similarity (SSIMs) and Pearson correlation coefficient (CC) between maps were calculated to evaluate the similarity between the parameters. Variograms and cross-variograms were also used to evaluate the spatial correlation in the maps.

4.1. Materials and methods

4.1.1. Data and instrumentation

GPS data used in this chapter were collected from three stations, PRU2 (51.41° W, 22.12° S), SAO0P (46.65° W, 23.55° S) located in Sao Paulo, Brazil and SNA0P (2.84° W, 71.67° S) located in Antarctica. This dataset was chosen because the data with scintillation is only available for this period and these stations. MP and ROTI were respectively derived from the 1/60 Hz and 1/30 Hz data, when S4 and σ_ϕ were generated from the 50 Hz data. The moving average was applied in ROTI calculation so that its time interval was consistent with other parameters. The receivers in PRU2, SAO0P and SNA0P stations are Septentrio PolaRxS 2.1.1, Septentrio PolaRxS 2.9.6 located in Sao Paulo, Brazil and Septentrio PolaRxS 2.9.0 located in Antarctica, respectively. The Septentrio PolaRxS is a multi-frequency multi-constellation receiver specialized for monitoring ionospheric activity. As scintillation activity is mainly strong in two global areas, namely the equatorial and polar regions, where the causes leading to the generation of scintillation are completely different (Jiao and Morton 2015), data from three stations located in these two regions is used. All the parameters are acquired with a sampling interval of 1 min for the purpose of comparison.

4.1.2. SSIM & CC

The structural similarity index (SSIM) is an index for quantifying the similarity between two images. Three aspects are combined: luminance, contrast and structure (Zhou et al. 2004). These three components can show different characteristics of images. The comparison of luminance ($l(m,n)$) and contrast ($c(m,n)$) show the difference in the means and variances respectively whereas structure ($s(m,n)$) quantifies the correlation. The similarities between images are higher with larger SSIM values. Therefore, SSIM is applied here for comparing maps of scintillation indices with those of MP and ROTI in order to describe spatial similarities. SSIM is calculated according to equations 4.1-4.3 (Zhou et al. 2004):

$$l(m,n) = \frac{2\mu_m\mu_n + C_1}{\mu_m^2 + \mu_n^2 + C_1}$$

$$c(m,n) = \frac{2\sigma_m\sigma_n + C_2}{\sigma_m^2 + \sigma_n^2 + C_2} \qquad 4.1$$

$$s(m,n) = \frac{\sigma_{mn} + C_3}{\sigma_m\sigma_n + C_3}$$

$$SSIM(m,n) = l(m,n) \times c(m,n) \times s(m,n) \qquad 4.2$$

$$C_1 = (K_1 L)^2$$

$$C_2 = (K_2 L)^2 \qquad 4.3$$

$$C_3 = C_2/2$$

where m and n are two non-negative image signals, μ_m is the mean of image m, μ_n is the mean of image n, σ_m^2 is the variance of image m, σ_n^2 is the variance of image n, σ_{mn} is the covariance between image m and n. The parameters C_1 and C_2 were introduced to prevent instability if the value of the denominator is small. Following convention, K_1 = 0.01, $K_2 = 0.03$ and L is the dynamic range of the pixel values (Zhou et al. 2004). In this research, the default SSIM command in MATLAB version 2019a was used.

The correlation coefficient (CC) between m and n is defined as $\sigma_{mn}/\sigma_m\sigma_n$. This is estimated using the standard Pearson CC. Note from equation 4.1 that this is the same as $s(m,n)$ except for the inclusion of C_3. CC and $s(m,n)$ can differ substantially when CC is small. This can also lead to high values of SSIM.

4.1.3. Variograms (semi-variance)

Geostatistics provides a set of tools and methods to analyze spatially referenced data. Of particular interest is the sample variogram, which is defined as:

$$\hat{\gamma}(h) = \frac{1}{n(h)} \sum_{k=1}^{n(h)} \big(y(u_k) - y(u_k + h)\big)^2 \qquad 4.4$$

where $\hat{\gamma}(h)$ is the semi-variance for two points separated by distance h, $y(u)$ is the attribute value at location u and $n(h)$ is the number of observations separated by distance h. The variogram provides information about the spatial dependence and spatial structure in the data. When $\hat{\gamma}(h)$ is small, the difference between two observations of y, separated by h is expected to be small. When $\hat{\gamma}(h)$ is large, the difference is expected to be large. An example variogram for field observations of the heavy metal, Cadmium, is shown in Figure 4.1.

The solid line in Figure 4.1 is a model that has been fitted to the sample variogram. This allows us to estimate $\gamma(h)$ for all values of h. The model is parameterized by the sill, nugget and range. The variogram sill represents the maximum variability in the data. The nugget represents a combination of non-spatial variability and micro-scale variability (variability at lags less than $\min(h)$). The range is the limit of spatial correlation. We expect two observations separated by

distances larger than the range to be uncorrelated. A flat variogram (commonly referred to as "pure nugget") indicates that there is no spatial structure in the data.

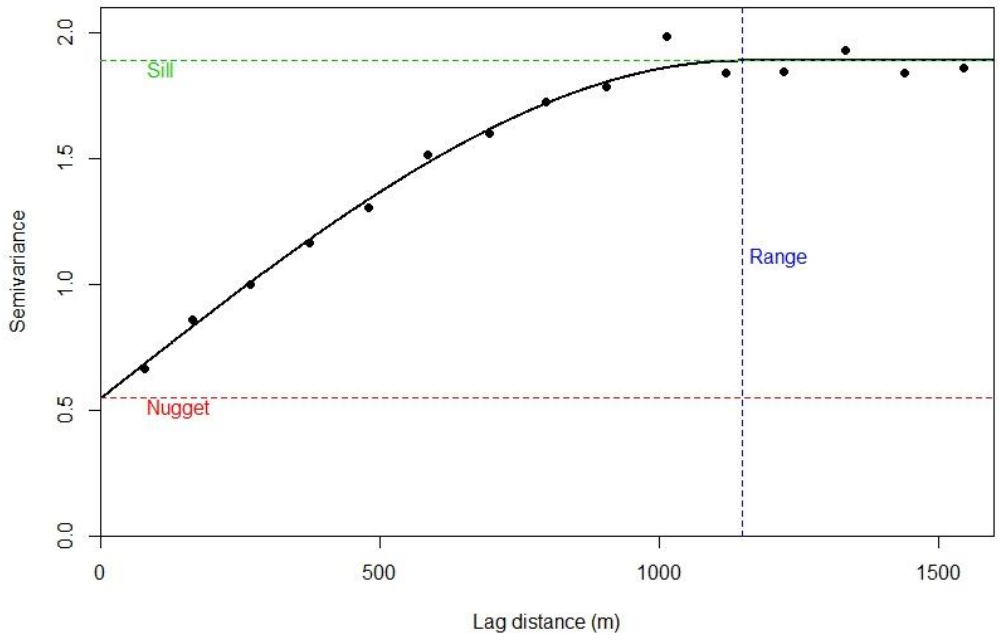

Figure 4.1 Illustration of the sample variogram (black points) and modelled variogram (black line). This is for an example dataset of heavy metals from the River Meuse in the Netherlands (Pebesma 2004).

The concept behind the variogram can be extended to consider the spatial cross-correlation between two variables. This allows us to investigate how correlated $y_1(u)$ is with $y_2(u+h)$. The sample cross-variogram is given as:

$$\gamma_{yz}(h) = \frac{1}{n(h)} \sum_{i=1}^{n(h)} \big(y_1(u_k) - y_1(u_k+h)\big)\big(y_2(u_k) - y_2(u_k+h)\big) \qquad 4.5$$

The sample variogram and modelled variogram can be used as exploratory tools to investigate the spatial structure in a dataset. They can also be used in predictive mapping to interpolate datasets. The concepts are further explained in detail by Goovaerts (1997), Webster and Oliver (2008) and Webster et al. (1994). Cressie (1993) gives a more detailed theoretical treatment. Examples in remote sensing are given by Curran and Atkinson (1998), van der Meer (2012) and Odongo et al. (2014).

4.1.4. Ionospheric Pierce Point (IPP)

As this thesis focuses on ionospheric effects, the results are analyzed at the ionospheric boundary, where the IPP coordinates are calculated. Prior to that, an intermediate quantity, which is the intersection angle of receiver and the IPP to the center of Earth, is calculated using equation 4.6:

$$p = \frac{\pi}{2} - ele - \sin^{-1}\left(\frac{R\cos(ele)}{R+H}\right) \quad 4.6$$

where ele is the elevation angle of the satellite as observed from the receiver. The coordinates of the IPP can then be calculated in latitude and longitude using equation 4.7 and 4.8:

$$\phi_{IPP} = \sin^{-1}(\sin(\phi)\cos(p) + \cos(\phi)\sin(p)\cos(azi)) \quad 4.7$$

$$\lambda_{IPP} = \lambda + \sin^{-1}(\sin(p)\sin(azi)/\cos(\phi)) \quad 4.8$$

where ϕ and λ are latitude and longitude of the receiver position.

4.1.5. Normalization

As various parameters vary greatly in their maximum and minimum values, normalization is applied so that parameters can be compared within a certain size range. P-Norm is applied in this research, which is defined by Mathworks (2019) as equations 4.9 and 4.10:

$$\|v\|_p = \left[\sum_{l=1}^{N}|v_l|^q\right]^{1/q} \quad 4.9$$

$$v_n = \frac{v_l}{\|v\|_p} \quad 4.10$$

where $\|v\|_p$ is P-Norm; v_l is the vector before normalization; l is the serial number of v_l; N is the total number of vectors; q can be any positive real value, which is selected to be 2 here namely 2-Norm because it is the standard norm and most widely applied in P-Norm; v_n is the normalized vector. As explained in section 3.3.5.1, multipath affects the evaluation of

scintillation indices values. With lower elevation, it is with higher possibility for signals to encounter multipath. Thus, multipath effects are supposed to be negatively correlated with elevation angle. To visually show the effect of elevation on S4, the normalization using elevation angles was applied to S4 as follows:

$$S4_{ele} = S4 \cdot \sin ele. \tag{4.11}$$

The normalization was applied to the other parameters in the same way. The mean value maps of all normalized parameters (MP_{ele}, $ROTI_{ele}$, $S4_{ele}$ and $\sigma_{\phi_{ele}}$) on March 12, 2011 at PRU2 is shown as an example at section 4.2.2.1.1.

4.1.6. Methodology

Figure 4.2 shows the flowchart of the methodology. As shown in Figure 4.2, 30° satellite elevation angle cutoff was applied to all the data. The time series plots of all four parameters were generated before normalization to observe the general relationship and the scintillation intensity. Then all the data was normalized using P-Norm (Mathworks 2019) as described in section 4.1.5 so that the different parameters varied in the same range. Next, two types of maps were generated, the mean value map and the occurrence percentage map, where each map was generated using data from a single station with a spatial resolution of 1°. The same resolution has been used in past research related to ionospheric map generation (Koulouri et al. 2020; Pan et al. 2021; Geng et al. 2020). Mean value maps were generated first to investigate the spatial relationship, where the mean values were calculated for each grid cell. To achieve this the parameter values with the IPP coordinates located in the same grid were averaged and visualized on a map. After that, in order to more clearly visualize high values, occurrence percentage maps were generated. These showed the percentage of values greater than a threshold for each 1° grid cell. The method for calculating the threshold was given in equation 4.13. Compared with the mean value map, this map showed only the extreme values.

To generate these extreme values a threshold was applied, which was determined using the standard deviation and mean of values for each parameter. For the Antarctic data, as the station was located in the high latitudes, phase scintillation was considerably more likely than amplitude scintillation (Jiao and Morton 2015; Shanmugam et al. 2012). Therefore, S4 was not considered for the Antarctic data, where MP, ROTI and σ_ϕ fluctuate with different magnitudes from each other during the period with low scintillation and with similar magnitudes to each other during the scintillation period. In order to mitigate biases, the values of different

parameters should be filtered first, where the values lower than a threshold as defined in equation 4.13 were not used for occurrence percentage calculation.

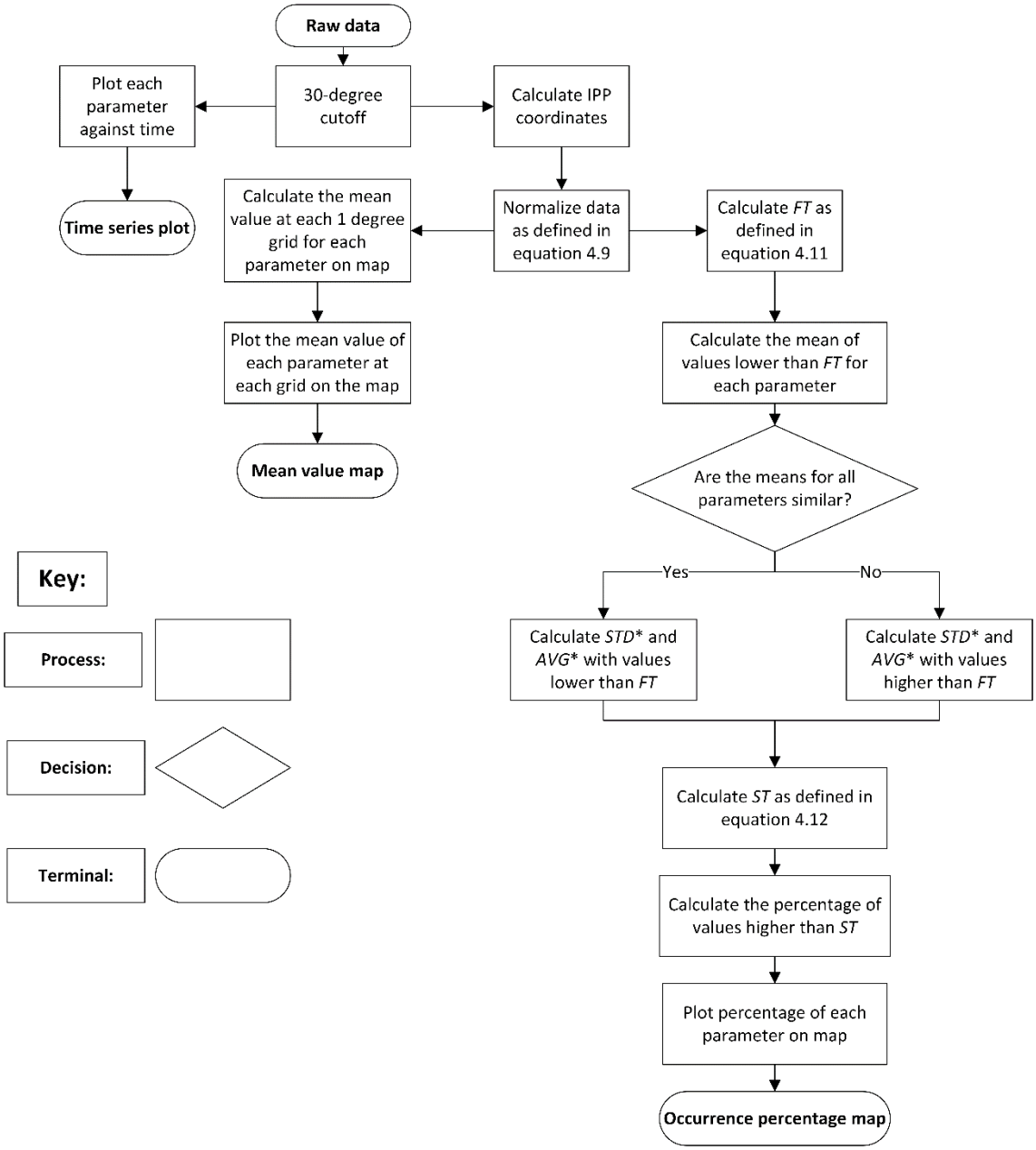

Figure 4.2 Flow chart for data processing and visualization.

This was realized by applying two thresholds, determined using equations 4.12 and 4.13 below:

$$FT = STD + AVG \quad (4.12)$$

$$ST = x \cdot STD^* + AVG^* \quad (4.13)$$

where FT and ST respectively represent the first threshold and the second threshold; STD and AVG are the standard deviation and mean of all values for each parameter; STD^* and AVG^* are the standard deviation and mean of values higher or lower than FT, dependent on the characteristics of the data, which is explained in more detail in Figure 4.2; x is a real number, which can be adjusted in order to distinctly show maps within different durations. For the Antarctic data, the size of the four parameters during the non-scintillation period were of different magnitude. Take the dataset in Antarctica on 2 April 2017 as an example, the mean of MP, ROTI, S4 and σ_ϕ during non-scintillation period (values lower than FT) respectively were 0.00026, 0.0032, 0.00051, 0.00066, where ROTI was not of the same magnitude as the other three parameters. Therefore, values higher than the FT was used for the ST calculation. For the Brazilian data, the situation was different, the sizes of all four parameters during non-scintillation period varied with similar magnitude to each other. Take the dataset in Brazil on 13 September 2017 as an example, the mean of MP, ROTI, S4 and σ_ϕ during non-scintillation period (values lower than FT) respectively were 0.00033, 0.00045, 0.00030 and 0.00057, which were similar to each other. Hence, the values lower than the FT were used for calculating ST for the Brazilian data. After following this process, the percentage of number of values larger than the thresholds could be drawn on each grid of maps. In this thesis, thresholds were chosen to be relatively large (x was comparatively large) in order to show distinct extreme value areas on percentage occurrence maps.

In addition to generating mean value maps for 6 h, maps were also constructed for 5-min duration during scintillation period. Maps containing data for five minutes with scintillation were generated in order to compare parameters at more specific time.

4.2. Brazil data

4.2.1. Temporal relationship

Figure 4.3a,b,c shows the time series of the four parameters, namely S4 (top row), σ_ϕ (second row from top), MP (third row from top) and ROTI (bottom row) respectively on 8 September 2017 and 13 September 2017 at SAO0P station and 12 March 2011 at PRU2 station.

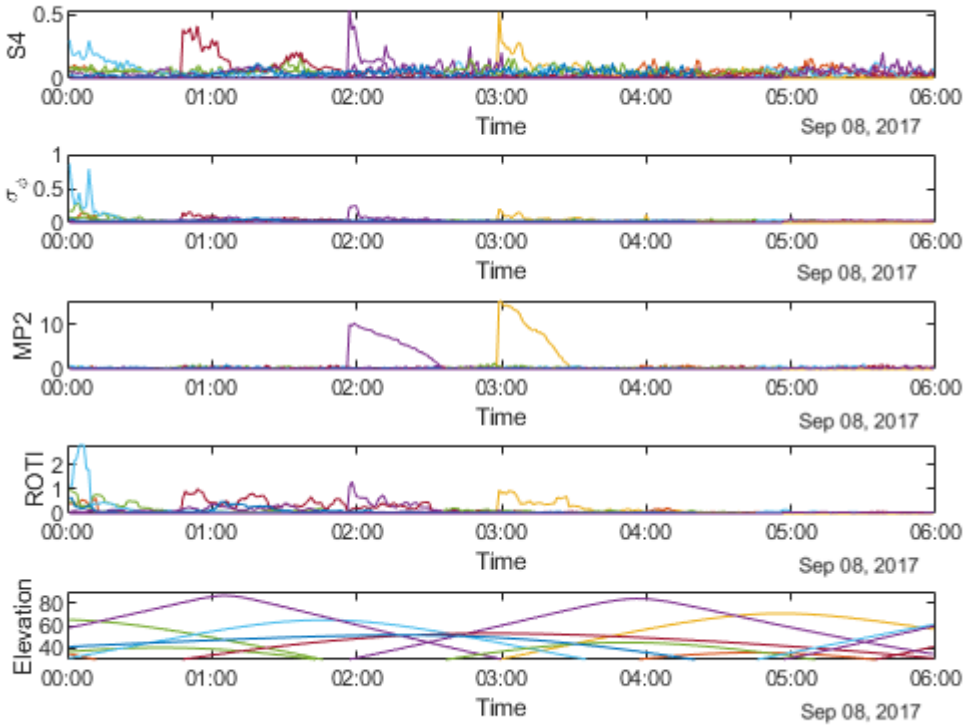
S4
0.5
0
00:00
01:00
02:00
03:00
04:00
05:00
06:00
Time
Sep 08, 2017
σ_ϕ
1
0.5
0
MP2
10
ROTI
2
1
Elevation
80
60
40

(a)

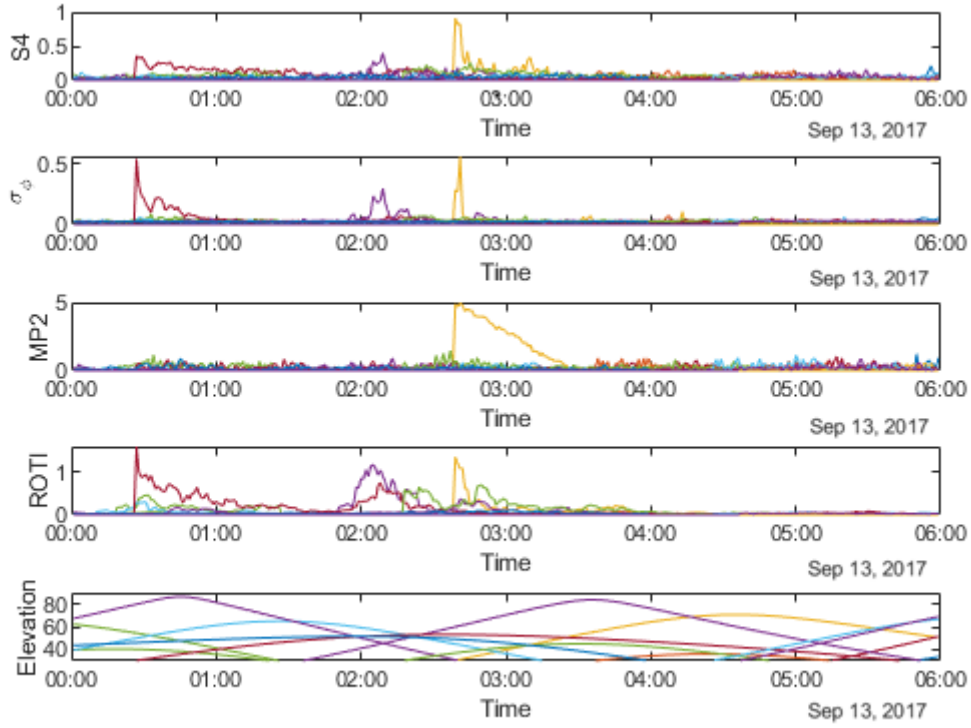
S4
1
0.5
0
00:00
01:00
02:00
03:00
04:00
05:00
06:00
Time
Sep 13, 2017
σ_ϕ
0.5
MP2
5
ROTI
Elevation
80
60
40

(b)

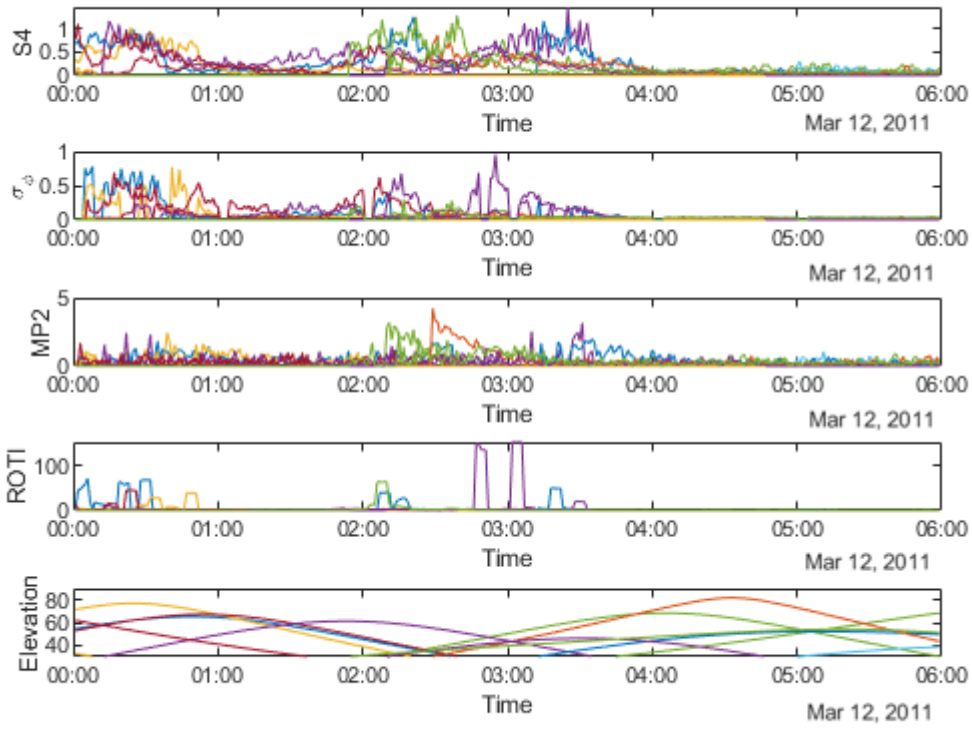

(c)

Figure 4.3 Time series plots of four parameters: (a) during 00:00:00–06:00:00 UTC on 8 September, 2017 at SAO0P station; and (b) during 00:00:00-06:00:00 UTC on 13 September 2017 at SAO0P station; (c) during 00:00:00–06:00:00 UTC on 12 March 2011 at PRU2 station. MP1 and MP2 are in meters, ROTI in TECU/min, σ_ϕ in radian, elevation in degree and S4 is dimensionless.

Figure 4.3 shows that all four parameters fluctuate during the first four hours on all the three days, which indicates a relationship between the parameters in the time domain. It can be seen from all the panels that there are fewer peaks on the MP plots which means that fewer satellites are affected by MP than scintillation. Figure 4.4a,b,c shows the time series plots of four parameters for G10,G10 and G25 respectively on 8 September 2017 and 13 September 2017 at SAO0P station and 12 March 2011 at PRU2 station. Herein, the satellite showing variability of all four parameters is selected. As shown in Figure 4.4, the temporal relationship becomes clearer with the time series plots for a single satellite, where all four parameters have a peak at around 3:00, 2:40 and 2:30 on the three days, respectively.

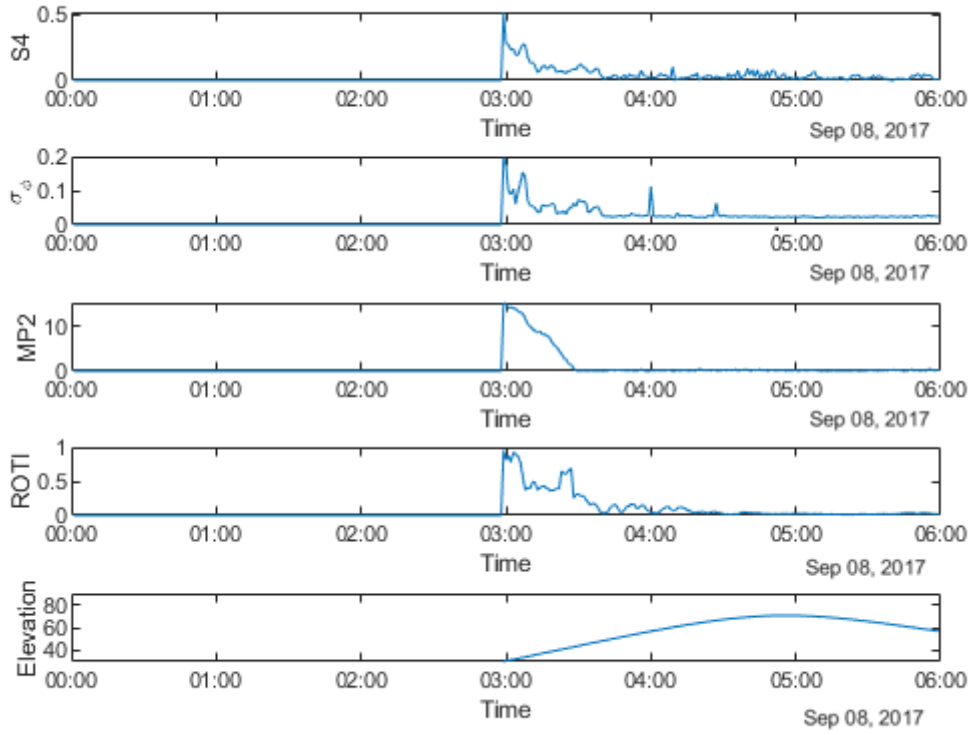
S4
0.5
0
00:00
01:00
02:00
03:00
04:00
05:00
06:00
Time
Sep 08, 2017
σφ
0.2
0.1
0
MP2
10
ROTI
1
0.5
Elevation
80
60
40

(a)

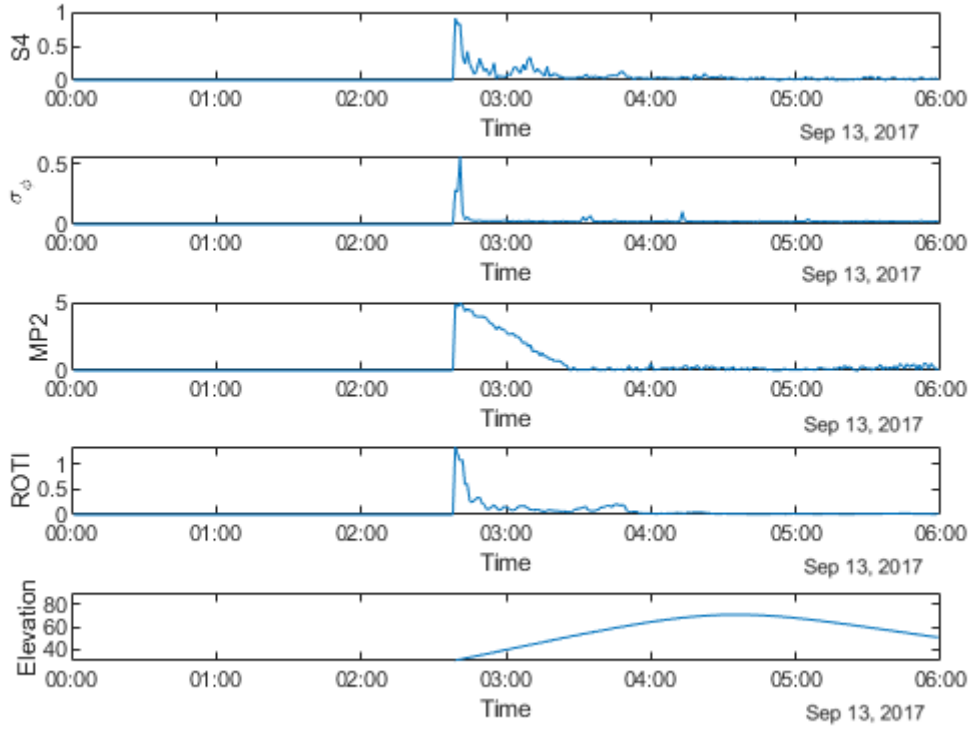
S4
1
0.5
0
00:00
01:00
02:00
03:00
04:00
05:00
06:00
Time
Sep 13, 2017
σφ
MP2
5
ROTI
Elevation
80
60
40

(b)

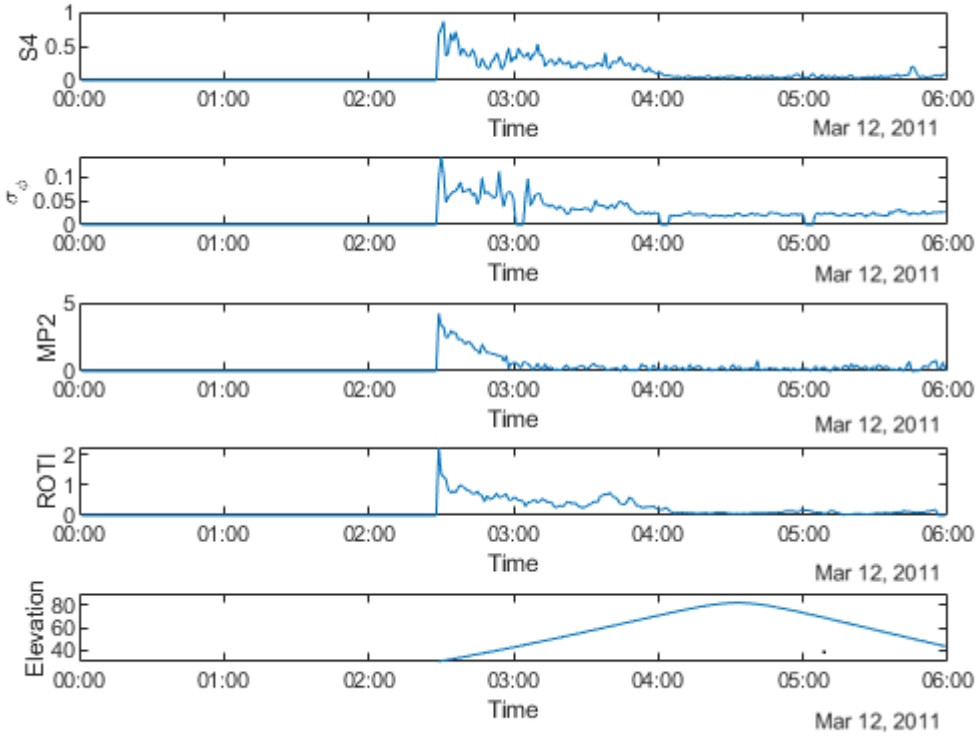

(c)

Figure 4.4 Time series plots of four parameters: (a) during 00:00:00-06:00:00 UTC on 8 September 2017 for G10 at SAO0P station; (b) during 00:00:00–06:00:00 UTC on 13 September 2017 for G10 at SAO0P station; (c) during 00:00:00–06:00:00 UTC on 12 March 2011 for G24 at PRU2 station. Units as in Figure 4.3.

4.2.2. Spatial relationship

4.2.2.1. Mean value map

4.2.2.1.1. Long duration

The panels a–c of Figure 4.5 show the spatial mean value 2D maps as a function of IPP latitude and longitude calculated in each 1◦ grid cell, for the four parameters respectively on 8 September and 13 September 2017 at SAO0P station and 12 March 2011 at PRU2 station.

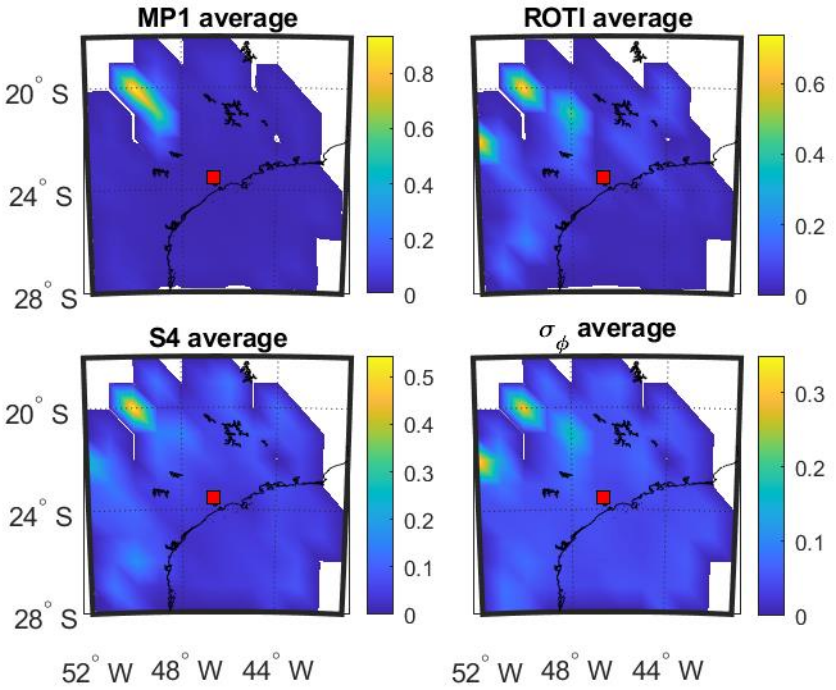
MP1 average
ROTI average
S4 average
σ_ϕ average
20° S
24° S
28° S
52° W
48° W
44° W
0.8
0.6
0.4
0.2
0
0.6
0.4
0.2
0
0.5
0.4
0.3
0.2
0.1
0
0.3
0.2
0.1
0

(a)

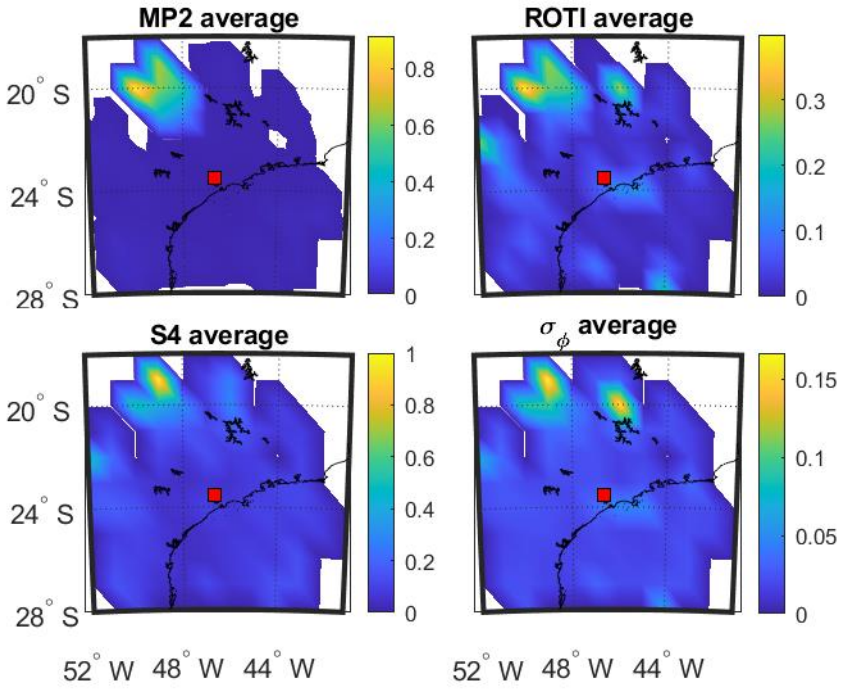
MP2 average
ROTI average
S4 average
σ_ϕ average
20° S
24° S
28° S
52° W
48° W
44° W
0.8
0.6
0.4
0.2
0
0.3
0.2
0.1
0
1
0.8
0.6
0.4
0.2
0
0.15
0.1
0.05
0

(b)

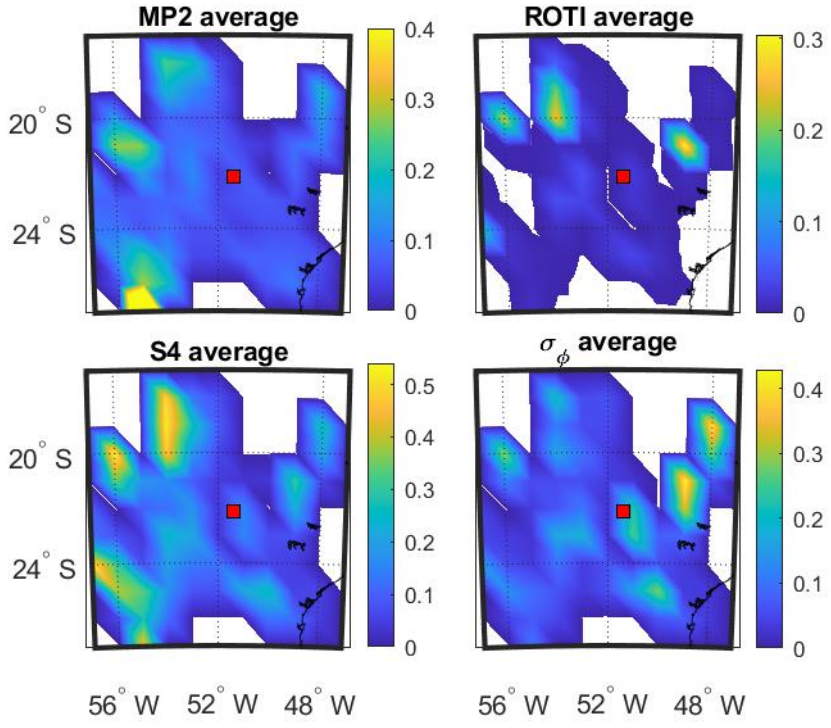
MP2 average
ROTI average
S4 average
σ_ϕ average
20° S
24° S
56° W
52° W
48° W
0.4
0.3
0.2
0.1
0
0.5

(c)

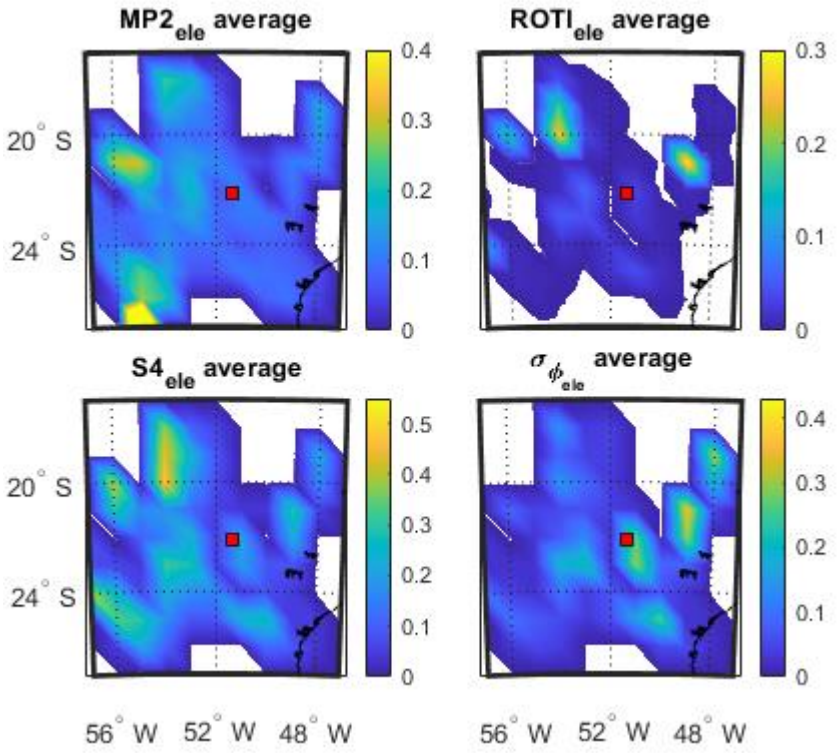

(d)

Figure 4.5 Mean value maps of four parameters: (a) during 00:00:00–06:00:00 UTC on 8 September 2017 at SAO0P station; and (b) during 00:00:00–06:00:00 UTC on 13 September 2017 at SAO0P station; (c) during 00:00:00-06:00:00 UTC on 12 March 2011 at PRU2 station; (d) with normalization using elevation angles during 00:00:00–06:00:00 UTC on 12 March 2011 at PRU2 station. Units as in Figure 4.3.

It can be observed from Figure 4.5a,b that the affected areas (shown in yellow) of all the parameters focus on the northwest corner on the maps, which indicates that there is a relationship between the parameters in the spatial domain. As shown in Figure 4.5c, high value areas of S4 and MP are both located on the left part of maps while ROTI agrees with σ_ϕ on the east part of maps, though ROTI also shows similarities in the northwest corner with S4. The same relationship pattern can also be observed from Figure 4.5a,b that MP mainly correlates with S4 while ROTI respectively correlates with part of S4 and σ_ϕ. To evaluate the influence of elevation on S4, the same maps are generated for all normalized parameters as shown in Figure 4.5d for comparison with maps in Figure 4.5c. It can be noticed that the high values in Figure 4.5d are slightly lower than those in Figure 4.5c, which may indicate that down-weighting by elevation mitigates a part of multipath effects on all parameters. However, the location of high

value areas Figure 4.5d remains unchanged compared with Figure 4.5c.

SSIM and CC

Table 4.1, Table 4.2 and Table 4.3 show the SSIM and CC calculated between the 4 parameters shown in Figure 4.5a,b,c respectively. From Table 4.1, Table 4.2 and Table 4.3, it is clear that MP is more correlated with S4 while ROTI is more highly correlated with σ_ϕ, although the CC in Table 4.3 shows a different pattern of ROTI. Most of the SSIM and CC values exceed 0.6 and some exceed 0.8. This indicates a high correlation between the parameters and a high level of structural similarity.

Table 4.1 SSIM and CC between the maps shown in Figure 4.5a.

	MP		**ROTI**	
Criteria	SSIM	CC (*p*-value)	SSIM	CC (*p*-value)
S4	0.75	0.81 (<0.01)	0.73	0.76 (<0.01)
σ_ϕ	0.67	0.74 (<0.01)	0.79	0.88 (<0.01)

Table 4.2 SSIM and CC between the maps shown in Figure 4.5b.

	MP		**ROTI**	
Criteria	SSIM	CC (*p*-value)	SSIM	CC (*p*-value)
S4	0.73	0.71(<0.01)	0.70	0.68 (<0.01)
σ_ϕ	0.65	0.58 (<0.01))	0.80	0.93 (<0.01)

Table 4.3 SSIM and CC between the maps shown in Figure 4.5c.

	MP		**ROTI**	
Criteria	SSIM	CC (*p*-value)	SSIM	CC (*p*-value)
S4	0.73	0.70 (<0.01)	0.63	0.77 (<0.01)
σ_ϕ	0.56	0.43 (<0.01)	0.80	0.66 (<0.01)

Variograms

The variograms and cross variograms for Figure 4.5a,b,c are shown in Figure 4.6a,b,c respectively. The variogram and cross-variograms show clear evidence of spatial structure, with a range of approximately 5° to 6°. This shows that the four variables (parameters) co-vary, suggesting that they have similar spatial structures.

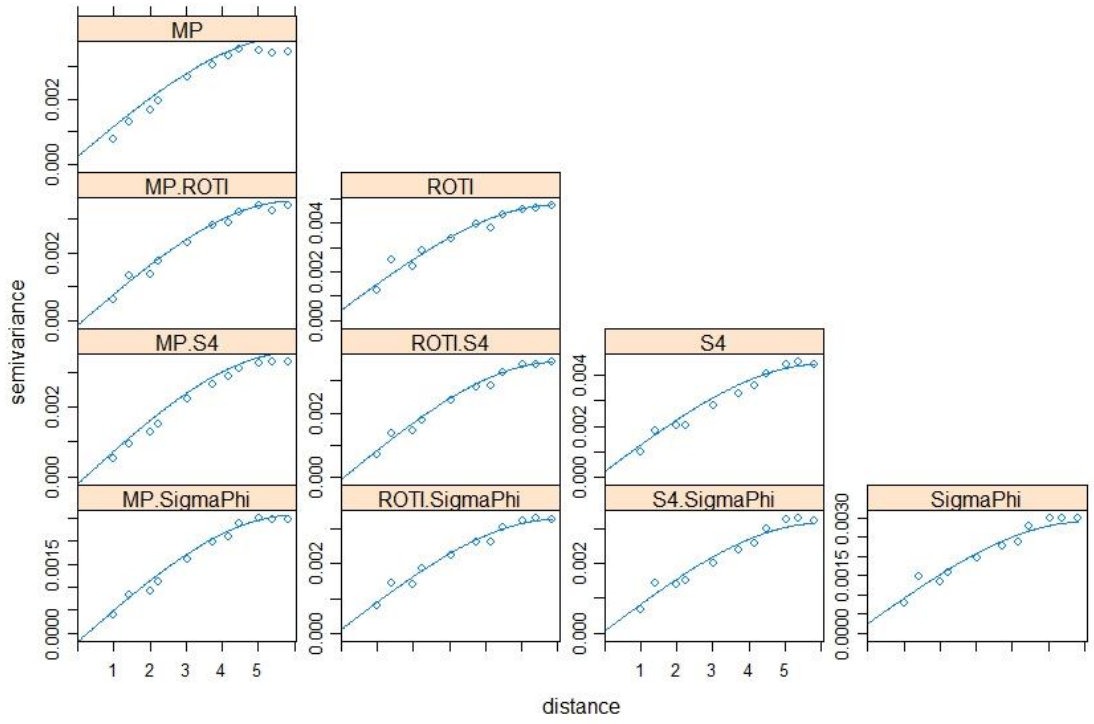
MP
MP.ROTI
ROTI
MP.S4
ROTI.S4
S4
MP.SigmaPhi
ROTI.SigmaPhi
S4.SigmaPhi
SigmaPhi
semivariance
distance

(a)

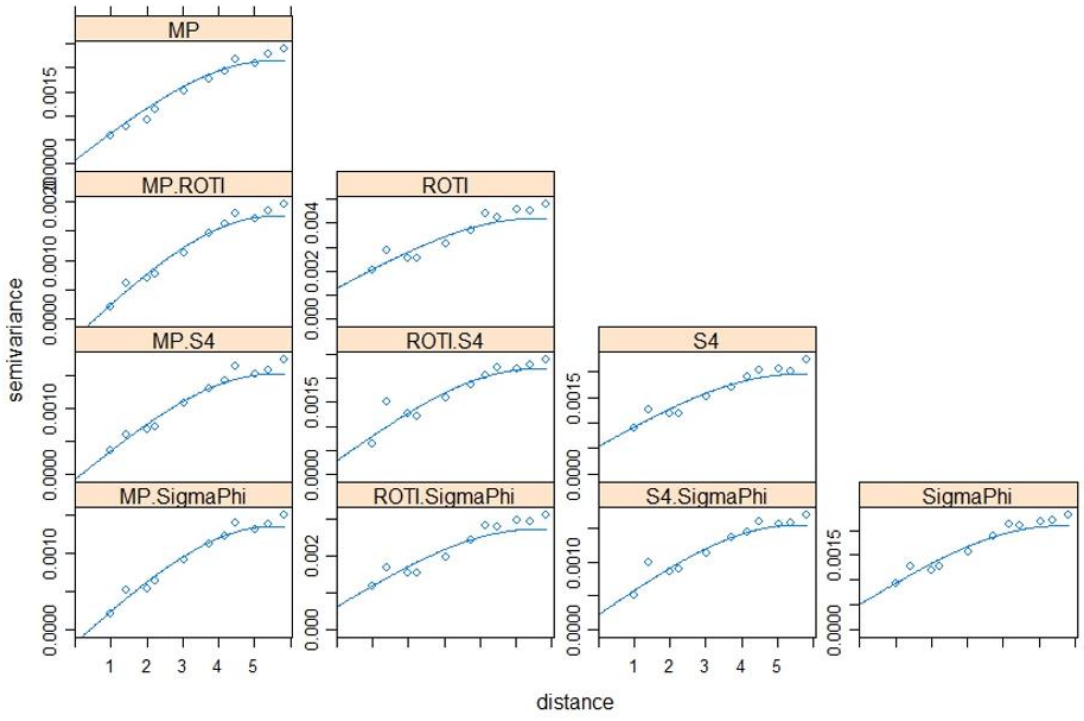
MP
MP.ROTI
ROTI
MP.S4
ROTI.S4
S4
MP.SigmaPhi
ROTI.SigmaPhi
S4.SigmaPhi
SigmaPhi
semivariance
distance

(b)

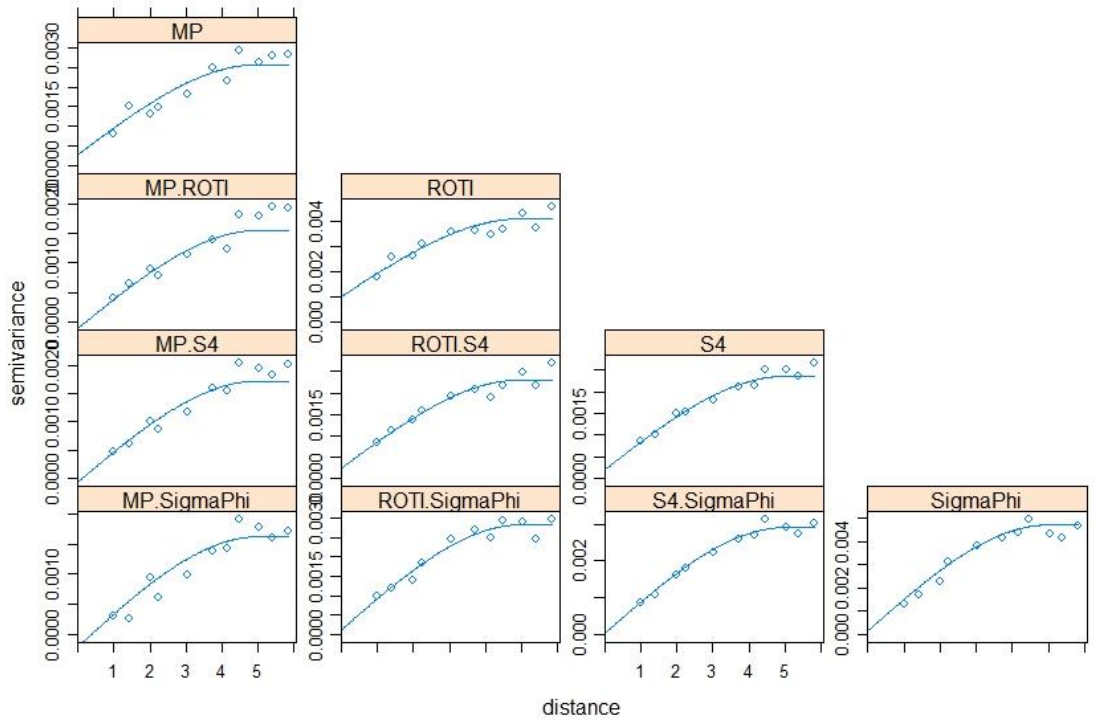

(c)

Figure 4.6 Variograms and cross-variograms for the four parameters. Figures 4.5a,b,c is for the data illustrated in Figure 4.5a,b,c.

4.2.2.1.2. Short duration

The time evolution of the four parameters at every 5 min interval on 08 September 2017 during 01:55–02:10 UT and on 13 September during 02:40–02:55 UT respectively are shown in Figure 4.7 and Figure 4.8, which are presented in the form of mean value maps. The SSIM and CC between the parameters in the maps of Figure 4.7 and Figure 4.8 are shown respectively in Table 4.4 and Table 4.5.

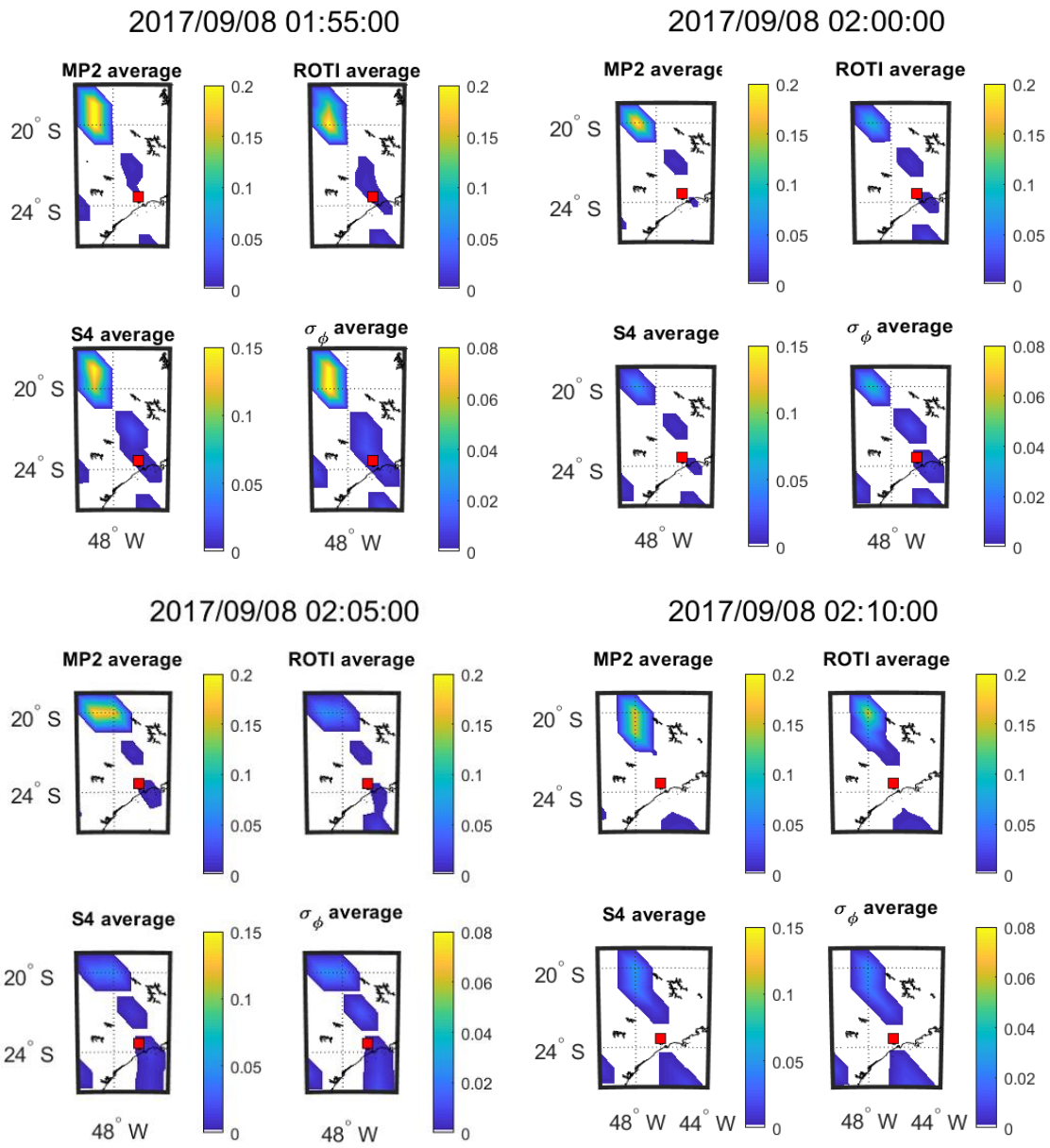

Figure 4.7 Consecutive 5 min means over 20 min at SAO0P station on 8 September 2017. Units as in Figure 4.3.

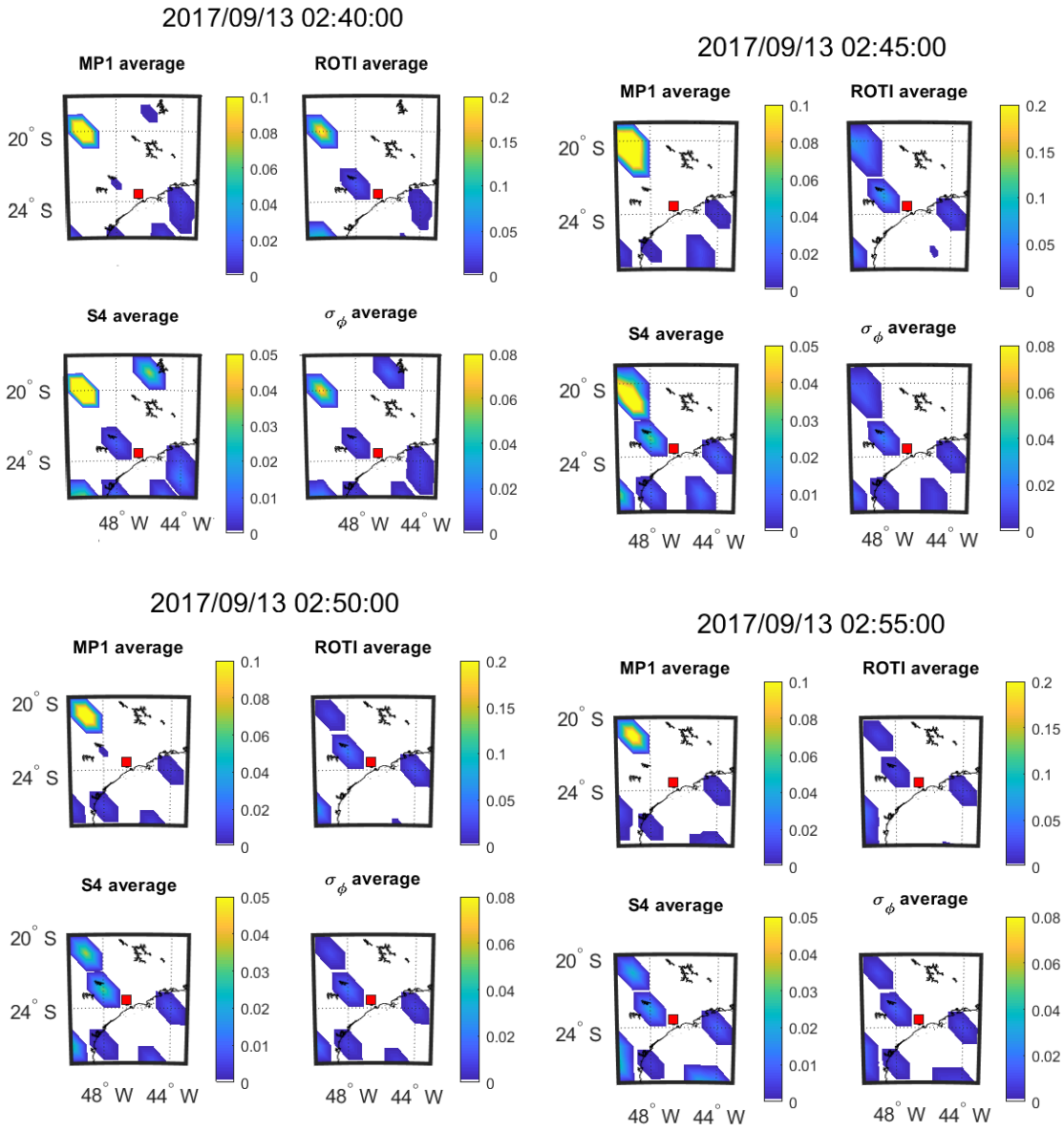

Figure 4.8 Consecutive 5 min means over 20 min at SAO0P station on 13 September 2017. Units as in Figure 4.3.

As shown in Figure 4.7 and Figure 4.8, mean value maps with 5-min interval are constructed to observe the movements of scintillation and the corresponding change of other parameters. It can be seen from Figure 4.7 that large value areas (yellow areas) of all the parameters move toward southeast after 20-min propagation. Similarly, it can be observed from Figure 4.7 and Figure 4.8 that large value areas of all the parameters move southeastward slightly over the 20 min. Therefore, MP, ROTI, S4 and σ_ϕ share the same propagation direction as observed on both the days from Figure 4.7 and Figure 4.8. Table 4.4 shows that the parameters in Figure 4.7 maintain very high

correlations (CC) throughout the 20-min period. The SSIMs fluctuate due to changes in the mean values of the parameters. For Table 4.4 and Table 4.5 shows that ROTI and S4 and ROTI and σ_ϕ maintain a high correlation across the 20-min period. The correlation between MP and S4 declines over the 20-min period. The correlation between MP and σ_ϕ is high in the first 5 min but drops sharply and these two parameters are uncorrelated for the remainder of the period.

SSIM and CC

Table 4.4 SSIM and CC between the maps shown in Figure 4.7.

2017 September 8	**01:55:00**		**02:00:00**		**02:05:00**		**02:10:00**	
Criteria	**SSIM**	**CC (*p*-value)**	**SSIM**	**CC (*p*-value)**	**SSIM**	**CC (*p*-value)**	**SSIM**	**CC (*p*-value)**
MP vs. S4	0.85	0.98 (<0.01)	0.39	0.99 (<0.01)	0.38	0.99 (<0.01)	0.50	0.98 (<0.01)
MP vs. σ_ϕ	0.59	1.00 (<0.01)	0.33	1.00 (<0.01)	0.27	0.94 (<0.01)	0.31	0.97 (<0.01)
ROTI vs. S4	0.88	0.88 (<0.01)	0.78	0.97 (<0.01)	0.89	0.93 (<0.01)	0.64	0.93 (<0.01)
ROTI vs. σ_ϕ	0.75	0.97 (<0.01)	0.73	0.98 (<0.01)	0.76	0.93 (<0.01)	0.40	0.93 (<0.01)

Table 4.5 SSIM and CC between the maps shown in Figure 4.8.

2017 September 13	**02:40:00**		**02:45:00**		**02:50:00**		**02:55:00**	
Criteria	**SSIM**	**CC (*p*-value)**	**SSIM**	**CC (*p*-value)**	**SSIM**	**CC (*p*-value)**	**SSIM**	**CC (*p*-value)**
MP vs. S4	0.84	0.95 (<0.01)	0.46	0.71 (0.03)	0.44	0.57 (0.24)	0.45	0.24 (0.57)
MP vs. σ_ϕ	0.73	0.96 (<0.01)	0.26	−0.09 (0.82)	0.28	−0.20 (0.71)	0.43	−0.11 (0.80)
ROTI vs. S4	0.74	0.88 (<0.01)	0.68	0.63 (0.07)	0.64	0.62 (0.19)	0.86	0.63 (0.09)
ROTI vs. σ_ϕ	0.60	0.93 (<0.01)	0.49	0.82 (<0.01)	0.51	0.93 (<0.01)	0.82	0.90 (<0.01)

4.2.2.2. Occurrence percentage map

4.2.2.2.1. Long duration

Figure 4.9a,b,c show the occurrence percentage maps as a function of IPP latitude and longitude for the four parameters on 8 September and 13 September 2017 at SAO0P station and 12 March 2011 at PRU2 station.

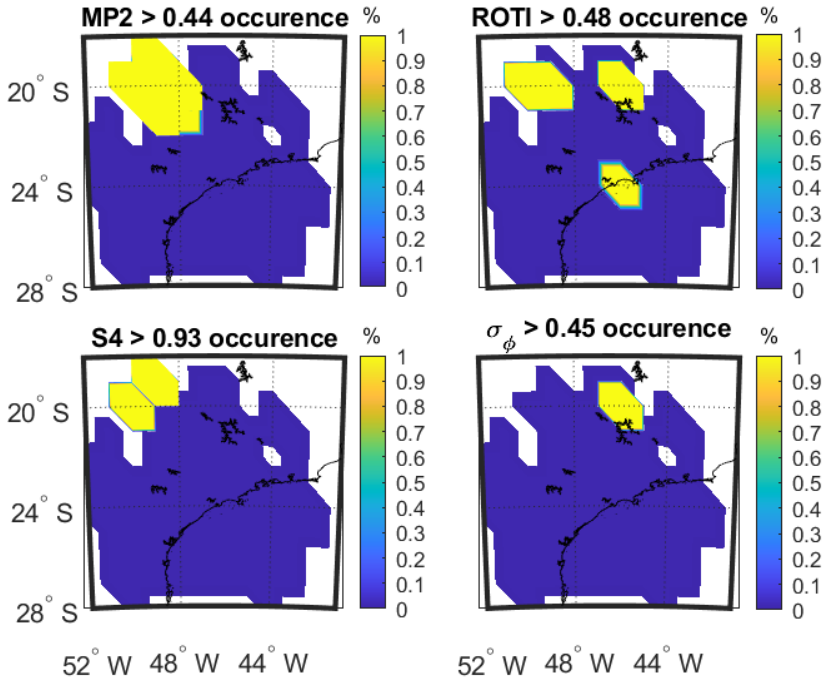
MP2 > 0.44 occurence
%
ROTI > 0.48 occurence
%
S4 > 0.93 occurence
%
σ_ϕ > 0.45 occurence
%
20° S
24° S
28° S
52° W
48° W
44° W
1
0.9
0.8
0.7
0.6
0.5
0.4
0.3
0.2
0.1
0

(a)

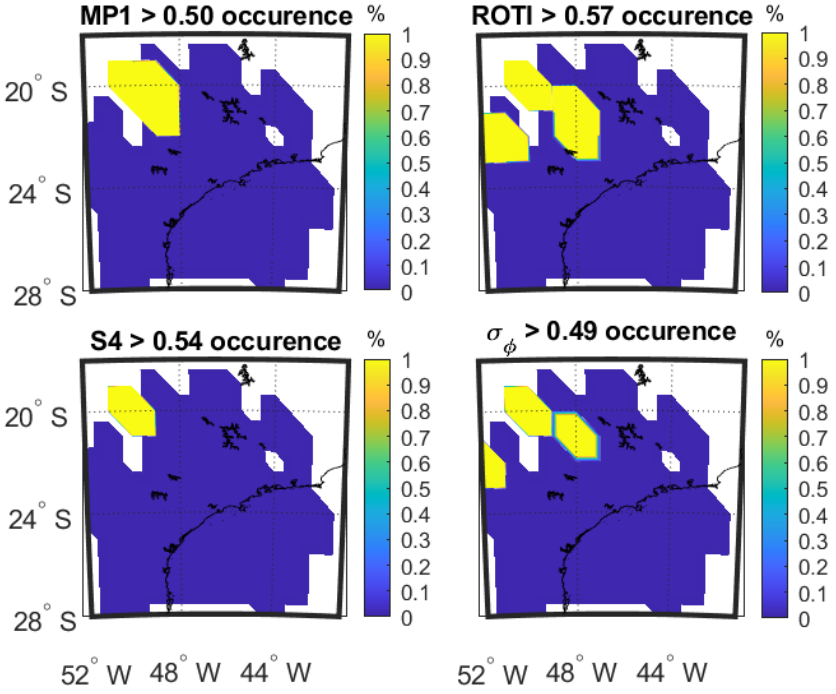
MP1 > 0.50 occurence
%
ROTI > 0.57 occurence
%
S4 > 0.54 occurence
%
σ_ϕ > 0.49 occurence
%
20° S
24° S
28° S
52° W
48° W
44° W
1
0.9
0.8
0.7
0.6
0.5
0.4
0.3
0.2
0.1
0

(b)

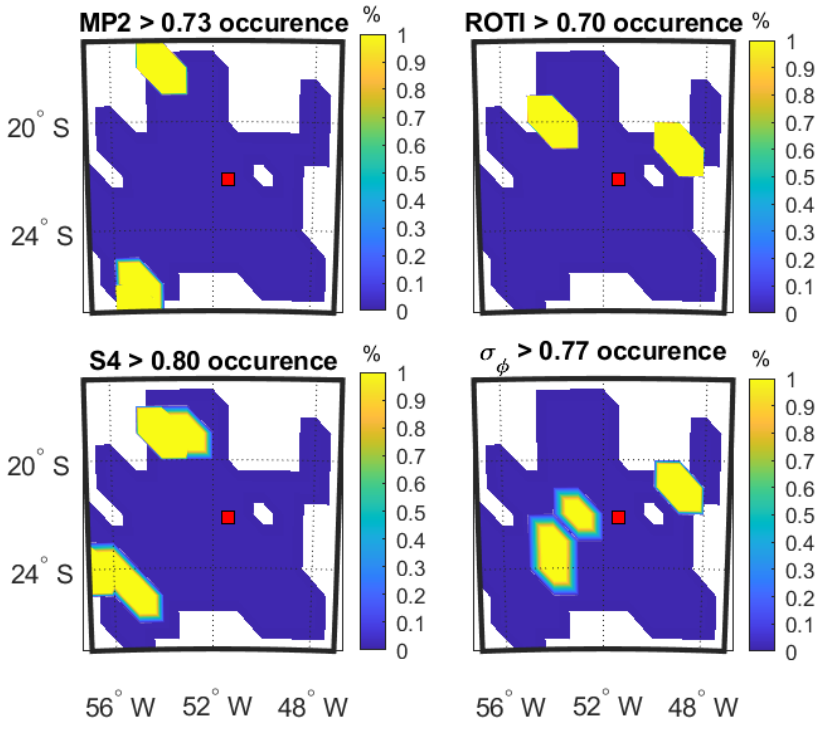

(c)

Figure 4.9 Occurrence percentage maps of four parameters: (a) during 00:00:00–06:00:00 UTC on 8 September, 2017 at SAO0P station; (b) during 00:00:00–06:00:00 UTC on 13 September 2017 at SAO0P station; (c) during 00:00:00–06:00:00 UTC on 12 March 2011 at PRU2 station. Thresholds are obtained from equation 4.13. Units as in Figure 4.3.

Figure 4.9a shows that high values of MP cover the high values of S4 while high values of ROTI cover high value of σ_ϕ. A similar result is observed in Figure 4.9b. For Figure 4.9c, high values of MP do not clearly overlap with high values of S4 and high values of ROTI do not clearly overlap with high values of σ_ϕ. These observations are reflected in the CC values shown in Table 4.6-Table 4.8.

SSIM and CC

Table 4.6 SSIM and CC between the maps shown in Figure 4.9(a).

	MP		**ROTI**	
Criteria	SSIM	CC (*p*-value)	SSIM	CC (*p*-value)
S4	0.71	0.52 (<0.01)	0.75	0.02 (0.87)
σ_ϕ	0.58	−0.03 (0.80)	0.79	0.83 (<0.01)

Table 4.7 SSIM and CC between the maps shown in Figure 4.9(b).

	MP		**ROTI**	
Criteria	SSIM	CC (*p*-value)	SSIM	CC (*p*-value)
S4	0.83	0.77 (<0.01)	0.70	0.66 (<0.01)
σ_ϕ	0.69	0.56 (<0.01)	0.71	0.98(<0.01)

Table 4.8 SSIM and CC between the maps shown in Figure 4.9(c).

	MP		**ROTI**	
Criteria	SSIM	CC (*p*-value)	SSIM	CC (*p*-value)
S4	0.64	−0.04 (0.77)	0.61	−0.04 (0.73)
σ_ϕ	0.63	−0.03 (0.79)	0.76	0.72 (<0.01)

4.2.2.2.2. Short duration

Figure 4.10a,b,c shows the occurrence percentage maps as a function of IPP latitude and longitude of four parameters on 8 September and 13 September 2017 at SAO0P station and 12 March 2011 at PRU2 station during the period when the parameters show the largest variation as observed from Figure 4.3.

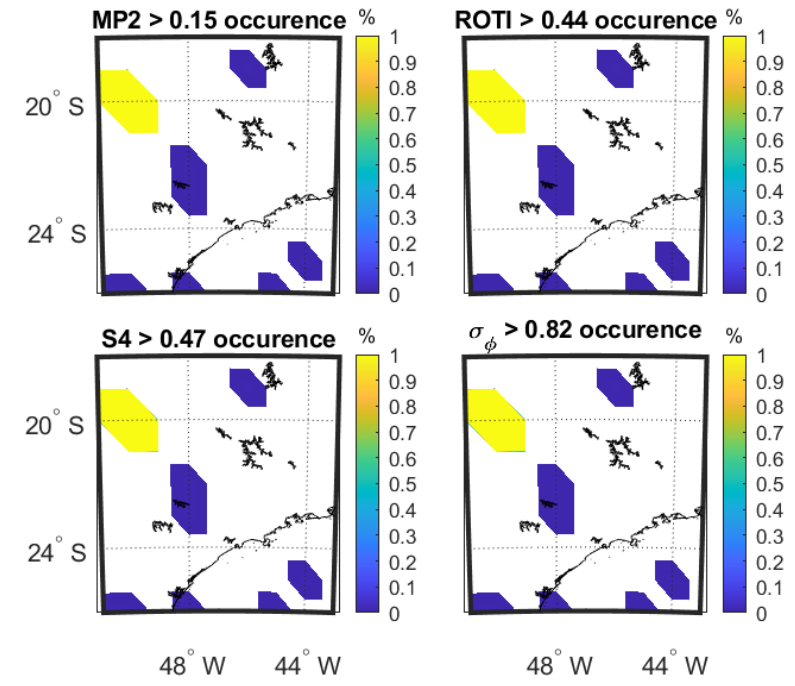
MP2 > 0.15 occurence %
ROTI > 0.44 occurence %
S4 > 0.47 occurence %
σ_ϕ > 0.82 occurence %
20° S
24° S
48° W
44° W
1
0.9
0.8
0.7
0.6
0.5
0.4
0.3
0.2
0.1
0

(a)

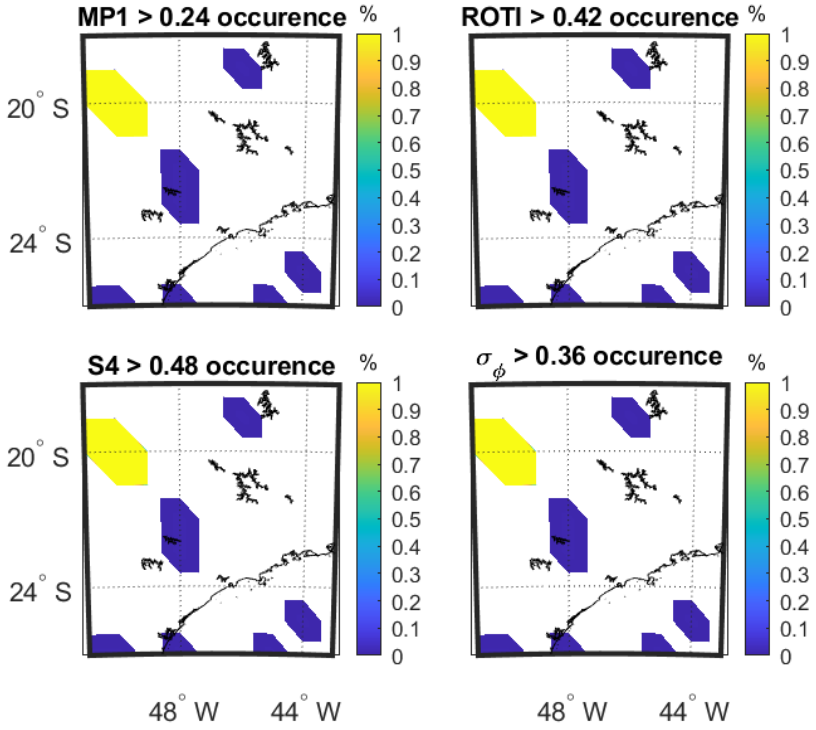
MP1 > 0.24 occurence %
ROTI > 0.42 occurence %
S4 > 0.48 occurence %
σ_ϕ > 0.36 occurence %
20° S
24° S
48° W
44° W
1
0.9
0.8
0.7
0.6
0.5
0.4
0.3
0.2
0.1
0

(b)

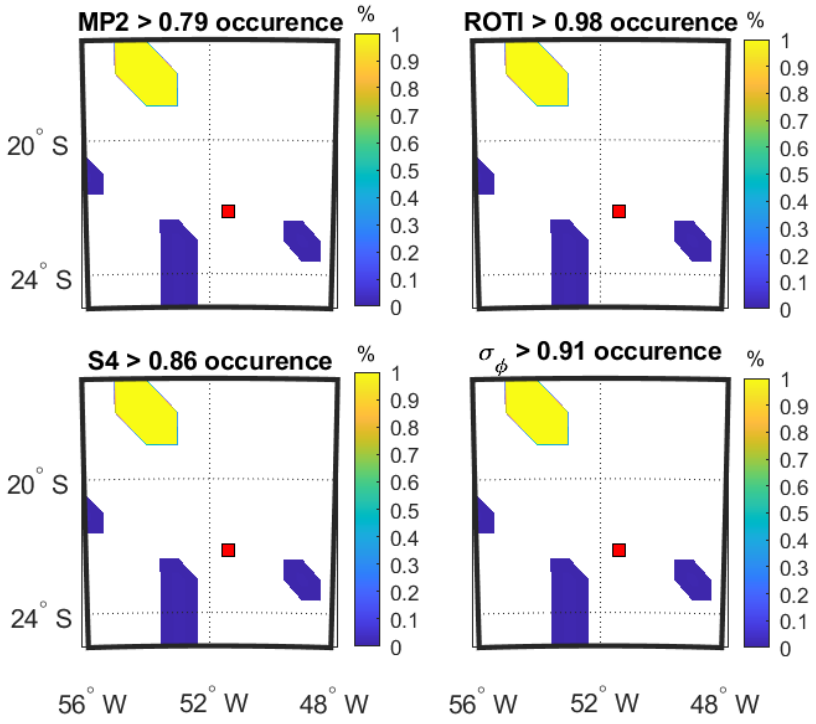

(c)

Figure 4.10 Occurrence percentage maps of four parameters: (a) during 02:59:00–03:04:00 UTC on 8 September 2017 at SAO0P station; (b) during 02:39:00–02:44:00 UTC on 13 September 2017 at SAO0P station; (c) during 03:31:00–03:36:00 UTC on 12 March 2011 at PRU2 station. Thresholds are obtained from equation 4.13. Units as in Figure 4.3.

Taking a data period of 5 min with scintillation, as shown in Figure 4.10, all the parameters are active at the same locations. The SSIM and CC between the parameters in the maps of Figure 4.10a,b,c are shown in Table 4.9-Table 4.11 respectively. These show that the four parameters are perfectly correlated in all four maps. The SSIMs are less than 1 in Table 4.9 and Table 4.10, indicating that the mean values of the parameters differ.

SSIM and CC

Table 4.9 SSIM and CC between the maps shown in Figure 4.10a.

	MP		**ROTI**	
Criteria	SSIM	CC (*p*-value)	SSIM	CC (*p*-value)
S4	0.96	1.00 (<0.01)	0.96	1.00 (<0.01)
σ_ϕ	0.59	1.00 (<0.01)	0.59	1.00 (<0.01)

Table 4.10 SSIM and CC between the maps shown in Figure 4.10b.

	MP		**ROTI**	
Criteria	SSIM	CC (*p*-value)	SSIM	CC (*p*-value)
S4	0.96	1.00 (<0.01)	0.96	1.00 (<0.01)
σ_ϕ	0.83	1.00 (<0.01)	0.83	1.00 (<0.01)

Table 4.11 SSIM and CC between the maps shown in Figure 4.10c.

	MP		**ROTI**	
Criteria	SSIM	CC (*p*-value)	SSIM	CC (*p*-value)
S4	1.00	1.00 (<0.01)	1.00	1.00 (<0.01)
σ_ϕ	1.00	1.00 (<0.01)	1.00	1.00 (<0.01)

4.3. Antarctica data

4.3.1. Temporal relationship

The time series plots of the four parameters at SNA0P station on 2 April, 13 October 2016 and 9 May 2016 are shown respectively in Figure 4.11a,b,c.

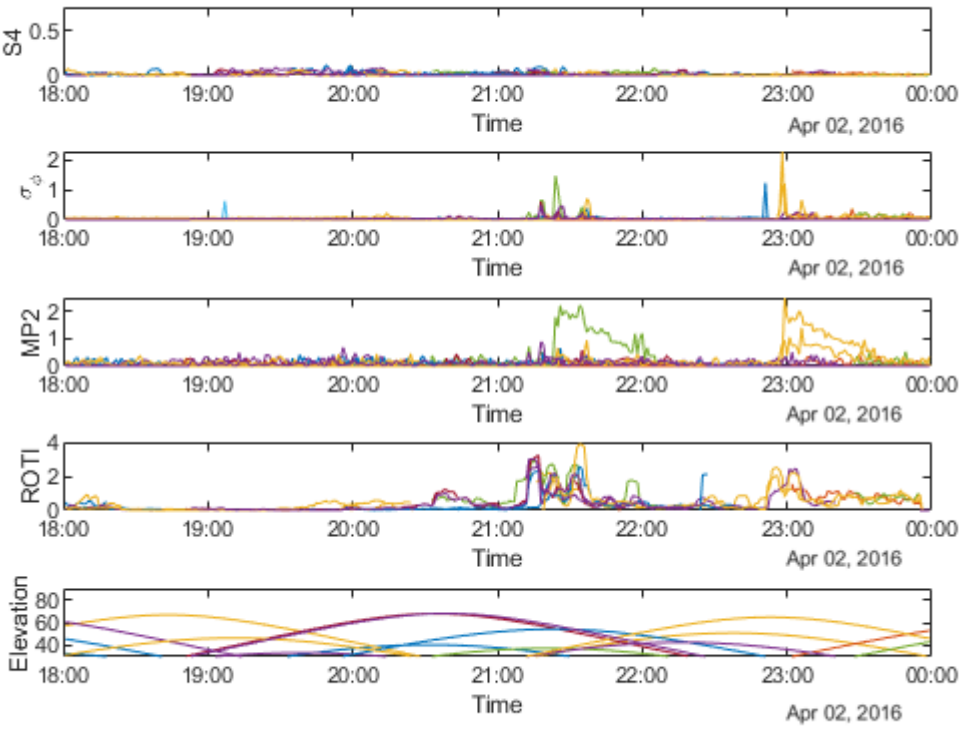
S4
0.5
0
18:00
19:00
20:00
21:00
22:00
23:00
00:00
Time
Apr 02, 2016
σ_ϕ
2
1
0
MP2
ROTI
4
Elevation
80
60
40

(a)

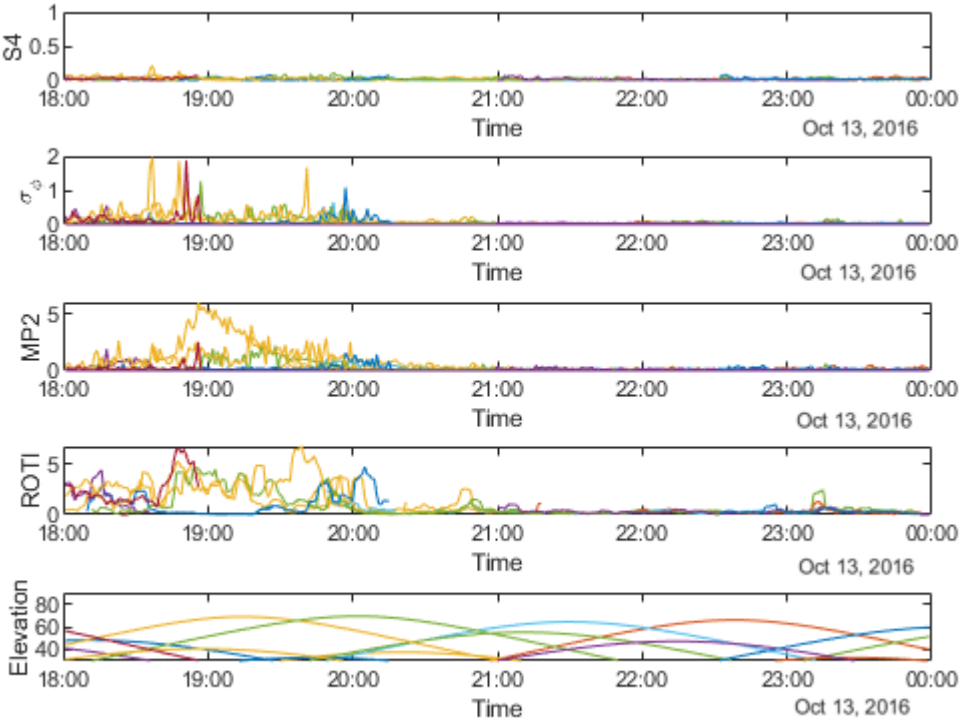
S4
1
0.5
0
18:00
19:00
20:00
21:00
22:00
23:00
00:00
Time
Oct 13, 2016
σ_ϕ
2
1
MP2
5
ROTI
Elevation
80
60
40

(b)

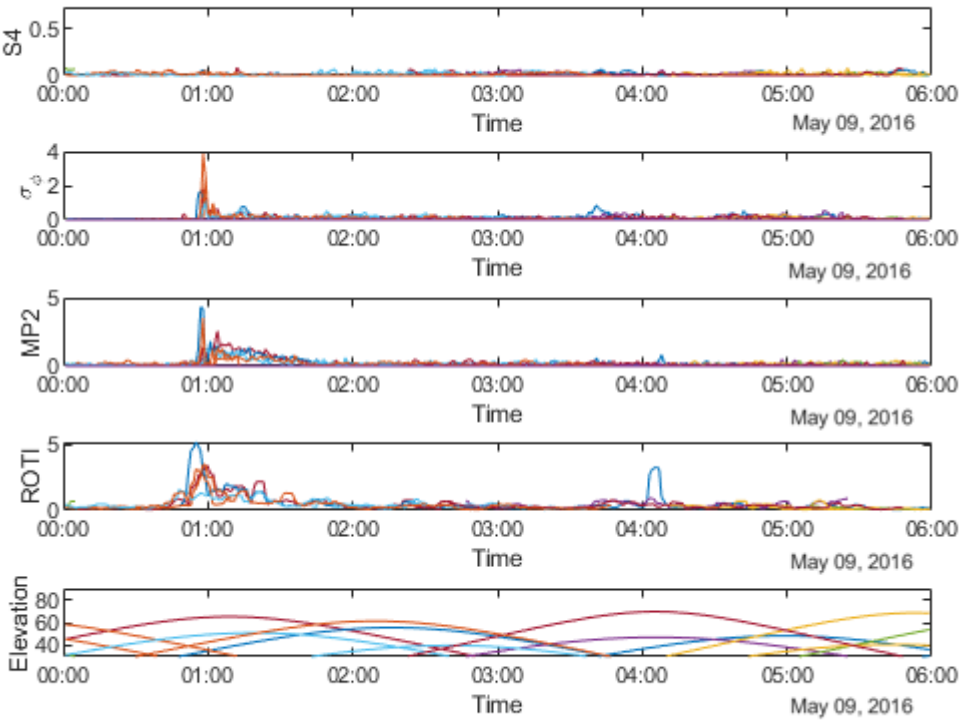

(c)

Figure 4.11 Time series plots of four parameters at SNA0P station: (a) during 18:00:00–24:00:00 UTC on 2 April, 2016; (b) during 18:00:00–24:00:00 UTC on 13 October, 2016; (c) during 00:00:00–06:00:00 UTC on 9 May, 2016. Units as in Figure 4.3.

As shown in Figure 4.11, S4 does not have any high values on all three days whereas σ_ϕ still fluctuates in accordance with the feature of scintillation occurrence observed at high latitudes. Therefore, S4 is not considered for comparison in the following paragraphs. Furthermore, it can be seen that all the other three parameters are mainly noisy during the last three hours on 2 April 2016, between 18 and 21 UT on 13 October 2016 and first two hours on 9 May 2016. Different from the data of SAO0P station (Figure 4.3), the number of satellites affected by scintillation and MP is similar at SNA0P station. Figure 4.12a,b,c shows the time series plots of the four parameters obtained from a single satellite at SNA0P station respectively on 2 April, 13 October 2016 and 9 May 2016. As shown in Figure 4.12, a similar high value period can be seen in plots of four parameters on 2 April 2016 and 9 May 2016 though a minor delay exists on 13 October 2016, which supports the temporal relationship between MP, ROTI and σ_ϕ.

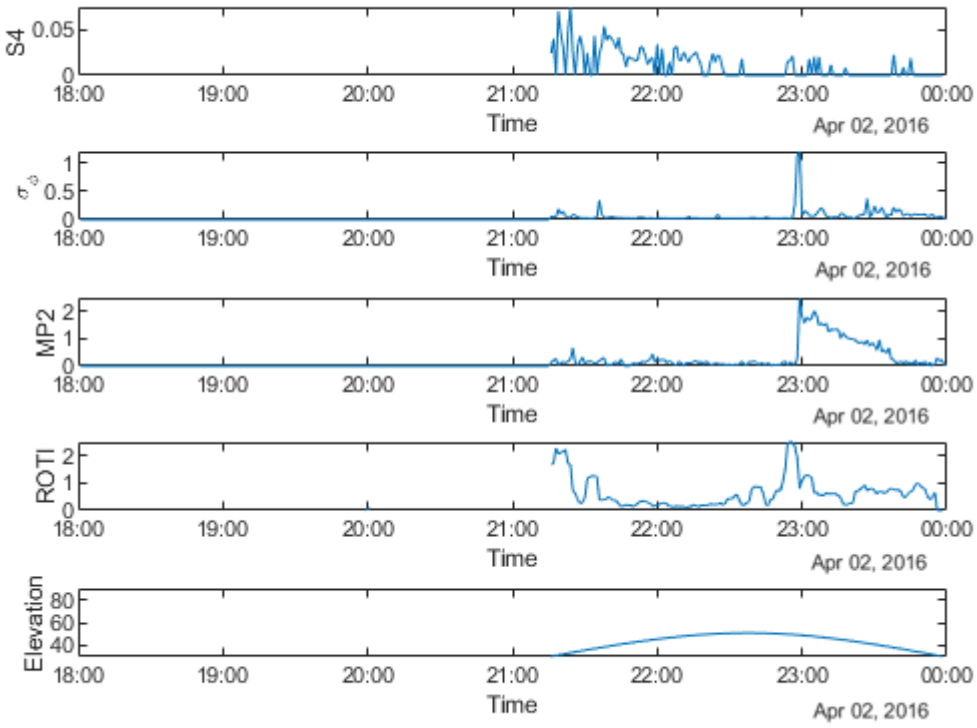
S4
0.05
0
18:00
19:00
20:00
21:00
22:00
23:00
00:00
Time
Apr 02, 2016
σ_ϕ
1
0.5
0
MP2
2
1
0
ROTI
Elevation
80
60
40

(a)

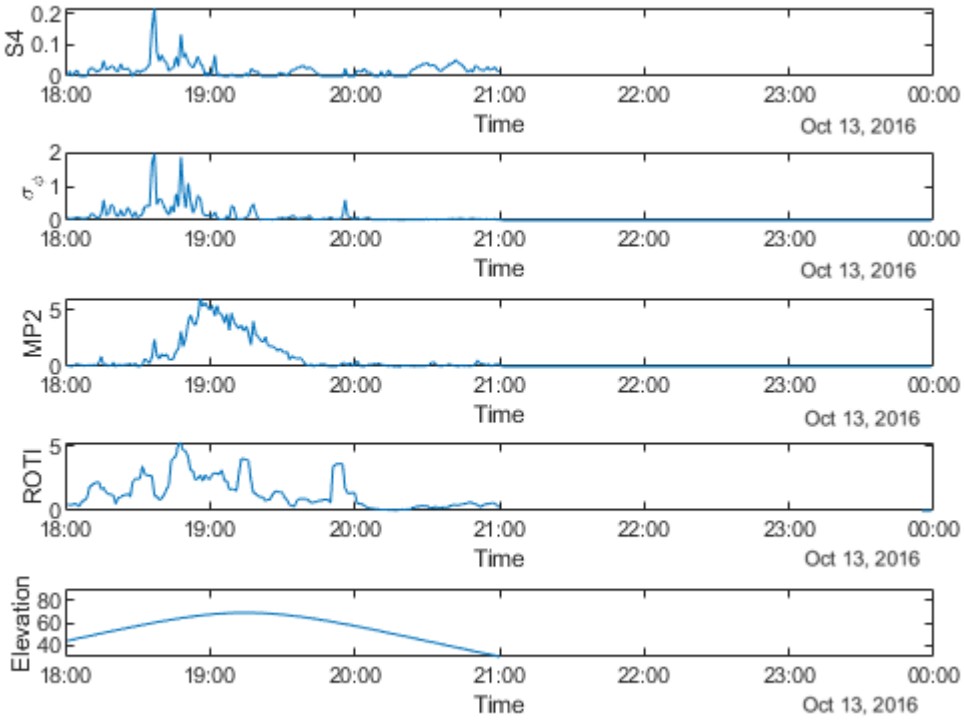
S4
0.2
0.1
0
18:00
19:00
20:00
21:00
22:00
23:00
00:00
Time
Oct 13, 2016
σ_ϕ
2
1
0
MP2
5
0
ROTI
Elevation
80
60
40

(b)

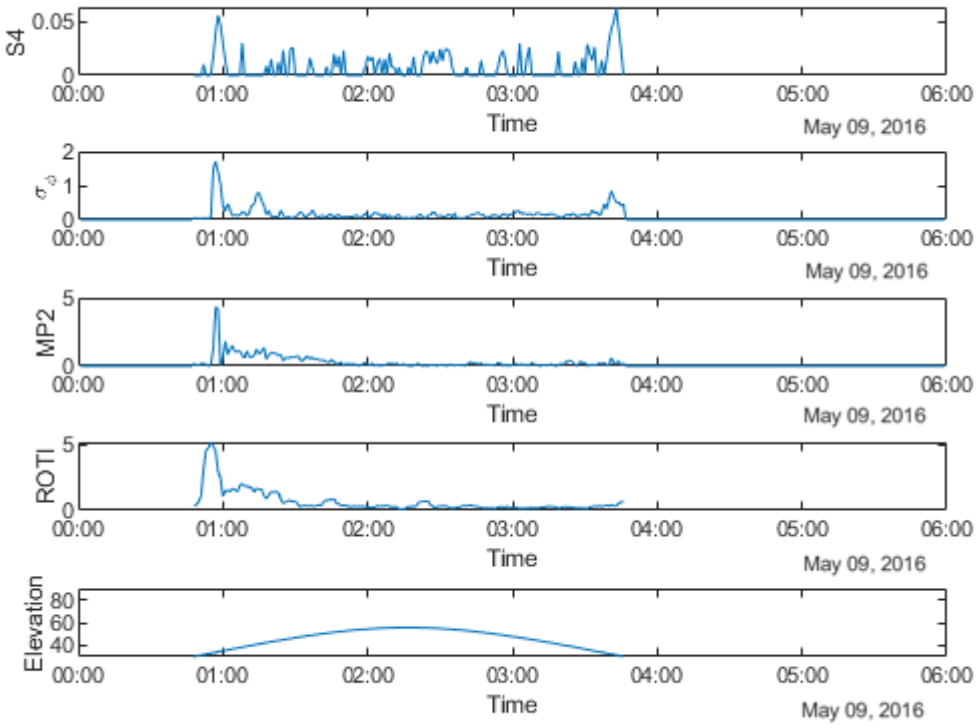

(c)

Figure 4.12 Time series plots of four parameters at SNA0P station on: (a) during 18:00:00–24:00:00 UTC on 2 April 2016 for G03; (b) during 18:00:00–24:00:00 UTC on 13 October 2016 for G17; (c) during 00:00:00–06:00:00 UTC on 9 May 2016 for G08. Units as in Figure 4.3.

4.3.2. Spatial relationship

4.3.2.1. Mean value map

4.3.2.1.1. Long duration

Figure 4.13a,b,c shows the mean value maps as a function of IPP latitude and longitude of the three parameters.

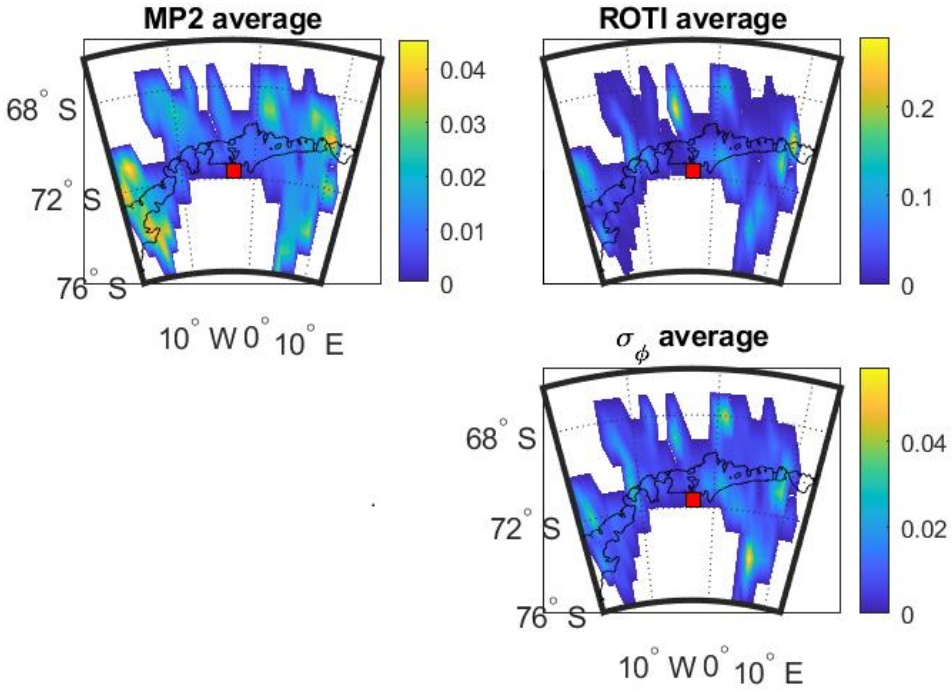
MP2 average
ROTI average
σ_ϕ average
68° S
72° S
76° S
10° W 0° 10° E
0.04
0.03
0.02
0.01
0
0.2
0.1
0.04
0.02

(a)

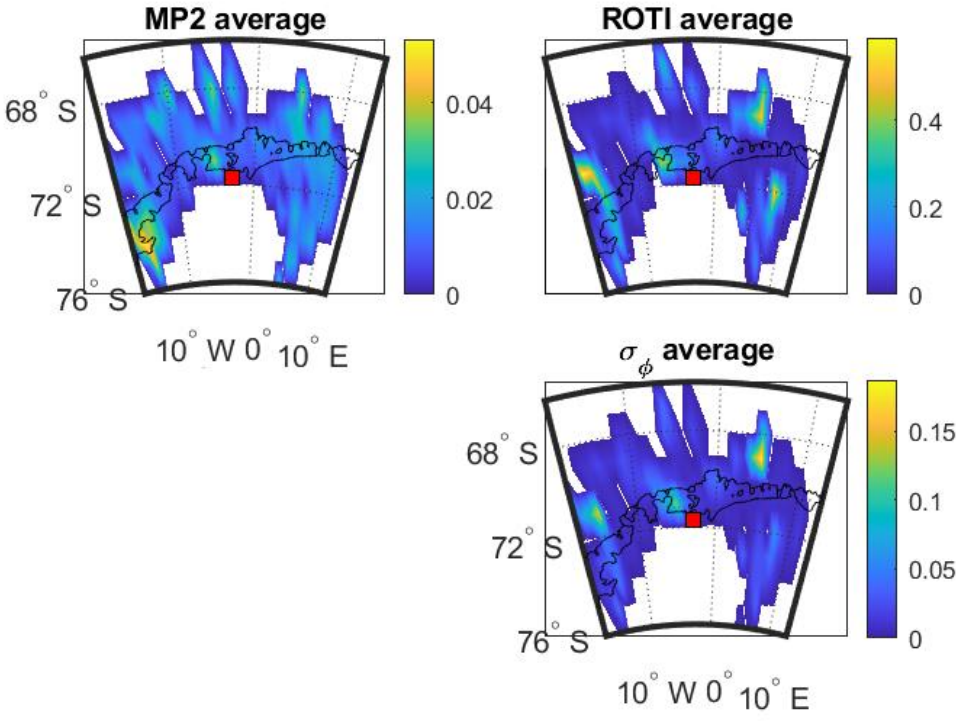
MP2 average
ROTI average
σ_ϕ average
68° S
72° S
76° S
10° W 0° 10° E
0.04
0.02
0
0.4
0.2
0.15
0.1
0.05

(b)

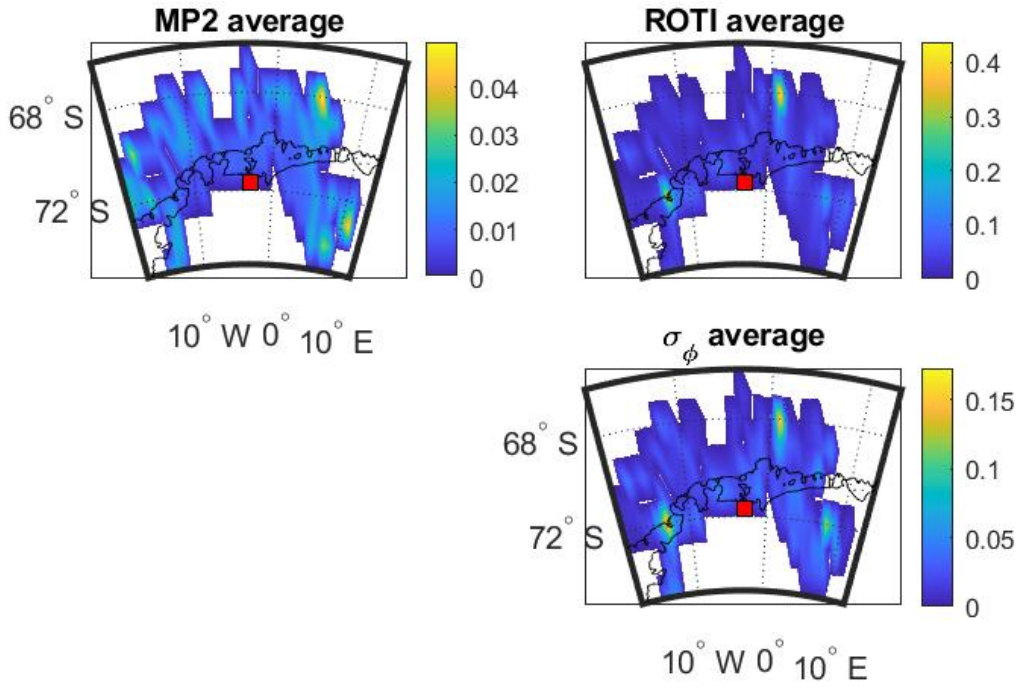

(c)

Figure 4.13 Mean value maps of three parameters at SNA0P station: (a) during 18:00:00–24:00:00 UTC on 2 April 2016; (b) during 18:00:00–24:00:00 UTC on 13 October 2016; (c) during 00:00:00–06:00:00 UTC on 9 May 2016. Units as in Figure 4.3.

As shown in Figure 4.13, the mean value maps are not as distinct as those in Brazil which can be caused by the sparse distribution of data at the high latitude area. Therefore, the occurrence percentage maps are more useful to this dataset in order to show more details. However, it can still be seen that the high value areas of σ_ϕ maps include those of MP and ROTI maps. The SSIM and CC values between the parameters shown in Figure 4.13a,b,c are illustrated in Table 4.12-Table 4.14 respectively. As shown in Table 4.12-Table 4.14, SSIM values between MP&ROTI and σ_ϕ are all higher than 0.6, where most exceed 0.7. CC values in Table 4.12-Table 4.14 show low correlation between MP and σ_ϕ, the correlations between ROTI and σ_ϕ are high.

SSIM and CC

Table 4.12 SSIM and CC between the maps shown in Figure 4.13a.

	MP		**ROTI**	
Criteria	SSIM	CC (*p*-value)	SSIM	CC (*p*-value)
σ_ϕ	0.73	0.23 (0.01)	0.77	0.65 (<0.01)

Table 4.13 SSIM and CC between the maps shown in Figure 4.13b.

	MP		**ROTI**	
Criteria	SSIM	CC (*p*-value)	SSIM	CC (*p*-value)
σ_ϕ	0.78	0.54 (<0.01)	0.69	0.76 (<0.01)

Table 4.14 SSIM and CC between the maps shown in Figure 4.13c.

	MP		**ROTI**	
Criteria	SSIM	CC (*p*-value)	SSIM	CC (*p*-value)
σ_ϕ	0.61	0.42 (<0.01)	0.79	0.69 (<0.01)

Variograms

Figure 4.14 shows the variograms and cross variograms for the results presented in Figure 4.13. The variograms and cross-variograms do show evidence of a common spatial structure in the three parameters; however, this is less clear than those for the Brazil data. In particular there is limited evidence of spatial correlation for the data from 2016 April 2 (Figure 4.13a). For 2016 October 13 the variograms and cross-variograms show a clear common spatial structure with a range of approximately 3.5°. For the dataset from 2016 May 9 there is weak evidence of spatial structure.

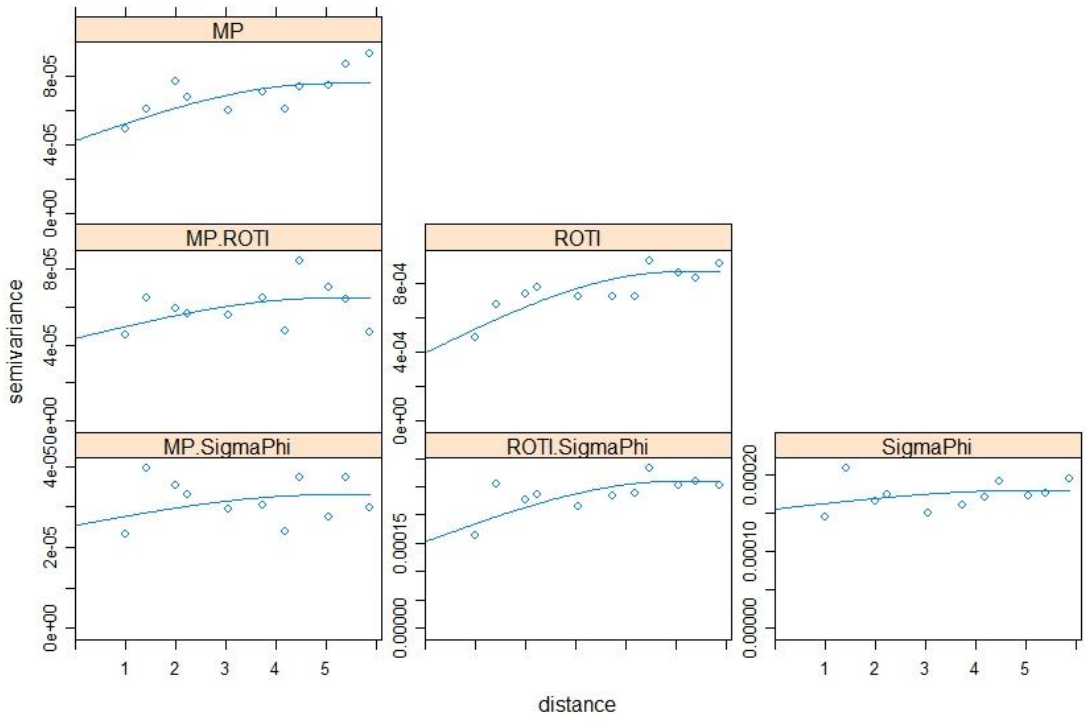
MP
MP.ROTI
ROTI
MP.SigmaPhi
ROTI.SigmaPhi
SigmaPhi
semivariance
distance

(a)

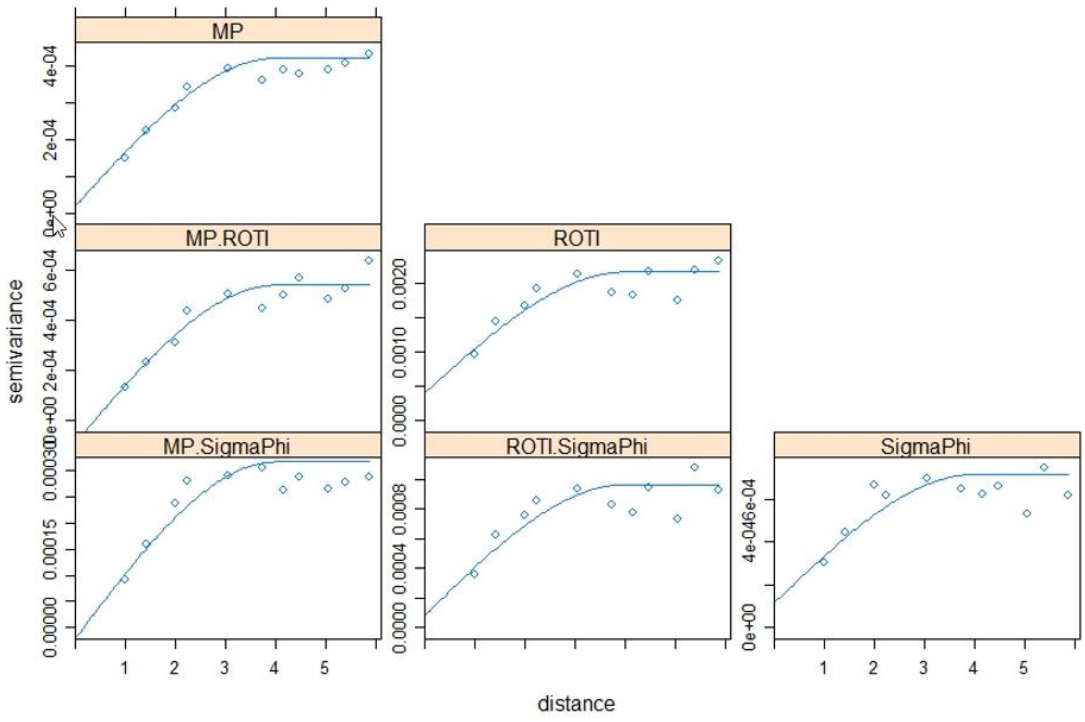
MP
MP.ROTI
ROTI
MP.SigmaPhi
ROTI.SigmaPhi
SigmaPhi
semivariance
distance

(b)

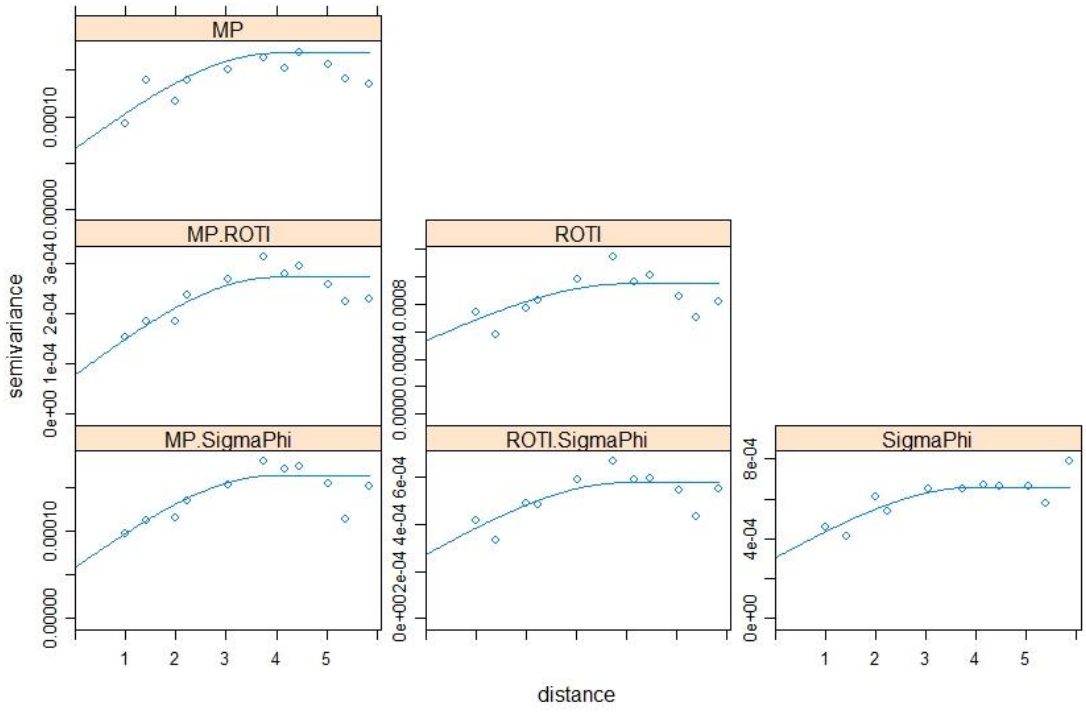

(c)

Figure 4.14 Figure 4.13a,b,c shows the variograms and cross-variograms associated with Figure 4.12a,b,c.

4.3.2.1.2. Short duration

Figure 4.15 and Figure 4.16 show the time evolution of the three parameters during 23:10–23:25 on 2 April and during 18:50−19:05 on 13 October 2016, respectively. The SSIM and CC between the parameters in the maps of Figure 4.15 and Figure 4.16 are shown in Table 4.15 and Table 4.16.

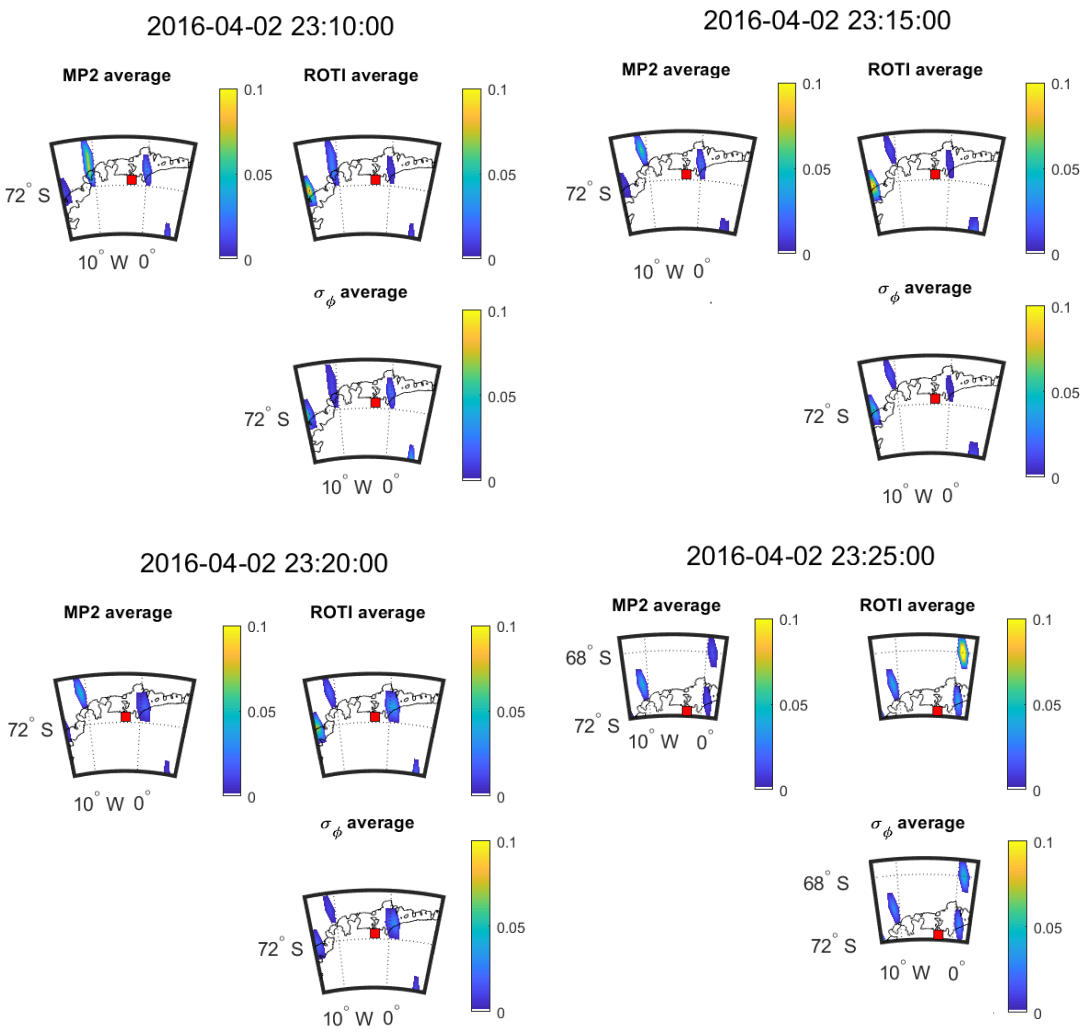

Figure 4.15 Consecutive 5 min means over 20 min at SNA0P station on 2 April 2016. Units as in Figure 4.3.

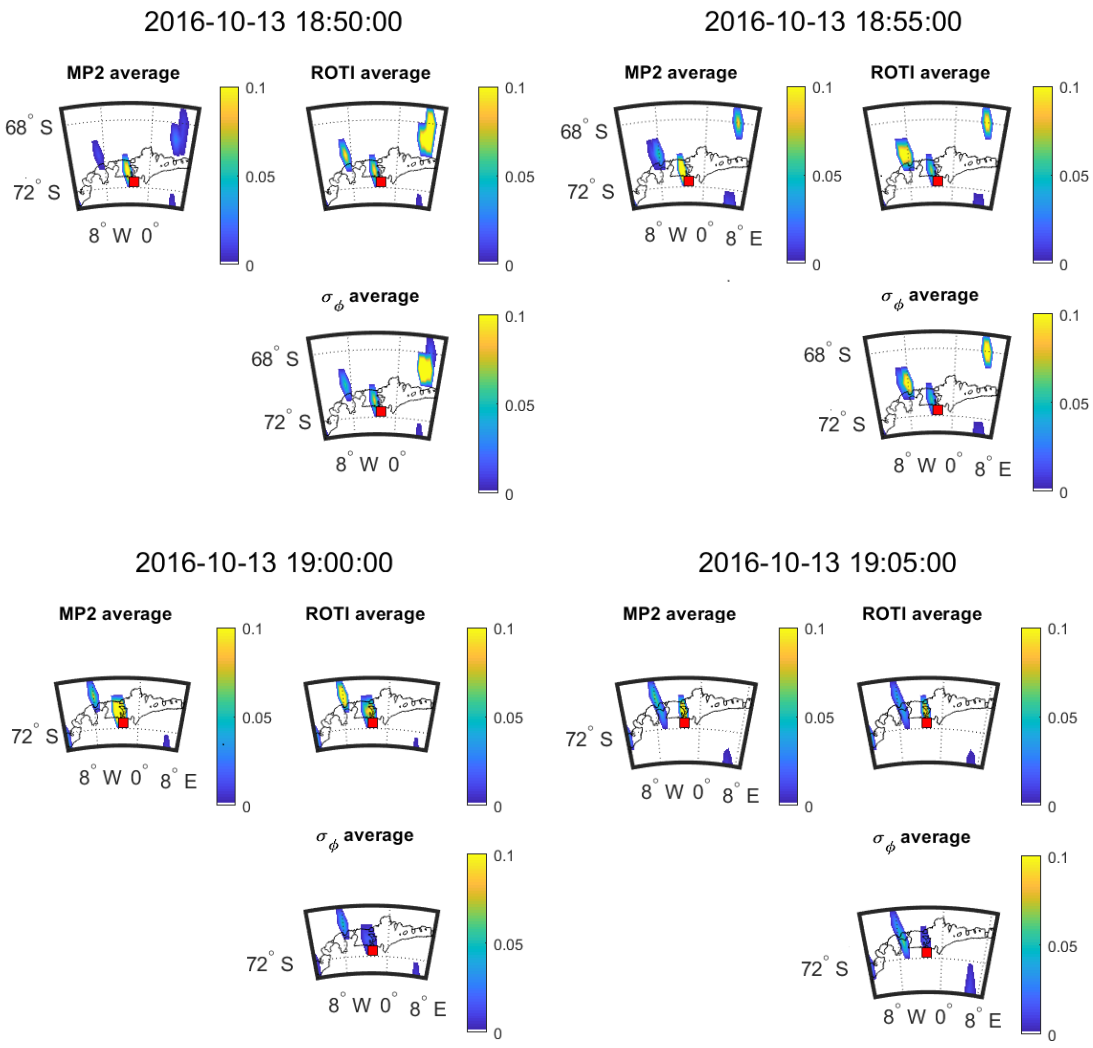

Figure 4.16 Consecutive 5 min means over 20 min at SNA0P station on 13th October, 2016. Units as in Figure 4.3.

SSIM and CC

Table 4.15 SSIM and CC between the maps shown in Figure 4.15.

2016 April 2	**23:10:00**		**23:15:00**		**23:20:00**		**23:25:00**	
Criteria	**SSIM**	**CC (*p*-value)**	**SSIM**	**CC (*p*-value)**	**SSIM**	**CC (*p*-value)**	**SSIM**	**CC (*p*-value)**
MP vs. σ_ϕ	0.02	−0.63 (0.18)	0.47	−0.33 (0.53)	0.70	−0.29 (0.58)	0.31	−0.50 (0.50)
ROTI vs. σ_ϕ	0.47	0.26 (0.62)	0.60	0.80 (0.06)	0.62	0.38 (0.45)	0.50	0.37 (0.63)

Table 4.16 SSIM and CC between the maps shown in Figure 4.16.

2016 October 13	**18:50:00**		**18:55:00**		**19:00:00**		**19:05:00**	
Criteria	**SSIM**	**CC (*p*-value)**	**SSIM**	**CC (*p*-value)**	**SSIM**	**CC (*p*-value)**	**SSIM**	**CC (*p*-value)**
MP vs. σ_ϕ	0.07	−0.00 (0.99)	0.36	0.32 (0.48)	0.14	0.08 (0.88)	0.31	0.25 (0.58)
ROTI vs. σ_ϕ	0.52	0.47 (0.29)	0.80	0.79 (0.03)	0.30	0.79 (0.06)	0.38	0.31 (0.50)

Figure 4.15 and Figure 4.16 show the change in the 5-min mean values for 2016 April 2 and 2016 October 3 respectively. Figure 4.15 shows that large value areas of all the parameters move towards northeast across 20 min. However, in Figure 4.16, the large value areas of parameters move towards the southeast over the 20 min. Again, all the parameters have the same direction for propagation. The results shown in Table 4.15 andTable 4.16 are calculated from six and four points, respectively, leading to a high level of uncertainty in the estimation of CC and SSIM. As such we can only make qualitative observations on these plots and cannot back those observations up with reliable CC or SSIM results.

4.3.2.2. Occurrence percentage map

4.3.2.2.1. Long duration

Figure 4.17a,b,c shows the occurrence percentage maps as a function of IPP latitude and longitude for the three parameters respectively on 2 April 2016, 13 October 2016 and 9 May 2016.

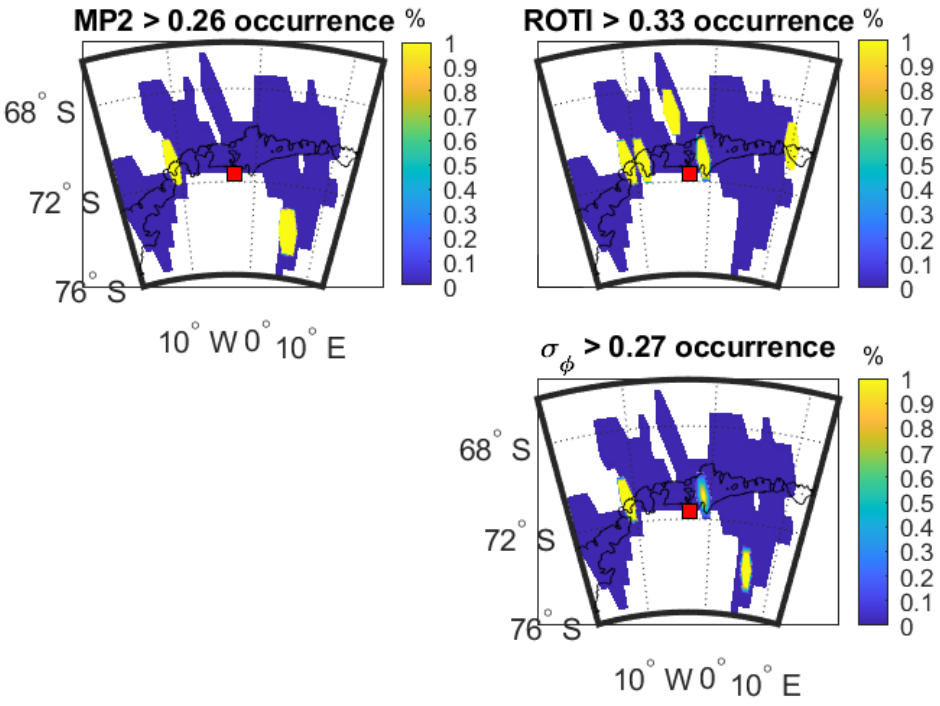
MP2 > 0.26 occurrence %
ROTI > 0.33 occurrence %
σ_ϕ > 0.27 occurrence %
68° S
72° S
76° S
10° W 0° 10° E
1
0.9
0.8
0.7
0.6
0.5
0.4
0.3
0.2
0.1
0

(a)

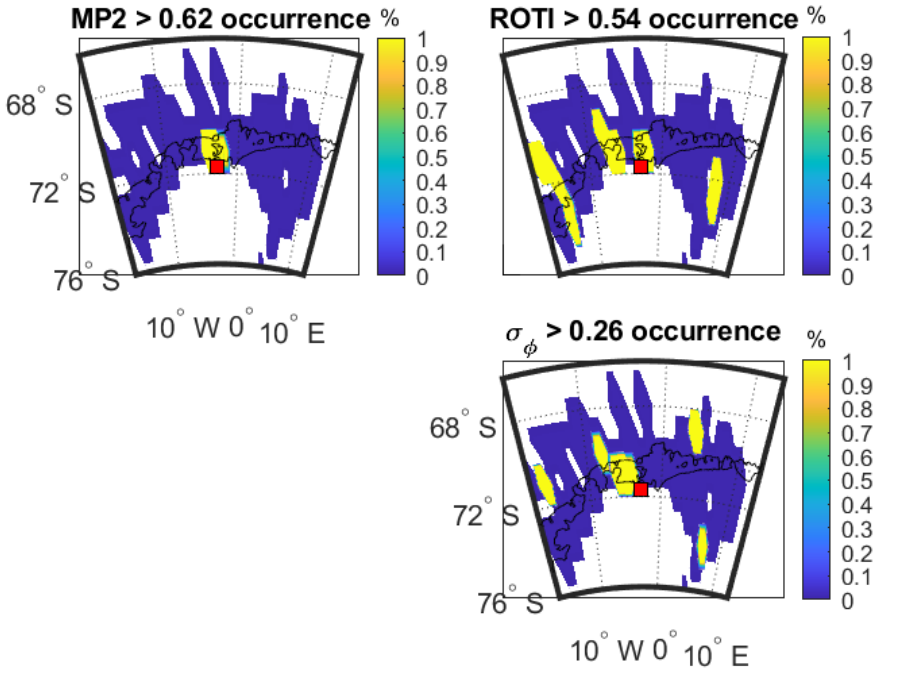
MP2 > 0.62 occurrence %
ROTI > 0.54 occurrence %
σ_ϕ > 0.26 occurrence %
68° S
72° S
76° S
10° W 0° 10° E
1
0.9
0.8
0.7
0.6
0.5
0.4
0.3
0.2
0.1
0

(b)

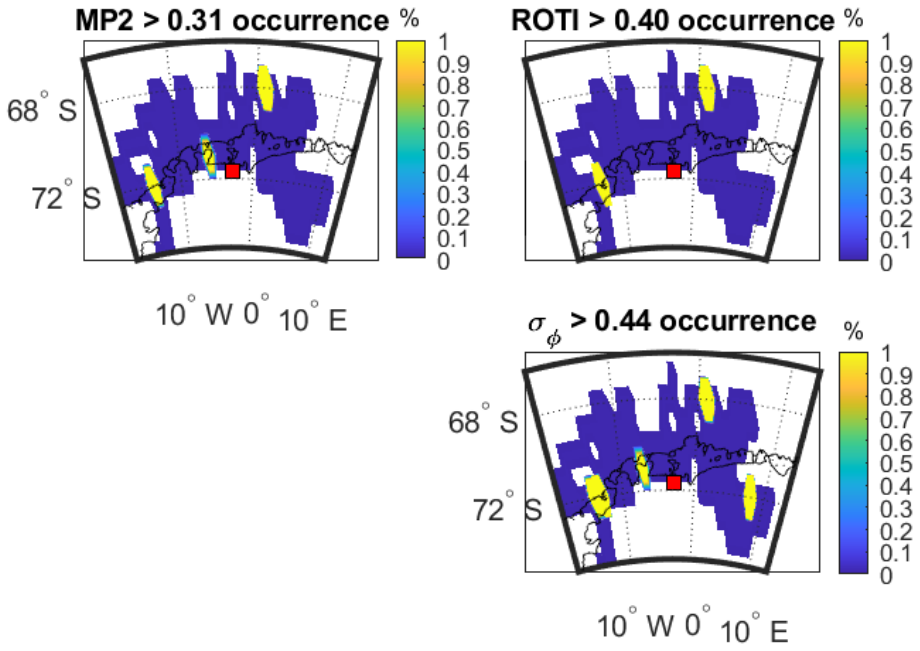

(c)

Figure 4.17 Occurrence percentage maps of three parameters at SNA0P station: (a) during 18:00:00–24:00:00 UTC on 2 April 2016; (b) during 18:00:00–24:00:00 UTC on 13 October 2016; (c) during 00:00:00-06:00:00 UTC on 9 May 2016. Thresholds are obtained from equation 4.13. Units as in Figure 4.3.

As shown in maps of Figure 4.17a, the high value areas of MP and ROTI separately correspond to different areas of σ_ϕ. For instance, some satellites signals less influenced by MP may be more affected by ROTI. Therefore, the combination of two parameters can cover more areas of σ_ϕ than a single parameter. As shown in Figure 4.17b, high-value areas of ROTI overlap high-value areas of σ_ϕ while MP does not. However, as shown in Figure 4.17c, MP includes more high-value areas that are spatially-coincident with high-value areas of σ_ϕ than ROTI on 9 May 2016. Table 4.17-Table 4.19 show the SSIM and CC between the three parameters shown in Figure 4.17a,b,c.

SSIM and CC

Table 4.17 SSIM and CC between the maps shown in Figure 4.17a.

	MP		**ROTI**	
Criteria	SSIM	CC (*p*-value)	SSIM	CC (*p*-value)
σ_ϕ	0.82	0.46 (<0.01)	0.65	0.03 (0.74)

Table 4.18 SSIM and CC between the maps shown in Figure 4.17b.

	MP		**ROTI**	
Criteria	SSIM	CC (*p*-value)	SSIM	CC (*p*-value)
σ_ϕ	0.71	0.41 (<0.01)	0.46	0.38 (<0.01)

Table 4.19 SSIM and CC between the maps shown in Figure 4.17c.

	MP		**ROTI**	
Criteria	SSIM	CC (*p*-value)	SSIM	CC (*p*-value)
σ_ϕ	0.86	0.45 (<0.01)	0.79	0.66 (<0.01)

4.3.2.2.2. Short duration

Figure 4.18 shows the occurrence percentage maps as a function of IPP latitude and longitude of three parameters during the time period when largest variations were observed in Figure 4.11.

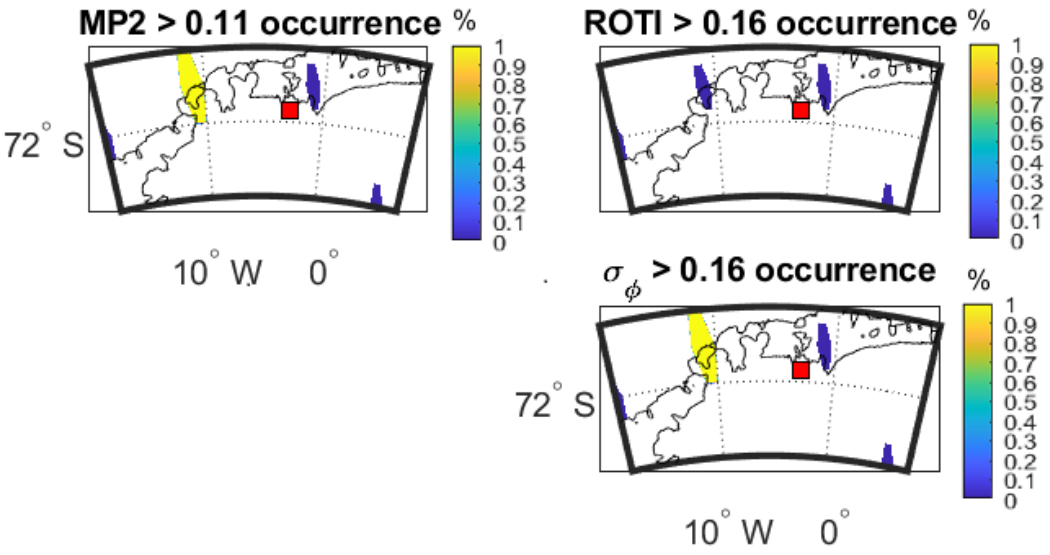

(a)

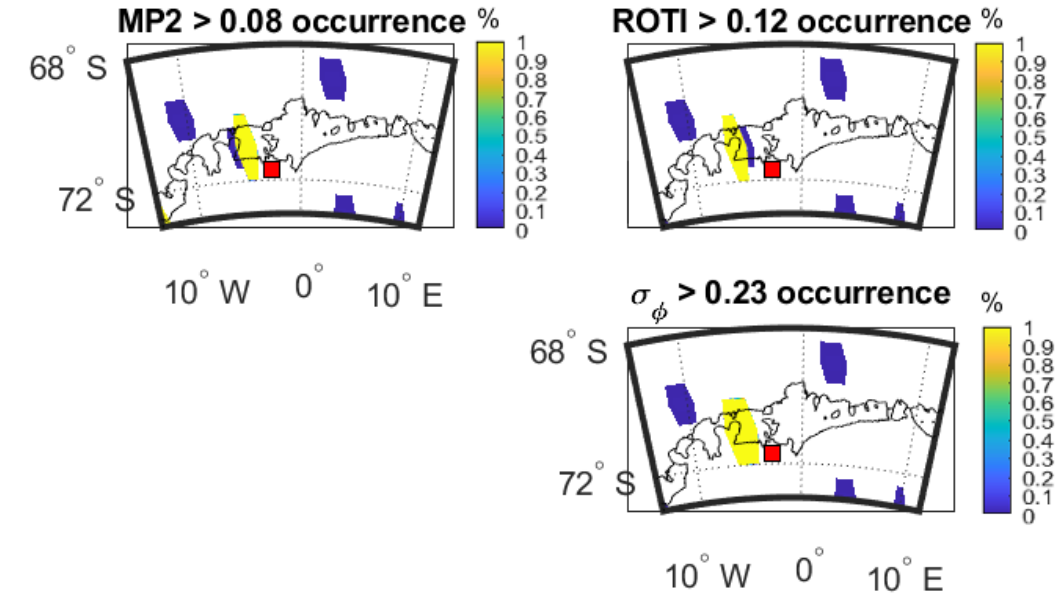

(b)

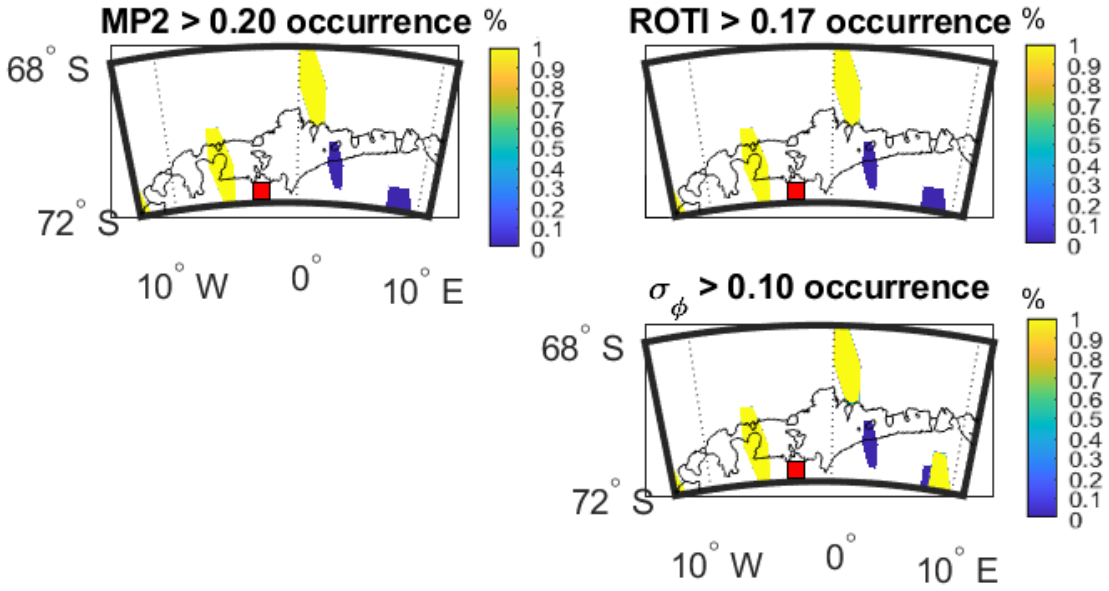

(c)

Figure 4.18 Occurrence percentage maps of four parameters: (a) during 02:59:00–03:04:00 UTC on 8 September 2017 at SAO0P station; (b) during 02:39:00–02:44:00 UTC on 13 September 2017 at SAO0P station; (c) during 03:31:00–03:36:00 UTC on 12 March 2011 at PRU2 station. Thresholds are obtained from equation 4.13. Units as in Figure 4.3.

Figure 4.18a shows that, within a specific time period, MP has the same high-value area as σ_ϕ.

Figure 4.18b shows that MP and ROTI both share the high-value areas with σ_ϕ. From Figure 4.18c, both MP and ROTI agree with σ_ϕ for most of the high value areas. These observations are reflected in the CC and SSIM values shown in Table 4.20-Table 4.22.

SSIM and CC

Table 4.20 SSIM and CC between the maps shown in Figure 4.18a.

	MP		**ROTI**	
Criteria	SSIM	CC (*p*-value)	SSIM	CC (*p*-value)
σ_ϕ	1.00	1.00 (<0.01)	0.01	0.00 (NaN)

Table 4.21 SSIM and CC between the maps shown in Figure 4.18b.

	MP		**ROTI**	
Criteria	SSIM	CC (*p*-value)	SSIM	CC (*p*-value)
σ_ϕ	0.17	−0.08 (0.83)	0.90	0.97 (<0.01)

Table 4.22 SSIM and CC between the maps shown in Figure 4.18c.

	MP		**ROTI**	
Criteria	SSIM	CC (*p*-value)	SSIM	CC (*p*-value)
σ_ϕ	0.44	0.72 (0.11)	0.63	0.92 (0.01)

4.4. Discussion

Data obtained from three stations respectively located at equatorial and high-latitude areas were utilized in order to investigate the relationship between MP, ROTI, S4 and σ_ϕ. First, as shown in Figure 4.3-Figure 4.4 and Figure 4.11-Figure 4.12, the relationship in the temporal domain could be observed from all twelve time series plots, where all the parameters showed the largest variations during the same time period. Figure 4.5 and Figure 4.13 illustrated the spatial relationship for 6-h mean value maps, where high value regions occurred at same location on maps. ROTI and σ_ϕ had different high value areas as compared with MP and S4 in Figure 4.5. This was because the relationship between ROTI and σ_ϕ and between MP and S4 might differ between satellites, due to different effects of ionospheric scintillation. In addition, as shown in Figure 4.13, high value areas of both MP and ROTI corresponded to those of σ_ϕ, but related to different parts of the maps. Hence, it might be possible to identify areas affected by scintillation by combining MP and ROTI maps. It also suggested that MP and ROTI related to different types of scintillation. This hypothesis could be further evaluated with the occurrence percentage maps. As shown in Figure 4.9, MP and ROTI separately showed similar high value areas as S4 and σ_ϕ. As shown in Figure 4.17, MP and ROTI agreed with σ_ϕ over different areas. Next,

occurrence percentage maps for 5 min as shown in Figure 4.10 and Figure 4.18 suggested similar high value areas for all parameters. Finally, the propagation maps as shown in Figure 4.7-Figure 4.8 and Figure 4.15-Figure 4.16, all the parameters moved in the similar direction over time, further indicated the spatial similarity between MP&ROTI and S4&σ_ϕ.

The Pearson CC and SSIM were both used to quantify the relationship between pairs of maps. CC evaluated the linear correlation whereas SSIM provided a more complete evaluation of map similarity (Kaur et al. 2012). As discussed in section 0, $s(m,n)$ could be inflated at low values of CC leading to an overoptimistic assessment of the map similarity. For the Brazil data, most of the SSIMs and CCs between S4 and MP exceeded those between S4 and ROTI while σ_ϕ correlates more with ROTI than MP. For the Antarctica data, both MP and ROTI sometimes had high similarities with σ_ϕ. The variograms and cross-variograms (Figure 4.6 and Figure 4.14) were used to illustrate the spatial correlation in the parameters as well the cross-correlation between parameters. The variograms showed clear spatial structure, with a range of 5 to 6°, for the Brazil data. Likewise, the cross-variograms showed a common spatial structure. Whereas CC quantifies the bi-variate correlation the cross-variograms quantified whether the spatial structure was common between the different parameters. This gave evidence of strong spatial correlation between the four parameters and backed-up the results observed for the SSIM and CC. For the Antarctica case study there was clear evidence of spatial correlation for the dataset from 2016-10-13, with a common range of approximately 3.5°. There was less clear evidence for the dataset from 2016-05-09 (common range of approximately 3.5°) and no evidence of spatial correlation for the dataset from 2016-04-02

The purpose of this chapter was to explore the relationship between MP, ROTI and scintillation parameters. We aimed to better understand the relationships first, leaving open the possibility to use these relationships to provide supplementary information that might assist in overcoming the limitations of using high-rate data. The past research on the relationship between MP and scintillation has been introduced in section 3.3.5.1. In this chapter, all the analyzed data had a 30° satellite mask which should significantly reduce any MP effect in the vicinity of the station. Therefore, the high values of S4, σ_ϕ and MP in this chapter all occurred for satellites at high elevations (>30°), giving support to the theory that the higher values of MP were being influenced by the scintillation events evidenced from the high scintillation indices values during the corresponding time window.

Following on Romano et al. (2013) and Hancock et al. (2017), this chapter provided a much deeper statistical analysis of the relationships between MP, S4 and σ_ϕ. Furthermore, the

ionospheric index ROTI was added in this chapter to give additional evidence that scintillation was real rather than a product of the physical environment around the receiver as claimed by Romano et al. (2013). In addition, the relationship between ROTI and scintillation has been introduced in section 3.3.5.2. As compared with the analysis of Yang and Liu (2016), both S4 and σ_ϕ ere analyzed and compared in this chapter with reference to their relationships with ROTI. Furthermore, analysis from the stations in this chapter showed evidence that ROTI was more similar to σ_ϕ than to S4 both visually and statistically, giving new valuable insights into the relationships between ROTI, S4 and σ_ϕ.

Previous research has focused principally on the linear relationship between ROTI and the scintillation parameters, this chapter added to this body of research by investigating the spatial relationship. This led to the possibility of using these data sets to generate scintillation risk maps, that might be similar in principle to tracking jitter maps generated by Sreeja et al. (2011a), and also similar to Figures 4–7 given by Koulouri et al. (2020), which visualized the effect of scintillation and could be used to identify and possibly mitigate risk caused by scintillation events. Figure 2 from Sreeja et al. (2011a) showed the S4 maps as a function of time and IPP latitude where strong scintillation activity was observed between 18° S and 26° S from 8pm to 0am local time on March 9–11, 2011. By comparison, Figure 4.3c, Figure 4.5c and Figure 4.9c in this chapter showed all the parameters were intense between 18° S and 26° S from 0 am to 4 am UTC (8 pm to 0 am in local time) on March 12 2011, which was similar to the output obtained by Sreeja et al. (2011a).

Additionally, ROTI was the major proxy to the scintillation parameters proposed in previous research, which has shown weaknesses in the ability of ROTI to replace S4 and σ_ϕ. In this research the relationship between ROTI and the scintillation parameters S4 and σ_ϕ has been further investigated and in addition this chapter showed that it might be possible to add MP as an additional parameter, in support of other parameters such as ROTI, computed from a standard GNSS receiver (i.e., non-scintillation monitoring receiver) that might be indicative of scintillation. However, the increase of MP does not generally indicate the occurrence of scintillation events as the scintillation measurements can be contaminated by real multipath effects (Romano et al. 2013).

4.5. Conclusions

Six days of data under strong scintillation from three stations, respectively located in Brazil and Antarctica, were utilized to research on the relationship between MP and ROTI and scintillation

indices. The relationship in the temporal and spatial domain was evaluated with a series of data science techniques, including 2D map comparison, Pearson CC, SSIM and variograms. The propagation patterns of all parameters were demonstrated to be similar. According to the discussion, it could be concluded that:

(1) A relationship between MP, ROTI and scintillation existed in both temporal and spatial domain.

(2) An integration between MP and ROTI could more completely represent scintillation than a single parameter. Precisely, MP and ROTI could reflect different types of scintillation. For equatorial data, MP was more correlated with S4 while ROTI was more relevant to σ_ϕ. For high latitude data, it was possible for both MP and ROTI to be correlated with σ_ϕ.

(3) The propagation patterns of MP, ROTI and S4, σ_ϕ were similar, which could contribute to the prediction of scintillation with MP and ROTI.

(4) MP was correlated with scintillation only when scintillation was active while ROTI correlated with scintillation during both quiet and intense periods.

5. A novel methodology to distinguish scintillation from multipath in GNSS signals

The purpose of this chapter is to provide a systematic methodology for distinguishing scintillation from multipath events. S4 and σ_ϕ can be contaminated by the multipath effects in certain circumstances. In a similar way, multipath parameter (MP) can also be affected by scintillation. Therefore, it is difficult to distinguish whether an increase in the scintillation parameters and MP is caused by scintillation or multipath effects. It is known that the static multipath effect is periodic as compared to scintillation if the receiver location is fixed. Based on this peculiar feature, this chapter proposes to use parameters MP, rate of change of Total Electron Content Index (ROTI), S4 and σ_ϕ to develop a technique to characterize the receiver station surroundings so that multipath and scintillation effects could be distinguished. The GPS data for one month recorded at two stations, namely SAO0P and SJCU located in Sao Paulo, Brazil was used to generate elevation layered plots and parameter value against elevation and azimuth (PEA) plots for each satellite on each day. The SJCU station was used as the reference station for validating the conclusion. The results show that the proposed methodology could identify multipath, scintillation and hybrid (of multipath and scintillation) events except for hybrid events lower than 30° elevation.

Based on the capability of ROTI to represent scintillation, we proposed a novel receiver station characterization methodology that utilized data generated from standard geodetic receivers (MP and ROTI) and optional scintillation data (S4 and σ_ϕ) to distinguish scintillation from multipath. This led to the following specific objectives:

1. Use the mean, standard deviation (STD) and coefficient of variation (CoV) of MP of each satellite on each day without scintillation to investigate whether different satellites were affected by multipath to the same degree.
2. Input 5° interval elevation layered plots into the methodology and followed the decision steps to judge whether the variability was more likely to be caused by the multipath or

scintillation.

3. Input one-month parameter value against elevation and azimuth (PEA plots, see Appendix 1) into the methodology and followed the decision steps to judge the dominant event and to analyze whether the event was hybrid, defined as the event when both multipath and scintillation occurred simultaneously.

5.1. Distinguishing scintillation from multipath

Olwendo et al. (2010) used S4 values above 20° to generate a threshold line and extrapolate the line towards lower elevations. The multipath effect was calculated by comparing the extrapolated and the observed S4 values below 20°. There were three drawbacks to this method: (i) it could only be applied to the scintillation index S4 when scintillation was not active; (ii) S4 was needed, whose alternative index S4c could be obtained from data with a frequency of at least 1 Hz (Luo et al. 2020) and (iii) S4 could also be influenced by multipath at high elevations, so the threshold value might be inaccurate. Then, a simple distinguishing method was proposed by McCaffrey and Jayachandran (2017), where scintillation and multipath events could be identified by subtracting the mean S4 of 2 sidereal shifted days from the S4 during the possible scintillation event. This method could identify the event type only when either multipath or scintillation events occurred, which means this method might not be effective in distinguishing a hybrid event. In addition, S4 was needed in this method. Based on non-decimated discrete wavelet transform, de Oliveira Nascimento Brassarote et al. (2017) proposed to estimate multipath effect by decomposing the S4 index. This method effectively removed the sidereal multipath effect from the S4 index. However, this method was based on S4 and the fast varying multipath effect still cannot be identified. In addition, the multipath effect has also been characterized by generating a map of the standard deviation of CCSTDDEV (Spogli et al. 2014; D'Angelo et al. 2015). Outliers beyond 1.5 × IQR (inter quartile range) were filtered out, mitigating the multipath effect (Spogli et al. 2014). This method significantly reduced the data loss from 35-45% when applying elevation mask to 10-20%. However, since the standard deviation for each grid cell of the map was calculated from the data of a whole year, this method was not sensitive to fine-scale variations. Furthermore, this method might remove the real scintillation when attempting to remove the multipath as scintillation might also contaminate

CCSTDDEV. Recently machine learning has been used to judge whether the signal was affected by scintillation, multipath or clean. The overall accuracy of this model was 96% (Imam and Dovis 2020). However, this method had the same limitation as the methods of Olwendo et al. (2010), McCaffrey and Jayachandran (2017) and de Oliveira Nascimento Brassarote et al. (2017), where S4 was needed. In addition, only the data that was confidently labeled as multipath or scintillation was used as input for model training. In other words, data influenced by both multipath and scintillation as well as clean data were not used. This could lead to biases in the model. For most of the current methods, scintillation parameters were necessary, which could be obtained from 1 Hz data that is less significantly available than 30s data (IGS 2021). Furthermore, the hybrid event could not be identified using these methods. Basu et al. (1999) found that the rate of change of total electron content index (ROTI) could be used to detect scintillation. Several other papers (Li et al. 2020; Yang and Liu 2016; Olwendo et al. 2018; Acharya and Majumdar 2019) have also shown that ROTI is capable of characterizing scintillation to a certain extent, which is backed up by studies of the theoretical relationship based on formulae of ROTI and S4 (Carrano et al. 2019). Furthermore, Bhattacharyya et al. (2000) proposed a quantitative equation for measuring S4 based on derivative ROTI (DROTI). Though there is uncertainty in the quantitative relationship between ROTI/DROTI and S4 due to the uncertain value of an empirical parameter and Fresnel Frequency in the equation 9 of Bhattacharyya et al. (2000), it does not affect the capability of ROTI to show the occurrence of scintillation.

5.2. Materials and methods

5.2.1. Data and instrumentation

GPS data collected during 2017-09-01 to 2017-09-30 from two stations, SAO0P (46.65° W, 23.55° S) and SJCU (45.96° W, 23.21° S) both located in Sao Paulo state, Brazil were used in this chapter. This dataset was chosen because it was the only available data covering one month. MP and ROTI were respectively derived from the 1/60 Hz and 1/30 Hz data, when S4 and σ_ϕ were generated from the 50 Hz data. The moving average was applied in the ROTI calculation so that its time interval was consistent with other parameters (60s). The receivers at SAO0P and

SJCU stations are Septentrio PolaRxS 2.9.6 and 2.9.0, respectively. According to de Paula et al. (2019), a geomagnetic storm occurred on September 6-10, 2017, which caused scintillation events on the night of September 8, 2017.The two stations are located at the same latitude, r, so it is highly possible that these stations experienced the same geomagnetic activity and thus the same scintillation event. However, the multipath environments for the two stations will be different, since they are ~80 km apart. Hence the variability is more likely to be caused by the ionosphere if both stations show uniform variability and by multipath otherwise.

5.2.2. Defining outliers

We define three types of event: ionospheric scintillation, multipath or hybrid. In order to classify the type of event, it is first necessary to identify outliers for all parameters. The confidence interval is a common means of identifying outliers when a parameter is normally distributed (Zhang et al. 2012; Hamm et al. 2012). However, Acharya and Majumdar (2019) showed that log-normal distribution is most suitable for ROTI and S4. Following Barnett and Lewis (1994), a method based on the interquartile range (IQR) defined as:

$$IQR = Q_3 - Q_1 \tag{5.1}$$

where Q_3 and Q_1 are the upper and lower quartiles respectively, was used. Mild and extreme outliers were defined as values larger than the relevant threshold, defined as follows:

$$MT = Q_3 + 1.5IQR \tag{5.2}$$

$$ET = Q_3 + 3IQR \tag{5.3}$$

where MT is mild threshold and ET is extreme threshold. Since only the high values are relevant, only outliers above Q_3 were considered and not those below Q_1. MT and ET were applied for defining outliers, as suggested by Spogli et al. (2014), leading to mild and extreme outliers.

5.2.3. Methodology

Figure 5.1 shows the flowchart of the method used to analyze the event type. The first step was to classify days with and without scintillation based on S4/σ_ϕ/ROTI outliers (equations 5.4-5.6). This is an initial classification, which may be incorrect, and will be refined in subsequent steps. Then, the data on days without scintillation was used to calculate the mean, STD and CoV of MP for each satellite and generate their scatterplots. Next, the parameter values on the scintillation day, as well as two days before and after, were divided into 18 layers with 5° elevation angle between adjacent layers. The elevation layered plots were generated by plotting the mean value of each parameter for each satellite. In order to visualize the outliers in more detail the parameter value was plotted against elevation and azimuth (PEA plot, see Appendix 1). If all the parameters showed no outliers, this indicated that there was no multipath or scintillation event. If only MP1 and MP2 showed outliers, the event was labelled as multipath and if only S4, σ_ϕ, or ROTI showed outliers, the detected event was identified as scintillation. When both S4/σ_ϕ/ROTI and MP1/MP2 had outliers and if the outliers did not show a repeated pattern, the event was labelled as scintillation. In this situation, further analysis using the PEA plot was required. If any isolated outliers were detected from PEA plots, the detected event was identified as hybrid (both multipath and scintillation) and multipath otherwise. It was simpler to generate and query the elevation layered plots as compared with the PEA plots. PEA plots were used when a more detailed investigation was needed.

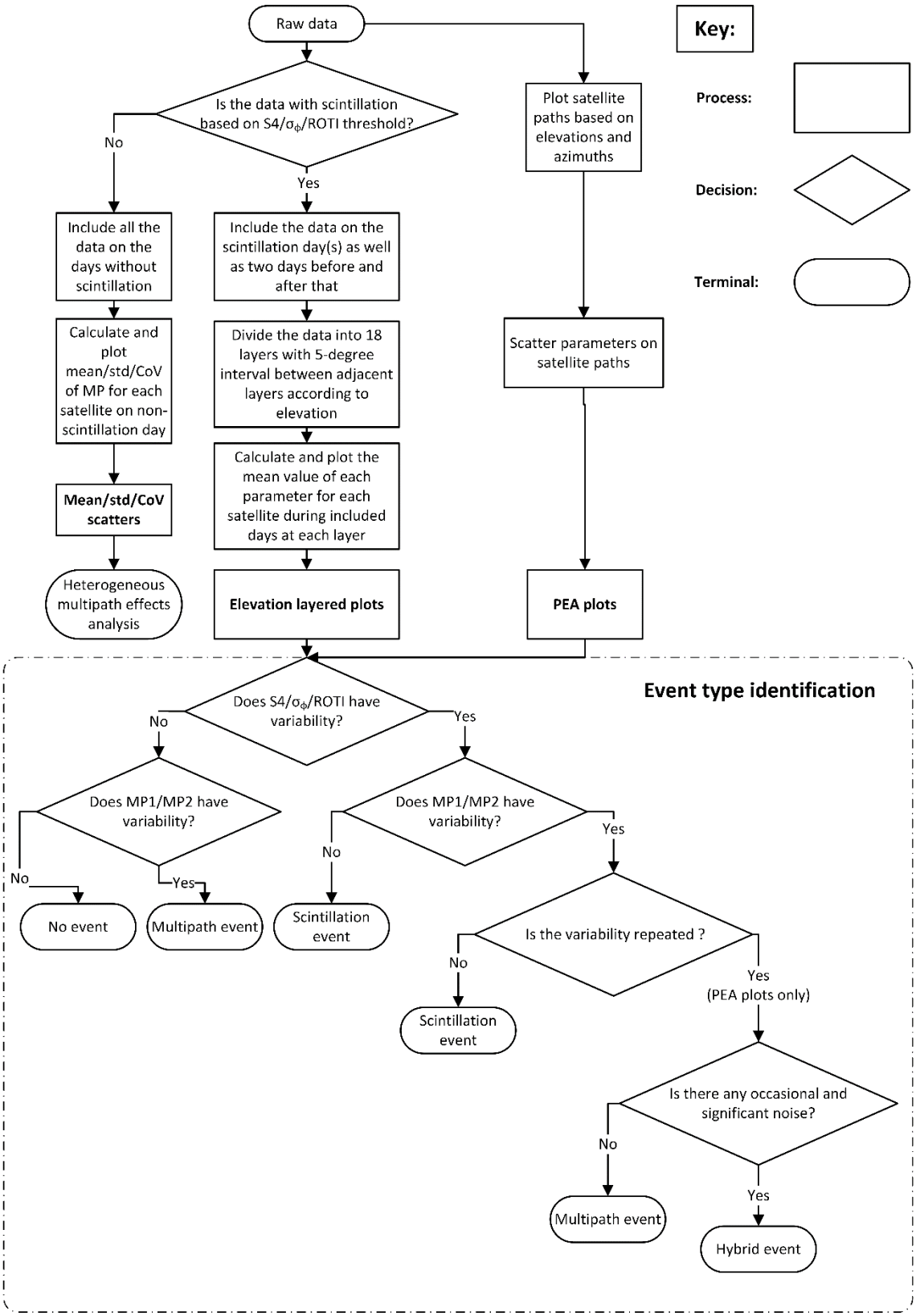

Figure 5.1 Method flow chart.

5.2.3.1. Analysis of heterogeneous multipath effects for different satellites

Satellites with different paths are differently affected by multipath. In order to evaluate this, three types of scatter-plots were made to evaluate how the multipath effect on each satellite varied on each day without scintillation. Individual days for the whole month were first classified into data with and without scintillation according to the threshold of ROTI, S4 and σ_ϕ (Olwendo et al. 2018; Vilà-Valls et al. 2020; Guo et al. 2017) shown in equations 5.4-5.6:

$$ROTI > 0.5\ TECU/min \quad 5.4$$

$$S4 > 0.3 \quad 5.5$$

$$\sigma_\phi > 0.25\ rad. \quad 5.6$$

In September 2017, 6 out of 30 days were classified as days with scintillation at SAO0P on the basis of ROTI, S4 and σ_ϕ. These were 7, 8, 9, 13, 19 and 25 September 2017. Thus, the data in the remaining 24 days without scintillation was used to generate scatterplots. First, the mean and STD of MP1/MP2 for each satellite on each day was calculated and plotted. However, the mean, m, and standard deviation, s, were not suitable for comparing the variability of parameters with different units or different ranges. Hence, the CoV was used as a unitless measure of variability.

$$CoV = \frac{s}{m} \quad 5.7$$

Note here that no cutoff was applied to scatter-plots.

5.2.3.2. Preliminary classification of the event type

The evaluation of the heterogeneous multipath effects was used to classify the event type. A preliminary evaluation was performed by comparing the behavior of the parameters at different elevations on days with and without scintillation. Thus, elevation layered comparison plots were generated. Two days before and after the scintillation event were selected for comparison. Each

parameter (S4, σ_ϕ, ROTI and MP) was divided into 18 layers with 5° interval between adjacent layers. The mean of each parameter for each satellite in each elevation layer was calculated and plotted so that the variation on scintillation days could be compared to the adjacent days without scintillation. According to Demyanov et al. (2019), there is a regular time shift between the multipath events on adjacent days, which may slightly change from one day to another. This time shift is supposed to be equal or greater than the sidereal day offset, which is typically taken to be 235.91s. However, as the graphs were plotted based on the elevation angle instead of time in this chapter, the effect of time shift was not present and considered. Thus, it was assumed that, if the outlier did not repeat every sidereal day, it was likely to be caused by scintillation rather than multipath. The MT line was also generated at each layer and for each satellite using data from the whole month. In past research, 30° was a typical value used to remove the majority of multipath effect (de Bakker and Tiberius 2017; Li et al. 2020; Yang and Liu 2016; Sreeja et al. 2011a). Thus, the multipath effect below 30° elevation was supposed to be significantly noisier than that above 30° elevation. Therefore, the analysis was divided into two parts: low and high elevation variability, which were defined as variability lower and higher than 30°, respectively.

5.2.3.3. Final classification of the event type

In order to confirm the event type and assess whether the event was hybrid, a more detailed comparison between days with and without scintillation was performed using PEA plots for the whole month. The path of each satellite was plotted based on elevation and azimuth (PEA) and the parameter value (MP, ROTI, S4, σ_ϕ) represented using a graduated symbol (a circle). The size of the circle was determined using an amplification factor, X_p. The magnitude of X_p was calculated as follows to allow comparison between different parameters:

$$X_p = round\left(\frac{m_r + s_r}{m_p + s_p}\right) \quad 5.8$$

where the mean, m, and standard deviation, s, were calculated for the whole month. The subscript p denotes the parameter, round was used to round the result to the nearest integer, r

represents the reference parameter. For the reference parameter $X_p = 1$. Any parameter could be chosen as the reference, but MP2 was used in this chapter. To compare the performance of MP1 and MP2, the X_p value for MP1 was also equal to 1. The X_p values were kept the same for both the SAO0P and SJCU stations.

Table 5.1 shows that the CoVs of all the parameters were similar, except for ROTI. This indicated that ROTI was substantially more variable than the other parameters. Therefore, the values of ROTI were investigated further. It was found that five and three ROTI values respectively from satellites G21 and G24 exceeded 60 TECU/min on 2017-09-07. Therefore, for G21 and G24 the 8 extreme values were excluded for visualizing ROTI ($ROTI_{Ex}$) and for the calculations provided in Table 5.1.

Table 5.1 Mean, STD, CoV and X_p values for parameters of SAO0P station. $ROTI_{Ex}$ is the value of ROTI after excluding 8 extreme values. The * indicates that MP2 was the reference parameter. The X_p for MP1 was chosen to be 1. Thus, the m and s of MP1 were not necessary.

Parameters	m	s	CoV	X_p
S4	0.0378	0.0289	0.7644	7
σ_ϕ	0.0262	0.0125	0.4761	11
MP1	-	-	1.0936	1
MP2*	0.2047	0.2330	1.1382	1
ROTI	0.0275	0.3798	13.7937	1
$ROTI_{Ex}$	0.0253	0.0327	1.2926	8

5.3. Results

5.3.1. Analysis of the heterogeneous multipath effects for different satellites

Figure 5.2 displays the mean, STD and CoV of MP for each satellite on each day without scintillation. The plots showed broadly similar values between satellites, although there are some important differences. In particular, some satellites showed greater variability between days and there are some outliers. Hence, it was necessary to assess each satellite individually and to set satellite-specific thresholds.

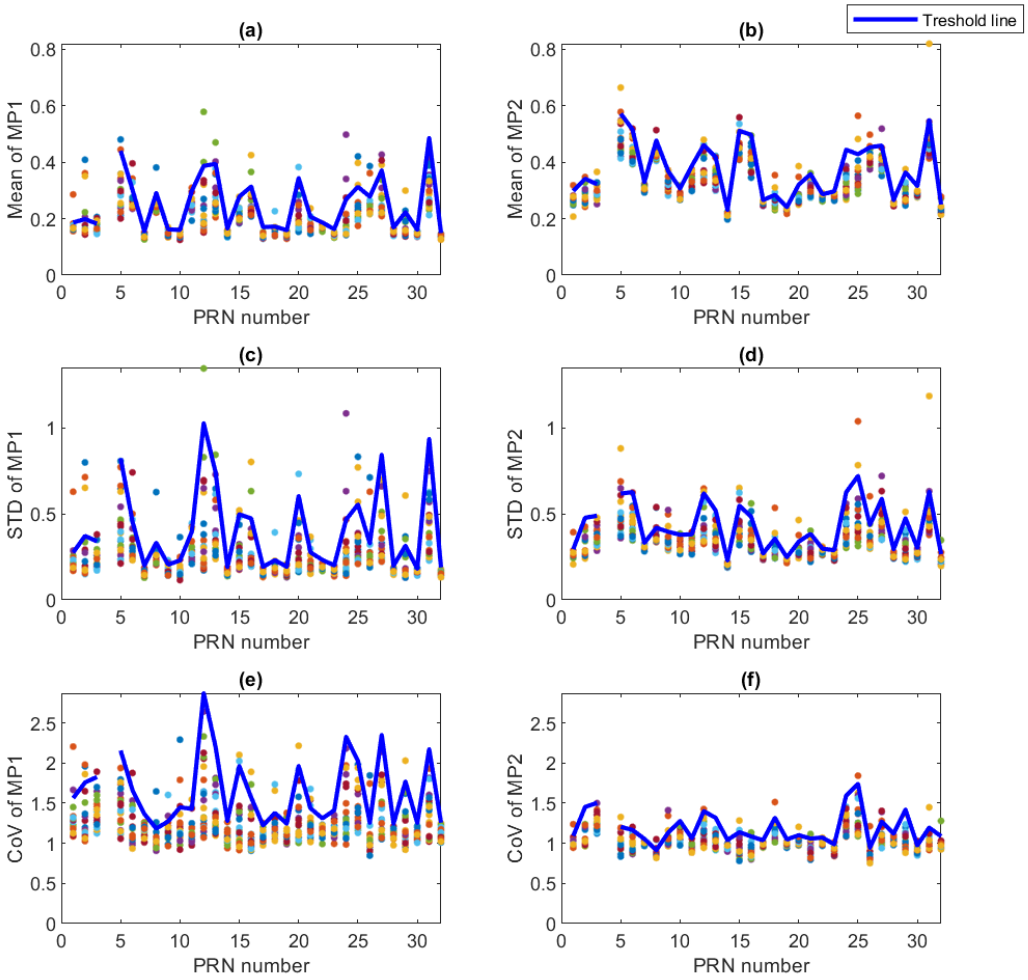

Figure 5.2 (a-b) Mean, (c-d) standard deviation and (e-f) CoV of MP on days without scintillation in September 2017 at the SAO0P station. The x-axis shows each satellite, referenced by the pseudo random noise (PRN) number. The different colored symbols indicate different days. The threshold is based on MT (equation 5.2). The mean and STD are in meters and CoV is dimensionless.

5.3.2. Preliminary distinction between scintillation and multipath events

5.3.2.1. Low elevation variability

Figure 5.3 shows the elevation layered plot of MP1, MP2, ROTI, S4 and σ_ϕ of G2 during 11-15 September 2017 at SAO0P station. This period was chosen as 13 September 2017 was classified as the day with scintillation as discussed in section 5.2.3.1. G2 was selected because parameters

showed low elevation outliers on this satellite. MP1 Figure 5.3a) showed several outliers at 10° and 15° on days without scintillation, although MP2 did not show outliers. Isolated outliers in ROTI are shown at 5° (Figure 5.3c). The mean values of S4 and σ_ϕ showed similar values on all days (Figure 5.3d, e) and did not show the effects of scintillation. Hence, by following the methodology illustrated in Figure 5.1, the variability in MP was more likely to be due to multipath. Furthermore, it has been shown by Delay et al. (2015) and Jiao and Morton (2015) that the scintillation effect on L2 is stronger than that on L1, where observations on L2 and L1 signals are used to calculate MP2 and MP1 respectively. However, the variability of MP1 is larger than that of MP2 as shown in Figure 5.3a and b, suggesting that this variability was not caused by scintillation. This supported that the event type was multipath.

Variability of MP1, attributed to the multipath effect at low elevation, only occurred on three days without scintillation and was non-periodic. This suggests that the environment at low elevations was relatively heterogeneous as compared with that at high elevation. Therefore, at low elevations, for G2, only multipath events could be identified. In other words, when scintillation was detected at low elevations, it was hard to judge whether a multipath event exists or not due to the heterogeneous and unstable environment. It should be noted that no similar phenomena were observed at high elevations for this dataset.

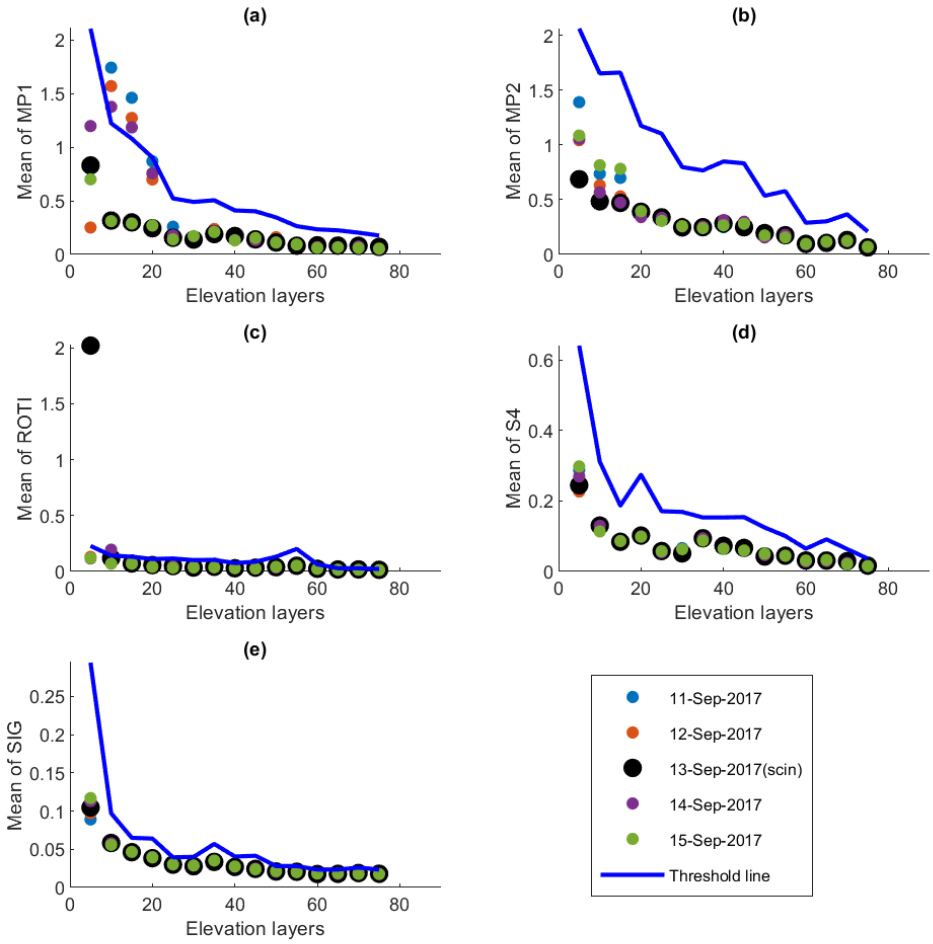

Figure 5.3 Elevation layered plots of (a) MP1, (b) MP2, (c) ROTI, (d) S4 and (e) σ_ϕ of Satellite G2 on September 11-15, 2017 at SAO0P station. MP1 and MP2 are in meters, ROTI in TECU/min, σ_ϕ in radian and S4 is dimensionless. The threshold line is the mild threshold (equation 5.2). '(scin)' after 13-Sep-2017 indicates the day with scintillation.

Figure 5.4 shows the equivalent results to Figure 5.3 but for the SJCU station. For MP1 and MP2 the results from the SJCU station showed less variability with no outliers above the mild threshold line. The patterns for ROTI, S4 and σ_ϕ were similar for both stations. As the two stations are close in longitude and latitude with similar ionospheric environment, MP of both stations should have similar variability if the outliers are caused by an ionospheric event. Thus, this further supports the conclusion that MP variability at the SAO0P station was likely to be caused by the multipath effect.

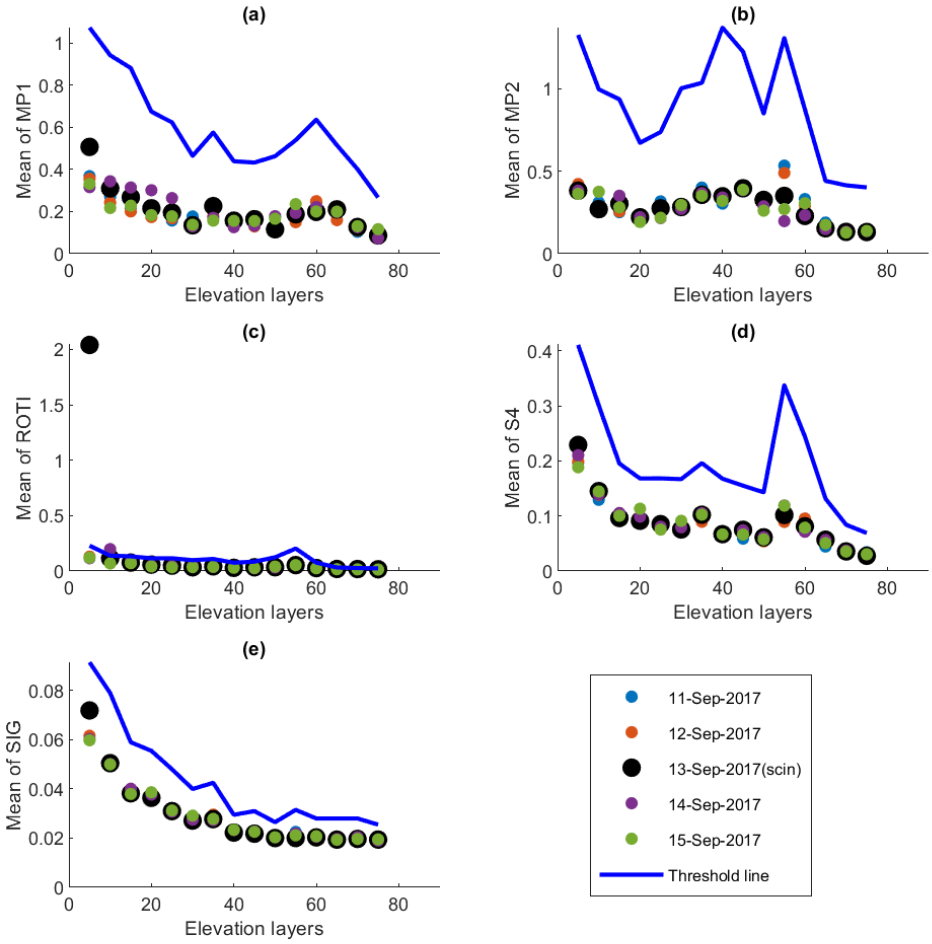

Figure 5.4 Elevation layered plot of (a) MP1, (b) MP2, (c) ROTI, (d) S4 and (e) σ_ϕ of G2 on September 11-15, 2017 at SJCU station. Units as in Figure 5.3. '(scin)' after 13-Sep-2017 indicates the day with scintillation.

Figure 5.5 shows the elevation layered plot for satellite G13 on 5-11 September 2017 at SAO0P station. As with G2 (11-15 September), variability at low elevations for MP1 and MP2 and outliers at low elevations for MP1 is observed. This period was chosen as 7-9 September 2017 was classified as the day with scintillation as discussed in section 5.2.3.1. G13 was selected because parameters showed low elevation outliers on this satellite. A single outlier for a day without scintillation for ROTI at 5° was observed, which corresponds to the case of high variability at low elevation. There is also an isolated outlier for σ_ϕ. Note here that G13 at SAO0P station was not affected by scintillation, although 2017-09-07 and 2017-09-08/09 were scintillation days according to equations 5.4-5.6

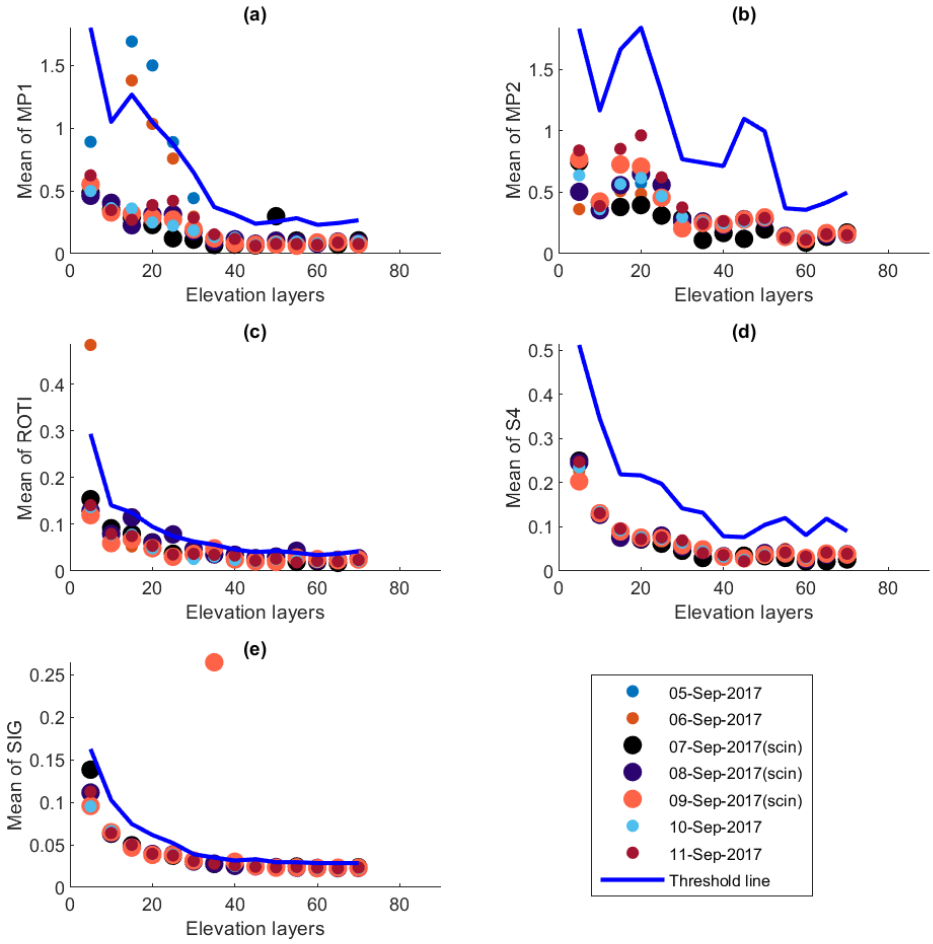

Figure 5.5 Elevation layered plot of (a) MP1, (b) MP2, (c) ROTI, (d) S4 and (e) σ_ϕ of G13 on September 5-11, 2017 at SAO0P station. Units as in Figure 5.3. '(scin)' after 7-9 September 2017 indicates the days with scintillation.

Figure 5.6 shows similar results as in Figure 5.5, but for the SJCU station. This shows broadly similar patterns for all satellites, although no outliers above the threshold line were observed for MP1. As can be observed in Figure 5.6, MP1 at SJCU station showed slight noise which was not as significant as that at SAO0P station. In addition, MP2 and S4 showed low variability while the ROTI and σ_ϕ values fluctuated in a similar fashion to those at the SAO0P station on the same days.

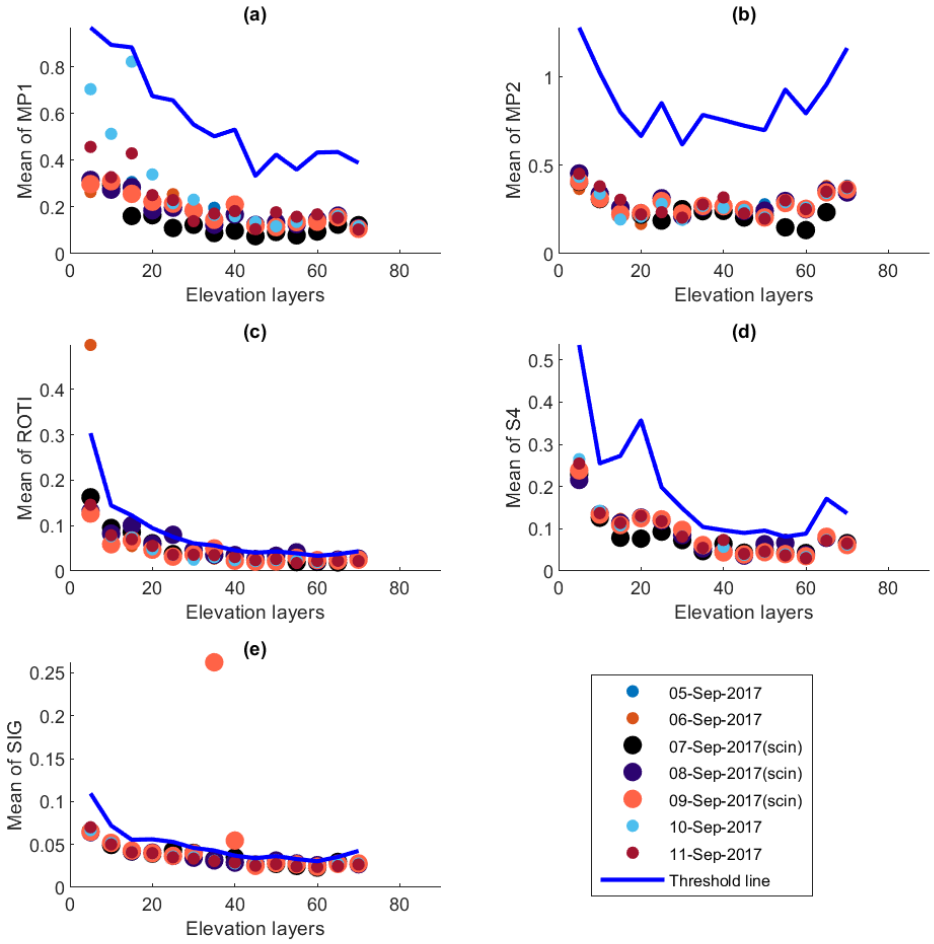

Figure 5.6 Elevation layered plot of (a) MP1, (b) MP2, (c) ROTI, (d) S4 and (e) σ_ϕ of G13 on September 5-11, 2017 at SJCU station. Units as in Figure 5.3. '(scin)' after 7-9 September 2017 indicates the days with scintillation.

5.3.2.2. High elevation variability

Figure 5.7 shows the elevation layered plots for satellite G10 on 11-15 September 2017 at the SAO0P station. This period was chosen as 13 September 2017 was classified as the day with scintillation as discussed in section 5.2.3.1. G10 was selected because parameters showed high elevation outliers on this satellite. This station shows outliers at high elevations. In particular, MP1 and MP2 showed outliers at 35° to 50° on 13 September, which was a scintillation day. However, for ROTI and σ_ϕ, no high elevation variability was observed as shown in Figure 5.7(c) & (e). Furthermore, the variability in S4 at both low and high elevations was observed clearly in Figure 5.7(d). For high elevation analysis, abnormal values of MP1/MP2 and S4 on

September 13, 2017 were not repetitive as compared with those on the other four days. By following the methodology illustrated in Figure 5.1, the high variability is more likely to be caused by scintillation events. As aforementioned, the scintillation affects L2C signal more significantly than L1CA signal (Delay et al. 2015; Jiao and Morton 2015). Moreover, the variability of MP2 is substantially larger than that of MP1, which is an opposite situation as compared with results on Figure 5.3 and Figure 5.5. Thus, it supported that the variability was more likely to be caused by scintillation.

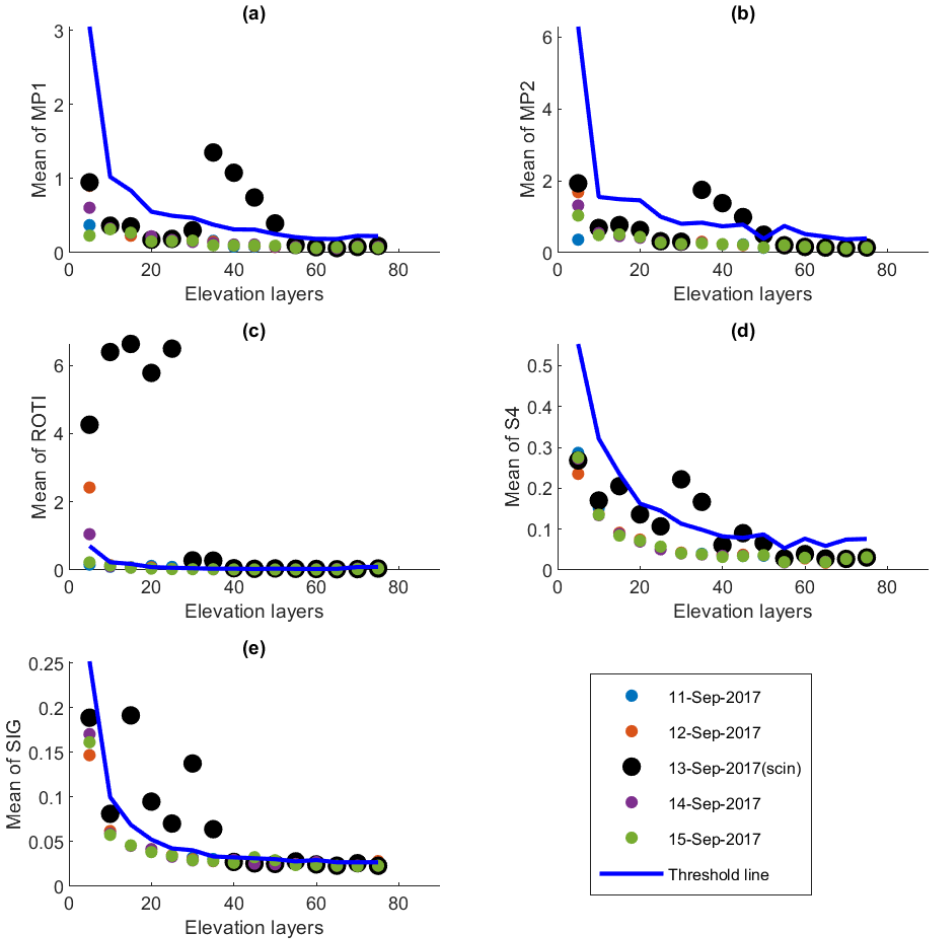

Figure 5.7 Elevation layered plot of (a) MP1, (b) MP2, (c) ROTI, (d) S4 and (e) σ_ϕ of G10 on September 11-15, 2017 at SAO0P station. Units as in Figure 5.3. '(scin)' after 13-Sep-2017 indicates the day with scintillation.

Figure 5.8 shows the result during the same period as Figure 5.6, but for the SJCU station. The patterns shown in Figure 5.7 and Figure 5.8 were broadly similar, although the outliers in S4

were more pronounced for the SJCU station. Considering that the two stations are ~80km apart, it is unlikely that they were affected by the same multipath event. We propose that the similar patterns at the two stations are likely to be attributed to scintillation events.

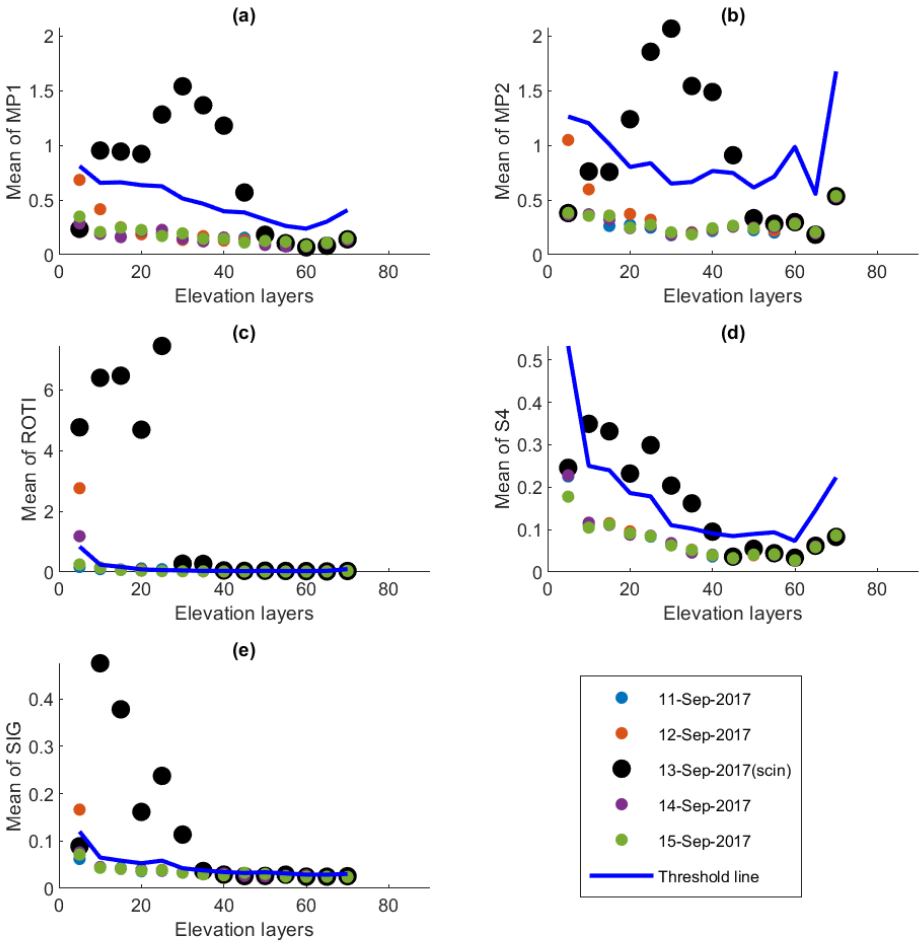

Figure 5.8 Elevation layered plot of (a) MP1, (b) MP2, (c) ROTI, (d) S4 and (e) σ_ϕ of G10 on September 11-15, 2017 at SJCU station. Units as in Figure 5.3. '(scin)' after 13-Sep-2017 indicates the day with scintillation.

Figure 5.9 shows the elevation layered plots for satellite G18 on September 5-11 2017 at the SAO0P station. This period was chosen as 7-9 September 2017 was classified as the days with scintillation as discussed in section 5.2.3.1. G18 was selected because parameters showed high elevation outliers on this satellite. It can be observed from Figure 5.9(a)-(e) that the high variability appeared at similar elevation layers for all parameters, though the peaks of MP1 and MP2 appeared at higher elevation as compared with that of ROTI, S4 and σ_ϕ. For observations

at high elevations, all the variability was not repetitive. Furthermore, the disturbance of MP2 was larger than that of MP1, which is similar to the result in Figure 5.7. This suggests that the observed variability was most probably caused by scintillation events.

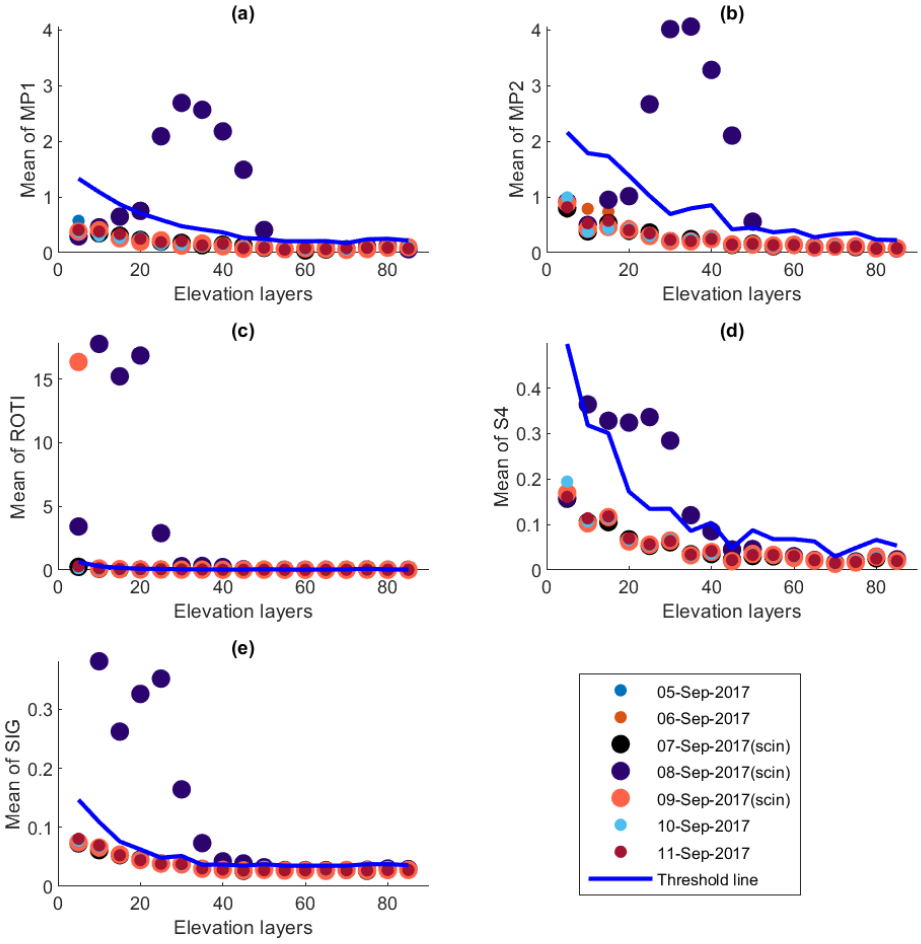

Figure 5.9 Elevation layered plot of (a) MP1, (b) MP2, (c) ROTI, (d) S4 and (e) σ_ϕ of G18 on September 5-11, 2017 at SAOOP station. Units as in Figure 5.3. '(scin)' after 7-9 September 2017 indicates the days with scintillation.

Figure 5.10 shows the elevation layered plots of MP1, MP2, ROTI, S4 and σ_ϕ of G18 on 5-11 September 2017 at the SJCU station. As shown in Figure 10, all parameters except MP2 showed similar variability to those in Figure 5.9. This comparison was similar to that between Figure 5.7 and Figure 5.8. Thus the variability is more likely to be caused by the scintillation event.

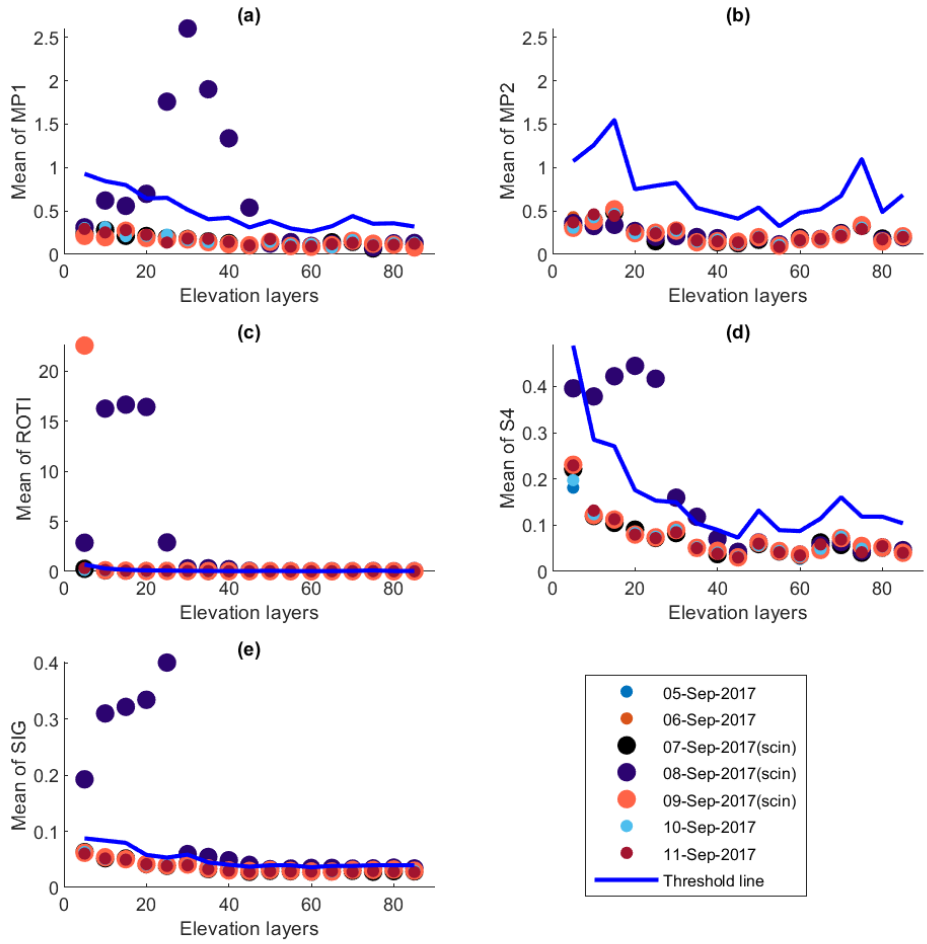

Figure 5.10 Elevation layered plot of (a) MP1, (b) MP2, (c) ROTI, (d) S4 and (e) σ_ϕ of G18 on September 5-11, 2017 at SJCU station. Units as in Figure 5.3. '(scin)' after 7-9 September 2017 indicates the days with scintillation.

5.3.3. Detailed distinction between scintillation, multipath and hybrid events

The PEA plots for each satellite at the SAO0P and SJCU stations are provided in Figures S1-S323 in Appendix 1. It could be seen in Figure S10 and S172 that variability in MP1 appeared for the satellite G10 from ~30° to 50° in elevation and 310° to 330° in azimuth on 2017-09-13 at both stations, which was in accordance with the results of MP2, ROTI, S4 and σ_ϕ shown in Figures S42/S204, S74/S236, S106/S269 and S138/S301, for SAO0P/SJCU respectively. An example was given in Figure 5.11 extracted from Figure S10 that showed the outliers on 2017-09-13. However, the variability in σ_ϕ was not as large as that observed for ROTI and S4 at both

the stations. These results reinforced those shown in Figure 5.7 and Figure 5.8 (G10). Furthermore, in the related Figures (S10/S172, S42/S204, S74/S236, S106/S269 and S138/S301), another significant variability could be seen for all parameters on G10 from around 30° to 40° in elevation and 320° to 330° in azimuth on 2017-09-08 at both stations. By comparing the results on 2017-09-08 and 2017-09-13 at the SAO0P station, the MP2 on the former day fluctuated more strongly than that on the latter day while S4 and σ_ϕ showed the opposite behavior, which suggested that the larger variability of MP was not necessarily caused by stronger scintillation.

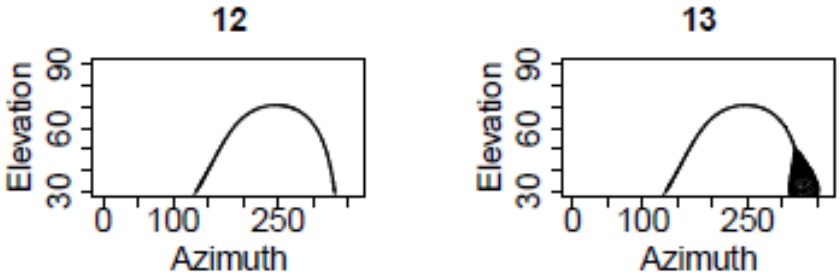

Figure 5.11 Example extracted from Figure S10: PEA plots of MP1 of G10 on September 12-13, 2017 at SAO0P station.

Similarly, as shown in Figures S18/S180, S50/S212, S82/S244, S114/S277 and S146/S309, all the parameters except MP2 at SJCU station displayed variability for G18 at the same position on 2017-09-08, which matched the result shown in Figure 5.9 and Figure 5.10. However, ROTI, S4 and σ_ϕ also displayed variability on 2017-09-13 for G18 when MP1 and MP2 did not. Moreover, as it could be seen in Figures S97/S259 and S151/S312 that ROTI and σ_ϕ showed a single extreme value at the same position of G21 on 2017 -09-07, when MP1, MP2 and S4 did not. This supported the conclusion of Li et al. (2020) that ROTI was more related to σ_ϕ. For the same satellite (S85/S247, S119/S280 and S151/S312), ROTI, S4 and σ_ϕ also showed variability on 2017-09-08 and 2017-09-13 though the intensity of ROTI was larger than for the other two. As for MP, MP1 and MP2 showed no variability in Figure S21/S183 and S53/S215. The same feature could be seen in Figures S24/S186, S56/S218, S88/S250, S122/S283 and S154/S315, where ROTI, S4 and σ_ϕ showed variability when MP did not, with the exception of MP2 at the SJCU station. This indicated that scintillation did not always influence MP and it was possible

that scintillation with certain characteristics led to variability in MP, which has been discussed in Section 3.3.5.1. It should be noted that the events reported in this chapter were non-repetitive and related to certain satellites on specific days (i.e. non-repetitive) and most of this occasional variability could be observed at both stations. Therefore, it was more appropriate to classify these events as scintillation.

Furthermore, a variety of multipath events could be seen on PEA plots. For example, in Figures S40 and S106, both MP2 and S4 showed repeated variability on G8 at SAO0P station during the whole month and there was no significant and occasional noise, which matched with the standard criteria of multipath event shown in the methodology (Figure 5.1). The same event could also be observed at SAO0P station on G2, G6, G7, etc.

5.4. Discussion

Data for September 2017 from the SAO0P and SJCU stations were used to characterize the station surroundings so that scintillation events could be distinguished from multipath. We developed a systematic methodology to achieve this. First, the mean, standard deviation and CoV scatter-plots of MP on days without scintillation were used to characterize the multipath environment of each satellite Figure 5.2. The key here was that each satellite could be characterized. Furthermore, the STD and CoV of MP1 were more variable than that of MP2. According to Delay et al. (2015) and Jiao and Morton (2015), scintillation affects the L2 signal more substantially than L1 signal. Thus, the variability of MP1 shown in Figure 5.3 was more likely to be caused by multipath instead of scintillation. Hence we propose that MP1 and MP2 should be used in combination to distinguish multipath and scintillation events. According to Demyanov et al. (2020), in the Septentrio receiver used in this paper, the L2P signal is tracked based on the L1-aiding technique while the L2C signal is not, which may lead to incorrect observations on the ionospheric effect of radio propagation due to the artificial connection between L1CA and L2P signals. Thus, it is noteworthy that the conclusion of Delay et al. (2015) and Jiao and Morton (2015) is valid only when L2C signals rather than L2P signals is used.

Following the analysis of heterogeneous multipath environments for different satellites,

elevation layered plots and PEA plots were the two primary components in the methodology to distinguish scintillation events from multipath. At the SAO0P station, MP1 showed high variability on satellites G2 (Figure 5.3) and G13 (Figure 5.5) at low elevations, whereas S4 and σ_ϕ showed no variability during 11-15 September 2017 and 5-11 September 2017 respectively. Following our methodology, this suggested that the variability was caused by multipath. This was corroborated when considering the equivalent results for the SJCU station (Figure 5.4 and Figure 5.6), where all the variability in MP1 and MP2 was below the threshold. ROTI showed some abnormal values and an outlier in Figure 5.3(c) and Figure 5.5(c), which could be caused by rapidly varying multipath effects or other types of interference as no scintillation was detected according to S4 and σ_ϕ. This conclusion is backed up by the results for the SJCU station (Figure 5.4(c) and Figure 5.6(c)) since the two stations, with different multipath environments, share the same ROTI variability. Further, MP1 fluctuated more intensely than MP2 at both stations (Figure 5.3 and Figure 5.4). This further suggests that the variability was caused by multipath (Delay et al. 2015; Jiao and Morton 2015). However, MP1 and MP2 in Figure 5.3 (a)-(b) showed variability on 2017-09-11, 12 and 14 that did not repeat on 2017-09-13 and 15 indicating that the environment at low elevations was unstable. This made it difficult to distinguish event types because the periodicity of multipath may have been obscured by the unstable environment. Thus, at low elevations, the events with only one of MP and scintillation could be distinguished. However, multipath usually affects satellites at low elevations, which makes it difficult to distinguish multipath from scintillation at low elevations when the hybrid event occurs and this is the main weakness of our methodology.

As shown in Figure 5.7 and Figure 5.8, the variability of MP and S4 on G10 appeared at both high and low elevations on 2017-09-13 while those of ROTI and σ_ϕ existed only at low elevation layers at both the SAO0P and SJCU stations. For the high elevation part, MP and S4 showed variability on 2017-09-13 that was not repeated on the other four days and the variability of MP2 was more intense than that of MP1 at theSAO0P station, which suggests that the variability was caused by scintillation (Delay et al. 2015; Jiao and Morton 2015). More details can be observed in the PEA plots as shown in Figures S10/S172, S42/S204, S74/S236, S106/S269 and S138/S301, where MP, ROTI, S4 and σ_ϕ, showed the variability at the same

locations, although σ_ϕ fluctuated less. It can clearly be observed that all the parameters showed variability only on 2017-09-13. Thus, the detected event was identified as scintillation. Furthermore, another event was observed in Figure 5.9 and Figure 5.10 that was similar to the event in Figure 5.7 and Figure 5.8. All the parameters, except MP2 at SJCU station showed high variability at both high and low elevations for G18 on September 8, 2017, though the variability of MP was larger at high elevations. Moreover, MP2 fluctuated more strongly than MP1. Similar results were observed at stations SAO0P/SJCU in Figures S18/S180, S50/S212, S82/S244, S114/S277 and S146/S309, where all the parameters except MP2 at the SJCU station showed variability on G18 at same elevation and azimuth, which was not periodic. Thus, following our methodology, the detected event was also identified as scintillation. Another similar scintillation event was observed for G10 on 2017-09-08 in Figures S10/S172, S42/S204, S74/S236, S106/S269 and S138/S301. In addition, there were several scintillation events that could not be detected by MP, such as variability of G20 on 2017-09-08 in Figures S84/S246, S118/S279 and S150/S311, G21 on 2017-09-07, 2017-09-08 and 2017-09-13 in Figures S85&S97/S247&S259, S119/S280 and S151/S312, G24 on 2017-09-07 in Figures S88/S250, S122/S283 and S154/S315. There were also scintillation events that could not be detected by both MP and ROTI, such as the variability of G20 on 2017-09-07 in Figure S118 and S150/S311. This indicates that scintillation does not always influence MP and ROTI and only scintillation with certain characteristics can lead to MP and ROTI variability. This will be the focus of future work.

In addition to scintillation events, a variety of multipath events could clearly be observed on G2, G6, G7, G8, G11, G17, G19, G25 and G29 respectively in Figure S100, S104, S105, S106, S109, S115, S117, S123 and S127. The fluctuations on MP and S4 were repeated for the whole month and there were no occasional outliers. Thus, it is highly possible that these events were multipath. Furthermore, several hybrid events were observed that could only be identified with PEA plots. For example, as shown in Figure S279, both repeated variability during the whole month and an occasional noise at 30° in elevation and 10° in azimuth on 2017-09-08 could be seen at the SJCU station. The same event was shown in Figure S163, S195 and S260, where both repeated and occasional variability could be observed at 70° in elevation and 250° in

azimuth on 2017-09-01 and 2017-09-04. Following our methodology, this conforms to the conditions for a hybrid event.

The purpose of this chapter is to distinguish multipath events from scintillation events. This has been partially realized in past research. Olwendo et al. (2010) tried to use S4 values above 20° in elevation to extrapolate towards low elevation so that the superimposed part caused by multipath events could be computed and mitigated by comparing the observed and extrapolated S4 values at low elevations. The main advantage of this method is that it can distinguish multipath and ionospheric scintillation at low elevations, which is only partially achieved using the methodology described in this chapter. However, S4 at high elevations can also be affected by multipath. Thus, the extrapolation may not be accurate. Furthermore, our methodology does not use the scintillation parameters S4 and σ_ϕ and uses ROTI as a proxy for the scintillation parameters. This is of key importance because S4 and σ_ϕ are less available over the globe than ROTI. Moreover, our methodology was able to distinguish multipath and ionospheric scintillation during strong scintillation events. McCaffrey and Jayachandran (2017) managed to identify scintillation and multipath events through subtracting the mean S4 of two adjacent sidereal days from the S4 during the event period. It was an easy-to-use method. However, S4 was needed in this method and the hybrid event could not be identified, where these issues were solved in this chapter. Spogli et al. (2014) also proposed to use the histogram of CCSTDDEV standard deviation and IQR to remove outliers, which also avoids losing a major part of data at low elevation. However, Spogli et al. (2014) used data of a whole year to generate the standard deviation of CCSTDDEV which reduced the sensitivity of detecting multipath variation. In contrast, the characteristic of each satellite on each day could be observed on the elevation layered plots and PEA plots, so that it can be more flexible to apply the data removal according to the behavior of the satellite on the specific day. Moreover, the method proposed by Spogli et al. (2014) may also mistakenly remove scintillation data as CCSTDDEV could be contaminated by scintillation. In addition, Imam and Dovis (2020) applied machine learning to classify the label of data into multipath, scintillation and clean, which utilized data labelled as only one of multipath and scintillation. In other words, hybrid events cannot be distinguished with the method of Imam and Dovis (2020), whereas this was achievable using the methodology

proposed in this chapter. Scintillation parameters are also necessary in the machine learning method, whereas these are not required for our methodology.

The methodology for distinguishing between multipath and scintillation proposed in this chapter primarily utilizes the repeatability and rarity of multipath and scintillation events, respectively. Thus, repeated and occasional variability were assumed to be caused by multipath and scintillation effects, separately. Then, the identification of event types could be achieved by following the decision steps shown in Figure 5.1. S4 and σ_ϕ are not essential for our methodology as ROTI can represent a part of scintillation occurrences. However, the relationship between scintillation and ROTI is not always clear. Therefore, using ROTI only can contribute to failed identification of scintillation. However, the fact that this methodology is not reliant on scintillation parameters is still one of the most significant advantages as compared with the aforementioned methods. A further advantage is that scintillation and multipath could be distinguished even when both scintillation and multipath events occurred simultaneously at high elevations. This has not been achieved previously. However, a deficiency of the methodology is that the hybrid events at low elevations could not be identified.

5.5. Conclusions

The effect of multipath and scintillation on each other and the method for distinguishing between them have been researched previously; however, there is still potential for improving all these methods. In particular, the hybrid events could be identified and scintillation parameters were necessary in those methods. The novel proposed methodology here is feasible with numerous advantages as compared with past methods. The primary novelty of the methodology in this chapter is that all of multipath, scintillation and hybrid events can be distinguished at high elevation and it demonstrates that scintillation can also lead to false alarm of MP. Previously it was only discussed that multipath can result in the inflation of scintillation parameters.

GPS data of two stations located in Sao Paulo State, Brazil were applied for characterizing the station environment, where SAO0P was the primary station and SJCU was the reference station.

In this chapter, it was assumed that the multipath effect at high elevations was stable and periodic. Two main types of graphs were generated, elevation layered plots and PEA plots. At low elevation, the periodicity of multipath was covered by the unstable environment, which is the fundamental assumption for the event identification. Thus, it was still not possible to differentiate between multipath and scintillation events at low elevations with a single station. However, this was possible when using a second, reference station close to the primary station, although the hybrid event still could not be distinguished. The results strongly suggest that the variability of all parameters for G10 on 2017-09-13 and G18 on 2017-09-08 at the SAO0P station were caused by ionospheric scintillation. Additionally, it is highly possible that the visualized repeated variability with and without irregular significant variability were caused by hybrid and multipath events, respectively. Moreover, scintillation parameters were not necessary in this methodology, and therefore can be realized with a standard geodetic receiver. Therefore, it significantly increases the practical applicability of our methodology. Finally, the addition of the reference station strengthened the conclusion.

6. Mitigation of scintillation effects on PPP

This chapter focused on mitigating scintillation effects on positioning outputs. The effects of scintillation have been discussed in section 3.2.3, which showed that the scintillation is one of the most urgent issues to be addressed in order to obtain more reliable GNSS positioning services. In addition, it has also been discussed in section 3.2.3 that Precise Point Positioning (PPP) is more sensitive to scintillations in terms of loss of lock than real-time kinematic (RTK). Thus, PPP is selected as the positioning technique instead of RTK in this chapter. Furthermore, existing methods to mitigate scintillation effects have been comprehensively introduced in section 3.2.4, which significantly improved the accuracy, reliability and robustness of positioning. However, most of these methods employed scintillation parameters that can be generated from data with a frequency of at least 1 Hz (Nguyen et al. 2019; Luo et al. 2020). Thus, rate of change of Total Electron Content Index (ROTI) and multipath parameter (MP) that can be computed from 30s data were proposed to characterize scintillation and the spatiotemporal relationship between ROTI, MP and S4, σ_ϕ has been investigated in Chapter 4. Both ROTI and MP can be generated using the low-rate data, which considerably increases the availability of data with the support of global GNSS agencies such as International GNSS Service (IGS). Based on past methods, we proposed three strategies for improving the PPP positioning quality with MP and ROTI values:

1) Remove satellite with MP/ROTI values exceeding the threshold;
2) Remove observation with MP/ROTI values exceeding the threshold;
3) Weight the measurement noise matrix of Kalman filter (KF) using MP/ROTI values.

Herein, in order to evaluate the effectiveness of MP and ROTI, the S4 and σ_ϕ values were also input into the three strategies for comparison.

6.1. Materials and methods

6.1.1. Data and instrumentation

Data of 75 days (including 15, 30 and 30 days from SNA0P, SAO0P and SJCU stations, respectively) used in this chapter were collected from three stations, SNA0P (2.84° W, 71.67° S) located in Antarctica, SAO0P (46.65° W, 23.55° S) and SJCU (45.96° W, 23.21° S) located in Sao Paulo, where the receiver type at SNA0P and SJCU station is Septentrio PolaRxS 2.9.0 and that at SAO0P station is Septentrio PolaRxS 2.9.6. Herein, data of 14 days (including 7, 3 and 4 days from SNA0P, SAO0P and SJCU stations, respectively) with scintillation was used in the PPP improvement experiment and all 75 days' data was used to generate MT and ET as introduced in Chapter 5, which was applied as the threshold for defining outliers in the observation removal strategy. Days with and without scintillation at each station were listed in Table 6.1. In addition, one day's data without scintillation was used to estimate the convergence time of the PPP software introduced in the section 6.1.2 . The data on 2016-05-29 at SNA0P was selected in this chapter. MP and ROTI were respectively derived from the 1/60 Hz and 1/30 Hz data, when S4 and σ_{ϕ} with a time interval of 1 minute were generated from the 50 Hz data. The moving average was applied in ROTI calculation so that its time interval was consistent with other parameters.

Table 6.1 The distribution of days with and without scintillation at each station.

Station	Days with scintillation	Days without scintillation
SNA0P	2016/01/20, 2016/02/03, 2016/02/08, 2016/05/19, 2016/05/29, 2016/07/18, 2016/10/11, 2016/10/31	2016/02/18, 2016/04/02, 2016/04/13, 2016/05/09, 2016/06/06, 2016/07/28, 2016/10/13,
SAO0P	2017/09/07, 2017/09/08, 2017/09/13	2017/09/01-2017/09/06, 2017/09/09-2017/09/12, 2017/09/14-2017/09/30
SJCU	2017/09/04, 2017/09/07, 2017/09/08, 2017/09/13	2017/09/01-2017/09/03, 2017/09/05-2017/09/06, 2017/09/09-2017/09/12, 2017/09/14-2017/09/30

6.1.2. Software

PPPH is a freely available MATLAB-based software developed and by Bahadur and Nohutcu (2018). It has also been validated by Bahadur and Nohutcu (2018) that the behavior of PPPH is comparable to that of another PPP software namely GPS Analysis and Positioning Software (GAPS-http://gaps.gge.unb.ca/ (2021-10-20 accessed)). Considering that the code of PPPH is freely available and open to user's preferences at all processing steps, PPPH was applied to modify the positioning algorithm and obtain the PPP results in this chapter. MATLAB version 2018a was applied to run PPPH and edit the code.

6.1.3. Methodology

Before the experiment on scintillation mitigation, the convergence time of PPPH on a day without scintillation was estimated using the data on 2017-09-01 at SAO0P station, 2017-09-01 at SJCU station and 2016-05-29 at SNA0P station. The convergence was defined by An et al. (2020) as the positioning accuracy reaching a specific level without leaving this level, which typically refers to 0.1 m for the Up component. Thus, this defintion of convergence was applied in this chapter. Figure 6.1 shows the flowchart of the method used to mitigate scintillation effects. First, the data on scintillation day was input, where the scintillation days could be determined with the method introduced in Figure 5.1. All the data was applied with an elevation mask of 10°. Then, the first strategy was conducted, where the satellite with the maximum value of each reference parameter was removed. As there were five parameters (MP1, MP2, ROTI, S4 and σ_ϕ), this step was repeated five times in order to compare the effectiveness of different parameters. It shoud be noted that S4 is not high in the antarctica station SNA0P. Thus, S4 was not applied to SNA0P station in the satellite and observation removal strategies. After that, the processed and original data was input into PPPH to obtain the height and 3D time series outputs. Based on the PPP outputs, root mean square error (RMSE) of both original and processed data during the period affected by scintillation as well as corresponding improvement rates could be calculated. If the scintillation occurs at the beginning of the day, the RMSE is calculated after the convergence period. When computing RMSE, a reference coordinate should be input. In this thesis, the Natural Resources Canada's Canadian Spatial Reference System (CSRS) PPP was

used to generate the reference coordinate by inputting the Receiver Independent Exchange (RINEX) file on a day without scintillation, which is an extensively-used online PPP post-processing software (Mireault et al. 2008). Moreover, the geometric dillution of precision (GDOP) was generated to invesitgate the change of position and clock quality of satellites before and after satellites or obserations were removed, which was calculated with the position of each visible satellite relative to that of the receiver and it started with a fraction of the design matrix H shown in equation 2.35 (Spilker 1996):

$$G = \begin{bmatrix} (x_0 - x^1)/\rho_0^1 & (y_0 - y^1/\rho_0^1) & (z_0 - z^1)/\rho_0^1 & c \\ \vdots & \vdots & \vdots & \vdots \\ (x_0 - x^g)/\rho_0^g & (y_0 - y^g)/\rho_0^g & (z_0 - z^g)/\rho_0^g & c \end{bmatrix} \quad 6.1$$

where G is the fraction that contains the information of position and clock of satellites. Then, GDOP is calcualted with the covariance of G:

$$GDOP = \sqrt{\sigma_x^2 + \sigma_y^2 + \sigma_z^2 + \sigma_t^2} = \sqrt{trace((G^T G)^{-1})} \quad 6.2$$

where σ_x, σ_y, σ_z and σ_t are the RMSEs of the estimated receiver coordinates and clock, respectively, and trace is the sum of the matrix dagonal. When satellites are far apart, the geometry is regarded to be strong and low DOP values can be obtained, thus, with a higher probability of accuracy. Typically, the geometric quality is reliable and acceptable with a DOP value less than 5 and 10, respectively (Lulu et al. 2020). To observe the variation in the small values of GDOP, GDOP values larger than 30 are set to 30.

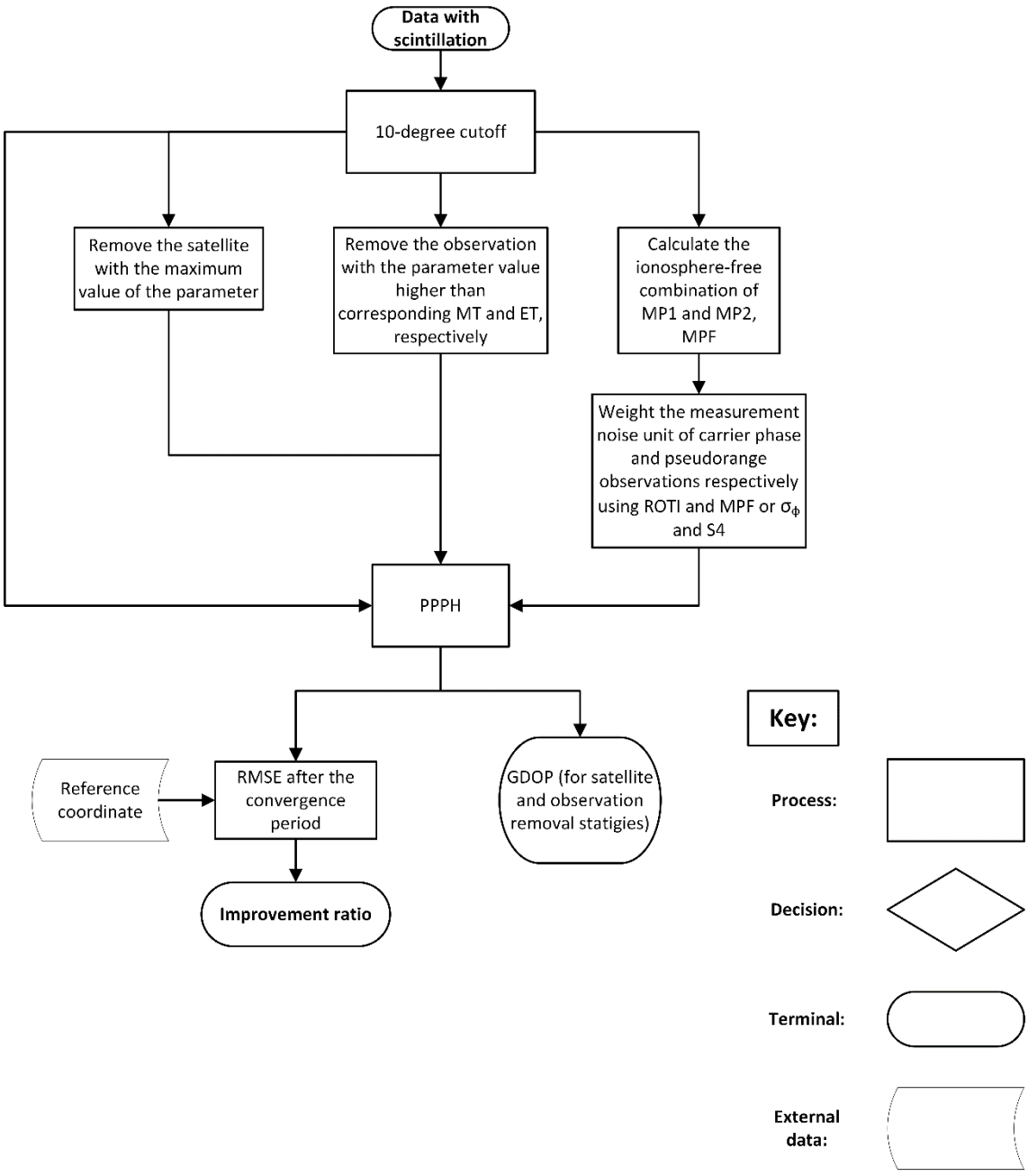

Figure 6.1 Method flow chart

The second strategy employed both mild threshold (MT) and extreme threshold (ET) (respectively defined in equations 5.2 and 5.3) as thresholds for defining outliers for comparison, where the observations with parameter values exceeding the threshold were removed. As different parameters may reflect different periods of data influenced by scintillation (Li et al. 2020), a series of permutations and combinations of parameters were used in observation removals so that the optimal combination could be determined. Standard (MP

and ROTI) and scintillation (S4 and σ_ϕ) parameters worked separately in order for comparison. Take scintillation parameters as an example, there were 3 combinations: 1) S4; 2) σ_ϕ; 3) S4 and σ_ϕ. Since there might be outliers in σ_ϕ that were not in S4, the combination of S4 and σ_ϕ could cover more outliers, and more outlier removals might lead to more accurate results. Similarly, there were 7 combinations of standard parameters. It should be noted that the same idea was not applied to the satellite removal because excessive satellite removals might result in complete failure of the positioning algorithm when the number of tracked satellites was less than four. The same procedures as satellite removal were repeated for observation removal after inputting into PPPH.

An additional step in the third strategy was to calculate the ionosphere-free (IF) combiniation of MP1 and MP2 (MPF) that was used to down-weight the multipath effect as proposed by Mohammed (2017). Though the primary ionospheric error in MPF was mitigated through IF combination, the cycle slip and corresponding IF ambiguity caused by scintillation could still affect MPF. As suggested by Roberts (2019), it is possible that only one of carrier phase and pseudorange observations is affected by scintillation, where the carrier phase is more susceptible to scintillation (Roberts et al. 2019). On the contrary, the effect of multipath on pseudorange observations is considerably greater than that on carrier phase observations. Furthermore, MPF was used mainly to characterize multipath, but also to describe scintillation and ROTI was used mainly to characterize ionospheric activity. Based on these propositions, MPF was applied to weight the IF combination of pseudorange observation and ROTI was applied to weight IF combination of carrier phase observation in PPP, which could achieve the best improvement as compared with other weighting strategies. In addition, S4 and σ_ϕ were respectively used to weight pseudorange and carrier phase as S4 was calculated based on signal intensity and σ_ϕ was obtained from signal phase, which in turn were the influence factors respectively of pseudorange and carrier phase. In Kalman filter (KF), the weights of observations were dependent on the measurement error covariance matrix R introduced in section 2.2.3.1. Assume that the numbers of pseudorange and carrier phase observations are both n. Thus, R could be initiated with an $2n$-by-$2n$ identity matrix as below (Axelrad and Brown 1996):

$$R = \begin{bmatrix} 1 & & \\ & \ddots & \\ & & 1 \end{bmatrix}_{2n\times 2n} \tag{6.3}$$

Then, an initial weight dependent on the *a priori* standard deviation (STD) of measurements was multiplied to each value on the diagonal of R (Axelrad and Brown 1996):

$$R = \begin{bmatrix} P_{w,0} & & & & \\ & L_{w,0} & & & \\ & & \ddots & & \\ & & & P_{w,0} & \\ & & & & L_{w,0} \end{bmatrix}_{2n\times 2n} \tag{6.4}$$

$$P_{w,0} = SD_{0,P}^2 \cdot (\frac{f_1^2}{f_1^2 - f_2^2})^2 \tag{6.5}$$

$$L_{w,0} = SD_{0,L}^2 \cdot (\frac{f_1^2}{f_1^2 - f_2^2})^2 \tag{6.6}$$

where $SD_{0,P}$ and $SD_{0,L}$ are the *a priori* STDs of code and phase measurements respectively, typically 3m and 0.03m, respectively (Axelrad and Brown 1996; Zhang et al. 2020); $P_{w,0}$ and $L_{w,0}$ separately indicate the initial weight for code and phase measurements. After that, a weight method dependent on satellite elevations is typically used like equation 2.56:

$$R = \begin{bmatrix} P_w & & & & \\ & L_w & & & \\ & & \ddots & & \\ & & & P_w & \\ & & & & L_w \end{bmatrix}_{2n\times 2n} \tag{6.7}$$

$$P_w = P_{w,0} \cdot \frac{1.001}{\sqrt{0.002001 + sin^2(ele)}} \tag{6.8}$$

$$L_w = L_{w,0} \cdot \frac{1.001}{\sqrt{0.002001 + sin^2(ele)}}. \tag{6.9}$$

Next, it was proposed in this chapter that the code and phase measurements should be respectively weighted by MPF and ROTI or S4 and σ_ϕ for down-weighting the scintillation

effect:

$$R = \begin{bmatrix} P_{w,scin} & & & \\ & L_{w,scin} & & \\ & & \ddots & \\ & & & P_{w,scin} \\ & & & & L_{w,scin} \end{bmatrix}_{2n \times 2n} \quad 6.10$$

$$P_{w,scin} = P_w \cdot MPF \text{ or } P_{w,scin} = P_w \cdot S4 \quad 6.11$$

$$L_{w,scin} = L_w \cdot ROTI \text{ or } L_{w,scin} = L_w \cdot \sigma_\phi \quad 6.12$$

where $P_{w,scin}$ and $L_{w,scin}$ are the weights for down-weighting the scintillation effect respectively on code and phase measurements and the proposal of these two weights is the primary novelty in the weight strategy proposed in this chapter. The linear combination in equations 6.11 and 6.12 that parameters were directly multiplied to P_w and L_w was selected through a series of tests. The original, square, square root and normalized values of parameters were tested, where the highest effectiveness was obtained by applying the original values. After the weighting process, the same procedures as previous strategy were repeated for the weight strategy after inputting into PPPH.

6.2. Results

There were results of 14 days with scintillation used in the PPP improvement experiment. Since excessive graphs were generated from all 14-day data, graphs on 2017-09-13 at SAO0P station were shown as an example for visualization in section 6.2.1 and the results on all the days were statistically tabulated and analyzed in section 6.2.2. In addition, all the strategies were also applied to the data on 2017-09-01 at SAO0P station to demonstrate for a day without scintillation in section 6.2.2.

6.2.1. Visualization example

The convergence time was estimated using the scintillation-free data on 2016-05-29 at SNA0P in section 6.2.1.1. The relationship between standard and scintillation parameters on 2017-09-13 at SAO0P station has already been investigated in Chapter 4, where the scintillation occurred

during the first three hours. In section 6.2.1.2, RMSE and GDOP changes of PPP positioning outputs before and after removing satellites with the strongest scintillation were presented. In section 6.2.1.3, because of excessive combinations, PPP outputs of 4 out of 7 combinations of standard parameters in the observation removal strategy based on MT were displayed as an example. The results of other combinations were presented in the statistical result section (6.2.2). In section 6.2.1.4, the RMSE changes of PPP outputs before and after weighting observations based on scintillation and standard parameters were shown.

6.2.1.1. Convergence time estimation

The height error variation on 2017-09-01 at SAO0P station, 2017-09-01 at SJCU station and 2016-05-29 at SNA0P station can be observed in Figure 6.2. According to the definition of convergence introduced at section 6.1.3, the convergence time at all three stations is around 30 minutes, where the height estimate reaches to the accuracy of 0.1 m without leaving. Thus, the convergence period of 30 minutes was applied for RMSE computation in the following results.

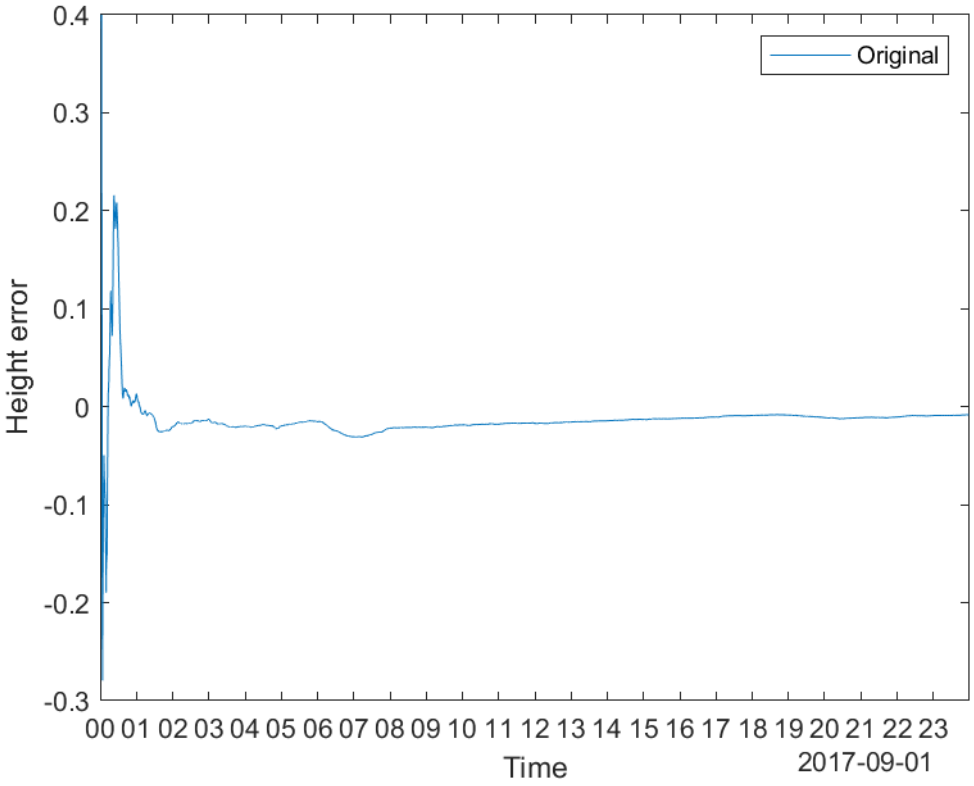
Original
Height error
0.4
0.3
0.2
0.1
0
-0.1
-0.2
-0.3
00 01 02 03 04 05 06 07 08 09 10 11 12 13 14 15 16 17 18 19 20 21 22 23
Time
2017-09-01

(a)

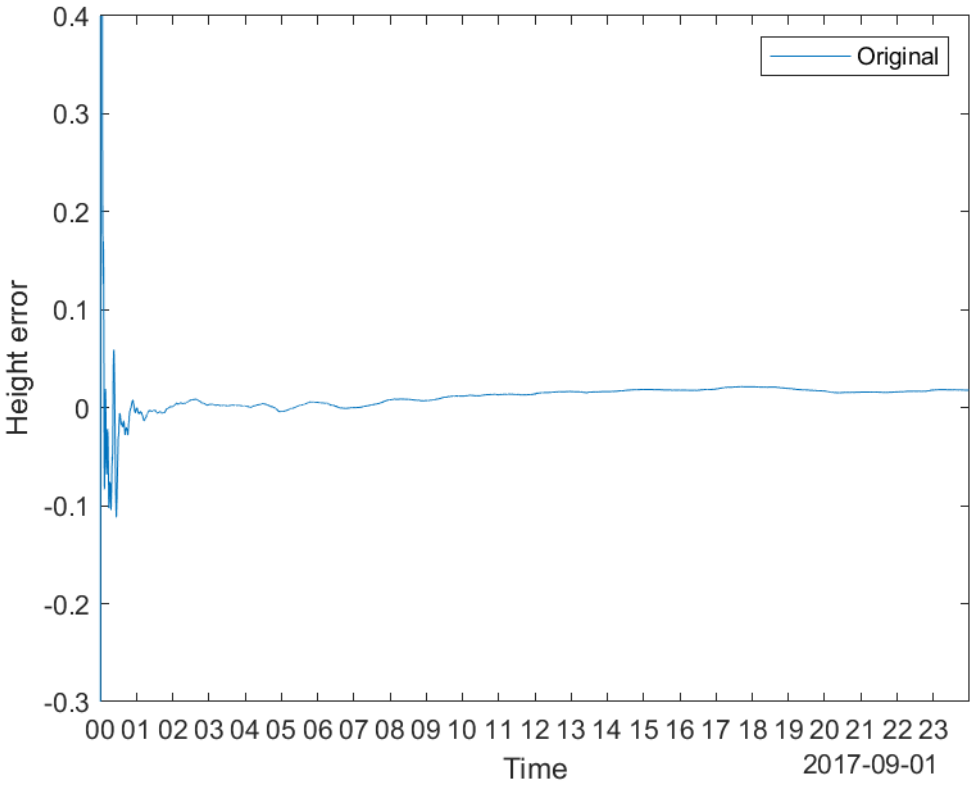
Original
Height error
0.4
0.3
0.2
0.1
0
-0.1
-0.2
-0.3
00 01 02 03 04 05 06 07 08 09 10 11 12 13 14 15 16 17 18 19 20 21 22 23
Time
2017-09-01

(b)

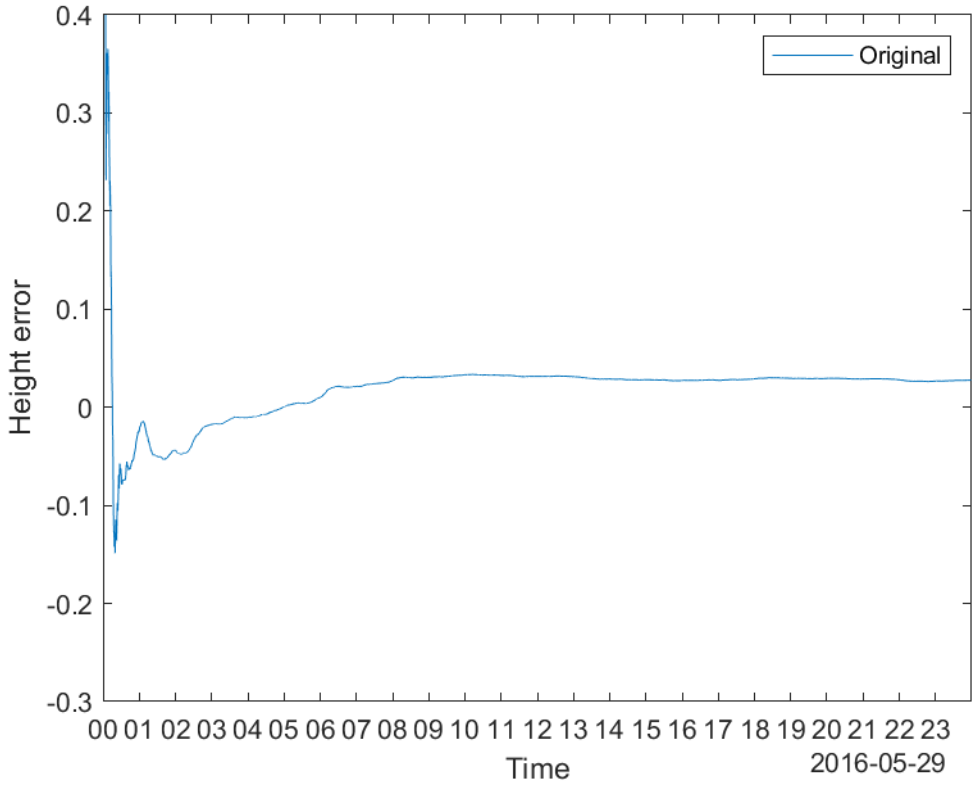

(c)

Figure 6.2 The height error variation on (a) 2017-09-01 at SAO0P station; (b) 2017-09-01 at SJCU station; (c) and 2016-05-29 at SNA0P station. The height error is in metres.

6.2.1.2. Satellite removal strategy

Based on MP1, MP2, S4 and σ_{ϕ}, G10 was considered to be the satellite with strongest scintillation while G21 was the most scintillated satellite according to ROTI on 2017-09-13 at SAO0P station. As shown in Figure 6.3, the original and G10-removed PPP height (a) and 3D (b) errors were compared based on RMSE on 2017-09-13 at SAO0P station. It can be observed from Figure 6.3 that the original height and 3D errors display variabillity during the first ten hours, which corresponds to the scintillation event shown on Figure 4.3(b). By comprison, the RMSE of both height and 3D errors barely changed after G10 was removed, which meant removing G10 did not contribute to error mitigation though it was the satellite with strongest scintillation according to MP and scintillation parameters. During the scintillation period, there were 8 to 11 visible satellites including G10. Thus, removing G10 scarcely affected the availability of satellites and the the positioning algorithm. Furthermore, another scintillation

satellite G21 was removed according to ROTI and the same comparison was conducted that is shown in Figure 6.4. On this occasion, the RMSE of height and 3D errors were slightly improved, where improvement rates of results on Figure 6.4(a&b) are 5.5% and 4.6%, respectively.

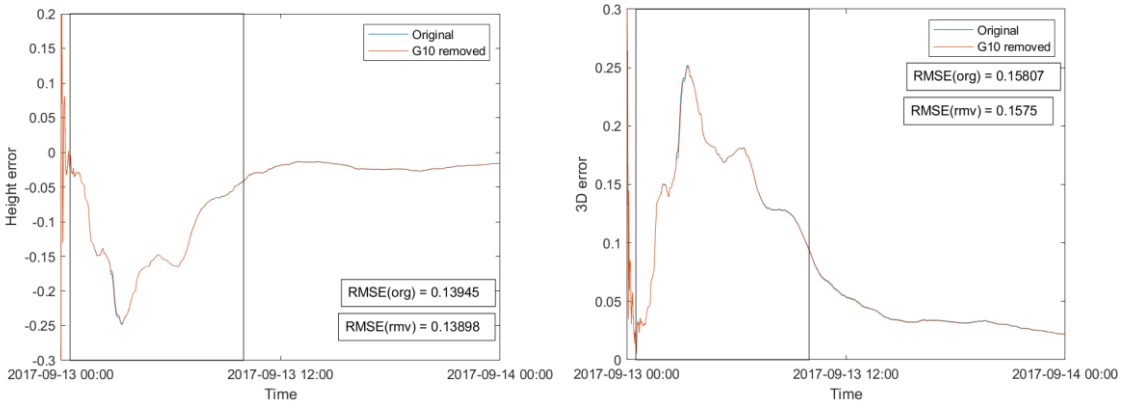

(a) (b)

Figure 6.3 Comparison between (a) the original and G10-removed RMSE of the height error, (b) the original and G10-removed RMSE of the 3D error on 2017-09-13 at SAO0P station. The RMSE of height and 3D errors is all in meters. The period affected by scintillation is framed in a rectangle (0.5-10 UT).

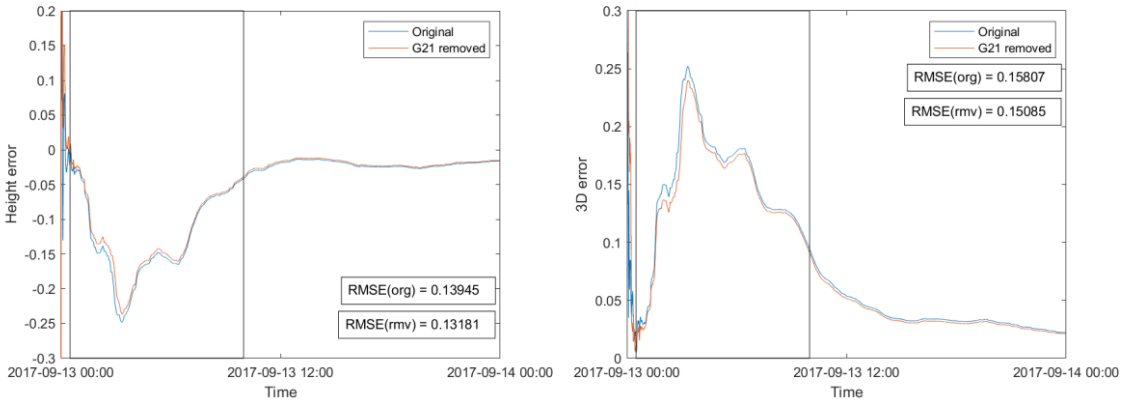

(a) (b)

Figure 6.4 Same as Figure 6.3 except G21 was removed rather than G10.

In order to invesitgate the influence of satellite removal on the GDOP, the GDOP time series plots before and after removing G10 or G21 were genereated as shown in Figure 6.5. Most of

GDOP values remain below 5 and all the GDOP values remain below 8. The GDOP values slightly increased during the first six hours in both graphs and in the last half hour in Figure 6.5 (b). As aforementioned, there were 8 to 11 satellites available during the scintillation period. However, 4 satellites are enough to complete the positioning algorithm. In this case, removing a single satellite barely affected the satellite geometry. Thus, when the number of visible satellites is enough, removing a single satellite barely affects the satellite geometry and the DOP.

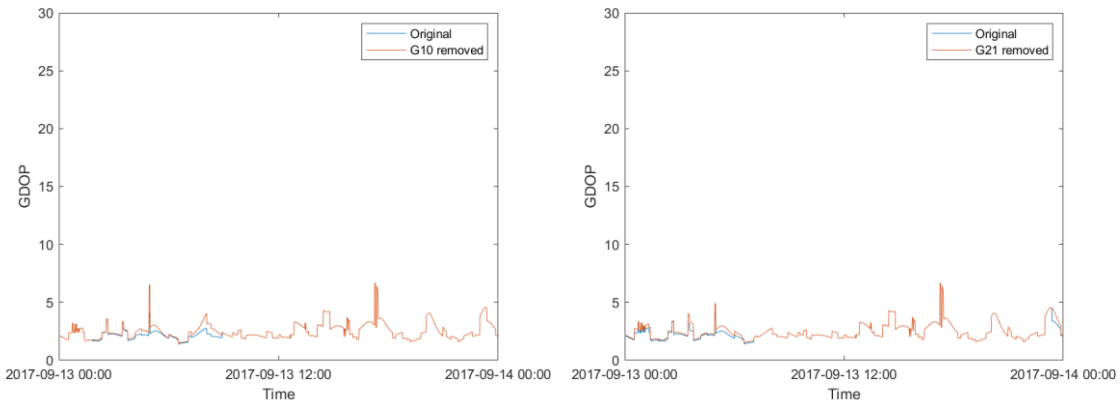

(a) (b)

Figure 6.5 Comparison between (a) the original and G10-removed GDOP, (b) the original and G21-removed GDOP on 2017-09-13 at SAO0P station. GDOP is dimensionless.

6.2.1.3. Observation removal strategy

As compared with satellite removal strategy, larger improvements in height and 3D can be observed in the observation removal strategy as shown in Figure 6.6 and Figure 6.7, where the variability during the period affected by scintillation and the general deviation from the reference coordinate were further mitgated though the improvement through MP2 was not substantial compared with the others parameters and the combination. As shown in Figure 6.6, it can be seen that using ROTI as the threshold leads to the best improvement. As shown in Figure 6.7, the combination of MP1, MP2 and ROTI improved the error in 3D more than the others. Improvement rates of results on Figure 6.6 (a-d) and Figure 6.7 (a-d) are 59.9%, 27.4%, 87.7%, 80.6%, 59.8%, 0.5%, 80.5% and 81.7%, respectively. The improvements by observation removal are larger than that by satellite removal, especially when ROTI and the combination of

MP1, MP2, ROTI were applied where the improvement exceeded 80%.

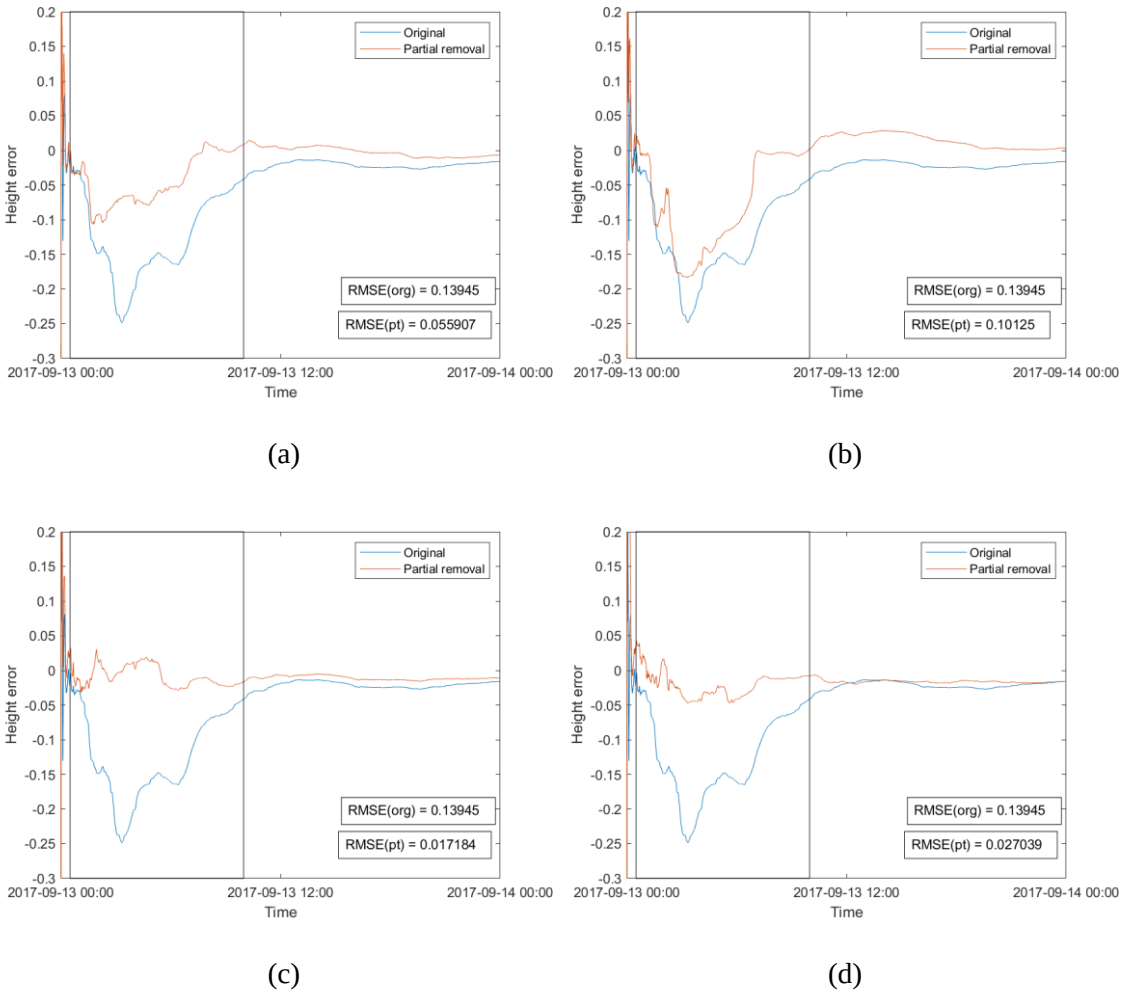

Figure 6.6 Comparison between (a) the RMSE of PPP height error of the original state and that after observation was removed based on the MT of MP1, (b) the RMSE of PPP height error of the original state and that after observation was removed based on the MT of MP2, (c) the RMSE of PPP height error of the original state and that after observation was removed based on the MT of ROTI, (d) the RMSE of PPP height error of the original state and that after observation was removed based on the MT of MP1, MP2 and ROTI. Units as in Figure 6.3. The period affected by scintillation is framed in a rectangle.

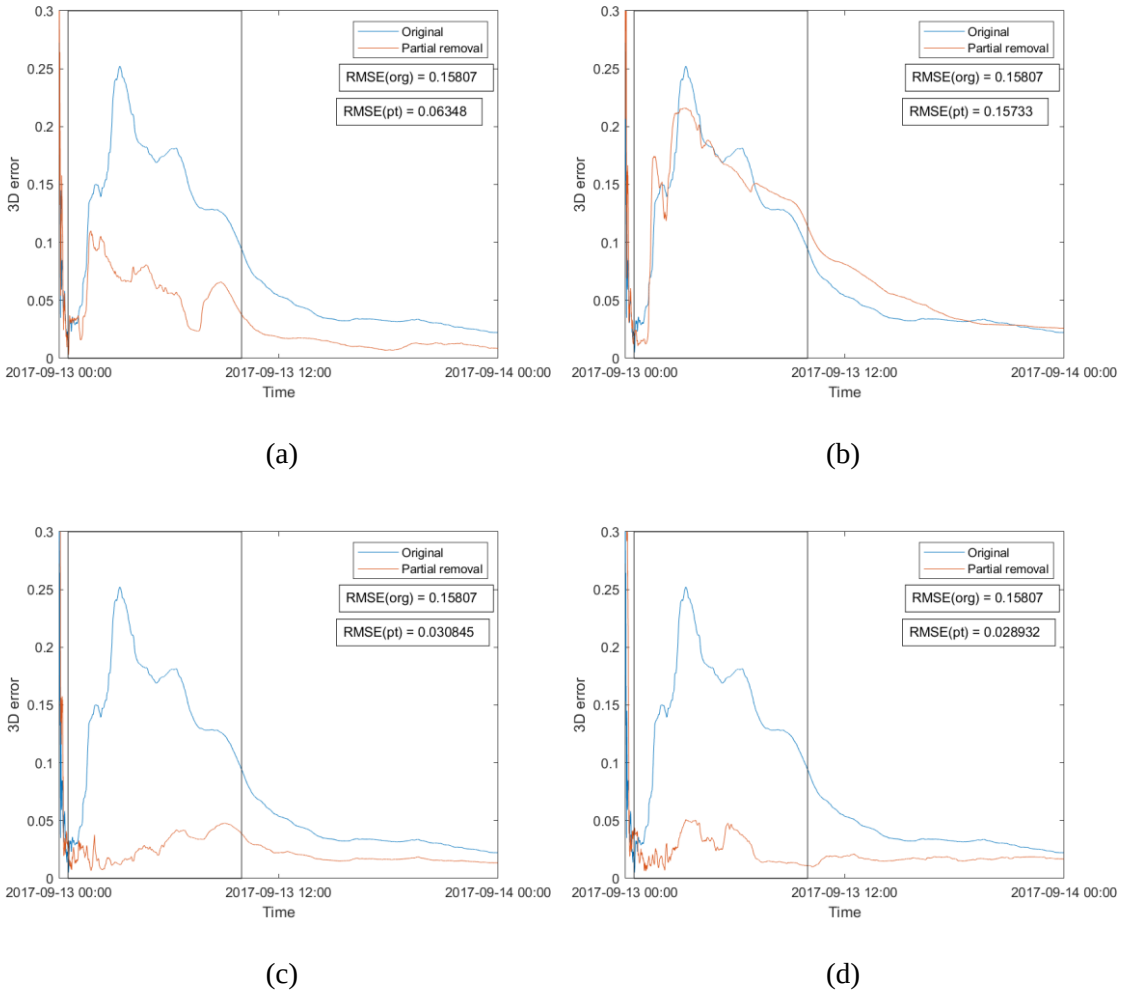

Figure 6.7 Same as Figure 6.6 except for 3D errors rather than height errors.

The GDOP change due to observation removal based on MP1, MP2, ROTI and the combination were shown in Figure 6.8 (a-d), respectively, which was considerably more intense than that due to satellite removal. The GDOP change in Figure 6.8 (a) was the smallest. The change is relatively more intense in Figure 6.8 (c) due to ROTI, where several GDOP values reached or even exceeded 30. Furthermore, the change was even more severe on Figure 6.8 (d) which is predictable as more observations were removed. Though the combination of MP1, MP2 and ROTI could lead to higher improvement than the others, the dramatically varying GDOP could lead to a decrease in the reliability of the results, which could be one of reasons for the lower height improvement with this combination than with ROTI.

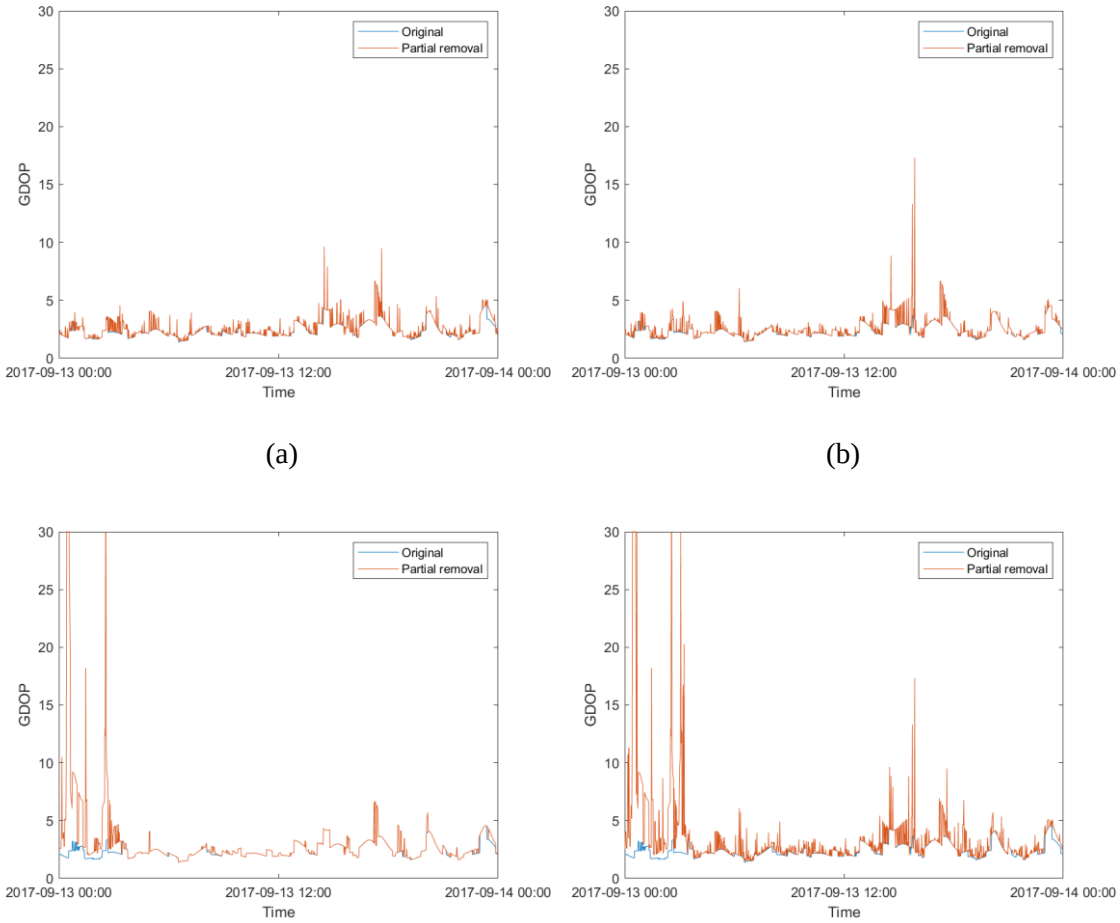

Figure 6.8 Comparison between (a) the GDOP before and after the observation was removed based on the MT of MP1, (b) the GDOP before and after the observation was removed based on the MT of MP2, (c) the GDOP before and after the observation was removed based on the MT of ROTI, (d) the GDOP before and after the observation was removed based on the MT of MP1, MP2 and ROTI.

6.2.1.4. Weight strategy

The RMSE improvement results based on scintillation and standard parameters through the weight strategy is shown in Figure 6.9. It can be observed that standard parameters improve the RMSE slightly more than scintillation parameters. The improvement rates on the Figure 6.9 (a-d) are 71.6%, 72.7%, 73.1% and 73.4%, respectively, which are comparable to those in Figure 6.6 (a-d) and Figure 6.7 (a-d). Though the best improvement is relatively higher through the observation removal than the weight strategy, extreme GDOP values are caused by the former strategy. High GDOP values typically indicate close distances bewteen satellites and low

confidence level of observations from these satellites, which may lead to large position uncertainty (Langley 1999). As weighting observations have no effect on the satellite availability, the GDOP remains unchanged after applying the weight strategy.

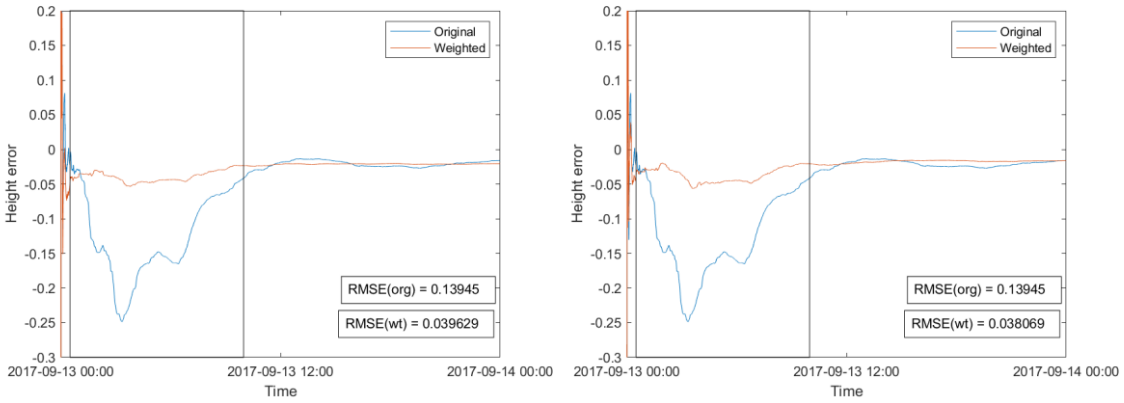

(a)

(b)

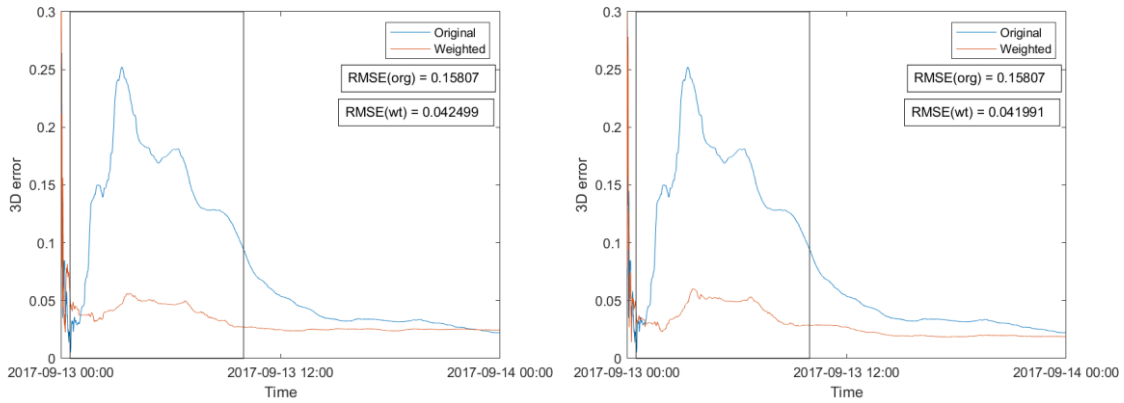

(c)

(d)

Figure 6.9 Comparison between (a) the original and weighted RMSE of the PPP height error based on S4 and σ_ϕ, (b) the original and weighted RMSE of the PPP height error based on MPF and ROTI, (c) the original and weighted RMSE of the PPP 3D error based on S4 and σ_ϕ, (d) the original and weighted RMSE of the PPP 3D error based on MPF and ROTI. Units as in Figure 6.3. The period affected by scintillation is framed in a rectangle.

6.2.2. Statistical results

6.2.2.1. Satellite removal strategy

The change of height and 3D positioning errors represented by the RMSE after removing the

satellite with the largest parameter value based on MP1, MP2, ROTI, S4 and σ_ϕ on 1 day without scintillation and 14 days with scintillation at 3 stations were summarized in Table 6.2, Table 6.3 and Table 6.4. The improved RMSEs were highlighted in bold. For scintillation days, it can be observed that the satellite removal strategy is effective to a certain extent, where the removal based on MP1, MP2, ROTI and σ_ϕ improved the positioning error on 7, 8, 6 and 5 days, respectively, within 14 days with scintillation, while S4 improved the positioning error on 2 within 7 days. The effectiveness of scintillation parameters was not higher than that of standard parameters, where S4 is even the least effective parameter. Additionally, the situation exists that MP can improve the error while the other parameters cannot, and vice versa. Furthermore, the height and 3D errors may not be improved simultaneously. Though the error can be improved on 8 out of 14 days at most, most of improvements were less than 0.05 m or even 0.01 m, which was not effective enough. For the day without scintillation, the highest values of MP1, MP2, ROTI, S4 and σ_ϕ were 1.5, 2.1, 0.12, 0.2 and 0.18, which were below the thresholds for scintillations defined in equations 5.4-5.6. On this day, the satellite removal strategy is ineffective. It is expected because removing a satellite without scintillation may lead to only a slight decrease in DOP and a slight increase in RMSE, as shown in Table 6.2.

Table 6.2 Change of the height and 3D positioning errors through the satellite removal strategy as represented by the RMSE at SAO0P. Improved RMSEs are highlighted in bold.

Station	Date	Original RMSE		Reference parameters	Removed satellite	Satellite-removed RMSE	
		height	3D			height	3D
SAO0P	20170901	0.0213	0.0314	MP1	G12	0.0231	0.0330
				MP2	G6	0.0213	0.0314
				ROTI	G32	0.0216	0.0316
				S4 σ_ϕ	G25	0.0228	0.0313
	20170907	0.0144	0.0180	MP1	G25	0.0178	0.0199
				MP2	G5	**0.0127**	**0.0139**
				ROTI	G20	**0.0141**	**0.0168**
				S4 σ_ϕ	G21	0.0144	0.0180
	20170908	0.6245	0.6422	MP1 S4	G18	0.6274	0.6465
				MP2	G10	0.6245	0.6422
				ROTI σ_ϕ	G24	**0.6077**	0.6428
	20170913	0.1395	0.1581	MP1 MP2 S4 σ_ϕ	G10	**0.1390**	**0.1575**
				ROTI	G21	**0.1318**	**0.1509**

Table 6.3 Change of the height and 3D positioning errors through the satellite removal strategy as represented by the RMSE at SJCU. Improved RMSEs are highlighted in bold.

Station	Date	Original RMSE		Reference parameters	Removed satellite	Satellite-removed RMSE	
		height	3D			height	3D
SJCU	20170904	0.0260	0.0345	MP1	G5	0.0262	**0.0271**
				MP2	G1	0.0263	0.0348
				ROTI	G8	0.0304	0.0381
				σ_ϕ			
				S4	G27	0.0277	0.0361
	20170907	0.0247	0.0311	MP1	G16	0.0294	**0.0299**
				MP2	G24	0.0290	0.0351
				ROTI			
				σ_ϕ			
				S4	G21	0.0310	0.0324
	20170908	0.1355	0.3454	MP1	G18	0.1463	0.3589
				σ_ϕ			
				MP2	G10	**0.1353**	0.3456
				S4	G24	**0.0737**	**0.1830**
				ROTI			
	20170913	0.0219	0.0329	MP1	G10	0.0221	0.0331
				MP2			
				ROTI			
				S4			
				σ_ϕ			

Table 6.4 Change of the height and 3D positioning errors through the satellite removal strategy as represented by the RMSE at SNA0P. Improved RMSEs are highlighted in bold.

Station	Date	Original RMSE		Reference parameters	Removed satellite	Satellite-removed RMSE	
		height	3D			height	3D
SNA0P	20160218	0.1699	0.2148	MP1	G14	0.1799	0.2247
				MP2	G15	0.1726	0.2192
				ROTI	G24	0.1769	0.2243
				σ_ϕ	G2	0.1750	**0.2145**
	20160402	0.0087	0.0329	MP1	G12	**0.0071**	0.0330
				MP2 ROTI	G17	**0.0066**	**0.0326**
				σ_ϕ	G14	0.0090	0.0329
	20160413	0.8233	0.8521	MP1	G9	1.0379	1.0559
				MP2	G21	**0.5325**	**0.6039**
				ROTI	G28	**0.6823**	**0.7235**
				σ_ϕ	G15	**0.7308**	**0.7599**
	20160509	0.4466	0.5796	MP1	G30	**0.4087**	**0.5206**
				MP2	G31	**0.4252**	**0.5588**
				ROTI	G8	0.4642	0.6033
				σ_ϕ	G21	0.4616	0.5839
	20160606	0.5636	1.1350	MP1	G16	0.6796	**1.0541**
				MP2	G1	0.6431	**1.1060**
				ROTI σ_ϕ	G21	0.7575	1.3633
	20160728	0.0099	0.0207	MP1	G24	**0.0089**	0.0212
				MP2 σ_ϕ	G32	**0.0085**	0.0303
				ROTI	G21	0.0112	0.0217
	20161013	0.0010	0.0228	MP1	G13	0.0024	0.0266
				MP2 σ_ϕ	G17	0.0010	0.0231
				ROTI	G1	0.0014	0.0245

6.2.2.2. Observation removal strategy

The improvement of height and 3D positioning errors after removing observations with scintillation based on the MT and ET of permutations and combinations of MP1, MP2, ROTI, S4 and σ_ϕ on 14 days with scintillation at 3 stations were summarized in Table 6.5. The detailed improvements of errors are presented in Table S2-S29 in Appendix 2. As there are excessive

combinations, results of the observation removal strategy were showed in a different way in the main body compared with the other strategies. Three criteria were used to evaluate the effectiveness of this strategy, proportions of days with improvement, best improvement rate and mean improvement rate, where the latter two were equated to the highest and mean improvement among the former. As S4 is low at SNA0P station, S4 is only used on 7 days at the other two stations in this strategy. When S4 is not considered for comparison, the highest proportions of days in height and 3D errors were 8/14 and 11/14, respectively. The highest best improvement rate in height and 3D errors were 91.7% and 87.9%, respectively. The highest mean improvement rate in height and 3D errors were 62.5% and 64.9%, separately. It can be observed that the highest day proportion in height errors could be obtained by both standard and scintillation parameters. Furthermore, the highest day proportion in 3D errors and best (or mean) improvements in both height and 3D errors were respectively obtained with the scintillation and standard parameters, which indicates that scintillation parameters could lead to higher possibility of improvement and standard parameters could result in higher degree of improvement. When MP1and MP2 were used alone or the combination of MP1and MP2 was used, the possibility and degree of improvement were relatively low. For example, when MP2 was used alone and ET was applied, the proportion of days with improvement and the best (mean) improvement in height errors were 3/14 and 16.3% (6.9%), respectively, substantially lower than the others. However, when MP was combined with ROTI, the improvement were comparable or even higher than when ROTI was used alone. For instance, when MP1 was combined with ROTI and MT was used, the proportions of improved days and the best or mean improvement in 3D errors slightly exceeded when ROTI was used alone. Moreover, σ_ϕ was more effective than S4 according to the best or mean improvement though it is largely because that S4 is not high on 7 days at the Antarctica station SNA0P and can only be applied on the other 7 days. In terms of the proportion day, S4 is comparable to σ_ϕ when only considering the 7 days' data. Thus, it may demonstrate that σ_ϕ is more effective than S4 in scintillation mitigation.

Moreover, MT was generally more effective than ET according to not only proportion of days with improvement but also the best or mean improvement. The proportion of improved days of 3D errors is generally higher than that of height errors and the case was contrary for best or

mean improvement rate. Furthermore, when a single reference parameter was applied, the effectiveness of ROTI and scintillation parameters was comparable. When combinations were applied, the improvement in effectiveness of scintillation parameters was not significant due to low S4 at SNA0P. However, combinations of standard parameters, such as the combination of MP1 and ROTI were able to further improve the results. For standard parameters, the combination of MP1and ROTI was more robust than the others, which was able to acquire higher possibility and extent of improvements. Thus, it was possible that the combination of MP and ROTI was able to cover and mitigate more errors than a single parameter.

Table 6.5 Summary of the height and 3D positioning errors improvement through observation removal.

Error type	Threshold type	Parameter type	Permutations and combinations	Proportion of days with improvement	Best improvement	Mean improvement
Height	MT	Scintillation parameters	σ_ϕ	8/14	84.3%	39.4%
			S4	4/7	79.7%	33.6%
			σ_ϕ, S4	7/14	83.3%	45.5%
		Standard parameters	ROTI	8/14	87.7%	49.7%
			MP2	5/14	69.7%	28.3%
			MP1	5/14	59.9%	25.0%
			MP2, ROTI	8/14	88.5%	57.0%
			MP1, ROTI	7/14	91.7%	62.5%
			MP1, MP2	5/14	89.9%	51.2%
			MP1, MP2, ROTI	8/14	90.3%	57.8%
	ET	Scintillation parameters	σ_ϕ	6/14	89.9%	43.3%
			S4	4/7	73.4%	30.5%
			σ_ϕ, S4	8/14	90.4%	35.0%
		Standard parameters	ROTI	8/14	88.2%	38.6%
			MP2	3/14	23.8%	14.5%
			MP1	8/14	53.4%	20.9%
			MP2, ROTI	8/14	84.0%	48.1%
			MP1, ROTI	7/14	82.9%	52.8%
			MP1, MP2	5/14	42.5%	19.7%
			MP1, MP2, ROTI	7/14	82.9%	49.9%
3D	MT	Scintillation parameters	σ_ϕ	11/14	80.5%	33.6%
			S4	4/7	79.7%	25.5%
			σ_ϕ, S4	9/14	83.6%	40.4%
		Standard parameters	ROTI	8/14	80.5%	46.5%
			MP2	5/14	68.4%	23.4%
			MP1	7/14	59.8%	20.5%
			MP2, ROTI	8/14	87.9%	53.5%
			MP1, ROTI	10/14	82.6%	45.9%
			MP1, MP2	6/14	79.8%	38.7%
			MP1, MP2, ROTI	8/14	85.3%	64.9%
	ET	Scintillation parameters	σ_ϕ	9/14	79.6%	32.7%
			S4	4/7	60.8%	22.5%
			σ_ϕ, S4	9/14	81.5%	30.9%
		Standard parameters	ROTI	9/14	77.9%	39.5%
			MP2	6/14	16.3%	6.9%
			MP1	8/14	75.7%	19.9%
			MP2, ROTI	8/14	86.3%	45.7%
			MP1, ROTI	9/14	79.2%	42.7%
			MP1, MP2	5/14	35.7%	17.0%
			MP1, MP2, ROTI	8/14	83.5%	44.7%

The same result for the day without scintillation were shown in 错误!书签自引用无效。 and Table 6.7. In this case, most of combinations were ineffective. Improvements were obtained using MT of σ_ϕ, S4, MP2, and ET of the combination of MP1 and ROTI, but the improvements were not substantial. This is similar to the result of the satellite removal strategy, where the DOP was the main factor affecting RMSE.

Table 6.6 Change of the height and 3D positioning errors through the observation removal strategy based on MT as represented by the RMSE at SAO0P on 2017-09-01. Improved RMSEs are highlighted in bold.

Station	Date	Original RMSE		Permutations and combinations	Observation-removed RMSE	
		height	3D		height	3D
SAO0P	20170901	0.0213	0.0314	σ_ϕ	**0.0211**	0.0318
				S4	**0.0182**	**0.0307**
				σ_ϕ, S4	**0.0194**	**0.0306**
				ROTI	0.0242	0.0392
				MP2	0.0238	**0.0300**
				MP1	0.0256	0.0324
				MP2, ROTI	0.0321	0.0479
				MP1, ROTI	0.0285	0.0427
				MP1, MP2	0.0347	0.0423
				MP1, MP2, ROTI	0.0336	0.0392

Table 6.7 Change of the height and 3D positioning errors through the observation removal strategy based on ET as represented by the RMSE at SAO0P on 2017-09-01. Improved RMSEs are highlighted in bold.

Station	Date	Original RMSE		Permutations and combinations	Observation-removed RMSE	
		height	3D		height	3D
SAO0P	20170901	0.0213	0.0314	σ_ϕ	0.0221	0.0321
				S4	0.0230	0.0329
				σ_ϕ, S4	0.0230	0.0329
				ROTI	0.0259	0.0424
				MP2	0.0354	0.0409
				MP1	0.0278	0.0396
				MP2, ROTI	0.0277	0.0384
				MP1, ROTI	**0.0197**	0.0369
				MP1, MP2	0.0323	0.0429
				MP1, MP2, ROTI	0.0262	0.0413

6.2.2.3. Weight strategy

The improvement of height and 3D errors as represented by the RMSE through the weight strategy on the day without scintillation and 14 days with scintillation at 3 stations are presented in Table 6.8, Table 6.9 and Table 6.10 and are summarized in Table 6.11. The improved RMSEs were highlighted in bold. Scintillation and standard parameters respectively improved the height RMSE on 6 and 8 out of 14 days, where the best (mean) improvement rates are 93.1% (68.8%) and 86.1% (66.2%), respectively. For 3D errors, scintillation and standard parameters separately improved 3D RMSE on 8 and 7 out of 14 days, where the best (mean) improvement rates are 85.5% (52.5%) and 73.4% (47.0%), separately. Thus, in weight strategy, standard parameters are comparable to scintillation parameters for improving both height and 3D errors according to the proportion of days with improvement and the best improvement rate. Furthermore, the improvement in height error is generally larger than that in 3D error. For the day without scintillation, RMSE even substantially increased. This may indicate that parameters not affected by scintillation could assign biased weights to observations and result in solutions with higher RMSEs.

Table 6.8 Change of the height and 3D positioning errors through the weight strategy as represented by the RMSE at SAO0P. Improved RMSEs are highlighted in bold.

Station	Date	Original RMSE		Parameter	Weighted RMSE	
		height	3D	type	height	3D
SAO0P	20170901	0.0213	0.0314	Scintillation	0.0723	0.1168
				Standard	0.0851	0.1032
	20170907	0.0144	0.0180	Scintillation	**0.0057**	**0.0094**
				Standard	**0.0030**	**0.0104**
	20170908	0.6245	0.6422	Scintillation	**0.0432**	**0.0930**
				Standard	**0.4053**	**0.4517**
	20170913	0.1395	0.1581	Scintillation	**0.0396**	**0.0425**
				Standard	**0.0381**	**0.0420**

Table 6.9 Change of the height and 3D positioning errors through the weight strategy as represented by the RMSE at SJCU. Improved RMSEs are highlighted in bold.

Station	Date	Original RMSE		Parameter	Weighted RMSE	
		height	3D	type	height	3D
SJCU	20170904	0.0260	0.0345	Scintillation	0.0609	0.0615
				Standard	**0.0168**	**0.0280**
	20170907	0.0247	0.0311	Scintillation	**0.0052**	**0.0227**
				Standard	**0.0038**	0.0430
	20170908	0.1355	0.3454	Scintillation	0.9587	0.9870
				Standard	0.2045	0.3538
	20170913	0.0219	0.0329	Scintillation	0.1220	0.1436
				Standard	**0.0101**	0.0415

Table 6.10 Change of the height and 3D positioning errors through the weight strategy as represented by the RMSE at SNA0P. Improved RMSEs are highlighted in bold.

Station	Date	Original RMSE		Parameter	Weighted RMSE	
		height	3D	type	height	3D
SNA0P	20160218	0.1699	0.2148	Scintillation	**0.0200**	**0.0392**
				Standard	**0.0297**	**0.0613**
	20160402	0.0087	0.0329	Scintillation	0.0095	**0.0189**
				Standard	0.0714	0.1036
	20160413	0.8233	0.8521	Scintillation	**0.6557**	**0.6956**
				Standard	**0.1144**	**0.3250**
	20160509	0.4466	0.5796	Scintillation	0.6886	0.7293
				Standard	0.7785	0.8130
	20160606	0.5636	1.1350	Scintillation	1.9631	2.5657
				Standard	2.2798	2.5189
	20160728	0.0099	0.0207	Scintillation	0.0193	0.0256
				Standard	0.0247	0.0296
	20161013	0.0010	0.0228	Scintillation	0.0039	**0.0128**
				Standard	0.0033	**0.0156**

Table 6.11 Summary of the height and 3D positioning errors improvement through the weight strategy.

Error type	Parameter type	Proportion of days with improvement	Best improvement	Mean improvement
Height	Scintillation parameters	6/14	93.1%	68.8%
	Standard parameters	8/14	86.1%	66.2%
3D	Scintillation parameters	8/14	85.5%	52.5%
	Standard parameters	7/14	73.4%	47.0%

6.3. Discussion

Data of 75 days from three stations, SAO0P, SJCU and SNA0P, were used in the PPP improvement experiment with the freely available and MATLAB-based software namely PPPH,

where data of 1 day without scintillation and 14 days with scintillation was applied with three strategies for improving positioning quality and all the data was used to generate MT and ET involved in the second strategy called observation removal strategy. In section 6.2, I evaluated the convergence time for PPPH at the three stations and concluded that it was around 30 minutes on a day without scintillation (Figure 6.2). Then, an example of visualization was given, which was based on the data on 2017-09-13 at SAO0P. In first strategy, G10 and G21 were regarded as the satellites with the most intense scintillation according to MP1, MP2, S4, σ_ϕ and ROTI, respectively. As shown in Figure 6.3 and Figure 6.4, removing G10 scarcely decreased the RMSE for both height and 3D errors when removing G21 mitigated 5.5% height error and 4.6% 3D error. Thus, it is possible that removing the scintillation satellite may not lead to the error improvement, which indicates the unreliability of the first strategy for error elimination. In this example, it was ROTI rather than MP, S4 or σ_ϕ that identified the scintillation satellite that influences the results though the improvement through ROTI was not substantial . Hence, scintillation parameters are not necessary to be effective in the first strategy. Furthermore, it is a part of future work to identify the characteristics of the removed scintillation satellite that could lead to improvements. In addition, the change of GDOP is not significant after removing a single satellite as shown in Figure 6.5, which means applying the first strategy barely affects the satellite geometry and thus the position quality.

More significant improvements could be obtained with the observation removal strategy as it could be seen in Figure 6.6 and Figure 6.7. When using a single parameter as the threshold reference to remove observations, the improvement based on ROTI was higher than that based on MP1 and MP2, which exceeded 80% and was substaintially more than the improvement through the satellite removal strategy. One possible reason of this phenomenon was that using ROTI as the threshold could identify more scintillation obeservations than MP. Furthermore, when using the combination of MP1, MP2 and ROTI to remove observations, the height improvement was larger than that of MP1 and MP2, but smaller than that of ROTI. However, this combination improved the 3D error more than ROTI alone. A possible reason for this phenomenon was that multipath effects are typically more severe at lower elevation. Thus, it is more likely that multipath contributes to the horizontal error rather than the height error, where

the former is contained in the 3D error. Further, MP can be used to characterize multipath effects. Therefore, using the combination of MP1, MP2 and ROTI was able to eliminate more types of errors in 3D than using ROTI alone. In addition, the GDOP was considerably influenced in the second strategy, especially when applying the combination of MP1, MP2 and ROTI, where several GDOP values exceeded 30 during first three hours as shown in Figure 6.8. This could be one of reasons why the height improvement using the combination was lower than than using ROTI.

Compared with the observation and satellite removal strategies, the weight strategy had no effect on the GDOP, which is one of its advantages. As shown in Figure 6.9, the improvements based on scintillation and standard parameters were comparable, which were also comparable to most of improvements based on the observation removal strategy. Thus, the weight strategy was more reliable and stable than the other two strategies with consistently high improvements based on this example.

All the results on 1 day without scintillation and 14 days with scintillation were statistically summarized in Table 6.2-Table 6.11. Compared with the other two strategies, the satellite removal strategy was relatively ineffective in improving the positioning error. As shown in Table 6.2-Table 6.4, the highest proportion of days with improvement was 8 out of 14 days based on MP2. However, most of the improvements were less than 0.05 m or even 0.01 m, which was not effective. There were two possible reasons for this phenomenon. First, it was highly possible that the observations from the satellite with the maximum parameter value encountered cycle slips, which might have been detected and repaired by the methods namely Hatch-Melbourne-Wübbena and the Geometry-Free Combination in the preprocessing process of PPPH before the positioning algorithm. Alternatively, the outlier detection algorithm in PPPH had identified and removed the noisy observations from the scintillation satellite in advance (Bahadur and Nohutcu 2018). As a consequence, removing this scintillation satellite scarcely impacted the output. Moreover, it was possible that multiple satellites were affected by the scintillation, resulting that removing a single satellite could not effectively eliminate the scintillation effect. However, it would not be appropriate to remove multiple satellites

simultaneously as the number of available satellites might drop below 4, or at least the DOP values could be severely impacted.

In contrast, the improvement achieved with the observation removal strategy was more substantial than the satellite removal strategy. As it could be seen in Table 6.5, the 3D error was improved on 11 out of 14 days based on MT and scintillation parameters, and the height error was improved by 91.7% at most based on MT and standard parameters. Hence, scintillation and standard parameters had their own advantages in in error improvement in the observation removal strategy. However, the combination of standard parameters can be more effective sometimes. For instance, the combination of MP1 and ROTI could improve the height error more substantially than scintillation parameters using MT. In this case, standard parameters were able to replace scintillation parameters. Compared with the satellite removal strategy, the observation removal strategy was able to remove scintillation observations from multiple satellites for an epoch once the corresponding parameter value exceeded the threshold. Furthermore, MT could lead to higher success rate of improvement and improvement percentage than ET in general. As MT was lower than ET, MT was able to remove more observations, which led to less measurements with errors. Therefore, the scintillation effect was more thoroughly mitigated, which explained the higher effectiveness of applying MT in the observation removal strategy. However, more observations removed could also lead to a worse satellite geometry resulting in the instability of positioning quality (Langley 1999). Thus, the observation removal strategy was less reliable than the weight strategy especially when MT was applied.

As shown in Table 6.8-Table 6.11, though the proportion of days with improvement obtained with the weight strategy was relatively lower as compared with the observation removal strategy, the weight strategy was capable of acquiring an even higher improvement that is 93.1% in height error. However, the errors considerably increased on 2017-09-08, 2017-09-13 at SJCU and 2016-06-06, 2016-07-28 at SNA0P. The same situation also occurred for the observation removal strategy as shown in Table S7, S8 and S13-S15, which did not occur for the satellite removal strategy. This is partially because the original RMSEs were already small on several

days, such as 2016-04-02, 2016-07-28 and 2016-10-13 at SNA0P, where the RMSEs did not even exceed 0.01 m. This meant that the positioning performance of PPP was not substantially affected by scintillation on these days. This might also indicate that when parameters sometimes cannot really reflect how observations are affected by scintillation, removing or weighting multiple observations simultaneously may even degrade the positioning performance of PPP. To further research why the errors did not get improve sometimes, the number of satellites affected by cycle slip was investigated. Take SAO0P and SJCU, stations close to each other, as an example. The errors on 2017-09-08 substantially decreased at SAO0P, but substantially increased at SJCU. During the scintillation period, 4 and 3 satellites were simultaneously affected by cycle slip at SJCU and SAO0P, respectively, and the numbers of visible satellite were 8 at both stations. This might indicate that more satellites affected by cycle slip could lead to the ineffectiveness of the weight strategy. To support this statement, the same investigation was conducted at SNA0P. During the scintillation period, the number of satellites affected by cycle slip were 5, 7 and 6 on 2016-04-13, 2016-05-09 and 2016-06-06, respectively, when the number of visible satellites were 11, 10 and 10, separately. In other words, 6, 3 and 4 satellites were free of cycle slip on the three days, respectively. Further, the improvement was obtained on 2016-04-13 but not on the other two days. Therefore, it was supported that less satellites affected by cycle slip could lead to the success of the weight strategy in error improvement.

Moreover, it was possible that standard parameters worked when scintillation parameters did not, and vice versa. Furthermore, it was also possible that either of standard and scintillation parameters led to a higher improvement. One possible reason is that MP included in standard parameters is also able to characterize multipath effect in addition to scintillation. Thus, standard parameters are capable of down-weighting more types of errors. On this occasion, standard parameters should be more effective in scintillation mitigation. However, MP and ROTI may fail to represent scintillation sometimes. In this case, scintillation parameters should be more effective in scintillation mitigation. Thus, standard parameters and scintillation parameters have their respective advantages in scintillation mitigation in this strategy.

For the day without scintillation, all three strategies were not effective. It was expected as

parameters that were not affected by scintillation were not able to represent the scintillation effect. Thus, in these strategies, it was possible that satellites and observations with good quality were removed or down-weighted. As a consequence, the error of solutions even increased.

As presented in section 3.2.4, a lot of research has been conducted to improve positioning accuracy under the scintillation condition. By weighting the least square stochastic (LSQ) model, the height positioning accuracy was respectively improved by 21 % and 38% at most by Aquino et al. (2007) and Aquino et al. (2009), and the 3D positioning accuracy was separately improved by up to 77.3% and 75% by Park et al. (2017) and Sreeja et al. (2020). In contrast, by weighting the KF model, the height and 3D error improvements respectively reached 93.1% and 86.1% in this thesis, which were substantially higher as compared with the results obtained by Park et al. (2017) and Sreeja et al. (2020). Moreover, scintillation parameters were required in all these methods when standard parameters (MP and ROTI) with comparable performance were alternative in the method in this chapter, which meant the data with the time interval of 30s could also be used to mitigate the scintillation effect. This significantly increased the coverage of scintillation study with the assistance of global agencies such as IGS that provides data from more than 500 permanent GNSS stations covering over 100 countries. Furthermore, Marques et al. (2018) integrated data from multiple constellations to improve the height and 3D error by 63% and 57%, respectively. This could be a part of the future work, where the effectiveness of the observation removal and weight strategies could be investigated. Especially for the observation removal strategy, the satellite geometry is supposed to be less degraded with more visible satellites from multiple GNSS than using GPS only.

6.4. Conclusions

In this chapter, the experiment on mitigating scintillation effects on PPP has been conducted based on three strategies: satellite removal, observation removal and weight. The satellite removal strategy led to the least effective improvement, the observation removal strategy resulted in the most consistent improvement and the weight generated the highest improvement rate. In the observation removal strategy, the effectiveness of standard parameters was comparable to that of scintillation parameters, especially with the combination of MP1and

ROTI. Though the observation removal strategy resulted in the most consistent improvement, the GDOP variation due to excessive removals led to the instability of this strategy. Using data from multiple constellations is a possible way to address the drawback of the observation removal strategy. In contrast, the weight strategy improved the height error by 93.1% at most. The standard parameters were also comparable to scintillation parameters in the observation removal and weight strategy. Thus, the primary novelty of the method in this chapter was that parameters from 30s data could also be used to effectively mitigate the scintillation effect on PPP. In addition, the observation removal strategy was proposed for the first time. Though there were some shortcomings in this strategy, it was easier-to-use than the weight strategy and could improve the errors more consistently.

7. Synthesis

In this chapter, each research objective is discussed separately. Then, the work is integrally discussed based on the whole thesis. Next, a comprehensive summary of outcomes and conclusions is given based on the discussion. Furthermore, the recommendations on future work are also presented based on the findings and existing drawbacks stated in this thesis.

7.1. Research objectives

The purpose of this thesis was to mitigate the scintillation effect based on the parameters obtained from standard geodetic receivers. Thus, three main objectives were extracted from this purpose: 1) investigation on the relationship between parameters from low-rate data (multipath parameter (MP) and rate of change of Total Electron Content Index (ROTI)) and those from high-rate data (S4 and σ_ϕ); 2) methodology for determining whether the hypothesized scintillation event was caused by real scintillation instead of multipath; 3) mitigation on scintillation effects, evaluated using the root mean square error (RMSE) of PPP results. Based on the objectives, this thesis proposed one methodology for investigating spatial relationship between different parameters, another for distinguishing scintillation from multipath and a final one for improving positioning reliability and accuracy under scintillation conditions. The first two objectives were the preconditions of the third one.

Objective 1. To investigate the spatiotemporal relationship between MP, ROTI and S4 and σ_ϕ.

To begin with, this thesis investigated the relationship between MP, ROTI and S4, σ_ϕ. As previous research focused primarily on the temporal relationship between these parameters, this thesis proposed two types of maps to study the spatial relationship, which were the mean value map and the occurrence percentage map. Then, with the assistance of statistical tools including Pearson Correlation Coefficient (CC), structural similarity (SSIM) and variograms, the relationship on these maps could be quantified. Both the mean value map and occurrence percentage map showed high similarity between MP, ROTI and S4, σ_ϕ as shown in Figure 4.5, Figure 4.9, Figure 4.10, Figure 4.13, Figure 4.17 and Figure 4.18. The corresponding quantified similarity was also high as shown in Table 4.1-Table 4.3, Table 4.6-Table 4.11, Table 4.12-Table 4.14, Table 4.17-Table 4.22, Figure 4.6 and Figure 4.14. In particular, it was shown that MP was more similar to S4 and ROTI was more related to σ_ϕ at the Brazil station. A possible reason for

this is that MP and ROTI may represent different types of scintillation. Thus, it is possible that using both MP and ROTI can identify more areas affected by scintillation than using a single parameter of them.

Objective 2. To distinguish scintillation from multipath in GNSS signals.

The second research emphasis was the identification of the event type that includes multipath, scintillation and hybrid event (when both multipath and scintillation occur). The methodology proposed in Chapter 5 managed to distinguish scintillation from multipath even when the hybrid event occurred at elevation higher than 30° (high elevation). As shown in the elevation layered plots Figure 5.7-Figure 5.10 and corresponding parameter value against elevation and azimuth (PEA) plots Figures S10/S172, S42/S204, S74/S236, S106/S269 and S138/S301, S18/S180, S50/S212, S82/S244, S114/S277 and S146/S309, the variability of parameters for G10 and G18 respectively on 2017-09-08 and 2017-09-13 at high elevation were identified to be caused by scintillation. Furthermore, the hybrid event on 2017-09-08 with both repeated and occasional outliers as shown in Figure S279 was identified.

For events lower than 30° (low elevation), a reference station could assist in identifying event types when only one of multipath and scintillation occurred. As shown in Figure 5.3-Figure 5.6, MP at low elevation at SAO0P station was regarded as outliers when those at SJCU station was significantly less variable. If the MP outliers at SAO0P was caused by the ionospheric effect, the MP at SJCU was supposed to show the similar variability due to the close range between two stations. Thus, the MP outliers were more possible to be caused by multipath. In addition, S4 and σ_ϕ were not necessary in this methodology as ROTI was able to partially replace them. Though the hybrid event at low elevation could not be identified with this methodology, an elevation mask is typically applied when processing GNSS data. Hence, the proposed methodology was able to meet the requirement of the second research objective.

Objective 3. To mitigate the scintillation effect on PPP positioning and improve the accuracy based on MP and ROTI.

The last research emphasis was improving the PPP accuracy and reliability under scintillation

conditions based on MP and ROTI. With the theoretical basis, relationship between standard and scintillation parameters observed in the Chapter 4, it was theoretically feasible to apply MP and ROTI to mitigate the scintillation effect instead of S4 and σ_{ϕ}. Based on the distinguishing methodology in Chapter 5, the data of 14 scintillation days was identified and used in the PPP improvement experiment. Among three strategies, the observation removal and weight strategies were able to effectively improve the RMSE of PPP results and mitigate the scintillation effect. For the observation removal strategy, the best improvement even reached 91.7% based on the combination of MP1 and ROTI as shown in Table 6.5. In this strategy, standard parameters were able to improve PPP accuracy to a greater extent on average when scintillation parameters were able to improve PPP accuracy on more days. In general, the performance of standard parameters was comparable to that of scintillation parameters in the observation removal strategy. Similarly, in the weight strategy, standard parameters were able to improve PPP accuracy comparably to scintillation parameters as shown in Table 6.8-Table 6.11. The observation removal was a novel strategy that has not been applied before, which was able to mitigate the error and was more consistent than the weight strategy in achieving improved accuracy. However, the significant GDOP change caused by observation removals led to the unreliability of this strategy. Hence, there were different advantages to the two strategies.

7.2. Discussion

By connecting the three objectives, the integrated methodology is established from the raw GNSS data to the improvement in positioning performance. As shown in Figure 7.1, the three objectives presented in the previous section constitutes the key steps in the integrated methodology. By inputting the GNSS data into the objective 1, the relationship between the proposed parameter and scintillation parameters could be evaluated, where the spatial relationship was assessed for the first time. If there was no relationship detected, the loop was activated and another parameter was input. With the relationship detected, the data flowed into the objective 2 in order to identify the subset of the data with scintillation. Thus, the objective 2 could be regarded as the filtering step for scintillation data. In this step, the hybrid of scintillation and multipath events could be identified for the first time and scintillation parameters were not necessary. Finally, the filtered data flowed into the objective 3 for

scintillation mitigation based on the proposed parameter. In this step, the observation removal strategy was proposed for the first time and scintillation parameters were also not necessary. All the three steps were essential in achieving the goal of this thesis as these steps shared the same purpose of not using scintillation parameters. It was worthy to note that this methodology could also be applied to other parameters to obtain the positioning improvement only if the relationship was detected between the used parameter and scintillation parameters. Thus, this methodology facilitated the application of various types of parameters in addition to multipath MP and rate of change of ROTI in scintillation mitigation. Therefore, it was possible that the elimination of the scintillation effect could be gradually optimized with an increasing number of parameters for characterizing scintillation and generalizing the research on it.

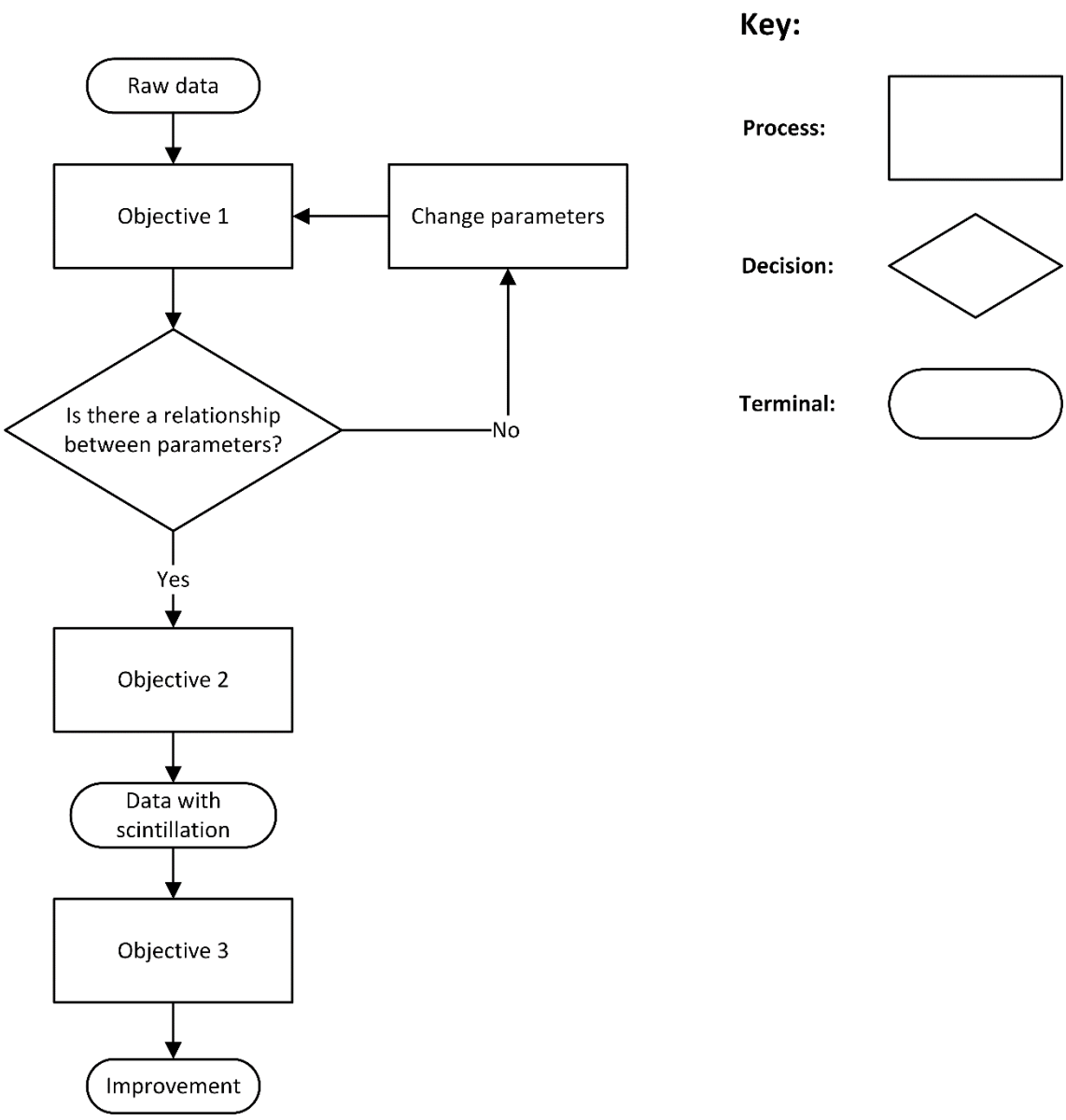

Figure 7.1 Integrated methodology

In terms of objective 1, it is also feasible to research on the spatial relationship of parameters in other applications. For example, the spatial relationship between signal-to-noise ratio (SNR) and the standardized residuals in Kalman filter (KF) can be investigated using the method in objective 1, with which it is possible to use SNR to weight observations before the adaptive factor in order to reduce the number of iterations and improve efficiency in adaptive KF (Zhang et al. 2018). In objective 1, three tools were used to evaluate the relationship, SSIM, Pearson CC and variograms. SSIM quantified the correlation based on the luminance, contrast and structure when CC and variograms are based on the linear correlation. Thus, the relationship could be

evaluated from different perspectives with the three tools, where SSIM and the other two tools respectively focused on the entirety and the detail. In addition, the evidence has been given in Chapter 4 that the combination of the three tools were practicable for spatial relationship assessment. Therefore, more comprehensive conclusions could be obtained by evaluating the spatial relationship using the all three tools. Furthermore, the three tools and the maps in objective 1 could be applied in spatial relationship in other applications or fields.

In objective 2, two tools were developed, the elevation layered plot and the PEA plot, where the variability of parameters lower than 30 degree could be observed in the former when the detail was more distinct in the latter. These tools could be applied in other applications where the repeatability needed to be evaluated. The proposal of the method in objective 2 was based on the fundamental characteristics of multipath and scintillation, which are periodic and non-periodic, respectively. Thus, this indicated that other characteristics of multipath and scintillation could also be used to distinguish them or improve the current method to create a more comprehensive methodology.

Based on the results in Chapter 6, it suggested that the major principle of objective 3, i.e., weighting observations in KF was effective in noise mitigation. Thus, it is possible to use MP or CCSTDDEV as weight to further mitigate multipath effects instead of elevation angle for scintillation-free data, or Total Electron Content (TEC) as weight to mitigate constant ionospheric delay when only single-frequency observations can be obtained. In inertial measurement unites (IMUs) that is an integration of accelerometers and gyroscopes primarily applied in indoor positioning, scale factors and biases can be used as weight to mitigate residual errors (Falletti et al. 2011). KF has been used as the critical algorithm to obtain the receiver position in GNSS for decades. However, KF has not previously been applied to mitigate scintillation effects, which was realized through the research in Chapter 6. In addition, this also indicated that it might be possible to use other elements in KF, such as the initial state, its covariance matrix, process noise matrix, etc., to mitigate scintillation or other effects. For example, using standard and scintillation parameters to weight the covariance matrix of the initial state might be able to reduce the effect of scintillation or multipath on the convergence of

PPP and reduce the convergence period.

The purpose of this thesis primarily consisted of two components, scintillation effect mitigation and parameters from low-rate data. Scintillation parameters were necessary in most of past methods for mitigating scintillation effects (Aquino et al. 2007; Aquino et al. 2009; Park et al. 2017; Sreeja et al. 2020), which are originally computed from high-rate (typically 1 kHz) in-phase and quadra-phase samples and (typically 50 Hz) GNSS data (Van Dierendonck et al. 1993). For a researcher investigating on the global scintillation effect, it is more feasible to use data from an open access platform that provides data from most of regions on Earth such as International GNSS Service (IGS), which typically provides data at the time interval of 30s and 1s. Though S4c and $\sigma_{\emptyset}$ can be computed from 1 Hz data (Luo et al. 2020; Nguyen et al. 2019), 1 Hz data is relatively less available than 30s data (IGS 2021). Thus, in order to further facilitate the research on the scintillation, the parameters that can be computed from 30s data and are also able to characterize scintillation should be applied in global scintillation effect mitigation. MP and ROTI meet the two requirements. Investigation of the relationship between multipath and scintillation was initiated by Van Dierendonck et al. (1993), where multipath can lead to the inflation of scintillation and this was also observed by Romano et al. (2013). Then, the false observations of multipath caused by scintillation was also detected by Hancock et al. (2017). The relationship between ROTI and scintillation was also thoroughly investigated (Basu et al. 1999; Yang and Liu 2016; Carrano et al. 2019; Olwendo et al. 2018; Acharya and Majumdar 2019). All these studies resulted in the selection of MP and ROTI to characterize and mitigate scintillation in this thesis. Before using MP and ROTI to mitigate scintillation effects, the relationship between MP, ROTI and S4, σ_{ϕ} should be further investigated as the spatial relationship was still a research gap, especially for MP. Thus, the results in the first research chapter strengthened the conclusion that there is a relationship between MP, ROTI and scintillation parameters. In addition, the first research chapter also laid the theoretical basis for the third research chapter as the relationship between these parameters was the precondition for MP and ROTI to replace S4 and σ_{ϕ} to mitigate scintillation effect. Additionally, it was novel to research on the spatial relationship between MP, ROTI and S4, σ_{ϕ}, which could be more advantageous than the temporal relationship researched in most of previous studies. For

instance, it is possible to further develop maps generated in the first research chapter to scintillation risk maps that visualize the effect of scintillation, similar to results of Sreeja et al. (2011a) and Koulouri et al. (2020). Thus, the effect of scintillation on satellites can be evaluated based on the MP and ROTI maps with plotting paths of satellites. Based on that, GNSS users are able to visually select satellites not contaminated by scintillation for positioning and the scintillation effect can be mitigated based on this simple strategy.

In previous research, ROTI was the primary proxy to scintillation parameters, which was not able to completely replace S4 and σ_ϕ, however. This meant ROTI could only represent a subset of scintillation with certain characteristics. To more thoroughly research on scintillation, MP was proposed with necessity to characterize scintillation in addition to ROTI. The results in Chapter 4 indeed showed that MP was able to show some scintillation events that ROTI was unable to characterize. Thus, MP was worthy to be used as an additional parameter to ROTI in scintillation detection, prediction and mitigation. Furthermore, ROTI has been researched to represent scintillation events for decades, while the research on MP to characterize scintillation was initiated in recent years. Thus, previous research conducted on ROTI can also be similarly applied to MP to learn more about the theoretical relationship between MP and scintillation, which can be in the future work.

The relationship between MP and scintillation parameters resulted in the possibility of replacing S4 and σ_ϕ with MP. However, the relationship also led to the difficulty in distinguishing the event types, which meant the variability in parameters could be caused by either or both of multipath and scintillation events. Therefore, this led to the necessity of developing the distinguishing method in the second research chapter. Several researchers managed to achieve this objective (Olwendo et al. 2010; Spogli et al. 2014; Imam and Dovis 2020). However, scintillation parameters were necessary in the methods of Olwendo et al. (2010) and Imam and Dovis (2020), which were less available than standard parameters. In addition, all the three methods were not able to identify hybrid events and the method of Olwendo et al. (2010) could only be used to identify multipath event though it was able to quantify the inflation caused by multipath effect on S4, which was achieved with the methodology in the second research

chapter based on standard parameters. However, our method was relatively complicated based on a variety of graphs as compared with the automatic processing method of Imam and Dovis (2020), where the reduction of complexity can be researched in the future.

With the theoretical basis in the first research chapter and the distinguishing method in the second research chapter, the scintillation mitigation experiment can be conducted. With the strategies in the third research chapter, it was the first time to use MP and ROTI to effectively mitigate the scintillation effect on Precise Point Positioning (PPP). Several models were used in past methods such as the Conker model used by Aquino et al. (2007), its improved version Conker′ model used by Park et al. (2017) and its extended version α-μ model used by Sreeja et al. (2020). These models are capable of accurately modelling scintillation effect. However, it is easier to obtain parameters than these models, where the former is applied in this thesis. Meanwhile, the best improvement rate obtained based on MP and ROTI in this thesis was comparable to or even better than that acquired with past methods. Thus, the method proposed in this thesis facilitated the simplification of scintillation mitigation without reducing effectiveness. Therefore, it is feasible for researchers all over the world to research on scintillation without high-rate data. However, there is still room to further improve the methods developed in this thesis, which is discussed in section 7.4.

7.3. Outcomes

Based on the contribution of this thesis discussed in the previous section, it is possible to conclude that:

- The spatiotemporal relationship existed between MP, ROTI and S4, σ_{ϕ}. Scintillation can also lead to false alarm of MP.
- Different scintillation events could be represented by MP and ROTI. Applying both MP and ROTI could detect more scintillation events than using a single parameter of them.
- The correlation between MP and scintillation could be observed only when scintillation was intense while that between ROTI and scintillation could be detected

no matter when scintillation was active or not.

- By using the distinguishing methodology, multipath, scintillation and hybrid events could be identified at high elevation and the first two events could be identified at low elevation with the assistance of the reference station at a close range.
- The strategy that removed the observation with parameter values above the mild threshold (MT) or extreme threshold (ET) was proposed for the first time. This strategy was able to effectively mitigate scintillation effect on PPP with lower stability when the conventional weight strategy was able to less effectively mitigate scintillation effect on PPP with higher consistency.
- The performance of standard parameters was comparable to that of scintillation parameters in the observation removal and weight strategy.

Therefore, the objectives and thus the aim have been achieved through the research in this thesis.

7.4. Recommendations on future work

As explained in section 3.3.2, the fixed cutoff frequency of 0.1 Hz for drending σ_ϕ was found not to be reasonable. Therefore, the impact of different cutoff frequencies on the characterization of σ_ϕ could be investigated in the future work.

It was observed in the first research chapter that MP is more similar to S4 and ROTI is more related to σ_ϕ at the Brazil station. However, more data should be looked into and deeper reasons for this phenomenon should be investigated. If this conclusion is demonstrated based on the theoretical explanation, it is possible to respectively use MP and ROTI to represent S4 and σ_ϕ. Further, it is feasible to judge which of MP and ROTI should be used under each scintillation case so that more precise prediction and characterization can be obtained.

It has been noticed in the second research chapter that ROTI and MP cannot always represent scintillation. Thus, this suggests ROTI and MP are only affected by certain types of scintillation. In other words, the characteristics of scintillations that leads to variability in ROTI and MP are

still unknown, which needs further research.

In the third chapter, the satellite removal strategy was generally ineffective in scintillation mitigation. One possible reason is that multiple satellites are simultaneously affected by scintillation. Thus, removing a single affected satellite could not effectively remove scintillation effects. Whereas, this can be achieved with the observation removal strategy as it can remove multiple observations from different satellites at the same time. However, this could also lead to a dramatic increase of GDOP, which led to the low reliability of the observation removal strategy. Hence, the observation removal strategy did not work sometimes. To prevent the substantial change of GDOP, a possible way is to use data from multiple constellations. With more alternative satellites, the satellite geometry should not be severely affected when multiple observations are removed at the same time. Therefore, it is worthy to research the effect of applying multi-GNSS on the observation removal strategy in the future.

Furthermore, though the weight strategy is able to mitigate the scintillation effect slightly more substantially, the improvement is not as consistent as the observation removal strategy. Thus, it is possible that the weights put on observations can still be further modified through algorithms such as Bayesian optimization, gene algorithm, machine learning, deep learning etc., so that the weight and corresponding improvement can reach the optimal value.

Reference

50th Space Wing Public Affairs. (2011). 50 SW completes GPS constellation expansion. Available: https://www.schriever.spaceforce.mil/News/Article-Display/Article/277054/50-sw-completes-gps-constellation-expansion/ [Accessed 2021/9/27].

Aarons, J. (1985). Construction of a model of equatorial scintillation intensity. Radio Science, 20(3), 397-402. https://doi.org/10.1029/RS020i003p00397

Abdel-salam, M. A.-t. (2005). Precise point positioning using un-differenced code and carrier phase observations. Ph.D., University of Calgary.

Acharya, R., Majumdar, S. (2019). Statistical relation of scintillation index S4 with ionospheric irregularity index ROTI over Indian equatorial region. Advances in Space Research, 64(5), 1019-1033. https://doi.org/10.1016/j.asr.2019.05.018

Afifi, A., El-Rabbany, A. (2016). Un-differenced precise point positioning model using triple GNSS constellations. Cogent Geoscience, 2(1), 1223899. 10.1080/23312041.2016.1223899

Ahmed, W. A., Wu, F., Marlia, D., Ednofri, Zhao, Y. (2019). Mitigation of Ionospheric Scintillation Effects on GNSS Signals with VMD-MFDFA. Remote Sensing, 11(23). 10.3390/rs11232867

An, X., Meng, X., Jiang, W. (2020). Multi-constellation GNSS precise point positioning with multi-frequency raw observations and dual-frequency observations of ionospheric-free linear combination. Satellite Navigation, 1(1), 7. 10.1186/s43020-020-0009-x

Anderson, D. N. (1973). A theoretical study of the ionospheric F region equatorial anomaly—I. Theory. Planetary and Space Science, 21(3), 409-419. https://doi.org/10.1016/0032-0633(73)90040-8

Anderson, D. N., Forbes, J. M., Codrescu, M. (1989). A fully analytic, low- and middle-latitude ionospheric model. Journal of Geophysical Research: Space Physics, 94(A2), 1520-1524. https://doi.org/10.1029/JA094iA02p01520

Anderson, D. N., Mendillo, M., Herniter, B. (1987). A semi-empirical low-latitude ionospheric model. Radio Science, 22(2), 292-306. https://doi.org/10.1029/RS022i002p00292

Aquino, M., Dodson, A., deFranceschi, G., Alfonsi, L., Romano, V., Monico, J., Marques, H., Mitchell, C. (2007). Towards forecasting and mitigating ionospheric scintillation effects on GNSS. ELMAR 2007, IEEE, Zadar, Croatia, September 12-14, 63-67.

Aquino, M., Monico, J. F. G., Dodson, A. H., Marques, H., De Franceschi, G., Alfonsi, L., Romano, V., Andreotti, M. (2009). Improving the GNSS positioning stochastic model in the presence of ionospheric scintillation. Journal of Geodesy, 83(10), 953-966. 10.1007/s00190-009-0313-6

Ashby, N., Spilker, J. (1996). Introduction To Relativistic Effects On The Global Positioning System. Global Positioning System: Theory and Applications, Volume I. American Institute of Aeronautics and Astronautics.

Axelrad, P., Brown, R. G. (1996). GPS Navigation Algorithms. Global Positioning System: Theory and Applications, Volume I. American Institute of Aeronautics and Astronautics.

Bahadur, B., Nohutcu, M. (2018). PPPH: a MATLAB-based software for multi-GNSS precise point positioning analysis. GPS Solutions, 22(4), 113. 10.1007/s10291-018-0777-z

Banville, S., Langley, R. B., Saito, S., Yoshihara, T. (2010). Handling cycle slips in GPS data

during ionospheric plasma bubble events. Radio Science, 45(6). https://doi.org/10.1029/2010RS004415

Barnett, V., Lewis, T. (1994). Outliers in Statistical Data, Chichester, John Wiley & Sons.

Bassiri, S., Hajj, G. A. (1993). Higher-order ionospheric effects on the GPS observables and means of modeling them. Manuscripta Geodetica, 18, 280-289.

Basu, S., Basu, S., Hanson, W. B. (1981). The role of in-situ measurements in scintillation modelling. In: Symposium on the Effect of the Ionosphere on Radiowave Systems, Naval Research Laboratory, Washington, DC, April 14-16.

Basu, S., Groves, K. M., Basu, S., Sultan, P. J. (2002). Specification and forecasting of scintillations in communication/navigation links: current status and future plans. Journal of Atmospheric and Solar-Terrestrial Physics, 64(16), 1745-1754. https://doi.org/10.1016/S1364-6826(02)00124-4

Basu, S., Groves, K. M., Quinn, J. M., Doherty, P. (1999). A comparison of TEC fluctuations and scintillations at Ascension Island. Journal of Atmospheric and Solar-Terrestrial Physics, 61(16), 1219-1226. https://doi.org/10.1016/S1364-6826(99)00052-8

Basu, S., MacKenzie, E., Basu, S. (1988). Ionospheric constraints on VHF/UHF communications links during solar maximum and minimum periods. Radio Science, 23(3), 363-378. https://doi.org/10.1029/RS023i003p00363

Béniguel, Y. (2002). Global Ionospheric Propagation Model (GIM): A propagation model for scintillations of transmitted signals. Radio Science, 37(3), 4-1-4-13. https://doi.org/10.1029/2000RS002393

Béniguel, Y., et al. (2009). Ionospheric scintillation monitoring and modelling. Annals of Geophysics, 52(3-4), 391-416. https://doi.org/10.4401/ag-4595

Berkner, L. V., Wells, H. W. (1934). F-region ionosphere-investigations at low latitudes. Terrestrial Magnetism and Atmospheric Electricity, 39(3), 215-230. https://doi.org/10.1029/TE039i003p00215

Bhattacharyya, A., Beach, T. L., Basu, S., Kintner, P. M. (2000). Nighttime equatorial ionosphere: GPS scintillations and differential carrier phase fluctuations. Radio Science, 35(1), 209-224. https://doi.org/10.1029/1999RS002213

Bilich, A., Larson, K. M. (2007). Mapping the GPS multipath environment using the signal-to-noise ratio (SNR). Radio Science, 42(6). https://doi.org/10.1029/2007RS003652

Bilitza, D., Rawer, K., Bossy, L., Kutiev, I., Oyama, K. I., Leitinger, R., Kazimirovsky, E. (1990). International reference ionosphere 1990. National Space Science Data Center/World Data Center A for Rockets and Satellites.

Black, H. D., Eisner, A. (1984). Correcting satellite Doppler data for tropospheric effects. Journal of Geophysical Research: Atmospheres, 89(D2), 2616-2626. https://doi.org/10.1029/JD089iD02p02616

Bong, V. P., Abidin, W. A. W. Z., Abdullah, M., Ping, K. H., Masri, T., Bahari, S. A., Abba, I. (2015). GPS signal strength due to ionospheric scintillation: Preliminary models over Sarawak. 2015 International Conference on Space Science and Communication (IconSpace), August 10-12, 89-94.

Bougard, B., Simsky, A., Sleewaegen, J.-M., Park, J., Aquino, M., Spogli, L., Romano, V., Mendonça, M., Monico, G. (2013). CALIBRA: Mitigating the impact of ionospheric scintillation on Precise Point Positioning in Brazil. In Proceedings of the GNSS

Vulnerabilities and Solutions Conference, Baška, Krk Island, Croatia, April 18–20.
Brown, R. A., Hwang, P. (1997). Introduction to random signals and applied kalman filtering, New York, Wiley.
Cai, C., Liu, Z., Xia, P., Dai, W. (2013). Cycle slip detection and repair for undifferenced GPS observations under high ionospheric activity. GPS Solutions, 17(2), 247-260. 10.1007/s10291-012-0275-7
Calvert, W. (1962). Equatorial Spread F. Technical Note. Washington D.C.
Cander, L., Leitinger, R., Levy, M. F. (1998). Ionospheric Models Including the Auroral Environment. Proceedings of the ESA Workshop on Space Weather, ESA Space Environments and Effects Analysis Section, Noordwijk, the Netherlands, November 11-13.
Carrano, C. S., Groves, K. M., Rino, C. L. (2019). On the Relationship Between the Rate of Change of Total Electron Content Index (ROTI), Irregularity Strength (CkL), and the Scintillation Index (S4). Journal of Geophysical Research: Space Physics, 124(3), 2099-2112. https://doi.org/10.1029/2018JA026353
Carrano, C. S., Groves, K. M., Rino, C. L., Doherty, P. H. (2016). A technique for inferring zonal irregularity drift from single-station GNSS measurements of intensity (S4) and phase (σφ) scintillations. Radio Science, 51(8), 1263-1277. https://doi.org/10.1002/2015RS005864
Ciraolo, L., Azpilicueta, F., Brunini, C., Meza, A., Radicella, S. M. (2007). Calibration errors on experimental slant total electron content (TEC) determined with GPS. Journal of Geodesy, 81(2), 111-120. 10.1007/s00190-006-0093-1
Coker, C., Bust, G. S., Doe, R. A., Gaussiran Ii, T. L. (2004). High-latitude plasma structure and scintillation. Radio Science, 39(1). https://doi.org/10.1029/2002RS002833
Coker, C., Hunsucker, R., Lott, G. (1995). Detection of auroral activity using GPS satellites. Geophysical Research Letters, 22(23), 3259-3262. https://doi.org/10.1029/95GL03091
Colominas, M. A., Schlotthauer, G., Torres, M. E. (2014). Improved complete ensemble EMD: A suitable tool for biomedical signal processing. Biomedical Signal Processing and Control, 14, 19-29. https://doi.org/10.1016/j.bspc.2014.06.009
Conker, R. S., El-Arini, M. B., Hegarty, C. J., Hsiao, T. (2003). Modeling the effects of ionospheric scintillation on GPS/Satellite-Based Augmentation System availability. Radio Science, 38(1), 1-1-1-23. https://doi.org/10.1029/2000RS002604
Cressie, N. A. C. (1993). Statistics for Spatial Data, New York, NY, USA, John Wiley and Sons.
Curran, P. J., Atkinson, P. M. (1998). Geostatistics and remote sensing. Progress in Physical Geography: Earth and Environment, 22(1), 61-78. 10.1177/030913339802200103
D'Angelo, G., Spogli, L., Cesaroni, C., Sgrigna, V., Alfonsi, L., Aquino, M. H. O. (2015). GNSS data filtering optimization for ionospheric observation. Advances in Space Research, 56(11), 2552-2562. https://doi.org/10.1016/j.asr.2015.10.002
Dabove, P., Linty, N., Dovis, F. (2020). Analysis of multi-constellation GNSS PPP solutions under phase scintillations at high latitudes. Applied Geomatics, 12(1), 45-52. 10.1007/s12518-019-00269-4
Datta-Barua, S., Walter, T., Blanch, J., Enge, P. (2008). Bounding higher-order ionosphere errors for the dual-frequency GPS user. Radio Science, 43(5). https://doi.org/10.1029/2007RS003772
Davies, K. (1990). Solarterrestrial relationships. In: ENGINEERS, I. O. E. (ed.) Ionospheric Radio.

Peregrinus.
de Bakker, P. F., Tiberius, C. C. J. M. (2017). Real-time multi-GNSS single-frequency precise point positioning. GPS Solutions, 21(4), 1791-1803. https://doi.org/10.1007/s10291-017-0653-2
de Bakker, P. F., van der Marel, H., Tiberius, C. C. J. M. (2009). Geometry-free undifferenced, single and double differenced analysis of single frequency GPS, EGNOS and GIOVE-A/B measurements. GPS Solutions, 13(4), 305-314. 10.1007/s10291-009-0123-6
de Oliveira Moraes, A., Costa, E., de Paula, E. R., Perrella, W. J., Monico, J. F. G. (2014). Extended ionospheric amplitude scintillation model for GPS receivers. Radio Science, 49(5), 315-329. https://doi.org/10.1002/2013RS005307
de Oliveira Nascimento Brassarote, G., de Souza, E. M., Monico, J. F. G. (2017). S4 index: Does it only measure ionospheric scintillation? GPS Solutions, 22(1), 8. https://doi.org/10.1007/s10291-017-0666-x
de Paula, E. R., et al. (2019). Ionospheric irregularity behavior during the September 6–10, 2017 magnetic storm over Brazilian equatorial–low latitudes. Earth, Planets and Space, 71(42), 1-15. https://doi.org/10.1186/s40623-019-1020-z
Decker, D. T., Valladares, C. E., Sheehan, R., Basu, S., Anderson, D. N., Heelis, R. A. (1994). Modeling daytime F layer patches over Sondrestrom. Radio Science, 29(1), 249-268. https://doi.org/10.1029/93RS02866
Delay, S., Carrano, C., Groves, K., Doherty, P. (2015). A Statistical Analysis of GPS L1, L2, and L5 Tracking Performance During Ionospheric Scintillation. In: Proceedings of the ION 2015 Pacific PNT Meeting, Institute of Navigation, Honolulu, Hawaii, USA, April 20-23, 1-9.
Demyanov, V., Sergeeva, M., Fedorov, M., Ishina, T., Gatica-Acevedo, V. J., Cabral-Cano, E. (2020). Comparison of TEC Calculations Based on Trimble, Javad, Leica, and Septentrio GNSS Receiver Data. Remote Sensing, 12(19), 3268. https://doi.org/10.3390/rs12193268
Demyanov, V. V., Yasyukevich, Y. V., Jin, S., Sergeeva, M. A. (2019). The Second-Order Derivative of GPS Carrier Phase as a Promising Means for Ionospheric Scintillation Research. Pure and Applied Geophysics, 176(10), 4555-4573. https://doi.org/10.1007/s00024-019-02281-6
Dey, A., Chhibba, R., Ratnam, D. V., Sharma, N. (2021). A combined iCEEMDAN and VMD method for mitigating the impact of ionospheric scintillation on GNSS signals. Acta Geophysica, 69(5), 1933-1948. 10.1007/s11600-021-00629-y
Dierendonck, A. J. V., Arbesser-Rastburg, B. (2004). Measuring Ionospheric Scintillation in the Equatorial Region Over Africa, Including Measurements From SBAS Geostationary Satellite Signals. Proceedings of the 17th International Technical Meeting of the Satellite Division of The Institute of Navigation (ION GNSS 2004), Salt Lake City, CA, September 21 - 24 316-324.
Doherty, P. H., Delay, S. H., Valladares, C. E., Klobuchar, J. A. (2003). Ionospheric Scintillation Effects on GPS in the Equatorial and Auroral Regions. NAVIGATION, 50(4), 235-245. https://doi.org/10.1002/j.2161-4296.2003.tb00332.x
Dragomiretskiy, K., Zosso, D. (2014). Variational Mode Decomposition. IEEE Transactions on Signal Processing, 62(3), 531-544. 10.1109/TSP.2013.2288675
Dungey, J. W. (1956). Convective diffusion in the equatorial F region. Journal of Atmospheric and Terrestrial Physics, 9(5), 304-310. https://doi.org/10.1016/0021-9169(56)90148-9

Duník, J., Straka, O., Kost, O., Havlík, J. (2017). Noise covariance matrices in state-space models: A survey and comparison of estimation methods—Part I. International Journal of Adaptive Control and Signal Processing, 31(11), 1505-1543. https://doi.org/10.1002/acs.2783

Elmas, Z. (2013). Exploiting New GNSS Signals to Monitor, Model and Mitigate the Ionospheric Effects in GNSS. Ph.D., The University of Nottingham, Nottingham, UK.

Elmas, Z., Aquino, M., Forte, B. (2011). The impact of ionospheric scintillation on the GNSS receiver signal tracking performance and measurement accuracy. 2011 XXXth URSI General Assembly and Scientific Symposium, IEEE, Istanbul, Turkey, August 13-20.

Eltrass, A., Scales, W. A., Erickson, P. J., Ruohoniemi, J. M., Baker, J. B. H. (2016). Investigation of the role of plasma wave cascading processes in the formation of midlatitude irregularities utilizing GPS and radar observations. Radio Science, 51(6), 836-851. https://doi.org/10.1002/2015RS005790

Estey, L., Meertens, C. (2014). Teqc Tutorial: Basic of Teqc Use and Teqc Products. Boulder, CO.

Estey, L. H., Meertens, C. M. (1999). TEQC: The Multi-Purpose Toolkit for GPS/GLONASS Data. GPS Solutions, 3(1), 42-49. https://doi.org/10.1007/PL00012778

Falletti, E., Rao, M., Savasta, S. (2011). The Kalman Filter and Its Applications in GNSS and INS. In: SEYED A. (REZA) ZEKAVAT, R. M. B. (ed.) Handbook of Position Location: Theory, Practice, and Advances. Hoboken, NJ: Wiley.

Fang, H., Yang, S., Wang, S. (2012). Spectra of L-band ionospheric scintillation over Nanjing. Chinese Science Bulletin, 57(25), 3375-3380. 10.1007/s11434-012-5365-y

Farooq, S. Z., Yang, D., Ada, E. N. (2020). A Cycle Slip Detection Framework for Reliable Single Frequency RTK Positioning. Sensors, 20(1). 10.3390/s20010304

Franke, S. J., Liu, C. H. (1985). Modeling of equatorial multifrequency scintillation. Radio Science, 20(3), 403-415. https://doi.org/10.1029/RS020i003p00403

Fremouw, E. J., Rino, C. L. (1973). An empirical model for average F-layer scintillation at VHF/UHF. Radio Science, 8(3), 213-222. https://doi.org/10.1029/RS008i003p00213

Fremouw, E. J., Secan, J. A. (1984). Modeling and scientific application of scintillation results. Radio Science, 19(3), 687-694. https://doi.org/10.1029/RS019i003p00687

Geng, W., Huang, W., Liu, G., Aa, E., Liu, S., Chen, Y., Luo, B. (2020). Generation of ionospheric scintillation maps over Southern China based on Kriging method. Advances in Space Research, 65(12), 2808-2820. https://doi.org/10.1016/j.asr.2020.03.035

Ghobadi, H., Spogli, L., Alfonsi, L., Cesaroni, C., Cicone, A., Linty, N., Romano, V., Cafaro, M. (2020). Disentangling ionospheric refraction and diffraction effects in GNSS raw phase through fast iterative filtering technique. GPS Solutions, 24(3), 85. 10.1007/s10291-020-01001-1

Goovaerts, P. (1997). Geostatistics for natural resources evaluation, Oxford, UK, Oxford University Press.

Guo, F., Zhang, X. (2014). Adaptive robust Kalman filtering for precise point positioning. Measurement Science and Technology, 25(10), 105011. 10.1088/0957-0233/25/10/105011

Guo, K., Zhao, Y., Liu, Y., Wang, J., Zhang, C., Zhu, Y. (2017). Study of ionospheric scintillation characteristics in Australia with GNSS during 2011–2015. Advances in Space Research, 59(12), 2909-2922. https://doi.org/10.1016/j.asr.2017.03.007

Hamm, N. A. S., Atkinson, P. M., Milton, E. J. (2012). A per-pixel, non-stationary mixed model

for empirical line atmospheric correction in remote sensing. Remote Sensing of Environment, 124, 666-678. https://doi.org/10.1016/j.rse.2012.05.033

Hancock, C. M., Ligt, H. D., Xu, T. (2017). The possibility of using GNSS quality control parameters to assess ionospheric scintillation errors. In Proceedings of the Fig WorkingWeek, Helsinki, Finland, May 29 – June 2.

He, Z., Zhao, H., Feng, W. (2016). The Ionospheric Scintillation Effects on the BeiDou Signal Receiver. Sensors, 16(11). 10.3390/s16111883

Hegarty, C., El-Arini, M. B., Kim, T., Ericson, S. (2001). Scintillation modeling for GPS-Wide Area Augmentation System receivers. Radio Science, 36(5), 1221-1231. https://doi.org/10.1029/1999RS002425

Hofmann-Wellenhof, B., Lichtenegger, H., Wasle, E. (2008). GNSS — Global Navigation Satellite Systems: GPS, GLONASS, Galileo, and more, Vienna, Springer.

Honório, B. C. Z., de Matos, M. C., Vidal, A. C. (2017). Progress on empirical mode decomposition-based techniques and its impacts on seismic attribute analysis. Interpretation, 5(1), SC17-SC28. 10.1190/INT-2016-0079.1

Huang, N. E., Shen, Z., Long, S. R., Wu, M. C., Shih, H. H., Zheng, Q., Yen, N.-C., Tung, C. C., Liu, H. H. (1998). The empirical mode decomposition and the Hilbert spectrum for nonlinear and non-stationary time series analysis. Proceedings of the Royal Society of London. Series A: Mathematical, Physical and Engineering Sciences, 454(1971), 903-995. 10.1098/rspa.1998.0193

Humphreys, T. E., Psiaki, M. L., Kintner, P. M. (2010). Modeling the effects of ionospheric scintillation on GPS carrier phase tracking. IEEE Transactions on Aerospace and Electronic Systems, 46(4), 1624 - 1637. 10.1109/TAES.2010.5595583

IGS. (2021). International GNSS Service [Online]. Available: https://igs.org/ [Accessed 2021/11/23].

Imam, R., Dovis, F. (2020). Distinguishing Ionospheric Scintillation from Multipath in GNSS Signals Using Bagged Decision Trees Algorithm. In: 2020 IEEE International Conference on Wireless for Space and Extreme Environments (WiSEE 2020), Vicenza, Italy, October 12-14, 83-88.

Jean, M. H., Conroy, J. P., Scales, W. A. (2017). Multi-constellation GNSS scintillation at mid-latitudes. 2017 XXXIInd General Assembly and Scientific Symposium of the International Union of Radio Science (URSI GASS), Montreal, QC, Canada, August 19-26 1-4.

Ji, S., Chen, W., Weng, D., Wang, Z., Ding, X. (2013). A study on cycle slip detection and correction in case of ionospheric scintillation. Advances in Space Research, 51(5), 742-753. https://doi.org/10.1016/j.asr.2012.10.012

Jiao, Y., Morton, Y. T. (2015). Comparison of the effect of high-latitude and equatorial ionospheric scintillation on GPS signals during the maximum of solar cycle 24. Radio Science, 50(9), 886-903. https://doi.org/10.1002/2015RS005719

Jiao, Y., Morton, Y. T., Taylor, S., Pelgrum, W. (2013). Characterization of high-latitude ionospheric scintillation of GPS signals. Radio Science, 48(6), 698-708. https://doi.org/10.1002/2013RS005259

Karaim, M., Elsheikh, M., Noureldin, A. (2018). GNSS Error Sources. In: RUSTAMOV, R. B. & HASHIMOV, A. M. (eds.) Multifunctional Operation and Application of GPS.

IntechOpen.
Kaur, A., Kaur, L., Gupta, S. (2012). Image Recognition using Coefficient of Correlation and Structural SIMilarity Index in Uncontrolled Environment. International Journal of Computer Applications, 59(5), 32-39. 10.5120/9546-3999
Kelley, M. C. (1989a). Chapter 1 - Introductory and Background Material. In: KELLEY, M. C. (ed.) The Earth's Ionosphere. Academic Press.
Kelley, M. C. (1989b). Chapter 4 - Equatorial Plasma Instabilities. In: KELLEY, M. C. (ed.) The Earth's Ionosphere. Academic Press.
Keskinen, M. J., Ossakow, S. L. (1983). Theories of high-latitude ionospheric irregularities: A review. Radio Science, 18(6), 1077-1091. https://doi.org/10.1029/RS018i006p01077
Khanafseh, S., et al. (2018). GNSS Multipath Error Modeling for Automotive Applications. Proceedings of the 31st International Technical Meeting of the Satellite Division of The Institute of Navigation (ION GNSS+ 2018), Miami, Florida, September 24-28, 1573 - 1589.
Kintner, P. M., Ledvina, B. M., de Paula, E. R. (2007). GPS and ionospheric scintillations. Space Weather, 5(9). https://doi.org/10.1029/2006SW000260
Klobuchar, J. A. (1996). Ionospheric Effects On Gps. Global Positioning System: Theory and Applications, Volume I. American Institute of Aeronautics and Astronautics.
Kouba, J., Lahaye, F., Tétreault, P. (2017). Precise Point Positioning. Springer handbook of global navigation satellite systems. 1st ed.: Springer International Publishing.
Koulouri, A., Smith, N. D., Vani, B. C., Rimpiläinen, V., Astin, I., Forte, B. (2020). Methodology to estimate ionospheric scintillation risk maps and their contribution to position dilution of precision on the ground. Journal of Geodesy, 94(2), 22. 10.1007/s00190-020-01344-0
Langley, R. B. (1999). Dilution of Precision. GPS World.
Li, C., Hancock, C. M., Hamm, N. A. S., Sreeja, V., You, C. (2020). Analysis of the Relationship between Scintillation Parameters, Multipath and ROTI. Sensors, 20(10), 2877. https://doi.org/10.3390/s20102877
Li, G., Ning, B., Ren, Z., Hu, L. (2010). Statistics of GPS ionospheric scintillation and irregularities over polar regions at solar minimum. GPS Solutions, 14(4), 331-341. 10.1007/s10291-009-0156-x
Linty, N., Minetto, A., Dovis, F., Spogli, L. (2018). Effects of Phase Scintillation on the GNSS Positioning Error During the September 2017 Storm at Svalbard. Space Weather, 16(9), 1317-1329. https://doi.org/10.1029/2018SW001940
Lonchay, M. (2019). Ingestion of Ionospheric Scintillation Skymaps into GNSS Algorithms. Ph.D., Université de Liège.
Lulu, W., Zaimin, H., Zhenxing, H., Yuanyuan, H., Gang, L. (2020). Single-chain hyperbolic positioning GDOP calculation based on longitude transformation method. Journal of Time and Frequency, 43(3), 196-203.
Luo, X., Gu, S., Lou, Y., Cai, L., Liu, Z. (2020). Amplitude scintillation index derived from C/N0 measurements released by common geodetic GNSS receivers operating at 1 Hz. Journal of Geodesy, 94, 27. https://doi.org/10.1007/s00190-020-01359-7
Luo, X., Liu, Z., Lou, Y., Gu, S., Chen, B. (2017). A study of multi-GNSS ionospheric scintillation and cycle-slip over Hong Kong region for moderate solar flux conditions. Advances in Space Research, 60(5), 1039-1053. https://doi.org/10.1016/j.asr.2017.05.038

Marques, H. A., Marques, H. A. S., Aquino, M., Sreeja, V., Monico, J. F. G. (2018). Accuracy assessment of Precise Point Positioning with multi-constellation GNSS data under ionospheric scintillation effects. J. Space Weather Space Clim., 8(A15).

Marques, H. A. S., Monico, J. F. G., Marques, H. A. (2016). Performance of the L2C civil GPS signal under various ionospheric scintillation effects. GPS Solutions, 20(2), 139-149. 10.1007/s10291-015-0472-2

Mathworks. (2019). MATLAB Function Reference. Available: https://www.mathworks.com/help/pdf_doc/matlab/matlab_refbook.pdf

McCaffrey, A. M., Jayachandran, P. T. (2017). Spectral characteristics of auroral region scintillation using 100 Hz sampling. GPS Solutions, 21(4), 1883-1894. https://doi.org/10.1007/s10291-017-0664-z

McCaffrey, A. M., Jayachandran, P. T. (2019). Determination of the Refractive Contribution to GPS Phase "Scintillation". Journal of Geophysical Research: Space Physics, 124(2), 1454-1469. https://doi.org/10.1029/2018JA025759

Melachroinos, S. A., et al. (2008). Ocean tide loading (OTL) displacements from global and local grids: comparisons to GPS estimates over the shelf of Brittany, France. Journal of Geodesy, 82(6), 357-371. 10.1007/s00190-007-0185-6

Mendillo, M., Klobuchar, J. A. (2006). Total electron content: Synthesis of past storm studies and needed future work. Radio Science, 41(5). https://doi.org/10.1029/2005RS003394

Michael, J., Maurice, R., David, S., Erich, M., Daniel, N. (2005). Estimation of ionospheric TEC and Faraday rotation for L-band SAR. SPIE 5979, Remote Sensing of Clouds and the Atmosphere X, Bruges, Belgium, September 19-22.

Millman, G. H. (1965). Atmospheric Effects on Radio Wave Propagation
In: BERKOWITZ, R. S. (ed.) Modern Radar, Analysis, Evaluation, and System Design. New York: John Wiley & Sons.

Millman, G. H., Reinsmith, G. M. (1974). An Analysis of the Incoherent Scatter-Faraday Rotation Technique for Ionospheric Propagation Error Correction. General Electric Technical Information Series Report.

Mireault, Y., Tétreault, P., Lahaye, F., Héroux, P., Kouba, J. (2008). Online precise point positioning: A new, timely service from Natural Resources Canada. GPS World, 19(9), 59-64.

Miriyala, S., Koppireddi, P. R., Chanamallu, S. R. (2015). Robust detection of ionospheric scintillations using MF-DFA technique. Earth, Planets and Space, 67(1), 98. 10.1186/s40623-015-0268-1

Mohammed, J. J. (2017). Precise Point Positioning (PPP): GPS vs. GLONASS and GPS+GLONASS with an alternative strategy for tropospheric Zenith Total Delay (ZTD) estimation. Ph.D., University of Nottingham.

Mushini, S. C., Jayachandran, P. T., Langley, R. B., MacDougall, J. W., Pokhotelov, D. (2012). Improved amplitude- and phase-scintillation indices derived from wavelet detrended high-latitude GPS data. GPS Solutions, 16(3), 363-373. 10.1007/s10291-011-0238-4

NASA. (2021). The Effects of Earth's Upper Atmosphere on Radio Signals. The Radio JOVE Project [Online]. Available: https://radiojove.gsfc.nasa.gov/education/materials/iono.htm [Accessed 2022/07/22].

National Oceanic and Atmospheric Administration. (2021). GPS Modernization. Available:

https://www.gps.gov/systems/gps/modernization/ [Accessed 2021/09/27].

Ng, J. (2010). First Block 2F GPS Satellite Launched, Needed to Prevent System Failure. Science [Online]. Available: https://web.archive.org/web/20170628162240/http://www.dailytech.com/First+Block+2F+GPS+Satellite+Launched+Needed+to+Prevent+System+Failure/article18483.htm.

Nguyen, V. K., Rovira-Garcia, A., Juan, J. M., Sanz, J., González-Casado, G., La, T. V., Ta, T. H. (2019). Measuring phase scintillation at different frequencies with conventional GNSS receivers operating at 1 Hz. Journal of Geodesy, 93(10), 1985-2001. https://doi.org/10.1007/s00190-019-01297-z

Noureldin, A., Karamat, T. B., Georgy, J. (2013). Global Positioning System. In: NOURELDIN, A., KARAMAT, T. B. & GEORGY, J. (eds.) Fundamentals of Inertial Navigation, Satellite-based Positioning and their Integration. Berlin, Heidelberg: Springer Berlin Heidelberg.

Odongo, V. O., Hamm, N. A. S., Milton, E. J. (2014). Spatio - temporal assessment of Tuz Gölü, Turkey as a potential radiometric vicarious calibration site. Remote sensing, 6(3), 2494-2513. 10.3390/rs6032494

Olwendo, J., Baki, P., Mito, C., Doherty, P. (2010). Elimination of superimposed Multipath effects on Scintillations index on solar quiet ionosphere at Low Latitude over the Kenyan Airspace from a lone Positioned SCINDA system. In: Proceedings of the 23rd International Technical Meeting of the Satellite Division of the Institute of Navigation, the Institute of Navigation, Portland, Oregon, USA, September 21-24, 386-392.

Olwendo, J. O., Cilliers, P., Weimin, Z., Ming, O., Yu, X. (2018). Validation of ROTI for Ionospheric Amplitude Scintillation Measurements in a Low-Latitude Region Over Africa. Radio Science, 53(7), 876-887. https://doi.org/10.1029/2017RS006391

Pan, Y., Jin, M., Zhang, S., Deng, Y. (2021). TEC Map Completion Through a Deep Learning Model: SNP-GAN. Space Weather, 19(11), e2021SW002810. https://doi.org/10.1029/2021SW002810

Park, J., Sreeja, V., Aquino, M., Yang, L., Cesaroni, C. (2017). Mitigation of Ionospheric Effects on GNSS Positioning at Low Latitudes. NAVIGATION, 64(1), 67-74. https://doi.org/10.1002/navi.177

Pebesma, E. J. (2004). Multivariable geostatistics in S: the gstat package. Computers & Geosciences, 30(7), 683-691. https://doi.org/10.1016/j.cageo.2004.03.012

Pi, X., Iijima, B. A., Lu, W. (2017). Effects of Ionospheric Scintillation on GNSS-Based Positioning. NAVIGATION, 64(1), 3-22. https://doi.org/10.1002/navi.182

Pi, X., Mannucci, A. J., Lindqwister, U. J., Ho, C. M. (1997). Monitoring of global ionospheric irregularities using the Worldwide GPS Network. Geophysical Research Letters, 24(18), 2283-2286. https://doi.org/10.1029/97GL02273

Priyadarshi, S. (2015). A Review of Ionospheric Scintillation Models. Surveys in Geophysics, 36(2), 295-324. 10.1007/s10712-015-9319-1

Priyadarshi, S. (2020). Ionospheric Scintillation Modeling Needs and Tricks. In: DEMYANOV, V. & BECEDAS, J. (eds.) Satellites Missions and Technologies for Geosciences. London, UK: IntechOpen.

Rino, C. L. (1979a). A power law phase screen model for ionospheric scintillation: 1. Weak scatter. Radio Science, 14(6), 1135-1145. https://doi.org/10.1029/RS014i006p01135

Rino, C. L. (1979b). A power law phase screen model for ionospheric scintillation: 2. Strong scatter. Radio Science, 14(6), 1147-1155. https://doi.org/10.1029/RS014i006p01147

Roberts, G. W. (2019). Noise comparison of triple frequency GNSS carrier phase, doppler and pseudorange observables. Measurement, 144, 328-344. https://doi.org/10.1016/j.measurement.2019.05.011

Roberts, G. W., Fossá, S., Jepsen, C. (2019). Temporal characteristics of triple-frequency GNSS scintillation during a visible aurora borealis event over the Faroe Islands amid a period of very low solar activity. GPS Solutions, 23(3), 89. 10.1007/s10291-019-0881-8

Rodrigues, F. S., Moraes, A. O. (2019). ScintPi: A Low-Cost, Easy-to-Build GPS Ionospheric Scintillation Monitor for DASI Studies of Space Weather, Education, and Citizen Science Initiatives. Earth and Space Science, 6(8), 1547-1560. https://doi.org/10.1029/2019EA000588

Romano, V., Pau, S., Pezzopane, M., Zuccheretti, E., Zolesi, B., de Franceschi, G., Locatelli, S. (2008). The electronic Space Weather upper atmosphere (eSWua) project at INGV: advancements and state of the art. Annales Geophysicae, 26(2), 345-351. 10.5194/angeo-26-345-2008

Romano, V., Spogli, L., Aquino, M., Dodson, A., Hancock, C., Forte, B. (2013). GNSS station characterisation for ionospheric scintillation applications. Advances in Space Research, 52(7), 1237-1246. https://doi.org/10.1016/j.asr.2013.06.028

Schunk, R. W. (1988). A mathematical model of the middle and high latitude ionosphere. pure and applied geophysics, 127(2), 255-303. 10.1007/BF00879813

Secan, J. A., Bussey, R. M., Fremouw, E. J., Basu, S. (1995). An improved model of equatorial scintillation. Radio Science, 30(3), 607-617. https://doi.org/10.1029/94RS03172

Shanmugam, S., Jones, J., MacAulay, A., Van Dierendonck, A. J. (2012). Evolution to Modernized GNSS Ionospheric Scintillation and TEC Monitoring. Proceedings of IEEE/ION PLANS 2012, Myrtle Beach Marriott Resort & Spa, South Carolina April 24 - 26 265-273.

Siejka, Z. (2018). Validation of the Accuracy and Convergence Time of Real Time Kinematic Results Using a Single Galileo Navigation System. Sensors (Basel, Switzerland), 18(8). 10.3390/s18082412

Skone, S., Knudsen, K., de Jong, M. (2001). Limitations in GPS receiver tracking performance under ionospheric scintillation conditions. Physics and Chemistry of the Earth, Part A: Solid Earth and Geodesy, 26(6), 613-621. https://doi.org/10.1016/S1464-1895(01)00110-7

Smyrnaios, M., Schön, S., Nicolás, M. L. (2013). Multipath Propagation, Characterization and Modeling in GNSS. In: JIN, S. (ed.) Geodetic Sciences - Observations, Modeling and Applications. InTech.

Space and Missile Systems Center Public Affairs. (2021). SMC and its mission partners successfully launch Fifth GPS III satellite. Available: https://www.losangeles.spaceforce.mil/News/Article-Display/Article/2662368/smc-and-its-mission-partners-successfully-launch-fifth-gps-iii-satellite/ [Accessed 2021/09/27].

Špánik, P., Hefty, J. (2017). Multipath detection with the combination of SNR measurements – Example from urban environment. Geodesy and Cartography, 66(2), 305-316. 10.1515/geocart-2017-0020

Spilker, J. (1996). Satellite Constellation And Geometric Dilution Of Precision. Global Positioning System: Theory and Applications, Volume I. American Institute of

Aeronautics and Astronautics.
Spogli, L., et al. (2014). A Filtering Method Developed to Improve GNSS Receiver Data Quality in the CALIBRA Project. In: NOTARPIETRO, R., DOVIS, F., FRANCESCHI, G. D. & AQUINO, M. (eds.) Mitigation of Ionospheric Threats to GNSS: an Appraisal of the Scientific and Technological Outputs of the TRANSMIT Project. London: IntechOpen.
Sreeja, V., Aquino, M., Elmas, Z. G. (2011a). Impact of ionospheric scintillation on GNSS receiver tracking performance over Latin America: Introducing the concept of tracking jitter variance maps. Space Weather, 9(10). https://doi.org/10.1029/2011SW000707
Sreeja, V., Aquino, M., Marques, H. A., Moraes, A. (2020). Mitigation of ionospheric scintillation effects on GNSS precise point positioning (PPP) at low latitudes. Journal of Geodesy, 94(2), 15. 10.1007/s00190-020-01345-z
Sreeja, V., Haralambous, H., Aquino, M. (2017). Observations of quiet-time moderate midlatitude L-band scintillation in association with plasma bubbles. GPS Solutions, 21(3), 1113-1124. 10.1007/s10291-016-0598-x
Sreeja, V. V., et al. (2011b). Tackling ionospheric scintillation threat to GNSS in Latin America. Journal Space Weather Space Climate, 1, A05. https://doi.org/10.1051/swsc/2011005
Stix, M. (2002). Characteristics of the Sun. In: STIX, M. (ed.) The Sun. Berlin, Heidelberg: Springer.
Susi, M., Andreotti, M., Aquino, M. (2014). Kalman Filter Based PLL Robust Against Ionospheric Scintillation. In: NOTARPIETRO, R., DOVIS, F., FRANCESCHI, G. D. & AQUINO, M. (eds.) Mitigation of Ionospheric Threats to GNSS: an Appraisal of the Scientific and Technological Outputs of the TRANSMIT Project. London, UK: IntechOpen.
Tanir Kayikçi, E., Karaaslan, Ö. (2017). Comparison of Least-Squares and Kalman Filter Solutions From Different VLBI Analysis Centers. In: HAAS, R. & ELGERED, G., eds. 23rd European VLBI Group for Geodesy and Astrometry Working Meeting, Gothenburg, Sweden, May 15-19.
van der Meer, F. (2012). Remote-sensing image analysis and geostatistics. International Journal of Remote Sensing 33(18), 5644–5676.
Van Dierendonck, A. J., Klobuchar, J. A., Hua, Q. (1993). Ionospheric Scintillation Monitoring Using Commercial Single Frequency C/A Code Receivers. In Proceedings of the 6th International Technical Meeting of the Satellite Division of the Institute of Navigation, Salt Lake City, UT, USA, September 22–24, 1333-1342.
Vani, B. C., Forte, B., Monico, J. F. G., Skone, S., Shimabukuro, M. H., Moraes, A. d. O., Portella, I. P., Marques, H. A. (2019). A Novel Approach to Improve GNSS Precise Point Positioning During Strong Ionospheric Scintillation: Theory and Demonstration. IEEE Transactions on Vehicular Technology, 68(5), 4391-4403. 10.1109/TVT.2019.2903988
Vilà-Valls, J., Linty, N., Closas, P., Dovis, F., Curran, J. T. (2020). Survey on signal processing for GNSS under ionospheric scintillation: Detection, monitoring, and mitigation. NAVIGATION, 67(3), 511-536. https://doi.org/10.1002/navi.379
Warren, D. L. M., Raquet, J. F. (2003). Broadcast vs. precise GPS ephemerides: a historical perspective. GPS Solutions, 7(3), 151-156. 10.1007/s10291-003-0065-3
Webster, R., Atteia, O., Dubois, J. P. (1994). Coregionalization of trace metals in the soil in the Swiss Jura. European Journal of Soil Science, 45(2), 205-218. https://doi.org/10.1111/j.1365-2389.1994.tb00502.x

Webster, R., Oliver, M. (2008). Geostatistics for Environmental Scientists, Chichester, UK, John Wiley and Sons.

Wernik, A. W., Alfonsi, L., Materassi, M. (2007). Scintillation modeling using in situ data. Radio Science, 42(1). https://doi.org/10.1029/2006RS003512

Wu, Z., Huang, N. E. (2009). ENSEMBLE EMPIRICAL MODE DECOMPOSITION: A NOISE-ASSISTED DATA ANALYSIS METHOD. Advances in Adaptive Data Analysis, 01(01), 1-41. 10.1142/S1793536909000047

Xiang, Y., Gao, Y., Li, Y. (2020). Reducing convergence time of precise point positioning with ionospheric constraints and receiver differential code bias modeling. Journal of Geodesy, 94(1), 8. 10.1007/s00190-019-01334-x

Xu, G. (2007). GPS Observables. GPS: Theory, Algorithms and Applications. 2nd ed. Berlin: Springer-Verlag Berlin Heidelberg.

Yacoub, M. D. (2007). The α-μ Distribution: A Physical Fading Model for the Stacy Distribution. IEEE Transactions on Vehicular Technology, 56(1), 27-34. 10.1109/TVT.2006.883753

Yang, Z., Liu, Z. (2016). Correlation between ROTI and Ionospheric Scintillation Indices using Hong Kong low-latitude GPS data. GPS Solutions, 20(4), 815-824. https://doi.org/10.1007/s10291-015-0492-y

Yeh, J.-R., Shieh, J.-S., Huang, N. E. (2010). COMPLEMENTARY ENSEMBLE EMPIRICAL MODE DECOMPOSITION: A NOVEL NOISE ENHANCED DATA ANALYSIS METHOD. Advances in Adaptive Data Analysis, 02(02), 135-156. 10.1142/S1793536910000422

Yokoyama, T., Jin, H., Shinagawa, H. (2015). West wall structuring of equatorial plasma bubbles simulated by three-dimensional HIRB model. Journal of Geophysical Research: Space Physics, 120(10), 8810-8816. https://doi.org/10.1002/2015JA021799

Yuan, Y. (2000). 基于 GPS 的电离层监测及延迟改正理论与方法的研究. Ph.D., 中国科学院测量与地球物理研究所.

Zhang, Q., Zhao, L., Zhao, L., Zhou, J. (2018). An Improved Robust Adaptive Kalman Filter for GNSS Precise Point Positioning. IEEE Sensors Journal, 18(10), 4176-4186. 10.1109/JSEN.2018.2820097

Zhang, X., Li, P., Tu, R., Lu, X., Ge, M., Schuh, H. (2020). Automatic Calibration of Process Noise Matrix and Measurement Noise Covariance for Multi-GNSS Precise Point Positioning. Mathematics, 8(4). 10.3390/math8040502

Zhang, Y., Hamm, N. A. S., Meratnia, N., Stein, A., van de Voort, M., Havinga, P. J. M. (2012). Statistics-based outlier detection for wireless sensor networks. International Journal of Geographical Information Science, 26(8), 1373-1392. 10.1080/13658816.2012.654493

Zhou, W., Bovik, A. C., Sheikh, H. R., Simoncelli, E. P. (2004). Image quality assessment: from error visibility to structural similarity. IEEE Transactions on Image Processing, 13(4), 600-612. 10.1109/TIP.2003.819861

Zumberge, J. F., Heflin, M. B., Jefferson, D. C., Watkins, M. M., Webb, F. H. (1997). Precise point positioning for the efficient and robust analysis of GPS data from large networks. Journal of Geophysical Research: Solid Earth, 102(B3), 5005-5017. https://doi.org/10.1029/96JB03860

Appendix 1: Supplementary figures for Chapter 5

Appendix 2: Supplementary tables for Chapter 6